Computational investigations of the speciation of Sr^{2+} in aqueous solution, and its interactions with the hydrated brucite (0001) surface

Eszter Makkos

A thesis submitted for the degree of

Doctor of Philosophy in Computational Chemistry

Department of Chemistry

University College London

April, 2017

I, Eszter Makkos confirm that the work presented in this thesis is my own. Where information has been derived from other sources, I confirm that this has been indicated in the thesis.

Abstract

The fundamental objective of this research project was to develop a computational model, using high-level quantum chemical techniques based on density functional theory (DFT), which is able to describe the aquo and hydroxide complexes of strontium and their interactions with hydrated brucite surfaces, aiming to create a general approach which can be subsequently modified for the investigation of other radioactive ions/surfaces. The first two chapters of this PhD thesis are a general introduction on the project's industrial relevance and on the computational methodology used. The subject of this study is strongly related to the decommissioning of the UK's nuclear legacy fuel storage ponds and therefore the thesis is organised such that, through the three main steps of the computational investigation, it eventually leads to an industrially relevant main conclusion.

In the third chapter, the possible strontium hydroxide complexes in aqueous environment have been investigated, in order to establish likely candidate species for the interaction of nuclear fission-generated strontium with the hydrated brucite surfaces in high pH spent nuclear fuel storage ponds. A combination of the COSMO continuum solvation model and one or two shells of explicit water molecules are employed for describing accurately the hydrolysis of Sr^{2+}.

The next chapter presents the periodic electrostatic embedded cluster model, developed for the brucite (0001) surface to be employed in the study of the adsorption reactions. Using the periodic electrostatic embedded cluster method (PEECM), implemented in the TURBOMOLE code, we have created a quantum chemically treated cluster in an infinite array of point charges and validated this surface model by exploring the adsorption of Sr^{2+} and other s block cations on bare and hydrated surfaces, comparing the PEECM data with those from a periodic DFT study using the CRYSTAL code.

In the fifth chapter, the results of the previous two chapters are combined to describe the Sr-surface interactions as realistically as possible. A theoretical reaction was created, in which the energy of the adsorbed Sr^{2+} ion on a hydrated brucite surface was compared with the energy of a solvated Sr^{2+} in the bulk solution, i.e. with the previously identified strontium complexes in aqueous phase. To achieve this, the PEECM model was extended with one and two layers of water molecules both in the quantum mechanical and point charge region, whose geometries are based on previous molecular dynamics studies. Several possible complexes are identified both in the presence or absence of solvated OH^- groups with different Sr-surface distances and complex conformation, and their adsorption energies were calculated in order to evaluate the general strength of the possible ion-surface interactions.

Acknowledgement

There are numerous people to thank for all the help and encouragement which I received during my PhD studies and in completing this thesis. First, I owe special gratitude to my supervisor Nik Kaltsoyannis; without his kind guidance and support throughout this work would never have been completed. He was there to keep me on track when I was about to be lost in details and he has always been calm and supportive even when I had doubts about my results. Similar thanks to Andy Kerridge, my second supervisor. All his help; his previous work on the topic, his incredibly useful advice and general encouragement; both fuelled and improved this thesis. I would like to extend my gratitude to all my fellow PhD students who were there during my studies at UCL. I feel very fortunate to have such a good friends, all of them intelligent, funny and helpful. Special thanks must go to the ”Eamonn’s Anti-abandonment group”: Abi, Belle, Eamonn, Joe, and Toby; it was an honour to be in the same shoe with you guys! I would like to mention by names two more of my friends in this paragraph, their advice and help in work, besides their friendship, means a lot to me: thanks David and Enrico.

This work was half-funded by the National Nuclear Laboratory and National Decommissioning Authority, I am very grateful for their financial and technical support. Particular mention to my industrial supervisor, Jonathan Austin, whose guidance concerning the nuclear industry and patient explanations of my project’s industrial relevance helped to finish this work with results beneficial on both sides. This amount of data would never been produced without the several computer sources accessible to me and I am grateful for all of these services. I would like to acknowledge the use of the ARCHER UK National Supercomputing Service, the computing resources from UCL via the Research Computing ”Legion” and ”Grace” clusters and associated services and the late EPSRC UK National Service for Computational Chemistry Software (NSCCS) at Imperial College London, and the ”Iridis” facility of the e-Infrastructure South Consortiums Centre for Innovation. Personally, I would like to thank my previous group at the Budapest University of Technology and Economics, for their invaluable support in my previous studies and in the field of quantum chemical calculations which lead me to start and complete a PhD in this field.

At last but not least, I would like to thank for every member of my family: especially my parents, my sister Vera, my grandparents, godparents, cousins and all of my friends from home or abroad (I cannot possibly list you on a single page, but I hope you all know who you are!). Their unquestioning belief in my capabilities and their unconditional love helped me to also believe that I can achieve anything that I start. Finally, I left you for last Örs, because I cannot possibly express my gratitude towards you. Thank you for your infinite care, optimism and willpower which were and still continue to be a great inspiration for me.

Szeretném magyarul is megköszönni családom minden tagjának: különösen szüleimnek, nővéremnek Verának, nagyszüleimnek, keresztszüleimnek, unokatestvéreimnek, és minden kedves barátomnak otthon és külföldön. (Egy oldal is kevés lenne mindannyiótokat névvel felsorolni, de remélem mind tudjátok, hogy rátok gondolok!) A ti kérdés nélküli bizalmatok a képességeimben és a feltétel nélküli szeretetek segített, hogy én is elhiggyem, képes vagyok bármit véghez vinni amibe belekezdek. És végül, útoljára hagytalak téged Örs, mert képtelenség szavakkal kifejezni a hálát amit feléd érzek. Köszönöm a végtelen gondoskodásod, az optimizmusod és akaraterőd, tulajdonságok amiket mindig is csodáltam benned és minden nap engem is új erővel töltenek el.

Contents

List of Figures

List of Tables

Chapter 1

Introduction

Much of the UK's nuclear legacy waste[i] has been stored in ponds, wet silos and tanks which contain a large quantity of radioactive sludge formed by the in-pond corrosion of the spent Magnox fuel cladding. The composition of the waste is heterogeneous and it can change with the changing environment, but due to the high biological hazard and the difficulties in accessing and analysing the old-time paper based records, the monitoring and investigation of the exact compositions is very difficult. Since the storage facilities are close to the end of their designed life-time, a decommissioning program was initiated by Sellafield Ltd. to remove the waste from those facilities with the ultimate aim to immobilise and prepare the nuclear waste for long-term storage. However, due to the lack of complete understanding of the conditions of the ponds, the decommissioning is very challenging and requires complex solutions involving the combination of experimental measurements on simulated systems, computational modelling and technological developments.[1]

With the improvement of computational technologies, modelling plays a key role in several stages of the investigation and waste management: it can help to interrogate key process variables, define future monitoring requirements, underpin operating envelopes and technical risks. Modelling of fundamental chemical behaviours can help to understand the chemical reactions, soluble speciation and thermodynamically stable phases existing in the ponds.[2]

The aim of my PhD project is to provide quantum chemical insight into the interactions between fission generated Sr^{2+} and hydrated brucite surfaces to help understand the fundamental chemistry behind the present conditions in the legacy ponds. To be successful in this task, first we need to understand the industrial background of the problem by studying the history of the legacy ponds (1.1), their content (1.2) and the proposed waste treatment (1.3), then identify the key challenges and objectives for the computational investigation of the chosen problem (1.4).

[i] The objective "legacy" refers to nuclear waste which was produced during the pioneering nuclear research and early civil or military nuclear power programmes.

1.1 The legacy of Magnox reactors

The first British civil nuclear power reactors were Magnox-type which were pressurised, carbon-dioxide cooled systems with graphite moderators. The fuel contained unenriched uranium metal encased in a magnesium-aluminium alloy, called Magnox (Magnesium non-oxidising, represented in Figure 1.1a.[3] The exact composition of the alloy could vary depending on reactor site, but the magnesium content was usually up to 90% and, in addition to other elements with very small concentration (e.g. Be, Ca, Zr, Fe ...), the aluminium concentration changed from less than 0.02 up to 0.9%.[4] The key advantage of this specific alloy was its relatively low neutron capture cross section, which made it applicable as neutron moderating, neutron reflecting cladding material. However, it could be used only at a limited maximum operating temperature, due to possible secondary recrystallisation and significant changes in the grain structure at high temperatures,[5, 6] which seriously limited the thermal efficiency of this type of reactor.

(a) Oldbury Magnox fuel element in graphite brick[7]

(b) Opened air legacy pond in Sellafield[8]

Figure 1.1: Example of a nuclear legacy pond and a Magnox-type fuel element

During the second part of the twentieth century, 26 Magnox reactors were built in the UK, most of them with slightly different designs[3, 9] and with modified Magnox compositions.[4] None of these is operating any more; the last of the Magnox-type reactors in Britain, Wylfa, was shut down in 2015. The used fuel rods and cladding material became part of the intermediate and high level nuclear waste (ILW and HLW)[10] and are currently stored in fuel storage ponds and wet silos in Sellafield and other reactor sites in the country. ILW materials still produce significant amounts of radiation, but not as much as HLWs which are so radioactive that the generated heat by these materials has to be taken into account during their storing period. Therefore the spent Magnox fuel rods are stored temporarily in ponds or other facilities, filled with water to act as a radioactivity shield and as a cooling medium, before final disposal or reprocessing. In some facilities, such as the one in Figure 1.1b, spent fuel has been stored

for decades and this material represents a hazard that needs to be addressed.

Another disadvantage of Magnox is its reactivity with water. More accurately, Magnox corrosion is accelerated by the presence of chloride in the pond water. Although NaOH is used to maintain the high pH, since the legacy ponds are opened to the air near to the coast, a chloride build-up from sea-salt aerosols and insufficient purging of the water has resulted in the corrosion of the cladding material during the long period of storage. The magnesium-aluminium alloy has corroded during the years of storage under water, and formed a large quantity of sludge, often referred to as corroded Magnox sludge (CMS). Gregson and co-workers analysed the composition of the CMS and showed that the main component of the solid phase corrosion product is brucite ($Mg(OH)_2$), which forms hexagonal plate structures as shown in Figure 1.2b. Other Mg based phases are present in smaller amounts in the sludge, as well as uranium oxide particles which are formed due to the oxidation of the fuel element (Figure 1.2c).[11] Besides the corrosion products, the waste contains aquo and hydroxide complexes of leached actinides (^{238}U, ^{239}Pu and ^{241}Am) and fission products (mostly ^{137}Cs and ^{90}Sr) in a significant concentration.[2] It has been shown experimentally that brucite can absorb some of the above mentioned ions,[12, 13] moreover, its sorption capacity increases with higher pH[14] and the base molality in the ponds is generally high.

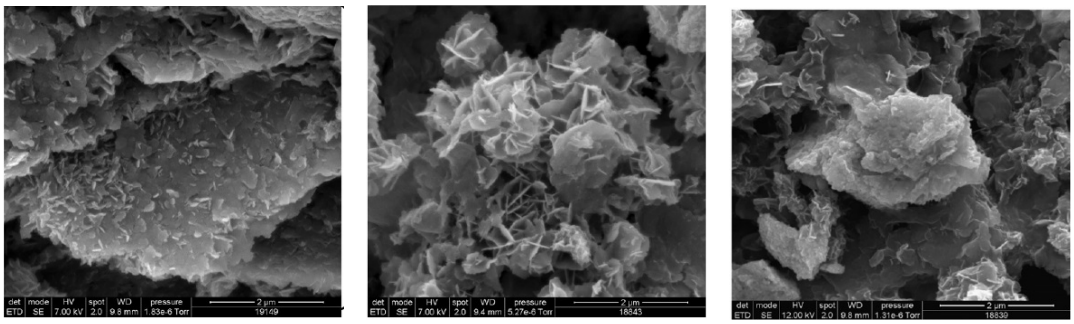

(a) simulated Magnox cladding before corrosion

(b) Brucite and other Mg based phases

(c) *in-situ* formed uranium-oxide particles

Figure 1.2: ESEM images of (a) a Magnox model sample, (b) corrosion products of Magnox: brucite and other Mg based phases (c) *in-situ* formed uranium-oxide particles[11]

Since the legacy ponds are open to the air, there are other potential components, such as various microbes, which can exist in the solution and affect the conditions, for example changing the pH and the redox environment.[15] This fact is important, since the pH conditions have a significant role in waste treatment to keep the solubility of the sludge components to a minimum and to avoid the further corrosion of Magnox as well as undesirable changes in the mobility of different redox sensitive actinides.[16–19] Furthermore, there is a notable

CO_2 dissolution in the open ponds over time. The dissolved CO_2 can induce significant structural changes, e.g. the transformation of the brucite to various Mg hydrocarbonate phases or carbonate complexation of the actinide ions in solution.[20, 21]

1.2 Hazardous radioactive ions in the ponds

The unenriched uranium metal contains a combination of three isotopes (0.711% ^{235}U, 99.284% ^{238}U and 0.0055% ^{234}U). When it is used as fuel for thermal reactors, ^{238}U captures one slow neutron and after two beta decaying steps becomes fissile ^{239}Pu. ^{235}U and ^{239}Pu, with the adsorption of a neutron, can undergo nuclear fission and produce a wide range of mostly radioactive elements as fission products according to the thermal fission yield diagram shown in Figure 1.3. The fissile reaction results in three more neutrons and generates a significant amount of energy (Eq. (1.1)) besides the two fission products (A and B), and continues to go on in a controlled cycle until most of the fuel is used up. Among all the possible fission products, the ones with a medium-long half life (several years) are the most important from the perspective of nuclear waste management as they will be responsible for the radioactivity during the temporary storage in the ponds. ^{90}Sr and ^{137}Cs stands out from this group with the highest production yield ($\sim$6% for the fission of ^{235}U), making them the most abundant radioactive elements in the high and intermediate level waste.[22]

$$^{235}_{92}\mathrm{U} + ^{1}_{0}\mathrm{n} \longrightarrow ^{236}_{92}\mathrm{U} \longrightarrow ^{\sim 95}\mathrm{A} + ^{\sim 138}\mathrm{B} + 3^{1}_{0}\mathrm{n} + 177\mathrm{MeV} \tag{1.1}$$

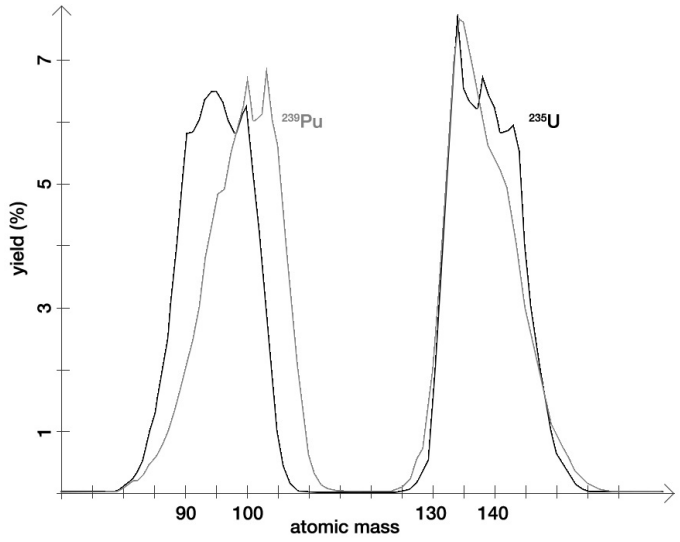

Figure 1.3: Schematic diagram of fission product yield for thermal neutron fission of ^{235}U and ^{239}Pu

^{90}Sr is a beta decaying radioactive element with a half life $\sim$29 years.[23] Its radioactivity is dangerous for human health and since it is soluble in water, if it enters the groundwater

or soil,[15, 24] it carries a major hazard for the environment. ^{90}Sr can be inhaled too, but ingestion in food and water is the greatest health concern. Because the biochemical behaviour of Sr is very similar to Ca, it deposits in the bones, teeth and bone marrow and can cause cancer there and in the surrounding soft tissues. [25–27] ^{137}Cs emits both beta particles and gamma rays with a half life of 30 years.[23] It also travels easily through air and is soluble in water, however, it is less likely to move in the ground than ^{90}Sr, as it bonds strongly to the soil.[26] ^{137}Cs is most dangerous through external exposure to a large amount due to its gamma radiation, but it hardly occurs in such a high concentration. When it enters the body it gets more or less uniformly distributed with the highest concentration in the soft tissues and increases the risk of cancer.[26]

The deposited used fuel rods still contain a high amount of solid uranium ($>$95%), which can also be partially released in the solution, along with to solvated ions of other alpha emitting by-products of the fissile/neutron capture reactions, such as different isotopes of Pu, Am and Cm.[28] The uranium most likely becomes UO_2^{2+} when it corrodes and it can be present both in the solid and aqueous phase of the waste.

1.3 SIXEP: the pond water treatment process

Filtration and ion exchange treatment plants are typically used to condition waste water prior to discharging, such as the Site Ion eXchange Effluent Plant (SIXEP) which has operated in Sellafield since 1985 and is used to remove almost all the radioactivity of the liquid effluent from the storage ponds before sea discharge.[29] The feed entering the SIXEP plant is quite heterogeneous: it is an alkaline (pH $>$ 11) water solution containing solid materials with various particle sizes and a range of mobile ions; of which the radioactive ones are primarily ^{90}Sr and ^{137}Cs, but some alpha emitting actinides too (e.g. Pu, ^{241}Am, ^{242}Cm and ^{244}Cm)[28]. There is also a large concentration of non-radioactive cations, mostly Na^+ Mg^{2+}, Ca^{2+} and K^+.[2] The concentration of the latter ions is an important factor as these ions are competitors of the radioactive solutes in the cation exchange process.

A schematic flow chart of the SIXEP operating in the Sellafield site is shown in Figure 1.4. Although the heart of the process are the ion exchange beds where the radioactive (and the non-radioactive) cations are swapped with cations of the ion exchanger material (usually some kind of zeolite e.g. clinoptilolite which is a natural zeolite particularly selective for Sr and Cs ions[2]), the feed has to go through several treatment processes before entering the ion exchange columns.[2, 30] First, the suspended solids have to be removed by settling and

filtration to avoid blocking the beds and to take away a significant amount of activity linked to the solid phase. Settling tanks are used to remove larger particulates and experimental results with simulated sludge have showed a significant strontium uptake at this step (by the solid phase) which was initially linked to the presence of brucite. In the reception tank, polyelectrolytes are added to the feed to enhance the filtration of smaller particles and colloids by the sand bed filters. 90% of the alpha emitters (Am and Cm) are filtered out at this point as they mostly sorb onto solid particulates, however Pu ions are less likely to absorb and therefore they are detected with an almost unaltered concentration at the end of this process.[28] The next step is the carbonation tower, where the entering alkaline liquor contacts with carbon dioxide and forms carbonates and hydrocarbonates while the pH reduces to close to neutral.

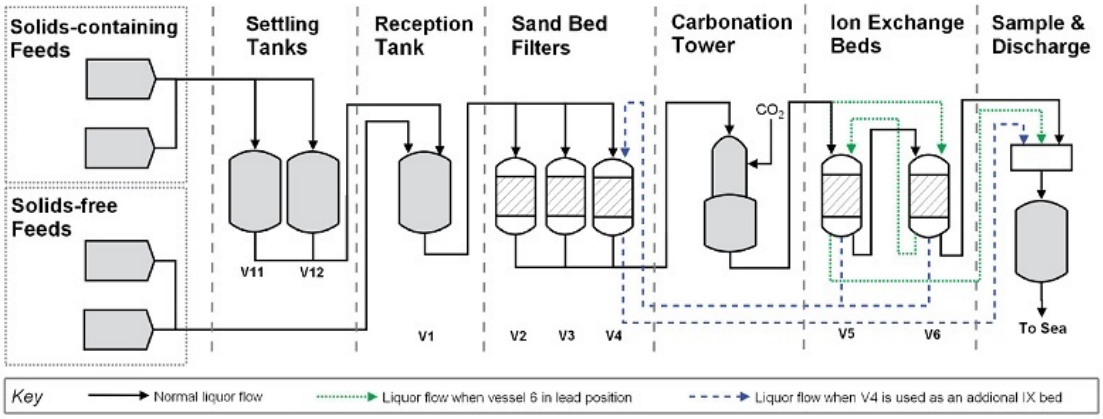

Figure 1.4: The process diagramm of SIXEP[2]

The ion exchange columns have a certain ion exchange capacity which is supposed to be constant and determined only by the number of functional groups available for ion exchange in the material. However, in the process design and operational point of view, the so-called breakthrough capacity is a more important factor, as it is refers to the volume of solution which can be treated in the plant before the concentration of the radioactive ions starts to increase in the leaving effluent.[31] It depends on several variables, such as the initial ion concentration of the entering liquor, ionic size and valence, temperature, nature of the functional group etc.; and once this volume is achieved, the used ion exchanger has to be physically removed from the vessels, disposed as solid radioactive waste and replaced with new material. In the case of uncertain feed composition, the SIXEP process has to run within big safety limits, assuming the highest possible concentration of movable ions, which can be extremely costly and inefficient, Besides the fact that the ion exchange beds are also part of the radioactive waste, there is a limited storage place for them, and during their replacement the SIXEP runs

only with half-capacity; all of these are good reasons to continue the investigation on the exact feed composition.

1.4 Computational challenges

Brucite, as the main corrosion product of the cladding material, coexists with radioactive solvated ions, such as the fission generated Sr^{2+}, in an alkaline aqueous solution in the ponds. When this solution enters the SIXEP plant for treatment, the solid phase is separated from the liquid phase. A significant but not constant strontium uptake is detected at this point and for the optimal operation of the plant, it is crucial to understand what is responsible for this uptake. If there are strong interactions between the Sr^{2+} ion and the solid $Mg(OH)_2$, a significant concentration of strontium may stay in the solid waste form sorbed to the brucite, leaving a lower concentration in the effluent entering the ion exchange beds.

Computational studies have been used on several occasions to provide insight into ion/surface interactions at the molecular level by predicting preferred reaction sites,[32–36] calculating the most stable structures during the interactions[35, 37–39] and allowing comparison of the interaction energies of competing species[40–42]. Moreover, there are several examples in the literature in which simulations have helped to improve our knowledge of radionuclide related transport mechanisms in minerals[43] by determining the strength and type of their interaction with transport media, such as molecular dynamics studies of the interaction of solvated uranyl ions with common soil components around nuclear waste depositories,[35, 44–47] and computational investigations of ionic transport mechanisms in the filtration media used during the decommissioning process such as sand and zeolite type ion exchangers[48, 49].

For this particular problem, first we have to know the thermodynamically stable complexes of the Sr^{2+} in a high pH environment and create a model capable of studying the energetics of ionic adsorption on a water/solid interface, to be able to investigate the proposed interactions between Sr and brucite.

1.4.1 Studying the hydrolysis of Sr^{2+} in aqueous environment

Although the speciation of $Sr(OH)_2$ in alkaline conditions and changing temperatures had been studied experimentally, there is no structural information on the geometry of the thermodynamically stable Sr^{2+} complexes in solution. With very few exceptions, hydrolysis constants are determined from pH-dependent solubility studies[50] or recently by AC conductivity measurements.[51] Therefore, as a first step of this PhD project, we have to identify the thermody-

namically stable Sr^{2+} species in the solution to be able to use them as candidate species for the interactions and as reference structures representing the solvated complexes in the bulk solvent.

Modelling solvation or ligand exchange in solvated complexes with quantum chemical methods requires different approaches than reactions involving strong chemical bonds, because these complexes are generally formed by weak and labile bonds where the effects of the solvent-solute interactions cannot be neglected.[52] Thus, in addition to the selection of an appropriate computational method and basis set, several other factors such as the continuum solvent model and the explicit inclusion of the first or even second solvation shells can have a significant effect on the results and have to be carefully considered during the investigation.[53] Chapter 3 of this thesis explains the work which has been carried out on this subject.

1.4.2 Creating a suitable surface representation of (0001) brucite surface

An important challenge for the project is to create a suitable brucite model for the proposed interaction. However, choosing a surface representation for the investigation of a particular adsorption mechanism is not always straightforward, and the choice can heavily influence the outcome of the results. One of the most common approaches to model surfaces is periodic density functional theory (DFT)[54], which operates with conventional unit cells and employs periodic boundary conditions. One popular alternative to modelling a surface with periodic DFT is to use embedded cluster methods to represent an isolated adsorption site on a periodic surface.[55–57]

For the given problem, we have to consider the following aspects before we decide on the surface model: for the sake comparability and continuity within the thesis, the developed system has to be compatible with previous results on the solvated Sr^{2+} complexes, and has to have the capability to contain at least the same number of water molecules above the surface as it is used in the solvation study. The model has to work for the adsorption of charged species too and has to be able to describe the energetics of adsorption interactions on the surface. Last but not least, ideally it should have moderate computational requirements to be possibly used in other nuclear industry related problems in the future. Our choice of modelling method and the steps toward surface optimisation and validation is the topic of chapter 4.

1.4.3 Studying the interactions between the solvated Sr^{2+} and hydrated (0001) brucite surface

The typical experimental studies which are carried out on simulated CMS, are measuring the activity released from the sludge before and after the separation of the solid content and calculating the activity release fraction (RF), the distribution coefficient (K_d) and the sorption capacity in percentage based on the results.[15] Besides the changing content of the sludge, many variables, such as the pH and temperature, can affect the interactions between ions and solids and it is hard to differentiate and prioritise between these factors. Quantum chemical calculations allow us an insight for the same absorption reactions from another, atomic-scale, perspective in which we can investigate the preferred structures of the absorbed complexes as well as the energetics and chemical background of the detected interactions; and ultimately provide important complementary information for the understanding of the measured behaviours.

Although there are several difficulties which limit the level of complexity that can be achieved in a quantum chemical model system, in chapter 5 we combine the results and conclusions of the two previous chapters to create a model as realistic as possible for the Sr adsorption on a hydrated brucite surface. Then we pursue the investigation by identifying possible structures for the absorbed complexes, calculating their adsorption energies and, after the careful analysis of the obtained results, by finally concluding on the theoretical possibility of Sr absorption on brucite.

Chapter 2

Electronic Structure Theory

a·b This thesis is entirely computational and involves the use of several different methods and theories. Therefore, in the first part of this chapter I attempt to summarise the basic ideas of electronic structure theory by first introducing the main approximations of quantum chemistry and the basics of Hartree-Fock theory, then continue with the density functional theory and related topics such as functionals and basis sets. More detailed descriptions can be found in the literature that I used as a basis for this summary.[58–60] In the second part I concentrate on specific methods which are relevant for this work, such as solvent models and periodic simulations, while in the last part of the chapter I write about the practical use of the previously introduced theories.

2.1 The Schrödinger equation and other approximations

In electronic structure calculations one always seeks an approximate solution for the non-relativistic *time-independent Schrödinger equation* (SE) shown in Eq. (2.1). The time-independent SE is an approximation itself, since it assumes that the wavefunction is invariant to time and ignores relativistic effects. The Dirac equation is a variation of the SE which is consistent with the theory of relativity, however, due to its complexity, when relativistic effects can be ignored[i], the solution of SE is the base of most electronic structure theories.

Eq. (2.1) is an eigenvalue problem, which can be solved based on the variational principle (Eq. (2.2)). $\hat{H}$ is the Hamiltonian, a Hermitian operator which acts on the ground state wavefunction ($\Psi_0(\boldsymbol{\tau})$) and results in the total energy of the system in the ground state, E_0 (i.e. the eigenvalue of the equation) as the expectation value of $\hat{H}$ with respect to the normalised wavefunction.

$$\hat{H}\Psi(\boldsymbol{\tau}) = \left[\hat{T}_e + \hat{T}_n + \hat{V}_{ne} + \hat{V}_{ee} + \hat{V}_{nn}\right]\Psi(\boldsymbol{\tau}) = E\Psi(\boldsymbol{\tau}) \tag{2.1}$$

$$\left\langle \Psi(\boldsymbol{\tau})|\hat{H}|\Psi(\boldsymbol{\tau})\right\rangle \geq E_0 \text{ if } \langle\Psi(\boldsymbol{\tau})|\Psi(\boldsymbol{\tau})\rangle = 1 \tag{2.2}$$

The Hamiltonian includes the following terms (showed in Eq. (2.3) in atomic units): the kinetic energy operator of N electrons ($\hat{T}_e$), the kinetic energy operator of M nuclei ($\hat{T}_n$) and the po-

[i] Relativistic effects in the first three periods of the Periodic Table are negligible.

tential energy operators describing the nucleus-electron attraction ($\hat{V}_{ne}$), the electron-electron ($\hat{V}_{ee}$) and nucleus-nucleus repulsion ($\hat{V}_{nn}$) interactions. In the extended form of $\hat{H}$ $\mathbf{r}_{iA}$ is the distance between the electron i and nucleus A, $\mathbf{r}_{ij}$ is the distance between electron i and j while $\mathbf{R}_{AB}$ is the distance between the A and B nuclei.

$$\hat{H} = -\sum_{i=1}^{N} \frac{1}{2}\nabla_i^2 - \sum_{A=1}^{M} \frac{1}{2m_A}\nabla_A^2 - \sum_{i=1}^{N}\sum_{A=1}^{M} \frac{Z_A}{\mathbf{r}_{iA}} + \sum_{i=1}^{N}\sum_{j>i}^{N} \frac{1}{\mathbf{r}_{ij}} + \sum_{A=1}^{M}\sum_{B>A}^{M} \frac{Z_A Z_B}{\mathbf{R}_{AB}} \tag{2.3}$$

The second assumption made to solve the SE for many-electron systems is the *Born-Oppenheimer approximation*. This theorem allows us to separate the movement of the nuclei from the electrons, based on the fact that the mass of the latter is 3-5 orders of magnitude smaller, therefore the velocity of their movement is much faster than that of the nuclei, which leads us to the following equations:

$$\hat{H}_e \Psi_e = E_e \Psi_e \tag{2.4}$$

$$(\hat{T}_n + \hat{H}_{tot})\Psi_n = (T_n + E_{tot})\Psi_n = E\Psi_n \tag{2.5}$$

Eq. (2.4) represents the motion of the electrons with respect to a fixed nucleus configuration (**R** constant). $\hat{H}_e$ contains $\hat{T}_e$ and the potential energy operators $\hat{V}_{ee}$ and $\hat{V}_{ne}$. Including the constant nuclear repulsion to describe the total energy of a fixed nuclei results in $E_{tot} = V_{nn} + E_e$ and substituting its Hamiltonian, $\hat{H}_{tot}$ into $\hat{H}$ gives the total energy of the system with respect to the movement of the nuclei (Eq. 2.5). Plotting E_{tot} as a function of the nuclear coordinates defines the so-called *potential energy surface* (PES) which can be analysed to obtain chemically meaningful information about the studied systems. The analysis of PES is discussed in more detail in section 2.7.1.

Before continuing with the next approximation, it has to be noted that although the electronic Hamiltonian is a function of spatial coordinates (**r**) only, particles with half spin, such as electrons, are specified by their spin coordinates too (w) and the electron wavefunction should reflect that by containing both and by satisfying the antisymmetry principle. Therefore, instead of simply using the *spatial orbital* ($\varphi(\mathbf{r})$) as the wavefunction of a single electron in the system, we use a more general definition, the so-called *spin orbital* ($\psi(\mathbf{x})$) in which $\mathbf{x} = \{\mathbf{r}, w\}$ containing both space (**r**) and spin (w) coordinates (Eq. (2.6)). Therefore, for a set of N spatial orbitals, $2N$ spin orbitals can be defined by multiplying each $\varphi(\mathbf{r})$ by one of the two spin

functions:

$$\psi(\mathbf{x}) = \begin{cases} \varphi(\mathbf{r})\alpha(w) \\ or \\ \varphi(\mathbf{r})\beta(w) \end{cases} \tag{2.6}$$

After defining an appropriate single-electron wavefunction, the simplest approximation to describe the many-electron wavefunction of a molecular system (Ψ_e in Eq. 2.4) is the *independent-electron model*, in which the probability of finding one electron in a certain point around the nuclei is uncorrelated with the position of the other electrons, i.e. the electron-electron interactions are neglected. In this way, the many-electron wavefunction is some kind of product of its electrons' wavefunctions and, to still be consistent with the Pauli-exclusion principle, it has the form of a determinant. The so-called *Slater determinant* of an N electron wavefunction is shown in Eq. (2.7), where $(N!)^{-1/2}$ is the normalisation constant. This form of Ψ_e satisfies the Pauli-exclusion principle: since changing two rows of a determinant only changes the sign of the wavefunction, allowing to interchange the coordinates of two electrons while satisfying the antisymmetry principle; and having two columns the same makes the determinant zero, i.e. two electrons with the same spin cannot occupy the same orbital.

$$\Psi_e(\mathbf{x}_1, \mathbf{x}_2, \cdots, \mathbf{x}_N) = \frac{1}{\sqrt{N!}} \begin{vmatrix} \psi_i(\mathbf{x}_1) & \psi_j(\mathbf{x}_1) & \cdots & \psi_k(\mathbf{x}_1) \\ \psi_i(\mathbf{x}_2) & \psi_j(\mathbf{x}_2) & \cdots & \psi_k(\mathbf{x}_2) \\ \vdots & \vdots & \ddots & \vdots \\ \psi_i(\mathbf{x}_N) & \psi_j(\mathbf{x}_N) & ... & \psi_k(\mathbf{x}_N) \end{vmatrix} \tag{2.7}$$

For closed-shell singlet systems (where each orbital contains two electrons with opposite spin) we often simplify the definition of the orbitals by considering only the spatial orbitals as eigenfunctions since the spin part of the determinant will always result a singlet wavefunction. As every calculation discussed in this thesis is a closed shell singlet system, I shall use spatial orbitals ($\varphi_i(\mathbf{r})$) for further discussions throughout this summary.

Although neglecting the electron-electron interactions significantly simplifies the description of many-body systems, it also leads to serious differences regarding the exact energy. Therefore, the independent-electron based model is not appropriate for electron structure calculations and some kind of assumption must be made to include the effect of electron-electron repulsion in the Hamiltonian.

2.2 Hartee-Fock theory (HF)

In Hartree-Fock theory, one derives the total electronic energy of the ground state by solving eigenvalue problems, as shown in Eq. (2.8), for each of its electrons. These single-electron equations are called *Hartree-Fock equations*[61, 62] and they take into account the electron-electron interactions by an effective potential (υ_i^{HF}) which is the average potential experienced by the i^{th} electron due to the other electrons present around it.

$$\hat{f}_i\varphi_i = \varepsilon_i\varphi_i \tag{2.8}$$

$$\hat{f}_i = \hat{h}_i + \upsilon_i^{HF} = \frac{1}{2}\nabla_i^2 - \sum_{A=1}^{M}\frac{Z_A}{\mathbf{r}_{iA}} + \upsilon_i^{HF} \tag{2.9}$$

In the HF equations, $\hat{f}_i$ is the one-electron *Fock operator* containing the Hamiltonian of a single electron in the field of the nuclei and the effective potential. υ_i^{HF} contains two operators ($\upsilon_i^{HF} = \sum_j^N(\hat{J}_j - \hat{K}_j)$), which both depend on the coordinates of two electrons and have the following expectation value with respect to the orbital φ_i:

$$\left\langle \varphi_i(\mathbf{r}_1)|\hat{J}_j|\varphi_i(\mathbf{r}_1)\right\rangle = \int \varphi_i(\mathbf{r}_1)^*\varphi_j(\mathbf{r}_2)^*\left(\frac{1}{\mathbf{r}_{ij}}\right)\varphi_i(\mathbf{r}_1)\varphi_j(\mathbf{r}_2)d\mathbf{r}_1 d\mathbf{r}_2 = J_{ij} \tag{2.10}$$

$$\left\langle \varphi_i(\mathbf{r}_1)|\hat{K}_j|\varphi_i(\mathbf{r}_1)\right\rangle = \int \varphi_i(\mathbf{r}_1)^*\varphi_j(\mathbf{r}_2)^*\left(\frac{1}{\mathbf{r}_{ij}}\right)\varphi_j(\mathbf{r}_1)\varphi_i(\mathbf{r}_2)d\mathbf{r}_1 d\mathbf{r}_2 = K_{ij} \tag{2.11}$$

$\hat{J}_j$ is the *Coulomb operator*, it represents the averaged classical repulsion potential acting on the electron in orbital φ_i at position $\mathbf{r}_1$ from the electron in orbital φ_j. $\hat{K}_j$ is the *exchange operator*, its name is coming from the fact that in $\hat{K}_j$ the spin orbital φ_j exchanges with φ_i to the right of $\mathbf{r}_{ij}^{-1}$. The exchange potential is the consequence of the antisymmetry principle: electrons of the same spin cannot occupy the same orbital which reduces the classical Coulomb repulsion term with a non-classical contribution. It is a non-local operator, i.e. the value of $\hat{K}_j\varphi_i(\mathbf{r}_1)$ depends on the value of φ_i throughout all space. It is easy to see that in case of $i = j$, J_{ii} is completely cancelled out by K_{ii}, thus there is no error arising from the electron interacting with itself.

The HF equations can be solved by using the variational principle, i.e. the energy of the orbital (ε_i) is the expectation value of the Fock operator with respect to the normalised orbital, φ_i. By separating $\hat{f}_i$ to its above described terms (Eq. (2.9), (2.10) and (2.11)) and applying the variational principle to each, we get the following solution for ε_i:

$$\varepsilon_i = h_{ii} + \sum_{j}^{N}(J_{ij} - K_{ij}) \tag{2.12}$$

Going back to the original assumption of the HF theory, the energy of the many-electron wavefunction is described as the sum of the orbital energies with a correction term (Eq. (2.13)); one has to subtract half of the interatomic terms, since applying a double sum ($\sum_i \sum_j$) on $(J_{ij} - K_{ij})$ would count the electron-electron interactions twice. By adding the energy of the constant nuclear-nuclear repulsion potential to Eq. (2.13), we can calculate the total energy of the system too: $E_{tot} = E_e + V_{nn}$.

$$E_e = \sum_{i}^{N}\varepsilon_i - \frac{1}{2}\sum_{i}^{N}\sum_{j}^{N}(J_{ij} - K_{ij}) = \sum_{i}^{N}h_{ii} + \frac{1}{2}\sum_{i}^{N}\sum_{j}^{N}(J_{ij} - K_{ij}) \tag{2.13}$$

The solution of the HF equations may seem straightforward at first, but one can easily see that the definition of the Fock operator contains the orbital itself. Therefore, it can only be solved iteratively, assuming the Fock operator is constructed from a trial set of orbitals first. Then, a new set of orbitals can be obtained by solving the HF eigenvalue equations which we can use to construct new $\hat{f}_i$ operators until the orbitals within the Fock operators are sufficiently close to be the same to the eigenfunctions, i.e. self-consistency is achieved. Even with the above described *self-consistent field* method (SCF) in theory there is an infinite number of possible solutions for the HF equations, as the exact form of the single-electron wavefunction is unknown. Practically, to limit the number of possible solutions, we expand the molecular orbital of the system with a linear combination of a finite set of basis functions (χ_α in Eq. (2.14)) which often have a form similar to the atomic orbitals (see more in section 2.4).

$$\varphi_i = \sum_{\alpha} c_{i\alpha}\chi_\alpha \tag{2.14}$$

In this approach, which is also known as the *Hartree-Fock-Roothaan method*,[63] instead of the basis functions or orbitals, one can vary only the linear coefficients of the basis functions ($c_{i\alpha}$) during the iteration process.

In theory, the more sophisticated the basis set, the lower the ground state energy is, i.e. it becomes closer to the true ground state energy. However, even with a theoretically complete basis set, there is a known limit of the ground state energy (the *Hartree-Fock limit*) due to the errors arising from the averaged electron-electron interactions in the HF approach. Although

relativistic effects can play an important role for heavy elements, typically, the biggest source of error is the assumption of an average potential field arising from the surrounding electrons. In fact, HF theory neglects the *electron correlation*.[ii] Therefore, to obtain more realistic energies, one has to use methods which include some kind of electron correlation description in their model, such as post-Hartree Fock theories or Density Functional Theory.

2.3 Density Functional Theory (DFT)

The advantage of DFT calculations compared to other quantum chemical methods is the combination of acceptable accuracy and modest computational cost. This has made the DFT method popular worldwide in quantum chemistry since the 1990s.[64, 65] While there are serious limitations in accuracy in the Hartree-Fock theory, in most post-HF theories solving the Schrödinger equation is a difficult many-body problem and the potential depends on the coordinates of all the interacting electrons. The key feature of the DFT is that in this case, one solves the Schrödinger equation as a non-interacting problem where the potential is a function of the electron density i.e. of three space coordinates.[iii]

But what does the *electron density* represent? It is a probability density ($\rho(\mathbf{r})$) which describes the possibility of finding any electron in a given volume. If one integrates the electron density ($\rho(\mathbf{r})$) over the three dimensional space coordinates ($\mathbf{r}$), one will get the number of electrons (N) in that volume:

$$\int \rho(\mathbf{r}) d\mathbf{r}^3 = N \tag{2.15}$$

The *first Hohenberg-Kohn theorem*[66] states that the electron density in the ground state uniquely determines the potential up to an arbitrary constant. It means that $\rho(\mathbf{r})$ can be used to characterise a system and so we can describe the ground state energy as the functional of the electron density. Based on this, the total energy of the system can be written in the following form:

$$E[\rho(\mathbf{r})] = T[\rho(\mathbf{r})] + V_{ee}[\rho(\mathbf{r})] + V_{ext}[\rho(\mathbf{r})] = F[\rho(\mathbf{r})] + \int \nu_{ext}(\mathbf{r})\rho(\mathbf{r}) d\mathbf{r} \tag{2.16}$$

$$E[\rho(\mathbf{r})] = T[\rho(\mathbf{r})] + J[\rho(\mathbf{r})] + K[\rho(\mathbf{r})] + V_{ne}[\rho(\mathbf{r})] \tag{2.17}$$

[ii] HF does not completely neglect the electron correlation, since the basic correlation of electrons with parallel spin, that they cannot occupy the same space, is included in the exchange term.

[iii] This is true for Kohn-Sham DFT, but not for Hohenberg-Kohn DFT which does not require any Schrödinger type equations. Besides, there is a spin dependence on the potential, which increases the number of variables to four, but as the calculations reported here are all on closed shell singlet species, I will not discuss spin-polarised DFT.

Where $E[\rho(\mathbf{r})]$ is the functional of the total energy of the system and $T[\rho(\mathbf{r})]$ is the kinetic energy functional of the electrons. $V_{ee}[\rho(\mathbf{r})]$ is the energy functional of repulsion between the electrons, and just like in the HF theory, it is separated to two terms: Coulomb $J[\rho(\mathbf{r})]$ and exchange parts $K[\rho(\mathbf{r})]$. $V_{ext}[\rho(\mathbf{r})]$ is the energy functional of the external potential, which, in most cases, equals to the Coulomb attraction of the nuclei: $V_{ext}[\rho(\mathbf{r})] = V_{ne}[\rho(\mathbf{r})]$.

We can rewrite equation (2.16) using two terms: one, which is invariant to the external potential ($F[\rho(\mathbf{r})] = T[\rho(\mathbf{r})] + V_{ee}[\rho(\mathbf{r})]$, universal functional of the density), and another which depends on it. The *second Hohenberg-Kohn theorem* states that there is a single $F[\rho(\mathbf{r})]$ which is different and exact for each electronic system and the exact ground state energy $E_0[\rho(\mathbf{r})]$ and electron density for a given external potential are obtained by minimising $E[\rho(\mathbf{r})]$ with respect to the density with the number of electrons held constant. The Hohenberg-Kohn theorems laid down the basic rules of DFT but did not make it an easy-to-solve computational method, since we still do not know the exact form of $F[\rho(\mathbf{r})]$.

In early models, all energy components were expressed as a functional of the electron density (orbital-free DFT). Using the classical definition of the Coulomb interactions, the Coulomb part of electron-electron repulsion (2.18) and the attraction of the nuclei (2.19) can easily described in this way:

$$J[\rho(\mathbf{r})] = \frac{1}{2}\int\int \frac{\rho(\mathbf{r})\rho(\mathbf{r'})}{\mid \mathbf{r} - \mathbf{r'} \mid} d\mathbf{r} d\mathbf{r'} \tag{2.18}$$

$$V_{ne}[\rho(\mathbf{r})] = -\sum_{a}^{N_{nuclei}} \int \frac{Z_a(\mathbf{R}_a\rho(\mathbf{r}))}{\mid \mathbf{R}_a - \mathbf{r} \mid} d\mathbf{r} \tag{2.19}$$

However, for the kinetic energy functional and the exchange part of $V_{ee}[\rho(\mathbf{r})]$ there is no exact definition with the electron density function as we know of, therefore, some assumptions have to be made. The *Thomas-Fermi-Dirac model*[67–69] uses the density of the uniform electron gas (a model which assumes that the electrons are homogeneously distributed in space) to evaluate these terms with the following equations:

$$T[\rho(\mathbf{r})] = A_F \int \rho_u^{5/3}(\mathbf{r}) d\mathbf{r} \tag{2.20}$$

$$K[\rho(\mathbf{r})] = -A_X \int \rho_u^{4/3}(\mathbf{r}) d\mathbf{r} \tag{2.21}$$

Where A_F and A_X are constants and $\rho_u(\mathbf{r})$ is the density of the uniform electron gas. Considering electrons as homogeneously distributed particles may work for valence electrons in certain metallic systems, but gives a very poor description of atoms and molecules. In fact,

the Thomas-Fermi-Dirac model always predicts bonding between atoms to be unfavourable.

What makes DFT extremely popular is the *Kohn-Sham approach* (KS),[70] which describes the kinetic energy with an auxiliary set of orbitals, taking advantage of the wave function based definition of the electron density, in which the electron density of an N-electron system ($\rho(\mathbf{r})$) is related to the normalised N-electron wave function with this equation:

$$\rho(\mathbf{r}) = N \int \Psi_*(\mathbf{r'}_1, \mathbf{r'}_2 ... \mathbf{r'}_N)\Psi(\mathbf{r}_1, \mathbf{r}_2 ... \mathbf{r}_N) d\mathbf{r}_2 ... d\mathbf{r}_N \tag{2.22}$$

The basic idea of the KS approach is similar to Hartree-Fock: it assumes a set of non-interacting electronic systems, which has the same electron density as the interacting system (many-electron system). With this assumption one can simplify the electron density from (2.22) to the sum of the one-electron wavefunctions ($\rho(\mathbf{r}) = \sum_{i=1}^{n} |\varphi_i(\mathbf{r})|^2$) and modify the equation of the energy functional (2.16) to contain the kinetic energy of the non-interacting system as an approximation to the exact kinetic energy.

$$E[\rho(\mathbf{r})] = \sum_{i=1}^{n} \int \varphi_i^*(\mathbf{r}) \left(-\frac{1}{2}\nabla^2 \varphi_i(\mathbf{r}) \right) d\mathbf{r} + \frac{1}{2} \int \frac{\rho(\mathbf{r'})\rho(\mathbf{r})}{|\mathbf{r} - \mathbf{r'}|} d\mathbf{r} d\mathbf{r'} + \int \nu(\mathbf{r})\rho(\mathbf{r}) d\mathbf{r} + E_{XC}[\rho(\mathbf{r})] \tag{2.23}$$

The first term of equation (2.23) is the kinetic energy of the non-interacting system, the second is the Coulomb electron-electron repulsion energy, the third is the energy of the external potential and the last term is the so-called exchange-correlation energy (see section 2.3.1). To calculate the energy of the ground state we still minimise $E[\rho(\mathbf{r})]$ with respect to $\rho(\mathbf{r})$ as it is written in the second Hohenberg-Kohn theorem, but in this case we can define the exact relation[iv] between the $E[\rho(\mathbf{r})]$ functional and the density if we use the wavefunctions of the non-interacting electrons, which have to satisfy individually an one-electron Schrödinger equation:

$$\left\{ -\frac{1}{2}\nabla^2 + \nu_s(\mathbf{r}) \right\} \varphi_i(\mathbf{r}) = \varepsilon_j \varphi_i(\mathbf{r}) \tag{2.24}$$

Here, ε_j are the Kohn-Sham (KS) eigenvalues, $\varphi_i(\mathbf{r})$ are the one-electron wavefunctions, in other words the KS orbitals, and $\nu_s(\mathbf{r})$ is the effective potential which is the sum of the following potential terms (2.25); the external potential (ν_{ext}), the Hartree potential ν_H which is related to the electrostatic self-energy of the density, and the exchange-correlation potential ($\nu_{XC}(\mathbf{r})$).

[iv] except for the $E_{XC}[\rho(\mathbf{r})]$ term, see section 2.3.1

$$\nu_s(\mathbf{r}) = \nu_{ext}(\mathbf{r}) + \nu_H(\mathbf{r}) + \nu_{XC}(\mathbf{r}) \tag{2.25}$$

Note that the exchange-correlation potential $\nu_{XC}(\mathbf{r})$, by definition ($\nu_{XC}(\mathbf{r}) = \frac{\delta E_{XC}}{\delta \rho(\mathbf{r})}$), comes from the electron density which is calculated from the solution of the one-electron Schrödinger equation. Therefore, we first have to make a guess for the one-electron wavefunction to construct an electron density which can be used to create the effective potential and then solve the eigenvalue problem in (2.24). The density which is calculated from the solution defines a new potential and this cycle goes on, until there is no change in the output density from one cycle to the next, i.e. self-consistency is achieved. Finally, the self-consistent electron density can be used to compute the total energy of the ground state, $E_0[\rho(\mathbf{r})]$.

2.3.1 Exchange-Correlation Functionals

The weakness of DFT is the definition of $E_{XC}[\rho(\mathbf{r})]$, *the exchange-correlation functional*. It contains everything which is left out of the other terms of the energy: the difference between the exact kinetic energy and the kinetic energy of the non-interacting system, and the non-Coulomb part of the electron-electron interaction energy. Generally, the exchange and the correlation part of the functional are treated separately. Their density dependence cannot be described exactly but there are several methods to approximate them. We can establish an order of the different approximations based on the level of chemical accuracy which can be achieved with them. This hierarchy is sometimes referred to as Jacob's ladder[71] in DFT.

The simplest approach is the so-called *Local Density Approximation* (LDA), in which the exchange part of $E_{XC}[\rho(\mathbf{r})]$ is calculated from the exact exchange energy per particle of a homogeneous electron gas with a given density.

$$E_X^{LDA}[\rho(\mathbf{r})] = A_X \int \rho(\mathbf{r})^{4/3} d\mathbf{r} = A_X \int \varepsilon_x(\rho) d\mathbf{r} \tag{2.26}$$

A_X is a constant and $\varepsilon_x = \rho(\mathbf{r})^{4/3}$ is the exchange energy per particle of the uniform electron gas. Unfortunately, there is no exact formula for the correlation energy part, therefore parametrisation is required to define one. For example Vosko, Wilk and Nusair[72] used series of Quantum Monte Carlo simulations[73] of the homogeneous electron gas to create an analytic interpolation formula for $E_C[\rho(\mathbf{r})]$.

A higher level approach compared to LDA is the *Generalised Gradient Approximation* (GGA), in which the description of the inhomogeneity of the electron density is improved with

an extra term in the exchange-correlation functional (2.27).

It has been found that it is difficult to use the gradient of the density function as an extra variable by itself.[74] Thus a reduced dimensionless gradient ($s(\mathbf{r}) = |\nabla\rho(\mathbf{r})|/2k_F\rho(\mathbf{r})$) is created to scale the changes in the density and is used to define the exchange energy functional.

$$E_X^{GGA}[\rho(\mathbf{r})] = A_X \int \varepsilon_x(\rho) F_X(s) d\mathbf{r} \tag{2.27}$$

A_X is a constant, $\varepsilon_x(\rho)$ is still the exchange energy per particle of the homogeneous electron gas and $F_X(s)$ is an enhancement factor which describes the increment of the exchange energy compared to the LDA value.

A common example of the GGA is the BLYP functional that is made up from an exchange part developed by Becke (1988) which contains one fitted parameter, and a correlation functional created by Lee, Yang and Parr and parametrised from simple systems.[75, 76] Another example is the PBE functional which was developed by Perdew, Burke and Ernzerhof in 1996; there is no fitted parameter in its exchange energy functional.[74].

The next step up Jacob's ladder is the so-called *meta-GGA*. Besides the electron density and its first derivative, meta-GGAs depend on the Laplacian of the density ($\nabla^2\rho(\mathbf{r})$) or the kinetic energy density ($\tau(\mathbf{r})$ in equation (2.28)) of the occupied Kohn-Sham orbitals ($\varphi_i^{occ}(\mathbf{r})$) which is also a functional of the density.

$$\tau(\mathbf{r}) = \frac{1}{2}\sum_i^{occ} |\nabla\varphi_i(\mathbf{r})|^2 \tag{2.28}$$

In this work a meta-GGA functional, called TPSS, was used for the calculations. It is a nonempirical functional that was developed by Tao, Perdew, Staroverov and Scuseria and it contains the $\tau(\mathbf{r})$ functional as an extra variable.[77]

The approaches so far do not consider the self-interaction problem. It occurs in DFT calculations because the approximations to the exchange-correlation functional do not completely cancel the Coulomb interaction of the electron with itself, as happens in the case of Hartree-Fock calculations.(see section 2.2) This type of error can be reduced with the use of *hybrid functionals* which have an exchange functional partially built up from a Hartree-Fock expression.

$$E_{XC} = (1-a)E_X^{DFT} + aE_X^{HF} + E_C^{DFT} \tag{2.29}$$

$0 < a < 1$ is the proportion of the HF exchange part in the functional. One of the most

common examples is the B3LYP[78, 79] functional which contains LDA, GGA approximations and a HF part with three fitted parameters:

$$E_{XC} = (1-a-b)E_X^{LDA} + aE_X^{HF} + bE_X^{GGA} + (1-c)E_C^{LDA} + cE_C^{GGA} \tag{2.30}$$

PBE0[80] and TPSSh[81] are also frequently used hybrid functionals, which were developed by Perdew *et al*. and feature fewer fitted parameters than B3LYP. For example PBE0 contains a=25% of the exact E_X^{HF} and 75% of PBE exchange, which has no fitted parameters at all.

The general differences in accuracy between the various exchange functional approximations are summarised in Table 2.1.[81, 82] HF is included in the comparison to show the general performance of DFT against this method. While there is only a small deviation from experimental values in optimised geometries depending on the used approximation, there is much more difference in binding energies.

Table 2.1: General differences in accuracy between HF and DFT with LDA, GGA (PBE,BLYP), meta-GGA (TPSS) and hybrid (PBE0,B3LYP) functionals, obtained by comparing the calculated values of different test sets to experimental results. †The T-96R test set was used for bond distances, G3/99 for computing formation enthalpies[81] and ‡the combined dataset of NHTBH38/04 and HTBH38/04 was used for reaction energies.[82] (MUE: mean unsigned errors, MSE: mean signed errors.)

statistical errors	HF	LDA	GGA		meta-GGA	Hybrid	
			PBE	BLYP	TPSS	PBE0	B3LYP
MUE (bond length) Å†	0.0249	0.0131	0.0159	0.0223	0.0142	0.0097	0.0104
MUE (enthalpy of formation) kcal/mol†	211.54	121.85	22.22	9.49	5.81	6.66	4.93
MSE (barrier heights) kcal/mol‡	10.60	-14.78	-8.66	-8.09	-8.14	-3.53	-4.15

Because of the lack of electron correlation HF tends to severely overestimate atomisation energies, i.e. underestimates the energy gained by molecular bonding. The local density approximation still overestimates the atomisation energies of molecules or solids, but GGA, meta-GGA or hybrid functionals show a significant improvement in accuracy. Reaction barrier heights are also overestimated by HF due to the poorly described interaction energies between reactants, while being seriously underestimated by LDA and slightly underestimated by GGA, meta-GGA or hybrid functionals. Generally, meta-GGA results are closer in accuracy to simple GGAs than hybrid functionals, which tend to perform slightly better than the former two. Overall, Table 2.1 shows that we can obtain accurate geometrical parameters and binding energies with the GGA or meta-GGA approximation of DFT, subsequently these functionals are good to describe adsorption energies of complexes. However, since both LDA, GGA and meta-GGA functionals contain the electron self-interaction error, they tend to favour delocalised solutions and therefore exaggerate covalent character in ionic bonds as well as

underestimate band gaps in semi-conductors or insulators. This type of error is more important in compounds and materials containing strongly localised d and f orbitals, for which the use of hybrid functionals is necessary for reliable results.

2.3.2 Dispersion correction

Dispersion type forces, when a temporary dipole arising from quantum fluctuations within system and induces another interim dipole in the interacting molecule, are generally not included in the density functionals. Although dispersion forces are the weakest type of secondary interactions, they can have significant roles in the formation of complexes and materials especially in systems where there are closed high level d orbitals or there are no other stronger interactions.

One way to include dispersion correction in the calculations is the DFT-D approach, which was developed by Stefan Grimme[83, 84] and implemented in the TURBOMOLE code. Equation (2.31) shows the Grimme-type dispersion correction energy term,[85] which contains correction coefficients (C_6^i) for each element, and depends on the distance between the two atoms (R_{ij}) as well as the type of the used DFT functional, which is included in the s_6 factor.

$$E_{disp} = -s_6 \sum_{i}^{N-1} \sum_{j=i+1}^{N} \frac{C_6^{ij}}{R_{ij}^6} f_{dmp}(R_{ij}) \tag{2.31}$$

The correction coefficients are based on empirical results, but consider the molecular environment of the atom too through its volume, because when an atom gets ”squeezed”, it becomes less polarizable.[84] The dispersion coefficient of an atom pair is calculated as the geometrical mean of the two atomic coefficients: $C_6^{ij} = \sqrt{C_6^i C_6^j}$. The damping function, $f_{dmp}(R_{ij})$ also depends on the atomic distances and helps to avoid having negative values within the sum. In DFT-D, the total energy of the system is the sum of the calculated DFT energy and the dispersion correction term.

2.3.3 Resolution of identity

In order to reduce the computational time of the calculations, it is possible to use a slightly modified term for the mathematical description of the Coulomb interaction in the DFT, without introducing any error within the calculations. The so-called *resolution of identity* method (RI-DFT) uses an approximated electron density to reduce the number of integrals during the calculation of J[86] and involves the use of auxiliary basis sets, which are defined in advance for the different type of atoms.[87] This technique is implemented for non-hybrid DFT function-

als and the HF method in TURBOMOLE and it can speed up the energy calculations tenfold compared with conventional DFT without any loss in accuracy.[88]

2.4 Basis Sets

For the practical use of DFT, just like in Hartree-Fock theory, the one-electron wavefunctions have to be defined with finite size basis sets. The general method to do this is to construct the Kohn-Sham orbitals (φ_i) from linear combinations of particular types of basis functions (χ). The quality and the size of the chosen basis sets is very important since it can significantly modify the results of the calculations.

One possibility is to consider the electrons as free particles and use *plane waves* as their basis functions. It is a very simple solution and, since plane waves are easily adjustable to the Bloch-theorem (see section 2.6.1), they are computationally accessible in case of periodic systems. However, electrons close to the nucleus are very far from being free particles and for their better description often a huge number of plane waves or so-called pseudopotentials (see section 2.4.1) are necessary.

Another possibility to construct basis sets is to use atom-centred orbitals. The functional form of the so-called *Slater Type Orbitals* (STOs)[89, 90] is similar to the wavefunctions of the hydrogenic atomic orbitals: they are described with polar coordinates (r, θ, φ), and have an exponential radial dependence ($\sim e^{-\zeta r}$); radial nodes are described by linear combinations of STOs. The universal equation of a Slater type basis function is shown in Eq. 2.32, where N is the normalisation constant, $Y_{l,m}$ are spherical harmonic functions, n,l and m are the corresponding quantum numbers and ζ is the Slater exponent, which is usually an empirically chosen value based on high-level atomic calculations.[v]

$$\chi_{\zeta,n,l,m}(r,\theta,\varphi) = NY_{l,m}(\theta,\varphi)r^{n-1}e^{-\zeta r} \tag{2.32}$$

Although STOs give good approximations, since they depend exponentially on the nucleus-electron distance, it is expensive to carry out integrations for bigger systems with them. The use of *Gaussian Type Orbitals* (GTOs) is much more common; because of their $\sim e^{-\zeta r^2}$ radial dependence (Eq. 2.33) the one electron integrals can be integrated analytically.[91]

$$\chi_{\zeta,n,l,m}(r,\theta,\varphi) = NY_{l,m}(\theta,\varphi)r^{2n-2-l}e^{-\zeta r^2} \tag{2.33}$$

[v] Originally the Slater exponent was defined by the nuclear charge with the following equation: $\zeta = (Z-s)/n^*$, where Z is the actual charge on the nucleus, s is a screening constant and n^* is the quantum number in the field of $(Z-s)$, but nowadays the empirical evaluation of ζ is more common.

Moreover, the product of two GTOs in two different centres is a third GTO with a new centre, which makes the integration of the two-electron integrals easier. However, they generally give a poorer description of the behaviour of the electron close to the nucleus and far from it, than STOs. Gaussian type functions decay more rapidly moving away from the nucleus and fail to predict the cusp behaviour of the atomic orbitals at the nucleus as shown in Figure 2.1. One way to increase the level of accuracy is to introduce more GTOs: the *contracted* GTOs (CTGOs) are fixed linear combinations of *primitive* GTOs (PTGOs).[92] In this way, a set of basis functions can be contracted into a smaller set of functions, and the more PTGOs are used, the more accurate the description of the orbital can be. But it is still worth using them, since their computational cost is less than STOs even with the higher number of basis functions.

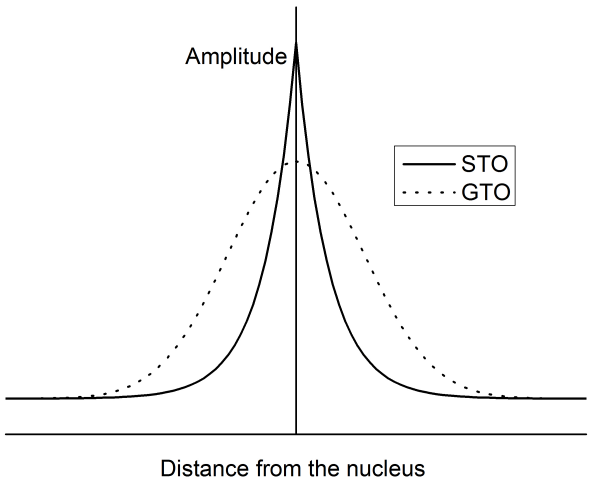

Figure 2.1: Schematic comparison of the radial function in Slater and Gaussian Type Orbitals

After the type of basis set, we have to make a decision about the number of functions used. In the case of plane waves, hundreds of functions are used for a certain volume, while for atom-centred orbitals the minimum size would have the same number of basis functions as there are hydrogenic orbitals on the atoms in the given molecule. The double-ζ(DZ) basis sets contain twice the number of atomic orbitals and the size can grow up to triple-ζ (TZ), quadruple-ζ (QZ) or more but the computational cost increases as well. The ζ letter in the names of the basis sets refers back to the exponent of the exponential radial dependence in the STO basis functions.

Since the valence electrons are chemically more important than the core electrons, basis sets which spend more computational effort on the outer electrons would be more appropriate.

Split valence basis sets separate the core and valence orbitals in the atoms, and while the core orbitals are a contraction of a number of PGTOs, the valence orbitals split into more functions. For example, in the 3-21G basis set which was developed by Pople *et al.*,[93] the core orbitals are described at single-zeta quality with a linear combination of three PGTOs, while the valence orbitals have double-zeta basis sets, which contain one CGTO formed the linear combination of two PGTOs and a single PGTO as the second function.

In the basis set family which was used in the present calculations (def2-SVP, def2-TZVP and def2-QZVP from R. Ahlrichs[94]), the core orbitals are represented by one CGTO, while the valence orbitals are described at the double-, triple- and quadruple-ζ level (SV, TZV and QZV respectively) and with a set of polarisation functions (P) which is a set of basis functions with a higher angular momentum than the occupied valence orbitals. They are used to improve the description of non-spherical electron distributions with their higher angular nodality, therefore allowing the definition of possible anisotropic interactions within the chemical bonds.

2.4.1 Effective Core Potentials (ECPs)

The core electrons of heavier elements do not play a significant role in the formation of molecular bonds but plenty of primitive GTOs are needed to expand them properly (to describe the electron-electron repulsion with the valence orbitals). Moreover, in the case of the elements from the lower part of the periodic table, relativistic effects cannot be neglected. With the use of the so-called *Effective Core Potentials*[95] one can significantly reduce the computational cost and take into account part of the relativistic effects as well.

In the ECPs, the core orbitals are replaced with a pseudopotential function constructed to model the chosen core electrons instead of a large number of basis functions. First, an accurate wavefunction is calculated with the use of a high-level all-electron basis set. Then the valence orbitals are replaced with nodeless functions, in a way that the created pseudo-orbitals of the valence electrons do not have core nodes, but still describe the nodal structure with the new core function correctly. The next step is to exchange the core electrons for a parametrised potential expanded as a set of analytical functions, and fit the parameters such that the Schrödinger equation produces pseudo-orbitals matching all-electron valence orbitals.

If GTOs are used for the valence orbitals, the ECP is a Gaussian type function too. In this case, the quality of the ECP depends on the number of electron orbitals chosen to be represented by the new core function. Evidently, having less electrons merged into the ECP and more on valence type orbitals increases the accuracy, while also increasing the computational

cost. In our case, the investigated systems have an ECP and the associated valence basis set to describe the core electrons in the 1s-3d orbitals of the Sr atom, similarly, ECPs are used for calculations involving the Rb (1s-3d orbitals), and Ba, Cs (1s-4d orbitals) atoms in section 4.5.1.[96, 97]

2.4.2 Basis Set Superposition Error (BSSE)

The use of finite size atomic centred basis sets introduces an error which is especially important in the case of weak interactions between molecules. The problem lies in the fact that in a complex formed by an interaction between two molecules, the energy of the complex is calculated with a basis set composed from the basis sets of both molecules. It means that the molecules in the complex are treated with a more complete basis set than the individual ones. Therefore the energy of the complex is artificially lower and the strength of the interaction is overestimated. This problem is the so-called *Basis Set Superposition Error* (BSSE) and one way to avoid it is to increase the size of the basis set, but this significantly increases the computational cost. Thus the most common way to compensate for the BSSE is to use an approximation, the *Counterpoise Correction* (CP),[98] to evaluate the error. In this method we use 'ghost functions' which are the basis sets of one molecule located at the corresponding nuclear position but without the nuclei or electrons, to improve the basis set of the other molecule. These modified basis sets are used to calculate the energy of the individual molecules ($E(A)^*_{ab}$,$E(B)^*_{ab}$). In addition, we calculate the energy of the individual molecules with the same geometries that they have in the complex but with their own basis sets only ($E(A)^*_a$,$E(B)^*_b$). The value of the error can be calculated from these results according to the following equation:

$$\Delta E_{CP} = E(A)^*_{ab} + E(B)^*_{ab} - E(A)^*_a - E(B)^*_b \tag{2.34}$$

The counterpoise correction was used here to compensate for the BSSE error in the studied adsorption reactions, since the basis set of the isolated ions or systems is significantly smaller than the overall basis set of the adsorbed complexes with the surface.

2.5 Solvent Models

If the studied systems are solvated, the effects of the solvent can significantly modify their properties compared to the results in vacuum. There are two ways to take into account the solvation; one is to describe explicitly the solvent molecules and the other is to consider the

solvent implicitly, as a continuous medium. Expanding the system with individual solvent molecules is necessary if one would like to include the short-range, specific, interactions between the solvent and the molecule, such as the effects of hydrogen bonds, van der Waals interaction etc. However, modelling the first solvation shell will not describe the long-range interactions: the polarisation or the dipole orientation effect of the solvation. In most cases the solute is ionic or it is a neutral molecule with a dipole moment, which arises due to the non-homogeneous charge distribution within the molecule. The solute polarizes the polarisable medium (described with a relative permittivity, ε_r) and modifies the orientation of its electric multipole moments, which then acts back on the solvated system. If the structure of the molecule (solute or solvent) is very symmetric or apolar, the dipole moment or the permittivity is very small and these non-specific interactions have no significant effect on the system. But in any other cases, the long-range interactions can modify the orientation of the surrounding solvent molecules, as well as the optimal geometry and the free energy of the solvated molecule.[99] Since including enough solvent molecule explicitly to model these non-specific effects is practically impossible with *ab-initio* quantum chemical methods, we have to use QM/MM methods or Continuum Solvent Models to efficiently consider their contribution. [100]

2.5.1 Continuum Solvent Models (CSM)

In the CSM methods, the solvent is treated as a *homogeneous polarisable medium* with a dielectric constant (which is the relative permittivity of the solvent, ε_r), while the molecule is surrounded with a suitably shaped cavity in the medium.[99] The solvation free energy can be described with the following terms in this system:

$$\Delta G_{solv} = \Delta G_{cavity} + \Delta G_{dispersion} + \Delta G_{electrostatic} \tag{2.35}$$

The term related to the formation of the cavity (ΔG_{cavity}) is positive, since the loss of the solvent-solvent interactions has a destabilising effect. The newly formed dispersion interactions between the solute and the solvent ($\Delta G_{dispersion}$) as well as the electrostatic interactions in term $\Delta G_{electrostatic}$ give a negative contribution to the energy of the solvated system.

One key question of CSM methods is the definition of the cavity, since ΔG_{cavity} and $\Delta G_{dispersion}$ are often assumed to be directly proportional to the the total surface area and the solution of $\Delta G_{electrostatic}$ is also related to the cavity. Although employing spherical or ellipsoidal shaped cavities would allow the analytical solution of the electrostatic term, gen-

erally a level of molecular surface description is needed for acceptable results compared to experimental data. One way to define molecular shaped holes is to consider every atom in the solute as a sphere with a radius of the atomic radius times the van der Waals radius of the atom. The atom-centred spheres overlap with each other and create the *van der Waals (vdW) surface*, shown in Figure 2.2. Most of the solvent models operate with vdW surfaces because it is computationally cheaper and still very similar to other more complicated surface descriptions, such as the so-called *solvent accessible surface* (SAS) traced out by the centre of solvent sphere rolling over the vdW surface or the molecular surface is the lower envelope generated by the rolling solvent.[101] They were both created because the vdW surface may contain small parts, where the solvent molecules are too big to enter. A different way to define a cavity is to use a surface related to a given electron density value. This approach is less common because we need the whole wave function for the density based surface construction.

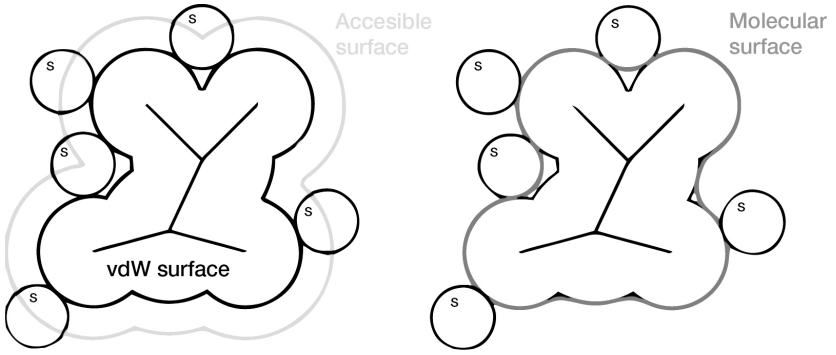

Figure 2.2: Different definitions of the cavity surface[102]

The electrostatic stabilisation arises because the charge distribution of the molecule (ρ_M) induces a charge moment in the solvent which acts back and polarises the molecule, changing its charge distribution. One can easily see that calculating this term is a self-consistent process, which requires an iterative solution.[101, 103] When the molecule is surrounded with a polarisible medium, the electrostatic potential term within the quantum mechanical framework (V) is extended with a *solvent reaction potential* (V_R), generated by the polarization of the dielectric medium:

$$V = V_\rho + V_R \tag{2.36}$$

Where V_ρ is the electrostatic potential related to the overall charge distribution including the electronic and nuclear components. The most common way to evaluate the reaction potential is to integrate the partial *surface charges* ($\sigma(\mathbf{s})$) screening the cavity surface (Eq. 2.37), where s is the position variable on the cavity surface. However, we need the total electrostatic

potential within the cavity to calculate $\sigma(\mathbf{s})$, using a simplified form of the classical Poisson equation, shown in Eq. 2.38, where **F** is the derivative of V perpendicular to the surface and ε_r is the dielectric constant of the solvent.

$$V_R = \int \frac{\sigma(\mathbf{s})}{|\mathbf{r}-\mathbf{s}|} d^2\mathbf{s} \tag{2.37}$$

$$\sigma(\mathbf{s}) = \frac{\varepsilon_r - 1}{4\pi\varepsilon_r}\mathbf{F} \tag{2.38}$$

Similarly to the previously shown self-consistent field process 2.2, we first have to make a guess for the charge density (ρ_M) to construct the electrostatic potential which can be used to calculate the surface charge on the cavity and the reaction potential. Including V_R modifies the total electrostatic potential, which gives a new surface charge and this cycle goes on, until there is no significant change in the output potential from one cycle to the next. The actual $\Delta G_{electrostatic}$ term is calculated based on the dipole moment and polarizability, evaluated from the final charge distribution.

Although CSMs are convenient to implement and use in QM codes, they have their limitations, since ε_r is the only parameter characterising the solvent. For example solvents with very similar dielectric constant will behave the same using this model while they might differ significantly in reality due to possible hydrogen bonds or differences in planarity. Besides, ε_r is treated as a constant in the continuum models, while it can depend for instance on the distance from the solute or the speed of the reaction.

In chapter 3 the so-called *conductor-like screening model* (COSMO)[104, 105] is used, as implemented in the TURBOMOLE code. It employs molecular shape cavities based on the van der Waals radii of the atoms in the molecule. The cavity is defined in the beginning of every SCF cycle and the dispersion free energy terms are parametrised based on the surface area of the cavity. The electrostatic contribution is defined from the electrostatic potential by partial atomic charges which are calculated with a self-consistent reaction field model, assuming an infinite dielectric constant $\varepsilon_r = \infty$, i.e. conductor-like behaviour for every solvent. This assumption results in zero potential on the cavity surface ($V = V_\rho + V_R = 0$), and significantly simplifies the use of Eq. 2.38, which instead of the normal component of V (**F**), only depends on a local value. However, the final surface charge obtained with an infinite permittivity ($\sigma^*(\mathbf{s})$) has to be corrected with an empirical scaling function ($f(\varepsilon_r)$) to recover the effect of the finite value of the ε_r (Eg. (2.39)).[101] The scaling factor is determined by comparing the unscaled COSMO results to known electrostatic solute-solvent energies and the following formula is

employed (where k is a small value, 0.5 in TURBOMOLE[106]):

$$\sigma(\mathbf{s}) = f(\varepsilon_r)\sigma^*(\mathbf{s}) = \frac{\varepsilon_r - 1}{\varepsilon_r + k} \tag{2.39}$$

To avoid any electron density "leaking out" from the molecular cavity for example due to diffuse basis sets on atoms close to the cavity surface, TURBOMOLE employs a so-called *outlying charge correction* (OC) during the COSMO calculations. At the end of the converged SCF a new outer surface with increased radii is constructed to evaluate the OC correction term for the dielectric energy and added to the value calculated with original cavity surface.[107]

As it was stated before, the cavity is defined at the beginning of every SCF cycle and checked for outlying charges at the end of SCF convergence. In case of vibrational frequency calculations a problem may arises due to the different time-scale of the molecular vibrations and the solvent re-orientation (the former is much faster than the latter). Since the normal modes are obtained by a series of single point calculations in which the individual atoms are slightly displaced to study their motion (see section 2.7.2), the cavity is defined differently for each distorted geometry and electrostatic energy difference arising from the electron density difference is evaluated.[106]

The COSMO solvent model plays and important role this thesis. First, in chapter 3 it is shown applying a constant dielectric continuum has a significant effect on the optimised geometries and its use is necessary to obtain realistic energies for the Sr^{2+} complexes. Subsequently, in chapter 5 a modified COSMO correction term is employed to allow the energetic comparison of the adsorbed complexes on the hydrated brucite surfaces with structures in the bulk solvent.

2.6 Periodic Electronic Structure Methods

Crystalline materials are rather different from isolated molecular structures: they are built up by a large number of atoms and/or molecules, which form a well defined symmetrical structure with significant intermolecular interactions between the structural units. Every crystal material has some kind of translational invariance, i.e. the atom in position **r** is equivalent to the atom in **r'**:

$$\mathbf{r'} = \mathbf{r} + \sum_{j=1}^{3} N_j \mathbf{a}_j \tag{2.40}$$

Where $\mathbf{a}_j$ are the basis vectors in the three spatial direction ($j = 1, 2, 3$ as a, b, c), N_j are the number of times that the translation was repeated in j directions.

Modelling solids heavily relies on the fact that there is a proven relation between the spatial symmetry of the systems and the physical property of the material. Based on the above shown translational invariance, one can apply *periodic boundary conditions*[108] (PBCs) to reduce the practically infinite size of the systems to finite size units while still aiming to calculate properties related to the whole material.

I briefly summarise the basics of two methods developed to model solid materials, both of which have their advantages and disadvantages depending on the interest of the solid phase study. Periodic density functional theory is the most common approach to investigate crystalline materials and their properties, while the periodic electrostatic embedded cluster method was specifically developed to study isolated defects or surface reactions of solid materials.

2.6.1 Periodic Density Functional Theory

For bulk studies, any effects related to the surfaces can be neglected to consider the real crystal as infinite and translation invariant.[54, 109] Assuming independent electrons moving in the periodic potential field of the solid material, described by a periodic function having the same periodicity as the crystal ($V(\mathbf{r'}) = V(\mathbf{r})$), one can apply the Schrödinger equation to describe the energy states of the studied solid. Since the Hamiltonian operator, containing V, has to be translation invariant too, we can write down the following equalities for the SE:

$$\hat{T}_g\left(\hat{H}(\mathbf{r})\Psi(\mathbf{r})\right) = \hat{H}(\mathbf{r})\hat{T}_g\Psi(\mathbf{r}) = \hat{H}(\mathbf{r})\Psi(\mathbf{r'}) \tag{2.41}$$

$\hat{T}_g$ is the translation operator, which leaves the Hamiltonian invariant, i.e. if $\Psi(\mathbf{r})$ is the eigenfunction of the Hamiltonian, $\hat{T}_g\Psi(\mathbf{r}) = \Psi(\mathbf{r'})$ is an eigenfunction with the same energy too.

The *Bloch theorem*[110] defines the relation between the periodic Hamiltonian and the wavefunction by stating that: wavefunctions, which are the solutions of the periodic SE eq. in equivalent positions in the lattice of different unit cells, only differ by a **k** related phase factor, $e^{i\mathbf{kg}}$ shown in (2.42), where **k** is the wave vector. Any $\Psi(\mathbf{r})$ obeying to this symmetry rule is a Bloch function (BF, also known as Bloch wave) $\Phi_{n\mathbf{k}}(\mathbf{r})$, and can be written as a product of a plane wave and a periodic function with the same periodicity as the crystal (2.43). Note that, not **k** nor the periodic function ($u_{n\mathbf{k}}$), only the wavefunction determines uniquely the quantum state of the electron because, there are more then one periodic functions for the same **k** differing by their n band index; while for a given n $\Phi_{n\mathbf{k}}$ varies continuously with **k**, creating a continuous energy band.

$$\Phi_{n\mathbf{k}}(\mathbf{r'}) = \Phi_{n\mathbf{k}}(\mathbf{r}+\mathbf{g}) = e^{i\mathbf{kg}}\Phi_{n\mathbf{k}}(\mathbf{r}) \tag{2.42}$$

$$\Phi_{n\mathbf{k}}(\mathbf{r}) = e^{i\mathbf{kr}}u_{n\mathbf{k}}(\mathbf{r}) \tag{2.43}$$

One can contract the problem originally spanned over the infinite crystal to a finite sized $N = N_1 \text{x} N_2 \text{x} N_3$ cell, by combining the Bloch theorem with the periodic boundary conditions (Eq. (2.40)) and define the allowed **k** vectors such that the phase vector equals to one for any integer α and every $j = 1, 2, 3$:

$$\Phi_{n\mathbf{k}}(\mathbf{r}+\alpha N_j \mathbf{a}_j) = e^{i\alpha N_j \mathbf{k}\mathbf{a}_j}\Phi_{n\mathbf{k}}(\mathbf{r}) \quad \text{where} \quad e^{i\alpha N_j \mathbf{k}\mathbf{a}_j} = 1 \tag{2.44}$$

The **k** points which satisfy this requirement are defined by the basis vectors of the reciprocal lattice ($\mathbf{b}_j$) and the m_j integer: $\mathbf{k} = \sum_{j=1}^{3} \frac{m_j}{N_j}\mathbf{b}_j$. There are $N = N_1 \text{x} N_2 \text{x} N_3$ number of **k** points allowed in every reciprocal lattice cell and when N is a huge number, **k** is practically a continuous variable. The fact that the wave vector is defined in the reciprocal space, makes every wavefunction translated by any reciprocal lattice vector ($\mathbf{K} = \sum_{j=1}^{3} m_j \mathbf{b}_j$) equal: $\Phi_n(\mathbf{k}) = \Phi_n(\mathbf{k}+\mathbf{K})$, and allows us to restrict the analysis of the Bloch functions entirely to the first Brillouin zone (BZ)[vi].

Operating with the Bloch functions in reciprocal space and using a finite number of them as basis functions simplifies the evaluation of the expectation value of the Hamiltonian. If all the integrals in the solution of the SE equations are periodic functions with the same periodicity of the lattice[vii] and the Bloch functions are expanded with a linear combination of plane waves ($\Phi_{n\mathbf{k}} = \sum_{\mathbf{K}} c_{\mathbf{k},\mathbf{K}} e^{i(\mathbf{k}+\mathbf{K})\mathbf{r}}$), the eigenvalue of the SE equation can be evaluated by summing up integrals only involving plane waves:

$$\left\langle \Phi_{n,\mathbf{k'}}(\mathbf{r}) | \hat{H}_{\mathbf{k},\mathbf{k'}}(\mathbf{r}) | \Phi_{n,\mathbf{k}}(\mathbf{r}) \right\rangle = \sum_{\mathbf{K}} c_{\mathbf{K}} \sum_{\mathbf{K'}} c_{\mathbf{K'}} \int e^{i(\mathbf{k'}+\mathbf{K'})\mathbf{r}} \hat{H}(\mathbf{r}) e^{i(\mathbf{k}+\mathbf{K})\mathbf{r}} d\mathbf{r} \tag{2.45}$$

Due to the orthogonality of the plane waves, these integrals are always zero except if the wave vectors of the functions are the same ($\mathbf{k} = \mathbf{k}'$).

Therefore, the Hamiltonian can be defined as a block diagonal matrix, containing $n \text{x} n$

[vi] The first Brillouin zone is basically the Wigner-Seitz type primitive cell of the crystal in reciprocal space; its defined by a collection of points which are closer to the origin of a given reciprocal lattice than any other reciprocal lattice points.

[vii] It was shown earlier that the potential energy function is periodic and the kinetic energy contains the second derivatives of $u_{n\mathbf{k}}$, therefore it has the same periodicity too.

blocks if there are n Bloch functions in the basis set. Each block is related to an individual **k** vector in the reciprocal unit cell, and can be calculated independently from the other blocks. One can calculate the total energy of the unit cell by solving SE equations for the first Brillouin zone of the periodic system at a finite number of **k** points sampling the Hamiltonian matrix (2.46), keeping in mind that the same number of **k** points applied for a bigger normal cell as for a smaller one, will mean a finer sampling in the reciprocal space.

$$\hat{H}\Psi_{n\mathbf{k}}(\mathbf{r}) = E_{n\mathbf{k}}\Psi_{n\mathbf{k}}(\mathbf{r}) \tag{2.46}$$

Similarly to the previously mentioned HF or DFT theories, the practical solution of the one-electron SE or KS equations is an iterative process in the solid state calculations involving the use of trial basis functions. In the CRYSTAL code the Bloch functions are constructed from the linear combination of atomic orbitals, which are usually defined by contracted GTOs[111] (see section 2.4). Since the Bloch waves have to be periodic with the same periodicity of the crystal, the AOs are chosen in the unit cell like $\chi_\mu(\mathbf{r}-\mathbf{r}_\mu)$, where $\mathbf{r}_\mu$ is the origin of the μ orbital in the first cell, and repeated in the other cells of the crystal to form the μth BF:

$$\Phi_{\mu,\mathbf{k}}(\mathbf{r}) = \frac{1}{\sqrt{N}}\sum_{\mathbf{g}} e^{i(\mathbf{kg})\mathbf{r}}\chi_\mu^{\mathbf{g}}(\mathbf{r}-\mathbf{r}_\mu) \tag{2.47}$$

The key step of the iteration process in periodic systems that to define the Bloch functions for the chosen **k** points in the Hamiltonian matrix, first its components (the one- and two-electron integrals) have to be defined in real space with the use of the basis functions and then Fourier transformed from real space to reciprocal space. Once the one-electron SE or KS equations are solved for each sampling **k** points in the first BZ and the electron density is evaluated, it has to be inverse Fourier transformed to real space again to repeat the evaluation of the integrals until self-consistency achieved.

2.6.2 Periodic Electrostatic Embedded Cluster Method (PEECM)

The primary application of the Periodic Electrostatic Embedded Cluster Method (PEECM) is to calculate the structure and the properties of isolated defects in ionic crystals or on their surfaces. With the electrostatic embedding of a finite quantum chemical (QM) region in a periodic infinite array of point charges (PCs), it is possible to treat the localised defect in the crystal on the level of any standard *ab initio* method with a modest computational cost. In contrast to the PEECM, in periodic DFT calculations the defect concentration is often higher

and to avoid false interactions between the defects large supercells are necessary which significantly increasing the computational cost.[56]

In this method, we divide the entire system to two main parts: an inner cluster and an outer part. A schematic representation of the subdivisions in the system is shown in Figure 2.3. The innermost part of the cluster is the local region which contains the defect, not repeated in any dimension and is treated quantum chemically. There is an isolating shell in the cluster around the QM region in which the cations are replaced by effective core potentials (ECPs, 2.4.1) or natural PCs to prevent the artificial polarisation of the electron density in the innermost part by the nearby point charges.[112] Surrounding the defect is the outer part which is described as infinite periodic array of PCs.

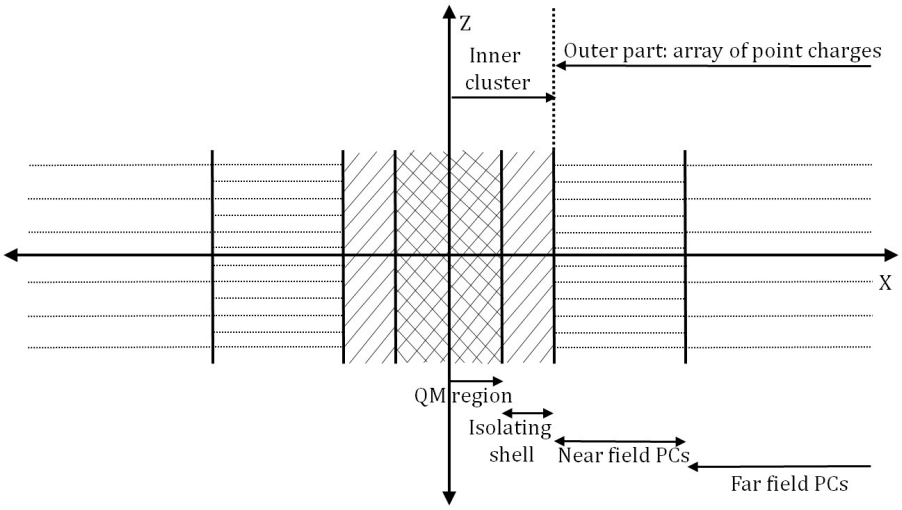

Figure 2.3: Schematic representation of the different regions in PEECM calculations in the x direction

An electrostatic potential arises in the QM region from the PC field environment which can be taken into account as an additional energy (J^{emb}) term in the total energy of the QM region:

$$J^{emb} = \sum_{\mathbf{L}\in O}^{\infty} \sum_{k}^{N\in UC} \left(\sum_{\mu\nu} D_{\mu\nu} q_k \int \frac{\mu(\mathbf{r})\nu(\mathbf{r})}{|\mathbf{r} - \mathbf{R}_k + \mathbf{L}|} d\mathbf{r} + \sum_{a} \frac{q_k Z_a}{|\mathbf{R}_a - \mathbf{R}_k + \mathbf{L}|} \right) \tag{2.48}$$

J^{emb} contains two terms, one describes the Coulomb interactions between the electrons of the QM region and the PCs, while the other contains the interactions between the nuclei of the inner cluster and the PCs. **L** is a direct lattice vector in the outer part *O*. *UC* is the unit cell and *k* is the index of an ionic PC, q_k at the position $\mathbf{R}_k - \mathbf{L}$. μ and ν are Gaussian basis functions, $D_{\mu\nu}$ is an element of the density matrix, and Z_a is the nuclear charge at position $\mathbf{R}_a$ in the cluster. Summing over **L** and *k* includes the images of all the PCs except the ones in

the inner cluster.

A difficulty of the PEECM is calculating J^{emb} for an infinitely large array of PCs, since a direct sum of all the Coulomb interactions is impossible. A usual approach often applied by other QM/MM methods is to evaluate the electrostatic energies in the PC field using *Ewald summation*.[113, 114] In this method the outer region is divided to two more parts: a near field part (NF) where the Coulomb interactions are summed up directly in real space, and a far field part (FF) in which the summation is made in Fourier space.

PEECM uses another approach called the *Periodic Fast Multipole Method* (PFMM)[115] which also divides the outer region to NF and FF, but employs multipole expansions for the FF interactions besides the analytical integration of the Coulomb interactions in the NF. The size of the near field region is usually given by the well-separateness criterion[115] defined by the size of the PC unit cell and a separateness constant; which is for instance 3.0 by default in the TURBOMOLE code. In general, the NF region has to be big enough to allow a rapid convergence for the multipole approximations in the far field. Using PFMM avoids having to convert integrations to reciprocal space and back, therefore it is less demanding computationally than the Ewald summation. First, the basis functions, the nuclear charges and the PCs are all evaluated by multipole moments of solid harmonics. Then the computed PC equivalents are expanded as Taylor expansions around the center of the system, using the periodicity of the unit cell. And finally, the far field components of the electrostatic potential are calculated using the defined multiple expansions for each term.

PFMM seriously speeds up the calculation of the additional electrostatic potential arising from the PCs, as a result, PEECM simulations in TURBOMOLE run in a similar time scale than a standard molecular DFT calculation, only requiring a small fraction of the total computational cost of a DFT optimisation.[56] This advantage of the PEECM calculations compared to other approaches played an important role in choosing this particular method to simulate the brucite surface. The optimisation of the brucite (0001) model in TURBOMOLE and its validation is the basis of chapter 4, in which we use the PEECM model of brucite to examine the adsorption of single solvated ions on a surface, a situation which can be compared with an isolated defect.

2.7 Calculations In Practice

Quantum chemical calculations are most often used for structural optimisation of chemical systems or calculating their energy derived properties, as thermodynamic properties, forces and electric moments etc. The basic principles of geometry optimisation and vibrational fre-

quency calculations are summarised within the sections 2.7.1 and 2.7.2. Besides, the results of electronic structure calculations, such as the optimised electron density function and molecular orbitals can be used to further investigate the molecular and atomic properties within the systems. Some of the electronic structure analysis methods are detailed in section 2.7.3.

The general steps of a quantum chemical calculation for obtaining the optimised geometry are the following: First, we have to create a geometry input, usually in the form of Cartesian or internal coordinates. Then, based on the Born-Oppenheimer approximation we optimise the electronic structure separately for the given nuclear coordinates by calculating the total energy of the system with a self-consistent iterative method. Taking the first and second derivative of the obtained energy with respect to the atomic displacements helps us to define a new set of coordinates and the SCF calculation has to be repeated for the new energy, continuing this process until self-consistency achieved for the geometry optimisation too. The optimised structure, together with its total energy and the electron density function related to the obtained atomic coordinates can be the input of further calculations investigating properties of the system.

2.7.1 Geometry Optimisation

During the geometry optimisation we are seeking specific points on the potential energy surface, which are stationary points of the energy function, i.e. their first derivative (the gradient) is zero and their second derivatives are all positive or contain one or more negative eigenvalues, depending on the nature of the characteristic point: the local minima (2^{nd} derivatives are all positive) correspond to stable structures such as reactants, products or intermediates, while stationary points with only one negative 2^{nd} derivative are related to transition states, i.e. to the lowest saddle point between two minima.

Most of the geometry optimisation methods used in this study follow an iterative procedure, during which the atomic coordinates are changed step by step towards the optimum, while the gradient vector is calculated analytically for each step and the matrix containing the second derivatives (Hessian matrix) is approximated. The optimisation is finished when the following criteria are all satisfied: the energy change between two optimisation steps is below a certain value and both the maximum displacement and the maximum gradient elements with the RMS of them are below a given value too. Most of the quantum chemical codes, such as TURBOMOLE, use a *quasi-Newton-Rapshon method*[116] to determine the atomic displacement of the steps, in which a restricted second order Taylor expansion of the energy

function is used to calculate the next step.[106] Controlling the step size and its direction is important to avoid regions where the *quasi*-NR approximation is not valid and to make sure that every step takes the energy closer to the minimum. TURBOMOLE uses a shift parameter to make the step size equal to the trust radius, which is known as the *quadratic method*. Since minimising the whole Hessian matrix and diagonalising it is the computationally most demanding part of the optimisation process, so-called *updating schemes* are employed to reduce the cost. In TURBOMOLE, the first guess of the Hessian is the scaled unity matrix if no other initial approximation is available, and it is improved rapidly with each step by considering the calculated gradient for that direction. With the use of the BFGS[117] updating algorithm, the Hessian is guaranteed to be always positive which can lead to the local minimum in fewer steps.[viii]

2.7.2 Frequency Calculation

Generally in electronic structure studies the ground state energy is calculated at 0K in a hypothetical, motionless state, while in reality the studied systems are at a finite temperature where they have translational, rotational and vibrational motions. For some cases it is possible to take these into account in the energy by calculating thermodynamic corrections for the investigated systems.[ix] In this way, the total energy is calculated as a sum of the zero point energy, and the translational, rotational and vibrational energy contribution at the given temperature. The energy related to the first two types of motion usually equals $2/3k_BT$ per molecule while the vibrational energy has to be calculated from its normal modes. There are $3N-6$ vibrational modes in a non-linear molecule and their frequencies and the displacements of the individual atoms can be evaluated from the Hessian matrix once a single point energy was calculated for the given motion. After making the elements of the Hessian matrix mass-dependent and diagonalising it, the vibrational frequencies are obtained from its eigenvalues, assuming that the energy surface is harmonic close to the energy minimum.

Depending on the size of the studied systems, the Hessian matrix may be calculated analytically or numerically; the latter is not exact and differences of $\pm$10 cm^{-1} in the frequencies can appear. These deviations are more apparent for the first six eigenvalues, which belong to the translational and rotational modes[x] and should be zero for a fully optimised structure.

[viii] BFGS stands for the Broyden-Fletcher-Goldfarb-Shanno method. For transition state optimisation another algorithm should be used to allow negative eigenvalues.[117]

[ix] Thermodynamic corrections are not applicable for systems with frozen coordinates.

[x] This is true when Cartesian coordinates are used for the structure.

2.7.3 Electronic Structure Analysis

Referring back to the first Hohenberg-Kohn theorem (2.3), the electron density of the ground state uniquely defines the external potential, and vice versa, the external potential arising from the nuclei uniquely determines the distribution of the electrons. This is a powerful statement, which means that atomic and molecular properties can be derived from the function of the electron density ($\rho(\mathbf{r})$). Among the several existing analysing techniques, this summary only concentrates on the methods which I applied during my PhD: the quantum theory of atoms in molecules (2.7.3.1), natural population analysis (2.7.3.2) and the 3D distribution of the electron density difference (2.7.3.3).

2.7.3.1 Quantum Theory of Atoms in Molecules (QTAIM)

In the QTAIM, developed by Richard F. W. Bader,[118, 119] the electron density is analysed in terms of its topology to describe atoms and their properties in molecules.[xi]

The general concept of this theory is to divide the molecular volume into so-called *atomic basins*, via the derivation of the electron density function with respect to its three spatial coordinates. The gradient of $\rho(\mathbf{r})$ is zero at the critical points (2.49), which can be classified into four categories based on the number of negative eigenvalues of the Hessian matrix of the electron density (A in Eq. (2.50)).[118, 120]

$$\nabla\rho(\mathbf{r}) = \begin{cases} 0 \text{ if } \mathbf{r} = \mathbf{r}_{\mathrm{C}} \text{ or } \infty \\ \neq 0 \end{cases} \tag{2.49}$$

$$A(\mathbf{r}_{\mathrm{C}}) = \begin{bmatrix} \frac{\partial\rho}{\partial x^2} & \frac{\partial^2\rho}{\partial x\partial y} & \frac{\partial^2\rho}{\partial x\partial z} \\ \frac{\partial^2\rho}{\partial y\partial x} & \frac{\partial\rho}{\partial y^2} & \frac{\partial^2\rho}{\partial y\partial z} \\ \frac{\partial^2\rho}{\partial z\partial x} & \frac{\partial^2\rho}{\partial z\partial y} & \frac{\partial\rho}{\partial z^2} \end{bmatrix} \tag{2.50}$$

The general notation of the different type of CPs is (m, n) where m is the number of non-zero eigenvalues of the Hessian matrix at the critical points and n is the difference between the number of positive and negative eigenvalues:

Critical points with three negative eigenvalues (3,-3), are local maxima and represent the nuclei, which attract the electrons with their positive charges, thus $\nabla\rho(\mathbf{r})$ points towards the strongest local nucleus at every point in space and goes to zero infinitely far from it. However, there are spacial trajectories of the maximum gradient, which terminate in other nuclei and

[xi] Molecules are understood in an extended meaning, i.e., it also contains molecular or ionic crystals, weakly bonded molecular complexes etc.

known as *bond paths*. Each atomic basin is associated with one nucleus and separated from the neighbouring basins by a two-dimensional surface, known as *zero-flux surface*, which is not intersected by the gradient vectors in any point. If a particular atomic property can be expressed in terms of a corresponding property density in space, we can integrate that term in an atomic basin to calculate that property, such as the atomic charge or the dipole, quadrupole moment of the atom etc. Consequently, molecular properties can be evaluated as a sum of the obtained atomic contributions.

Critical points with two negative and one positive eigenvalues (3, -1), are called *Bond Critical Points* (BCPs). They are situated on bond paths and are local minima along the direction of the nuclei and maxima in the plane perpendicular to this axis.

Ring Critical Points (RCPs) have one negative eigenvalue (3, 1), and they are most likely positioned close to the middle of the atomic rings in molecules.

Cage Critical Points (CCPs) have no negative eigenvalues (3, 3), in the Hessian matrix.

An other important parameter derived from the second derivatives is *the Laplacian of the electron density* $[\nabla^2\rho(\mathbf{r})]$, which is the trace of the diagonalised Hessian matrix, i.e. the sum of its eigenvalues. The Laplacian at the BCPs describes the nature of the bond: if the electron charge is locally depleted, the sign of $\nabla^2\rho(\mathbf{r})$ is positive, which is most likely occur in closed-shell interactions such as hydrogen-bonds; while if the electron charge is increased within the intermolecular region, the Laplacian is negative, as happens for covalent bonds.[121]

The strength and nature of the chemical bonds is also reflected in the electron density at the BCPs (ρ_b). In general, it is greater than 0.2 a.u. for covalent bonds and smaller than 0.10 a.u. for weaker, closed shell interactions. There are several examples in the literature where strong correlation was found between QTAIM properties such as ρ_b values or the$[\nabla^2\rho(\mathbf{r})]$ and other properties e.g. bond lengths[122–125] or bonding energies[121, 126–128].

In a typical QTAIM calculation, first a wavefunction is generated from an electronic structure calculation. The hereby used file format, .wfn, holds the atomic coordinates along with the orbital energies, occupancy numbers and the used Gaussian type functions and their expansion coefficients. Since this file format may not be directly available in the used quantum chemistry code, the use of a converter program, such as molden2aim[129], can be necessary. The electron density is obtained from the wavefunction and used point-by-point for the topological analysis. After the CPs and bond paths are calculated, the atomic partitions can be defined along the zero-flux surfaces in the molecular space and the required atomic properties can be evaluated via integration over the atomic basins. The QTAIM theory is implemented in

several codes, such as AIMALL,[130] which was developed by T. A. Keith. In order to obtain meaningful QTAIM analysis, basis sets which are capable to accurately describe the bonding regions in molecules have to be used to calculate the electron density, i.e. basis sets containing polarization functions are necessary. If effective core potentials (ECPs, 2.4.1) are used for any atoms in the molecule (such as Sr), only certain parameters, which depend only on the spatial coordinates like the electron density, can be calculated via QTAIM and at least one sub-valence shell has to be included explicitly to be able calculate the integrated properties.

2.7.3.2 Natural Population Analysis (NPA)

Natural Population Analysis (NPA) was first introduced by Weinhold *et al.*[131] to use the concept of *natural atomic orbitals* (NAOs) for calculating atomic charges (natural charges) and for deriving molecular bonds between atoms. The basic idea of NPA is to construct the atomic orbitals in the molecular environment based on the one-electron density matrix, similarly to the *natural orbitals* (NOs), which are the molecular orbitals of maximal occupancy for the given molecular wave function derived from the molecular first order density matrix ($\Gamma(1|1')$).[132, 133]

NAOs are the atomic orbitals of maximal occupancy for the same molecular wave function as NOs, but obtained from the atomic angular symmetry segments of the original density matrix, i.e. Γ is defined in terms of matrix block of basis functions belonging to the atomic centers (e.g. Γ^{AA}) as it is shown in equation 2.51. While NOs are completely delocalised over the molecule, NAOs are localised on individual atoms.

$$\Gamma = \begin{bmatrix} \Gamma^{AA} & \Gamma^{AB} & \Gamma^{AC} & \dots \\ \Gamma^{AB} & \Gamma^{BB} & \Gamma^{BC} & \dots \\ \Gamma^{AC} & \Gamma^{BC} & \Gamma^{CC} & \dots \\ \vdots & \vdots & \vdots & \ddots \end{bmatrix} \tag{2.51}$$

The diagonalization of each atom-centred block leads us to the so-called pre-NAOs, which already have the one centred angular symmetry but are non-orthogonal, therefore they still contain interatomic overlaps (functions which belong to two atomic centres). The orthogonalisation of these pre-orbitals is done through three main steps, for which we have to divide them based on their occupancy first: to strongly occupied pre-NAOs (occupation number close to 2) and to the remaining formally unoccupied orbitals. Then an occupancy-weighted orthogonalising matrix is created so that the basis related to the former type of pre-NAOs stay as

close to the original set as possible, while the weakly occupied orbitals are allowed to change more significantly. First the strongly-occupied pre-NAOs on two different atomic centres are changed to be orthogonal to each other, then a formally unoccupied and occupied orbitals on one center are orthogonalised, before we make the weakly occupied pre-NAOs of the two different centres orthogonal. This process leads to the final set of orthonormal natural atomic orbitals. The natural population analysis calculates the NAOs and determine the orbital population as the eigenvalues of the one-center angular symmetry density matrix using this basis, while summing up all contributions from orbitals belonging to one center gives the atomic charge (natural charge).

As shown above, NAOs are made orthonormal and formed directly from Γ, i.e. they are intrinsic to the wavefunction. Hence NAOs converge smoothly as the quality of the wavefunction is improved and the obtained natural populations are always positive, contrary to the Mulliken population analysis[134] which can result in negative population values and known to be overly sensitive to basis set accuracy.

2.7.3.3 Mapping the Electron Density Difference

Comparing the electron density distribution of a whole system to its individual fragments can provide useful information about the driving force of the interactions between the fragments and their contribution to the whole electron density. This analysis is usually done by subtracting the combination of the electron densities of the separate fragments from the electron density of the whole complex and visualising it by mapping the resulting electron density difference as an isosurface[xii] related to a chosen electron density value.[135] By a consensual agreement, blue regions are related to electron accumulation, i.e. the electron density is higher in the complex than it was originally in the fragments in those regions; while red regions show electron depletion.

For mapping the electron density, one first has to create files containing the relevant information of the optimised wavefunction for the whole system and the fragments. In our case, we used the molden2aim program[129] to create one from the TURBOMOLE results. Then the chosen wavefunction analysis program (such as Multiwfn) performs the operations needed to obtain the electron density difference function and writes the results to a grid data file, containing the atomic coordinates and the set of grid data in real space for the function which we are interested in.

[xii] Isosurface is a 3D surface connecting the points with a constant electron density value in space.

2.7.4 Codes

The majority of the presented results are based on calculations carried out with the 6.5 or 6.6 version of the TURBOMOLE code,[136, 137] while the CRYSTAL14[138] program was used for periodic DFT calculations in section 4.5.3 and 4.5.4. The wavefunction analysis techniques used in the thesis were supported by AIMALL[130] and the Multiwfn[139] codes.

2.7.4.1 TURBOMOLE

TURBOMOLE[88, 106, 137] is a highly-optimised, multifunctional software package for *ab initio* electronic structure calculations on molecules, clusters (and periodic solids), developed for academic and industrial purposes. It was started at 1987 in the group of Professor Reinhart Ahlrichs at the University of Karlsruhe and at the Forschungszentrum Karlsruhe. Today, the development of the code is done under the supervision of the TURBOMOLE GmbH company, which was founded by the main developers of the original software.

The premier focus of this code is to investigate molecules at reasonable time and memory requirements, working with standard UNIX environment and PCs. Consequently, TURBOMOLE is designed to be very robust, fast and easily editable with UNIX tools. To lower disk space and memory requirements, besides the full use of molecular symmetry point groups, the implemented methods are combined with ultra-efficient and numerically stable algorithms such as resolution-of-the-identity and fast multipole expansion techniques.

TURBOMOLE is a multifunctional code featuring several electronic structure methods from Hartree-Fock, to post-HF methods or DFT for the calculation energies and structures in the ground state, and time dependent DFT for electronic excited states; besides the wide range of possible calculations predicting electronic, optical and magnetic properties, such as UV-VIS, Raman, IR and NMR spectra. The code uses only Gaussian-type basis functions, but it has a big family of split valence basis sets with contracted GTOs available up to very high level of quality for all elements, with effective core potentials if they are necessary. Similarly, DFT functionals at all levels of accuracy are implemented within the code, combined with the previously mentioned resolution-of-the-identity approximations to speed up the calculations. The most relevant additional features of TURBOMOLE for this particular study are the continuum solvent model (COSMO) and the periodic electrostatic embedded method (PEECM), which are both crucial for different parts of this project. The fact that they are implemented within the same code helps to integrate the results obtained.

TURBOMOLE is primarily designed for medium-sized computer clusters and although par-

allel versions are integrated into the code, the scalability of the calculations is restricted: the practical limit of linear scalability is up to 32 cores, after that the improvement in computational performance rapidly decays. However, due to the numerous efficiency increasing algorithms, TURBOMOLE is compatible, even faster, in many circumstances than other massively parallelised codes.

2.7.4.2 CRYSTAL

The first publicly available *ab initio* code using Gaussian type basis sets for periodic systems was CRYSTAL88,[140] developed to study the physical and chemical properties of solid state materials by the Theoretical Chemistry Group of the University of Turin. It was followed by six other version until the newest release of the code: CRYSTAL14.[138, 141]

The most important feature of periodic systems is their symmetry, and CRYSTAL allows the use of a wide range of symmetry operators in each step of the calculations, significantly reducing the computational costs. Systems with zero dimensionality (molecules) up to three dimensional systems, such as crystals, solid solutions or to some extent, disordered systems can be investigated. Furthermore, with the use of automatic tools implemented within the program, structures with lower dimensionality can be easily created e.g. slabs, nanotubes, nanorods, polymers etc.

The available methods to calculate the electronic structure and energy of the ground state are Hartree-Fock and Density Functional Theory, both using Bloch functions (BFs) for the expansion of one-electron wavefunctions. Uniquely in CRYSTAL, instead of commonly used plane wave basis functions, atom-centred Gaussian-type orbitals (GTOs) are used to define the crystal orbitals, which makes this method very applicable for comparative studies with PEECM. All-electron basis sets and ones including effective core potentials are both available in the code, beside a wide range of DFT functionals up to the fourth and fifth levels of Jacob's ladder. Using hybrid functionals such as B3LYP and PBE0 is generally very expensive in periodic DFT codes employing plane waves, but in CRYSTAL even calculations with double hybrids and range-separated hybrids can run relatively efficiently.

Modelling adsorption on surfaces or defects in solids requires a large unit cell with low symmetry, in which case using symmetry operators can do little to reduce the computational costs. But in CRYSTAL14, a massive parallel version (MPPCRSYTAL) is available beside the serial and normal parallel option (PCRSYTAL), which allows the use of hundreds or thousands cores in parallel with a good time and memory scalability respect to the system size and

required number of CPUs. The main difference between MPPCRSYTAL and PCRSYTAL is that while in the latter the important matrices and determinants are copied in whole to each node, they are divided and distributed over the cores in the former. Since in my PhD project, I used this CRYSTAL for investigating surface reactions on brucite, I made a good use of the massively parallel version implemented on the ARCHER supercomputer cluster.

2.7.4.3 AIMALL

AIMALL[130] is a commercially available software package developed for quantitative QTAIM analysis and visualisation of the obtained results. It is developed by Todd A. Keith and heavily based on a previous software package originally developed in Bader's group. AIMALL can perform full topological analysis and calculate a large selection integrated properties relying on the QTAIM information, directly from a wavefunction containing file. The time requirement depends on the system size and the desired elaboration of the analysis, but one analysis, even with the use of more than one processor on a normal PC, can take up a significant time (days).

2.7.4.4 Multiwfn

Multiwfn[135, 139] is a publicly accessible, open-source wavefunction analysis code, which has almost every commonly used analysis technique implemented in, such as QTAIM, Mulliken, Hirshfield and Löwdin population analysis etc. Besides, it can visualise molecular orbitals, natural orbitals and more importantly, modify and/or output several real space functions derived from the wavefunction. In this work, Multifwn was used to create electron density difference plots in section 4.5.1. Depending on the required technique, the computational performance can vary, but due to the well-optimised algorithms of the code, it can often run on a normal PC and some parts are parallelised for an OpenMP environment.

Chapter 3

Simulation of hydrated Sr^{2+} hydroxide complexes: the importance of second shell effects

3.1 Introduction

In order to investigate the interactions between brucite surfaces and solvated ions, it is essential to have a detailed understanding of the microsolvation of those ions, such as Sr^{2+}, for the identification of possible candidate species for surface adsorption. In this chapter, density functional theory at the meta-GGA level is employed to study the microsolvation of Sr^{2+} hydroxides in aqueous environment, in order to establish likely candidate species for the interaction of nuclear fission-generated strontium with corroded Magnox fuel cladding in high pH spent nuclear fuel storage ponds. A combination of the COSMO continuum solvation model (2.5.1) and one or two shells of explicit water molecules is employed.

3.2 Literature review: Previous solvation studies on Sr^{2+}

This short literature review concentrates on previous experimental and theoretical investigations of the solvated strontium cation and its hydrolysis. It starts with a short summary of previous studies on Sr^{2+} hydrates, as these results can be an important starting point for further investigation, it then continues with the available information about the hydroxide complexes.

Studying the formation of aqueous species experimentally in solution is challenging due to several difficulties, like the low concentration of the investigated ions, or because the structure of the studied complex is dominated by the coordinated solvent molecules.[142] Therefore alternative data sources, such as looking at gas phase hydration experiments[143–145], the solid state structure analysis of the hydrated ions[146, 147], or theoretical solvation studies, can reveal important information to aid understanding of solvation, and will be considered in this summary.

3.2.1 Sr^{2+} hydrates in gas phase

Although the structures of Sr^{2+} hydrates are both experimentally and theoretically well studied, their exact coordination number is still under research. For the gas phase hydra-

tion reaction of Sr^{2+} ($Sr^{2+}(H_2O)_{n-1}$+$H_2O \longrightarrow Sr^{2+}(H_2O)_n$) accurate thermodynamic data from threshold collision-induced dissociation (TCID) measurements[144], and from high-pressure mass spectrometry (HPMS)[145] can be found in the literature. Based on these results, the most stable coordination of the Sr^{2+} aqua complex is 6 in the gas phase. Calculations with the MP2 method by Glendening *et al.*[148] resulted in a very good agreement with the experimental binding energies and enthalpies reported in the above mentioned studies and found the most stable coordination to be 6, however, the authors did not consider higher coordination numbers than 6 in their study. Whilst Felmy *et al.* predicted a higher coordination number of 8 by studying the structure and relative stability of $Sr(H_2O)_n^{2+}$ up to $n = 8$ with DFT calculations,[142] higher quality DFT calculations with the TPSS and B3LYP functionals[149] agreed with the experimental results, finding a coordination number of 6 in gas phase even for $n = 7 - 8$, in which the 7^{th} and 8^{th} water molecules occupy the second solvation shell. The recent study of Boda *et al.*,[150] in which they explored possible coordination of Sr^{2+} hydrates for $n = 1 - 24$ by a statistical approach, suggests that 6 is the preferred coordination number until the $n \leq 10$, then 8-coordination becomes more favourable. They reported only one stable isomer for the biggest system: $Sr(H_2O)_{24}^{2+}$, shown in Figure 3.1, which they obtained by systematically increasing the number of water molecules around the complex. Applying the COSMO solvent model to this structure resulted in an increase in the Sr-O distances but did not change the coordination number.

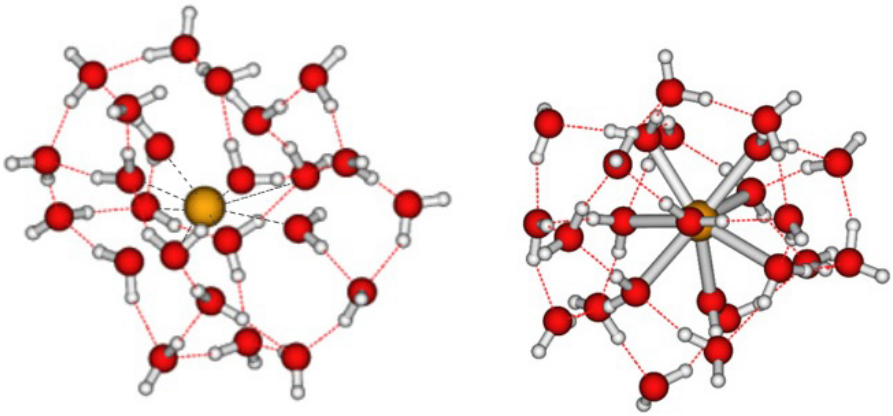

Figure 3.1: The most stable $Sr(H_2O)_{24}^{2+}$ according to Boda *et al.* contains 8 water molecules directly coordinated to the Sr^{2+} ion. The left structure is optimised in gas phase, while the right one with the COSMO implicit solvation model.[150]

3.2.2 Sr^{2+} hydrates in aqueous phase

The coordination number and ion-water distances of solvated alkaline earth metals are known to be dependent on the size of the ionic radii and are summarised in Figure 3.2 by Mehandzhiyski *et al.*[151]. The Born-Oppenheimer molecular dynamic simulations of Mehandzhiyski, involving 86 water molecules around a single cations in an NVT ensemble, showed that while the Mg^{2+} ion strongly attracts 6 water molecules in its first hydration shell with an average 2.19 Å Mg-O distance and a regular octahedral shape, ions with bigger ionic radii gradually attract more waters but less and less strongly. Therefore the coordination number of the first shell becomes less well defined with a wider ion-water interaction range and with a less ordered structure.

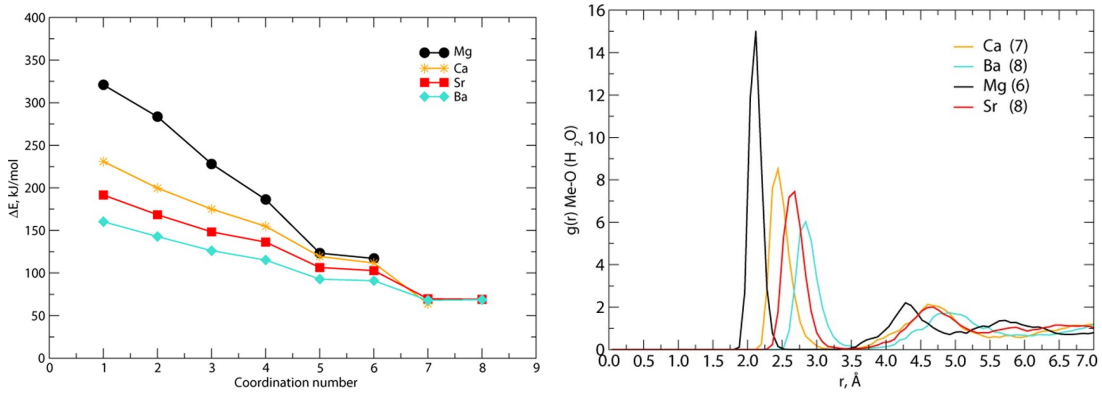

Figure 3.2: Mehandzhiyski *et al.* studied the solvated complexes of alkaline earth metal ions with different ionic radii by BOMD simulations[151]: (a) Successive water binding energies ($\triangle E$) for different alkaline earth metal cations as a function of the coordination number (b)Radial distribution functions between the metal ions and the oxygen of the water molecules

In the case of Sr^{2+}, despite the significant number of publications about its solvation in aqueous phase, the exact coordination number and Sr-O distances are still ambiguous. A summary of the reported values in different studies is shown in Table 3.1. X-ray diffraction (XRD) studies in aqueous solution showed 8 as the most stable coordination,[152, 153] although Albright indicated that a coordination number of 6 or 8 is both possible, based on the analysis of the electron radial distribution function, they found the 8-coordination be more likely.[152] The anomalous x-ray diffraction study (AXD) of Ramos *et al.* on a concentrated $SrCl_2$ solution showed 8 or 9 water molecules directly coordinated to the cation at an average distance of 2.67 Å.[154] Extended X-ray adsorption fine structure spectroscopy (EXAFS) measurements reported coordination numbers over a wide range: 7.3[155] and 8[156] up to 10.3[157]. There are several factors which can vary between different studies and cause

deviation in the calculated coordination number: such as the concentration of the cation or the temperature, both of which are known to affect the coordination number and also the Sr-O distance[153, 158, 159] and most of all, the chosen model compound for interpreting the measured results. For instance, Persson *et al.*[146] found 8.1 water molecules in the first shell with an average Sr-O distance of 2.63 Å at room temperature, choosing the crystal structure of the solid Sr hydroxide octahydrate as their model system. D'Angelo and coworkers[157] analysed the data based on molecular dynamics simulations of Spohr *et al.*[160] and included double-electron excitations in their model to obtain 10.3 as an average coordination number. In another more recent publication, however, D'Angelo *et al.*[161] reported an 8-fold hydration complex, using X-ray adsorption near-edge structure spectroscopy (XANES) and $Sr(OH)_2{\cdot}8H_2O$ from Persson[146] as the standard sample.

The counter ion used may also affect the overall coordination number, however, this variable is also connected to the concentration and the temperature. For example in concentrated nitrate solutions the Sr^{2+} cations are claimed to have a 'quasi-close-packed' distribution, while no particular order was observed with halide counter ions.[162] Besides, Ramos and coworkers showed that chloride ions are present in the second solvation shell of Sr^{2+} in a 3.5M solution[154], but Parkman *et al.* suggested otherwise in the case of diluted $SrCl_2$ solutions[163]. Driesner and Cummings estimated the strontium-chloride speciation in a 0.68M solution via molecular dynamic simulations for different temperatures, and reported a 68% single ion, 21% $SrCl^-$ and 11% $SrCl_2$ distribution at 300K, rapidly changing towards more strontium-chloride species with increasing temperature.

Early theoretical work by Spohr and coworkers yielded 9.8 as the average coordination from molecular dynamics, although later computational works narrowed down the range of coordination numbers; the classical molecular study of Driesner *et al.* gave 9.7[159], while Palmer and coworkers[164] found 8.2 and Dang *et al.*[165] predicted a coordination number of 7.9. The computational approach, such as the type of water models and the ion-water ion-ion pair potentials, can have an effect on the obtained classical MD results. For example Driesner and Cummings found that the so-called BJH water model (Bopp-Jancsó-Heinzinger) gives more realistic results than the rigid or flexible SPC model (simple point charge), which was previously used by Palmer *et al.*; while Dang and coworkers reported a coordination number of 7.9 by using polarisable potential models and suggested that the application of those is necessary for a good description. D'Angelo *et al.* carried out both classical and *ab initio* MD simulations and found that with DFT-based dynamics they could not reproduce their XANES

experimental data and obtained an outstandingly long Sr-O distance. However, other *ab initio* MD simulations[24, 151, 166] predicted a coordination number from 6.7 to 7.5 with Sr-O distances well within the previously reported literature. Kerridge and Kaltsoyannis[149], similarly to Boda *et al.*, applied quantum chemical calculations with the COSMO solvent model on a system containing 24 explicit water molecules and found a maximum coordination number of 7.

Table 3.1: Previously reported Sr^{2+} coordination numbers and Sr-O distances (Å) in aqueous phase. Values collected here are all measured or calculated at room temperature. XRD= X-ray diffraction, EXAFS= extended X-ray adsorption fine structure spectroscopy, LAXS= large angle X-ray scattering, XANES = x-ray adsorption near-edge structure spectroscopy, NRD= neutron diffraction and AXD = anomalous x-ray diffraction. (n_w represents the number of water molecules in the reported simulations.)

Method	Ref	Solution	CN	d_1(Sr-O)	d_2(Sr-O)	Used standard / Computational details
XRD	Albright[152]	concentrated $SrCl_2$	**8**	**2.6**		
XRD	Caminiti[153]	2M $SrCl_2$	**8**	**2.64**	**4.94**	
XRD/Raman	Cabaço[162]	2.7M $Sr(NO_3)_2$	**8**	**2.64**		
EXAFS	Pfund[155]	0.2M $Sr(NO_3)_2$	**7.3**	**2.62**		SrO powder
EXAFS	Palmer[164]	$SrCl_2$	**7.7**	**2.63**		SrO powder/MD
EXAFS	Seward[158]	0.1M $SrCl_2$	**7.8**	**2.57**		classical MD
EXAFS	Moreau[156]	0.14M $Sr(O_3SCF_3)_2$	**8**	**2.600**		$Sr(H_2O)_8(OH)_2$[146]
LAXS/EXAFS	Persson[146]	0.1M $Sr(CF_3SO_3)_2$	**8**	**2.63**	**4.780**	$Sr(H_2O)_8(OH)_2$
EXAFS	Parkman[163]	0.1M $SrCl_2$	**8.3**	**2.62**		-
EXAFS	Axe[167]	0.05M $Sr(NO_3)_2$	**8.93**	**2.62**		SrO powder
EXAFS	D'Angelo[157]	3.0M $SrCl_2$	**10.3**	**2.643**		classical MD[160]
XANES	D'Angelo[161]	0.2M $Sr(H_2O)_8(OH)_2$	**8**	**2.6**		$Sr(H_2O)_8(OH)_2$
NRD	Neilson[168]	3M $Sr(ClO_4)_2xD_2O$	**-**	**2.3-2.65**		
AXD	Ramos[154]	3.5M $SrCl_2$	**8-9**	**2.67**	**4.97**	
classical MD	Spohr[160]	1.1M $SrCl_2$ n_w=200	**9.8**	**2.63**		H_2O: Central Force model, Sr^{2+}, Cl^- parametrised based on HF calculations
classical MD	Driesner[159]	0.5M $SrCl_2$ n_w=250 (NVT)	**9.7**	**2.64**	**4.92**	H_2O: BJH model, Sr^{2+}, Cl^- from Spohr[160]
classical MD	Boda[150]	0.1M $SrCl_2$ n_w=511 (NPT)	**8.24**	**2.58**	**4.82**	H_2O: TIP4P model, PPPM method
classical MD	Palmer[164]	∼0.2M $SrCl_2$ n_w=253	**8.2**	**2.57**		H_2O: SPC/E model, Sr^{2+}: parameters by Dang[164]
classical MD	D'Angelo[161]	0.05 Sr^{2+}(aq) n_w=819 (NVT)	**8**	**2.60**	**4.78**	H_2O: SPC/E model, Sr^{2+}: parameters by Åqvist[169]
classical MD	Dang[165]	n_w=600 (NPT)	**7.9**	**2.60**		H_2O: SPC/E model, Sr^{2+}: parameters by Dang
QM/MM	Hofer[170]	0.11M $SrCl_2$ n_w=499 (NVT)	**9**	**2.69**	**4.97**	QM: HF-SCF/DZP r_{QM}=3.9 Å MM: potentials constructed based on HF calculations
BOMD	Harris[166]	$Sr(H_2O)_n^{2+}$ n_w=30 (NVT)	**7.5**	**2.6**		PBE/USPP-PW
BOMD	Mehandzhiyski[151]	$Sr(H_2O)_n^{2+}$ n_w=86 (NVT)	**7-8**	**2.67**	**4.6**	BLYP-D/GWP-DZVP-GTH
CPMD	D'Angelo[161]	$Sr(H_2O)_n^{2+}$ n_w=90 (NVT)	**7.5**	**2.72**	**4.92**	revPBE/DCACPs
CPMD	Di Tommaso[24]	$Sr(H_2O)_n^{2+}$ n_w=53 (NVT)	**6.7**	**2.60**	**4.70**	PBE/USPP-PW
DFT/MP2(COSMO)	Boda[150]	$Sr(H_2O)_n^{2+}$ n_w=24	**8**	**2.64**		B3LYP/TZVP and MP2/TZVP
DFT(COSMO)	Kerridge[149]	$Sr(H_2O)_n^{2+}$ n_w=24	**7**	**2.614**		TPSS/def2-TZVP

3.2.3 The order and dynamics of hydration shells

Neilson and Broadbent[168] used neutron diffraction to study the structure of Sr^{2+} in a highly concentrated $Sr(ClO_4)_2$ solution in heavy water, but they were not able to resolve the water structure around the ion into Sr-O and Sr-H correlations, due to the disordered structure of the first solvation shell. Moreau,[156] Axe[167] and Persson[146] also concluded that the inner solvation shell of the Sr^{2+} is highly disordered and the outer shell is diffuse, which could

be a reason for the wide range of average coordination numbers reported and for the lack of agreement about the geometry of the solvation shell. D'Angelo *et al.*[161] looked at the angular distribution function of the O-Sr-O angle to study the geometrical arrangement of the coordinated water molecules and found that they are most likely alternate between two 8-fold structures: a bicapped trigonal-prism and a square antiprism geometry.

The relatively weak binding energy of the water molecules and the disordered solvation shell are linked to dynamic behaviour of the hydration. Several molecular dynamics simulations were carried out to study ligand exchange reactions within the solvation shells and they all found a short mean ligand residence time for the water molecules,[24, 166, 170] indicating fast ligand exchange between the first and second solvation shell. The model study of Hofer, Randolf and Rode[170] reported ligand exchange rates between the solvation shells in the picosecond scale and showed that this behaviour can lead to the simultaneous existence of several different coordinations within the solution (Figure 3.3). However, it remains unclear which kind of mechanism (associative, dissociative or interchange) is mainly responsible for the quickly changing solvation environment.

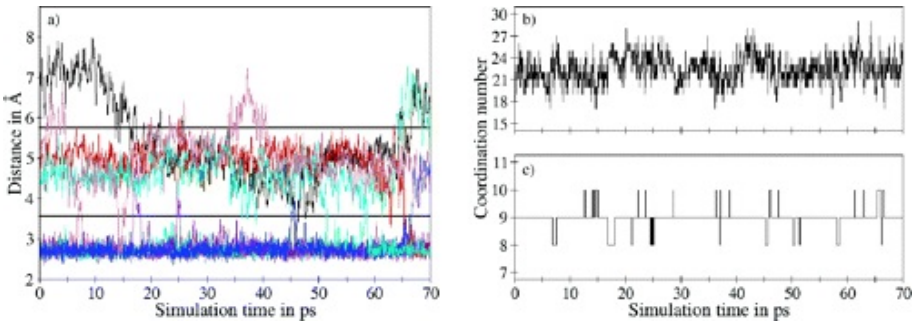

Figure 3.3: The plots, delivered by Hofer *et al.*[170], show the changes in the Sr-O distances during the simulation period (a); and the coordination numbers as a function of time in the second (b) and first solvation shell (c)

3.2.4 Sr^{2+} hydroxides

Sr^{2+} hydroxide can be crystallised in several hydrate forms: $Sr(OH)_2$, $Sr(OH)_2{\cdot}H_2O$ and $Sr(OH)_2{\cdot}8H_2O$. It acts as a moderate base in aqueous solution and is highly soluble in water at room temperature (8 g/l in 20℃), although its solubility depends on its crystal structure and decreases at higher pH.[171, 172] Studying the formation of hydroxide species in solution is especially challenging, since it is very difficult to differentiate between Sr-OH and Sr-H_2O interactions, due to their very similar behaviour and that the water is dominating the structure. To our knowledge, there are no experimental data regarding Sr hydroxide structure in aqueous solution in the literature, although solid state structural analysis can reveal important

information to aid understanding of solvation. XRD data of Grueninger and Bärnighausen have shown that anhydrous $Sr(OH)_2$ has a polyhedral coordination in which the Sr^{2+} ion is surrounded by seven OH^- ions with Sr-O distances between 2.496-2.767 Å (average of 2.60 Å).[147] Strontium hydroxide monohydrate is reported to be relatively unstable, partially decomposing to the anhydrous hydroxide by prolonged exposition at room temperature.[173] Its structure was intensively studied with IR and Raman single crystal measurements by Lutz *et al.*[174, 175] and reported to have a hydroxide coordination in a trigonal prismatic structure around the Sr^{2+} ion, bicapped by the oxygen atoms of the water molecules. IR and Raman spectra reveal that in such formations, coordinating waters are strongly hydrogen bonded but, by contrast, the hydroxide ions do not act as hydrogen-bond donors at all, presumably because water molecules are much stronger hydrogen bond donors than hydroxide ions in general.[175] $Sr(OH)_2{\cdot}8H_2O$ has an entirely different structure; it contains hydrogen donating OH^- ions. Based on XRD,[146, 176] and neutron diffraction studies[177] oxygen atoms from eight water molecules coordinate the Sr^{2+} ion in a tetragonal antiprismatic conformation, with each water engaged at least in three hydrogen bonds. According to Ricci *et al.*[177] a significant difference can be detected in the length of the O-H bonds within the water molecules, which makes their structure asymmetric in the crystal: the longer bonds are H-bond donors to OH^- ions ($\sim$ 1.005 Å), while the shorter ones are donors to another water molecule ($\sim$ 0.975 Å). The hydroxide ions in solid $Sr(OH)_2{\cdot}8H_2O$ are not coordinated directly to the Sr^{2+} centre, but instead form chains of acceptor and donor bonds, with each hydroxide oxygen involved in four hydrogen bonds with neighbouring waters.[146]

Only gas phase theoretical studies exist concerning the hydrolysis of Sr^{2+}. Felmy *et al.*[142] introduced a hydroxide ion into hydrate complexes by removal of a proton from $Sr(H_2O)_6^{2+}$ and $Sr(H_2O)_8^{2+}$. The obtained monohydroxide structures are shown in Figure 3.4. Interestingly, they found that the addition of water molecules to the system dissociates the hydroxide ion from the central ion, i.e. in $Sr(H_2O)_7(OH)^+$ the OH^- ion is not directly connected to the Sr^{2+}; instead, it has three hydrogen bonds to water molecules in the primary solvation shell. This result suggests only weak hydrolysis of aqueous Sr^{2+}, although the authors note that the delocalization of the hydroxide ion may be overestimated in the gas phase compared with aqueous phase calculations due to the lack of a background potential and/or competitive explicit second shell water molecules.

Kerridge *et al.*[122] published a more detailed investigation of the hydroxide complexes of Sr^{2+} in 2011, in which they studied a series of $Sr(H_2O)_{(8-n)}(OH)_n^{(2-n)+}$ complexes up to

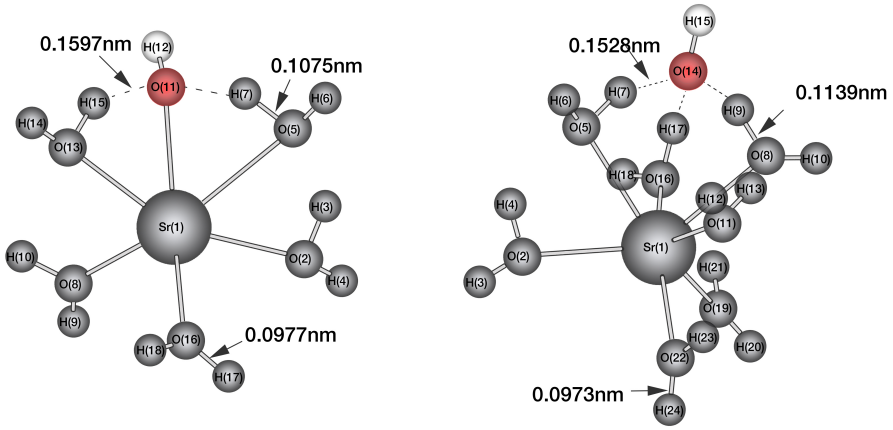

Figure 3.4: Optimised structures of $Sr(H_2O)_5(OH)^+$ and $Sr(H_2O)_7(OH)^+$complexes in gas phase by Felmy[142]. The OH^- is coloured on the pictures.

$n = 4$. From thermodynamic analysis of the coordination modes they deduced that systems with more than $(8 - n)$ coordination number are not stable. QTAIM analysis revealed that hydroxide ions have a weakening effect on the Sr interactions with water oxygens (O_w), with hydrogen bonding between water molecules becoming energetically more favourable and waters consequently beginning to occupy the second solvation shell instead of directly coordinating the Sr^{2+}.

As it was previously discussed, modelling solvated complexes with quantum chemical methods is relatively difficult (see section 1.4.1) and factors such as the solvent model used or the number of explicitly considered solvent molecules can have a significant effect on the results.[53, 178] Thus in the present chapter, these effects were investigated on different Sr^{2+} hydroxide complexes in order to find a suitable and robust solvation model. The aim was to understand the dependence of the coordination on the number of hydroxide ions in the model and to rationalise the previously reported hydroxyl group migration into the second solvation shell[142]. The presented results were published in the following paper: E. Makkos, A. Kerridge, N. Kaltsoyannis, Dalton Transactions, (2015) 44, 11572.[179]

3.3 Computational details

The model chemistry was chosen to be the same as in the previous work of Kerridge *et al.*[122] since this was tested for small gas-phase Sr^{2+} hydrates and exhibited excellent agreement with experimental results. The present calculations were therefore carried out with version 6.5 of the TURBOMOLE code[136] using resolution-of-the-identity density functional theory (RI-DFT).[180] The TPSS exchange-correlation functional,[77] which employs the meta-

generalised gradient approximation, and the def2-TZVP basis sets of polarised triple-ζ quality[94, 97, 181] was used for all atoms along with the associated Sr effective core potential (ECP), which replaces the electrons occupying the core 1s-3d orbitals. Calculations were carried out with the m4 integration grid and the following tight convergence criteria: SCF energy: 10^{-9} a.u., structural energy: 10^{-6} a.u. and energy gradient: 10^{-3} a.u..

3.3.1 Solvation effects

The effects of the bulk solvent (water) were taken into account via the COSMO continuum solvent model[104, 105] with the default TURBOMOLE 6.5 parameters, i.e. a relative permittivity of $\varepsilon = \infty$ and molecular cavities constructed of spheres of radius 2.223 Å for Sr, 1.720 Å for O, 1.300 Å for H. The Grimme-type[84] DFT-D3 dispersion corrected single point energies were calculated only in the case of two complete solvation shells (in brackets in Table 3.8).

Water has one of the highest dielectric constant among usual solvents, therefore assuming that is an ideal conductor ($\varepsilon = \infty$) only results in a slight difference in energy compared to values calculated with its experimental dielectric constant ($\varepsilon = 80$ the dielectric constant of water at 20 ℃, $f(\varepsilon) = 0.981$). As proof for this statement, test calculations using $\varepsilon = 80$ were carried out for structures with small energy differences between them, as it was requested by one paper reviewers (systems in columns 2 and 3 of Table 3.8). The comparison of results with infinite or finite dielectric constants revealed extremely small changes in geometry: an average $\varepsilon = \infty \; vs. \; 80$ difference in r(Sr-O) and r(O-H) in hydroxide groups and neighbouring water molecules is c.a. 0.0001 Å and the average change in the H-O-H angle in those water molecules is 0.004°. The energy difference in relative Gibbs free energy is a maximum of 0.6 kJ/mol, shown in Table 3.2.

Table 3.2: Dependence of the relative SCF and Gibbs free energies on the dielectric constant (ε) of the COSMO calculation. The studied systems were named using the notation introduced in Eq. (3.1)

	Type of hydroxide	$\varepsilon = 80$	$\varepsilon = \infty$	$\varepsilon = 80$	$\varepsilon = \infty$
		ΔE_{SCF} (kJ/mol)		ΔG (kJ/mol)	
2	**mono [Sr:5/17:1/1]**	0.0	0.0	0.0	0.0
	di [Sr:4/18:2/0]	3.2	3.0	3.1	2.9
3	**mono [Sr:5/16:1/2]$^-$**	2.8	2.8	3.4	2.9
	di [Sr:4/17:2/1]$^-$	0.0	0.0	0.0	0.0
	tri [Sr:3/18:3/0]$^-$	5.4	5.1	2.4	1.8

3.3.2 Thermodynamic contributions

Zero-point vibrational frequencies and thermochemical enthalpic and entropic contributions at 298.15 K were obtained via numerical frequency analysis in the aqueous media. A

frequency scaling factor of 1 was used throughout, since according to test calculations with the TPSS functional and a basis set of similar quality to that employed here (6-311G(d,p)) a scaling factor of 0.9999 was found to be appropriate in order to minimise the RMS error of the zero-point vibrational energies (ZPVEs).[182] Results were visualised with the MOLDRAW chemical graphical software[183–185].

3.4 Results

In this section we present the results of quantum chemical calculations in which a combination of the COSMO implicit solvent model and explicit solvent molecules was used to study the aqueous solvation of strontium mono-, di-, tri-, and tetrahydroxides. The following labelling scheme is employed to classify the studied systems:

$$[Sr : a/b : \alpha/\beta]^{(2-n)+} \tag{3.1}$$

a and b are the numbers of explicit waters in the first and second shell, respectively, α and β are the corresponding number of hydroxyl groups, and *n* is the total number of OH^- ions in the system. For instance, the structure labelled [Sr:5/17:1/1] is a neutral, 6 coordinated Sr^{2+} monohydroxide with five water molecules and one OH^- ion in the first shell, and 17 waters and one OH^- ion in the second.

3.4.1 Sr^{2+} hydroxide complexes with a first solvation shell

Previous gas phase studies have identified the maximum coordination number of Sr^{2+} hydroxide complexes to be seven, with a tendency to decrease with increasing number of OH^- ions in the system.[122] Therefore, we kept the total number of molecules in the system at seven and studied structures with one to four hydroxyl groups while the number of explicit waters was reduced concurrently from six to three. A continuum solvent model was employed in all cases.

We attempted to map all possible coordinations while keeping the number of waters and OH^- ions constant in the system. However, despite repeated efforts, we were unable to stabilise complexes with certain coordination numbers. Hence the following complexes are absent from our study: $[Sr:4/2:1/0]^+$, $[Sr:5/1:1/0]^+$, $[Sr:6/0:1/0]^+$, [Sr:5/0:2/0] and $[Sr:3/0:4/0]^{2-}$. Attempts to optimise these structures resulted in imaginary frequencies which proved impossible to eliminate. For all other complexes, optimised structures together with their relative SCF and Gibbs energies ($\Delta E_{\mathrm{SCF}}/\Delta G$) are summarised in Table 3.3. Relative energies were calcu-

lated with reference to the energy of the most stable complex for a given number of hydroxide ions and water molecules.

Table 3.3: Ball and stick images of optimised strontium hydroxides with a 1st solvation shell, along with their relative SCF and Gibbs free energies ($\Delta E_{\mathrm{SCF}}/\Delta G$). ($Sr^{2+}$=magenta, O=red in water molecules, O=blue in OH^- ions, H=white). All energies are given in kJ/mol

Coordination number	System composition			
	1 OH^-/6 H_2O	2 OH^-/5 H_2O	3 OH^-/4 H_2O	4 OH^-/3 H_2O
4	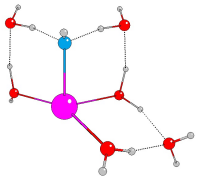 [Sr:3/3:1/0]$^+$ 0.0 / 0.0	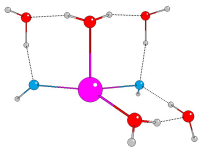 [Sr:2/3:2/0] 0.0 / 2.7	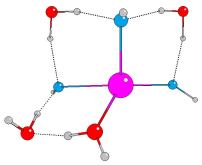 [Sr:1/3:3/0]$^-$ 0.0 / 10.2	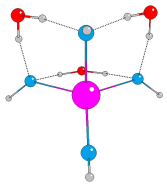 [Sr:0/3:4/0]$^{2-}$ 0.0 / 0.0
5	-	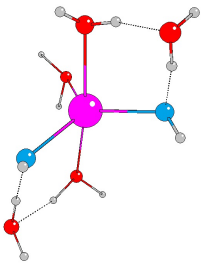 [Sr:3/2:2/0] 11.3 / 0.0	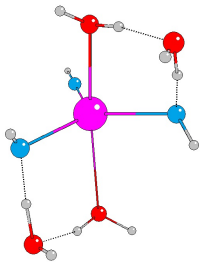 [Sr:2/2:3/0]$^-$ 10.3 / 0.0	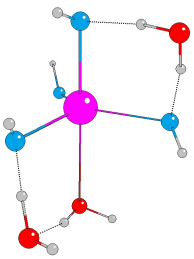 [Sr:1/2:4/0]$^{2-}$ 28.3 / 8.3
6	-	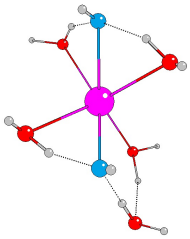 [Sr:4/1:2/0] 13.5 / 9.1	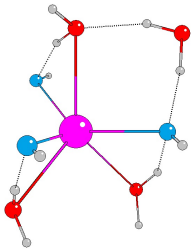 [Sr:3/1:3/0]$^-$ 16.6 / 19.9	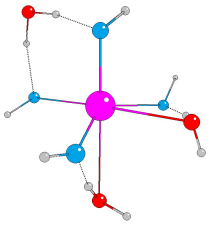 [Sr:2/1:4/0]$^{2-}$ 27.8 / 17.2
7	-	-	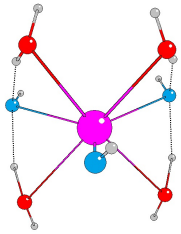 [Sr:4/0:3/0]$^-$ 26.5 / 28.9	-

When we compare the relative stabilities obtained from SCF energies to the order based on Gibbs free energies, we find quantitative differences, demonstrating that thermochemical effects are crucial to the understanding of strontium hydroxide speciation in aqueous envi-

ronments. Considering the ΔG results, the most stable coordination number is five for the di- and trihydroxide complexes ([Sr:3/2:2/0] and [Sr:2/2:3/0]$^{-}$), while it is four for the tetrahydroxides ([Sr:0/3:4/0]$^{2-}$). These results are in partial agreement with the previous gas phase study[122] in which the maximum coordination number of seven decreases to four with an increasing number of hydroxide ions. Furthermore, the reduction in total coordination number from five to four found here is consistent with the previous observation from QTAIM analysis that increasing the number of hydroxide ions destabilises higher coordinations.

Inspection of Table 3.3 reveals that for most species, large parts of the first coordination sphere are open, an unphysical situation which would not be possible in real solvated systems. This, and the problems we encountered with energetic instability in several structures, led us to conclude that the combination of an implicit bulk solvent and explicit first coordination shell does not contain enough explicit coordination to accurately model the solvation of Sr^{2+} hydroxides. To overcome this problem, we moved on to study the effect of using additional explicit waters in our solvation model.

3.4.2 Sr^{2+} hydroxide complexes with a first and second solvation shells

When deciding on the total number of water molecules required to complete two solvation shells, we took into account the possibility that the hydroxide ions can in principle migrate to the second shell, in which case it would be possible to form an eight coordinated hydrate complex.[146] Therefore we chose the maximum number of water molecules to be 24-*n*, (where *n* is the number of hydroxide ions in the system) considering that only two second shell waters are able to coordinate each first shell water.

We attempted to create complexes with a second solvation shell by two different approach: by systematically increasing the number of water molecules around the previously optimised 'single shell' complexes and by using a pre-optimised water cluster as solvation shell. While the first approach is more common and was used by Boda *et al.*[150], the latter one was also successfully used before to model the effect of first solvation shell for organic reactions.[186, 187] We applied a 24 water molecule cluster (W24) previously optimised by Ludwig and Weinhold, as a starting point.[188] These authors found that a tetrakaidecahedral cluster composed of two hexagons and twelve pentagons was energetically most stable (see Figure 3.5) and it was confirmed by later conformation studies too.[189] For modelling the solvation of Sr^{2+} hydroxides, we modified this cluster by placing a Sr^{2+} ion at its centre and replacing between one and four waters with hydroxide ions.

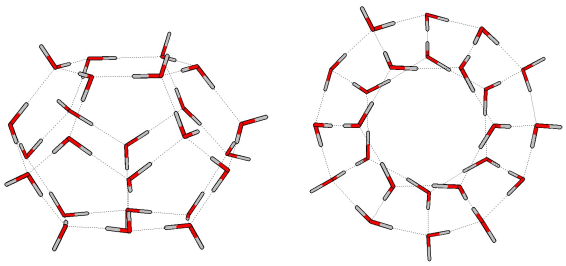

(a) side view **(b) top view**

Figure 3.5: Optimised structure of the W24 water cluster reported by Ludwig and Weinhold[190]

To verify the suitability of the chosen water cluster for this particular problem, we first studied simple Sr^{2+} hydrates. We found 6 and 7 coordinated aqua complexes to be energetically very similar; the 6 coordinated structure is 6.0 kJ/mol more favoured based on the SCF energies,and Gibbs free energies show that both coordination is equally likely (see Figure 3.6). These results are at the lower end of the previously published coordination range (shown in Table 3.1)[155, 158, 164] and in a relatively good agreement with the existing quantum chemical results in which the preferred coordination was seven.[24, 149, 151, 161, 166]

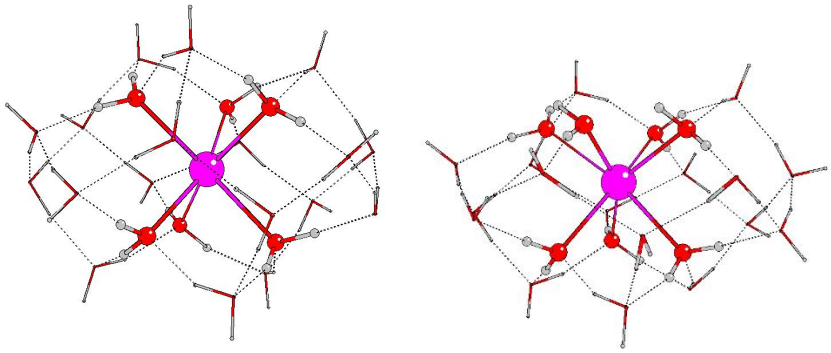

(a) [Sr:6/18:0/0]$^{2+}$
0.0 / 0.0

(b) [Sr:7/17:0/0]$^{2+}$
6.0 / 0.0

Figure 3.6: Optimised structures of two Sr^{2+} hydrates with a first solvation shell (ball and stick) surrounded by an explicit second solvation shell (represented as tubes), along with their relative SCF and free energies (ΔE_{SCF} /ΔG). (Sr^{2+}=magenta, O=red in water molecules, H=white). Energies are given in kJ/mol.

Table 3.4, 3.5, 3.6 and 3.7 compare all obtained structures by both methods containing 1,2,3 or 4 OH^- ions in the system respectively. Complexes which were optimised based on the W24 water cluster, all have names starting with W24_OH_x, while structures obtained by introducing water molecules one-by-one around the 1^{st} shell complexes are called such as C1m_x, C1g_x etc. We found, that the "built-up" structures, with the exception of systems containing single OH^- ion (W24_OH1 and C1c_23b in Table 3.4), were always energetically

unfavourable when compared with those based on the W24 cluster.

Table 3.4: SCF energies and relative free energies of the differently coordinated Sr^{2+}+ 1 OH^-/23 H_2O systems (w=waters)

name	number of w	CN	System	SCF Energy (a.u.)	$\triangle$(*E*+*G*) (kJ/mol)
W24_OH1	23	6	[Sr:5/18:1/0]+	-1865.79174	0.0
C1c_23b	23	7	[Sr:6/17:1/0]+	-1865.782917	0.7
C1c_23e	23	7	[Sr:6/17:1/0]+	-1865.783906	10.0
C1c_23c	23	7	[Sr:6/17:1/0]+	-1865.778736	11.0
C1c_23a	23	6	[Sr:5/18:1/0]+	-1865.78045	16.7
C1c_23d	23	8	[Sr:7/16:1/0]+	-1865.769851	25.7

Table 3.5: SCF energies and relative free energies of the differently coordinated Sr^{2+}+ 2 OH^-/22 H_2O systems (w=waters)

name	number of w	CN	System	SCF Energy (a.u.)	$\triangle$ (*E*+*G*) (kJ/mol)
W24_OH2_c	22	6	[Sr:5/17:1/1]	-1865.328083	0.0
W24_OH2_f	22	6	[Sr:4/18:2/0]	-1865.326953	4.9
W24_OH2_d	22	6	[Sr:4/18:2/0]	-1865.326822	5.3
W24_OH2_a	22	6	[Sr:4/18:2/0]	-1865.326241	6.2
W24_OH2_e	22	6	[Sr:4/18:2/0]	-1865.32702	7.7
W24_OH2_b	22	6	[Sr:5/17:1/1]	-1865.323885	8.4
W24_OH2_g	22	6	[Sr:4/18:2/0]	-1865.326924	9.0
W24_OH2_h	22	5	[Sr:5/17:2/0]	-1865.31842	19.0
C1m_22d	22	7	[Sr:6/16:1/1]	-1865.317876	14.2
C1m_22c	22	7	[Sr:6/16:1/1]	-1865.317711	17.2
C1g_22b	22	6	[Sr:4/18:2/0]	-1865.304548	19.8
C1m_22b	22	6	[Sr:4/18:2/0]	-1865.310444	20.3
C1g_22a	22	6	[Sr:4/18:2/0]	-1865.309586	27.0
C2v_22a	22	7	[Sr:6/16:2/0]	-1865.313432	28.5
C1m_22a	22	6	[Sr:4/18:2/0]	-1865.308421	33.9
C1p_22d	22	6	[Sr:4/18:2/0]	-1865.298353	35.1
C1p_22b	22	6	[Sr:4/18:2/0]	-1865.300346	45.0
C1p_22c	22	6	[Sr:4/18:2/0]	-1865.308074	45.8
C1p_22a	22	6	[Sr:5/17:1/1]	-1865.302422	50.5

Table 3.6: SCF energies and relative free energies of the differently coordinated Sr^{2+}+ 3 OH^-/21 H_2O systems (w=waters)

name	number of w	CN	System	SCF Energy (a.u.)	$\triangle$ (*E*+*G*) (kJ/mol)
W24_OH3_d	21	6	[Sr:4/11/6:2/1]-	-1864.861327	0.0
W24_OH3_a	21	6	[Sr:4/10/6:1/2]-	-1864.860268	1.7
W24_OH3_i	21	6	[Sr:3/12/6:3/0]-	-1864.859386	3.2
W24_OH3_f	21	6	[Sr:4/11/6:2/1]-	-1864.859552	4.1
W24_OH3_e	21	6	[Sr:4/11/6:2/1]-	-1864.859564	4.4
W24_OH3_g	21	6	[Sr:4/11/6:2/1]-	-1864.859279	5.3
W24_OH3_j	21	6	[Sr:4/11/6:2/1]-	-1864.85938	5.4
W24_OH3_h	21	6	[Sr:4/11/6:2/1]-	-1864.855337	6.9
W24_OH3_k	21	6	[Sr:4/11/6:2/1]-	-1864.858083	10.3
W24_OH3_c	21	5	[Sr:2/13/6:3/0]-	-1864.855145	14.9
W24_OH3_l	21	6	[Sr:3/12/6:3/0]-	-1864.846248	38.8
W24_OH3_b	21	6	[Sr:3/12/6:3/0]-	-1864.840551	54.7
W24_OH3_m	21	6	[Sr:3/12/6:3/0]-	-1864.843614	42.3
C1c_21d	21	6	[Sr:3/15/3:3/0]-	-1864.834741	28.3
C1j_21a	21	7	[Sr:4/14/3:3/0]-	-1864.826113	74.7
C1j_21b	21	7	[Sr:4/14/3:3/0]-	-1864.827915	75.5

Table 3.7: SCF energies and relative free energies of the differently coordinated Sr^{2+}+ 4 OH^-/20 H_2O systems (w=waters)

name	number of w	CN	System	SCF Energy (a.u.)	$\triangle$ (*E*+*G*) (kJ/mol)
W24_OH4_d	20	5	[Sr:2/12/6:3/1]-2	-1864.381777	0.0
W24_OH4_e	20	5	[Sr:1/13/6:4/0]-2	-1864.380833	1.2
W24_OH4_h	20	5	[Sr:3/11/6:2/2]-2	-1864.377637	10.0
W24_OH4_i	20	4	[Sr:0/14/6:4/0]-2	-1864.376659	10.8
W24_OH4_g	20	5	[Sr:1/13/6:4/0]-2	-1864.370424	14.0
W24_OH4_a	20	6	[Sr:4/8/10:2/0/2]-2 broke the cluster	-1864.364326	25.7
W24_OH4_f	20	5	[Sr:1/13/6:4/0]-2	-1864.368755	28.4
W24_OH4_c	20	5	[Sr:1/7/12:4/0]-2 broke the cluster	-1864.367502	37.6
W24_OH4_b	20	6	[Sr:4/8/10:2/0/2]-2 broke the cluster	-1864.358611	64.8

To understand the effect of the COSMO continuum model on the obtained geometries, we carried out test calculations with the systems containing 2 OH^- ions, in which the structures optimised with the COSMO solvation model and reported in Table 3.5 were reoptimised without the implicit solvent (in gas phase). Comparing the relative free energies of structures to the most stable complex obtained with COSMO (Figure 3.7) shows a significant difference in the energetic order which is also accompanied by geometrical changes within the structures. Moreover, some of the complexes, which were originally found to be stable with the solvent

model, were predicted to be unstable in gas phase (had imaginary frequencies). These results suggest that employing the COSMO solvent model has a significant effect on the obtained complexes and plays an important role in finding the most realistic hydroxide complexes in water.

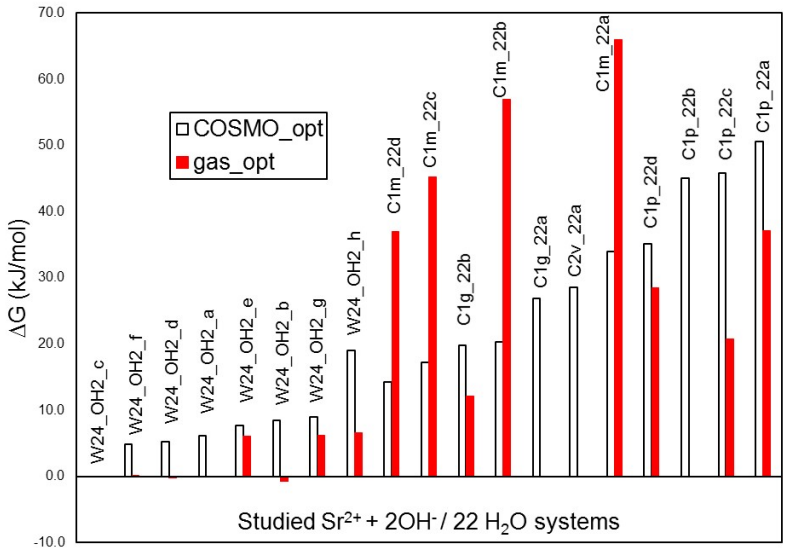

Figure 3.7: Relative free energies ($\triangle G$) of structures containing 22 water molecules and 2 hydroxide ions calculated compared to the most stable structure optimised with COSMO (W24_OH_c). Complexes optimised with and without solvent model are represented with white and red bars respectively.

Following the previous test calculations, single point energies with the implicit solvent model were evaluated for the thermodynamically stable gas phase structures. Plotting the relative SCF energies of the same gas phase structures and their calculated COSMO single point energies (Figure 3.8) shows that the SCF energies obtained with the implicit solvent model tend to be generally lower and follow the energetic trend of the gas phase structures, which shown to be significantly different from the complexes optimised with COSMO. Therefore, we conclude that a simple modification of the gas phase energies with the solvent related correction term is not enough in the case of the Sr^{2+} hydroxides and full geometrical optimisation is necessary to obtain realistic complexes in the aqueous phase.

We also considered the extent to which our model produces structures in which the second shell of water molecules is complete. Defining an accurate number of second shell water molecules however, or measuring the completeness of the shell, is not necessarily straightforward, as the water molecules beyond the well-defined first shell are generally weakly bound and can move easily from one shell to the other.[146, 156, 167] However, we can take the average number of hydrogen bonds per second shell water molecules as a measure of com-

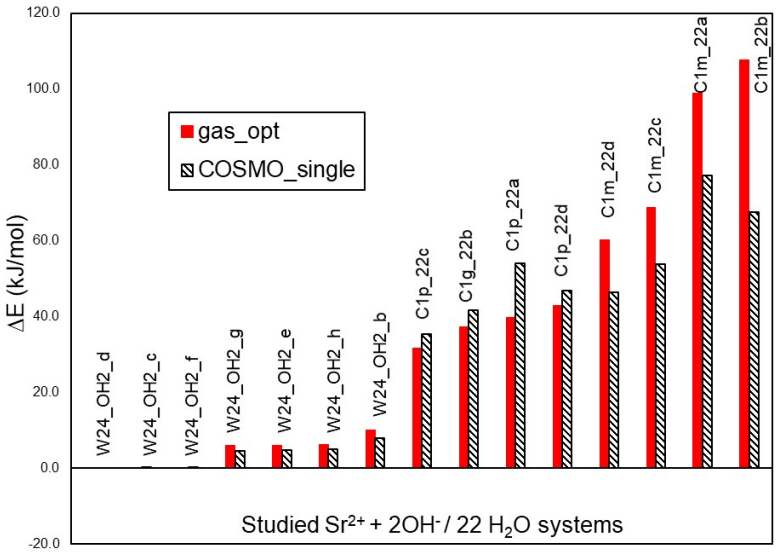

Figure 3.8: Relative SCF energies ($\triangle E$) of structures containing 22 water molecules and 2 hydroxide ions calculated compared to the most stable structure optimised with gas phase (W24_OH2_d). Complexes optimised without solvent model are represented with red bars, while COSMO single point energies with black diagonal stripes.

pleteness of the second shell, and find this to be an average 3.47 for all of our most stable W24 type structures (shown in Table 3.8). This average lies towards the top of the range of values previously determined for bulk water;[191–197] between 2.2[191] and 3.73[197] depending upon the definition of hydrogen bonding and the method of investigation. While for example, if we compare the average number of hydrogen bonds per total number of water molecules within the two structures of Figure 3.9, we find that the built-up structure (3.9a) has a value 2.8 compared to 3.3 in water cluster (3.9b).

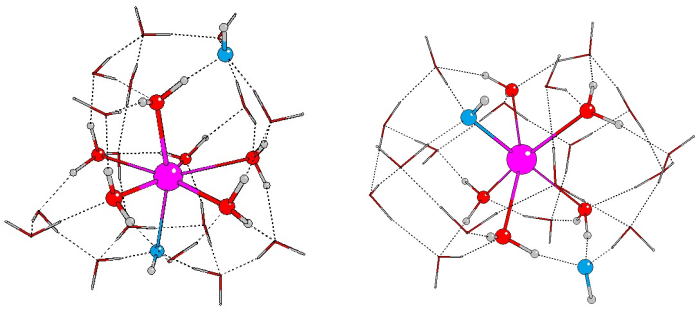

(a) [Sr:6/16:1/1] 26.8 / 14.2 **(b) [Sr:5/17:1/1] 0.0 / 0.0**

Figure 3.9: Optimised structures of two Sr^{2+} hydroxides, surrounded with 24 water molecules. The non-directly coordinated ligands are represented as tubes. The [Sr:5/17:1/1] (W24_OH2_c in Table 3.5), which are based on a pre-optimised water cluster, is 14.2 kJ/mol more stable than the 'built-up' structure (C1m_22d in Table 3.5), [Sr:6/16:1/1], and contains more hydrogen-bonds. (relative SCF and free energies are shown as ($\triangle E_{\mathrm{SCF}}$ /$\triangle G$); Sr^{2+}=magenta, O=red in water molecules, O=blue in OH^- ions, H=white). Energies are given in kJ/mol.

Presumably the high symmetry of the W24 cluster and the closed hydrogen bond network stabilises the systems obtained from this approach. Since the W24 cluster based complexes are generally more stable and have more complete second shell than the 'built-up' structures, we concluded that the use of the pre-optimised cluster approach provides an appropriate starting point from which to model two complete solvation shells and after this point only the W24 cluster based results are presented in this chapter and summarised in Table 3.8. Relative energies are calculated compared to the most stable structures for a given number of OH^- ions and waters in the system.

Table 3.8: Optimised structures with a first solvation shell (ball and stick) surrounded by an explicit second solvation shell (represented as tubes), along with their relative SCF, dispersion corrected and free energies ($\Delta \boldsymbol{E}_{\mathbf{SCF}}$ ($\Delta \boldsymbol{E}_{D3}$) /$\Delta \boldsymbol{G}$). ($Sr^{2+}$=magenta, O=red in water molecules, O=blue in OH^- ions, H=white). All energies are given in kJ/mol.

Hydroxide coordination	System composition			
	1 OH^-/23 H_2O	2 OH^-/22 H_2O	3 OH^-/21 H_2O	4 OH^-/20 H_2O
mono	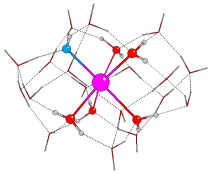 [Sr:5/18:1/0]$^+$ 0.0 (0.0) / 0.0	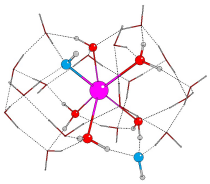 [Sr:5/17:1/1] 0.0 (0.0) / 0.0	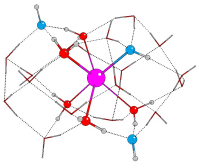 [Sr:5/16:1/2]$^-$ 2.8 (1.8)/ 2.9	-
di	-	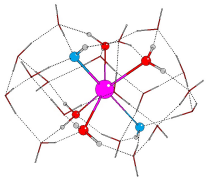 [Sr:4/18:2/0] 3.0 (4.4) / 2.9	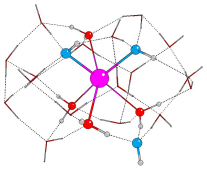 [Sr:4/17:2/1]$^-$ 0.0 (0.0) / 0.0	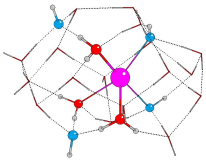 [Sr:4/16:2/2]$^{2-}$ 10.9 (9.0) / 10.1
tri	-	-	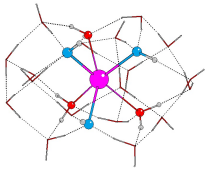 [Sr:3/18:3/0]$^-$ 5.1 (6.9) / 1.8	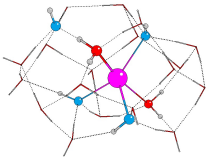 [Sr:2/18:3/1]$^{2-}$ 0.0 (0.0) / 0.0
tetra	-	-	-	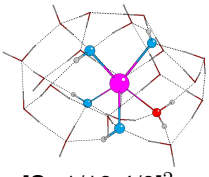 [Sr:1/19:4/0]$^{2-}$ 2.5 (4.5) /0.2

By contrast to the single-shell complexes reported in section 3.4.1, here we found no diffi-

culties in optimising the geometries. Furthermore, examination of the structures in Table 3.8 reveals that they all have a largely closed hydrogen bond network, without the open spaces of the structures presented in Table 3.3. Comparing the average number of hydrogen bonds per molecule in the system confirms this statement, since the average number of hydrogen bonds is higher in the systems with two complete solvation shells (3.39 for water molecules and 3.27 for hydroxide groups), than for the structures with one solvation shell (only 2.33 for water molecules and 2.26 for hydroxides). These differences support our previous assertion that a second explicit solvation shell is required to accurately describe hydroxide speciation.

We find a coordination number of six to be preferred in the mono-, di-, and trihydroxides, whereas the tetrahydroxide is most stable with a coordination number of five.[i] Therefore the inclusion of two explicit solvation shells results in an increase in the coordination number of the most stable complexes when compared with the structures determined with only a single shell.

The six coordinated complexes have a slightly distorted trigonal antiprismatic structure and in all cases only molecules from the two hexagons (visible on the top and bottom of the W24 cluster in Figure 3.5a) are coordinated to the Sr^{2+} ion. On complex formation, the original planes of the hexagons distort and the cluster compresses as shown in the example in Figure 3.10. Those molecules not directly coordinating the Sr^{2+} ion occupy the second and form a partially occupied third solvation shell, but since the third shell water molecules cannot clearly be identified based on their distances from the Sr^{2+} ion, they are treated as forming part of the second shell.

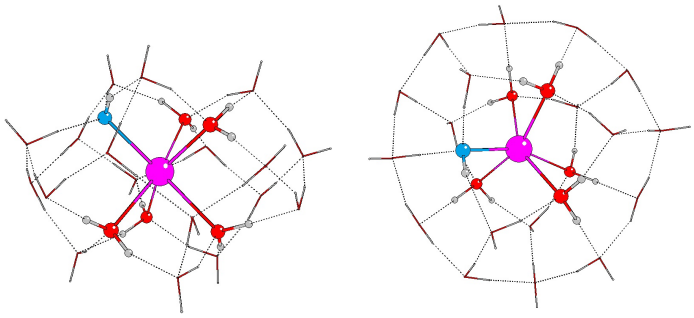

(a) side view **(b) top view**

Figure 3.10: Ball and stick figure of the optimised geometry of the $[Sr:5/18:1/0]^{+}$ monohydroxide with two complete solvation shell, based on the W24 water cluster, viewed from the side (a) and the top (b). The second shell waters are represented by tubes. (Sr^{2+}=magenta, O=red in water molecules, O=blue in OH^{-} ions, H=white).

[i] Inclusion of the DFT-D3 dispersion corrections does not result in any qualitative difference in the relative energies of the isomers of a given system.

The average Sr-O distances for the Sr^{2+} hydroxides and hydrates with a complete second shell are summarised in Table 3.9. The average Sr-O_w distance in the first shell of the hydrate complexes varies from 2.570[158] to 2.643 Å[157] in previous experimental studies, in very good agreement with our calculated bond length (2.616 Å). With more hydroxide ions in the system, the Sr-O_w distances of the first shell water molecules increase; it was previously noted that higher hydroxide coordination weakens these bonds.[122] It might be expected that the increasing Sr-O_w distances would be accompanied by a reduction of the partial charge on the metal, and the average Mulliken Sr charge does indeed decrease from +1.151 to +1.089, +1.024 and +1.019 in the mono through tetra hydroxo systems. The Sr-O_{OH} distances in the first and second shells also increase, presumably for the same reason. Conversely, the Sr-O_w distances to the second shell waters decrease, as the weakening of the Sr first shell water bonds leads to a stronger bonding between the first and second shells. However, the calculated average bond length for the hydrate complex (4.464 Å) is still some way from the experimentally determined 4.940 Å[153]. It is even less than the Sr-O_w distance measured in the solid crystal structure (4.78 Å).[146] This may well be the effect of overestimated hydrogen bond strength in the whole system, due to the incomplete description of the environment by the COSMO model.

Table 3.9: The average Sr-O_w and Sr-O_{OH} distances (Å) in the first and second solvation shell for Sr^{2+} hydrates and each type of hydroxide. For simplicity, water molecules in the third shell are included in the second shell averages. Standard deviations (SD) are presented in parentheses

	Sr-O_{OH}				Sr-O_w			
	first		second		first		second	
	Average	SD	Average	SD	Average	SD	Average	SD
hydrate	-	-	-	-	2.616	(0.037)	4.464	(0.333)
hydrate[153]	-	-	-	-	2.640	-	4.940	-
hydrate[146][ii]	-	-	-	-	2.63	-	4.78	-
hydrate[158]	-	-	-	-	2.57	-	-	-
hydrate[157]	-	-	-	-	2.643	-	-	-
mono	2.455	(0.008)	3.818	(0.009)	2.621	(0.020)	4.409	(0.324)
di	2.476	(0.027)	3.874	(0.101)	2.634	(0.027)	4.401	(0.342)
tri	2.481	(0.028)	4.049	-	2.668	(0.027)	4.394	(0.376)
tetra	2.482	(0.018)	-	-	2.708	-	4.397	(0.410)

3.4.2.1 Proton transfer between solvation shells

If we compare the geometries of the different type of hydroxides in a given column of Table 3.8, we find that structures which have fewer OH^- ions coordinated to the Sr^{2+} can

[i] Ref [146] is an XRD result based on solid state crystal structure.

be derived directly from those with more coordinated hydroxides via a proton transfer from a second shell water molecule to a first shell hydroxyl group. In addition, the energies of the structures in a given column are close to one another. For example, the Gibbs free energies of the systems with three hydroxide ions and 21 water molecules span less than 3 kJ/mol: A room temperature Boltzmann distribution suggests that these structures may coexist in the following proportions: 19%, 26% and 55% for mono-, tri- and dihydroxides respectively (Table 3.10). Such small energy differences can be rationalised by the fact that OH^- ions are stronger hydrogen bond acceptors and weaker hydrogen bond donors than water molecules.[175, 177] Therefore, a system which contains a direct Sr^{2+}-OH^- interaction with the coordinated OH^- ion involved in two strong hydrogen bonds as a donor and one weak hydrogen bond as an acceptor (e.g. [Sr:4/18:2/0]) is competitively close in energy to a system with a direct Sr^{2+}-H_2O interaction and an uncoordinated OH^- ion which forms 3 strong hydrogen bonds with its oxygen atom while its hydrogen atom is directed away from the structure (e.g. [Sr:5/17:1/1]).

Table 3.10: Boltzmann distribution of differently coordinated Sr^{2+} hydroxide complexes calculated based on the Gibbs free energies at room temperature

Hydroxide coordination	System composition			
	1 OH^-/23 H_2O	2 OH^-/22 H_2O	3 OH^-/21 H_2O	4 OH^-/20 H_2O
mono	100%	76%	19%	-
di	-	24%	55%	1%
tri	-	-	26%	51%
tetra	-	-	-	48%

A tendency for one hydroxide ion to migrate from the first to the second solvation shell was reported previously for gas phase Sr^{2+} hydroxide complexes with one complete solvation shell[122, 142] but, to the best of our knowledge, proton transfer between shells has not been previously studied in the aqueous phase. We therefore sought the transition state for the Sr^{2+} dihydroxide ([Sr:4/18:2/0]) $\longrightarrow$ Sr^{2+} monohydroxide ([Sr:5/17:1/1]) reaction. The transition state was obtained by first exploring the energy profile along the H(H_2O)-O(OH) reaction coordinate, then carrying out a transition search at the H-O distance of the maximum of the energy profile. The optimised transition state had one negative frequency in the vibrational spectrum related to studied O-H stretching. The results are summarised in Table 3.11 and the energy profile plotted in Figure 3.11, from which we can see that the Gibbs free energy barrier for this reaction is very small (3.0 kJ/mol). Thus, the coordination can easily interchange between di- and monohydroxide in this system, suggesting that our explicit two shell model well reflects the dynamical nature of the solutions, i.e. the frequent exchange of solvent molecules

and anions between the ion solvation shells and the bulk solvent.[198, 199]

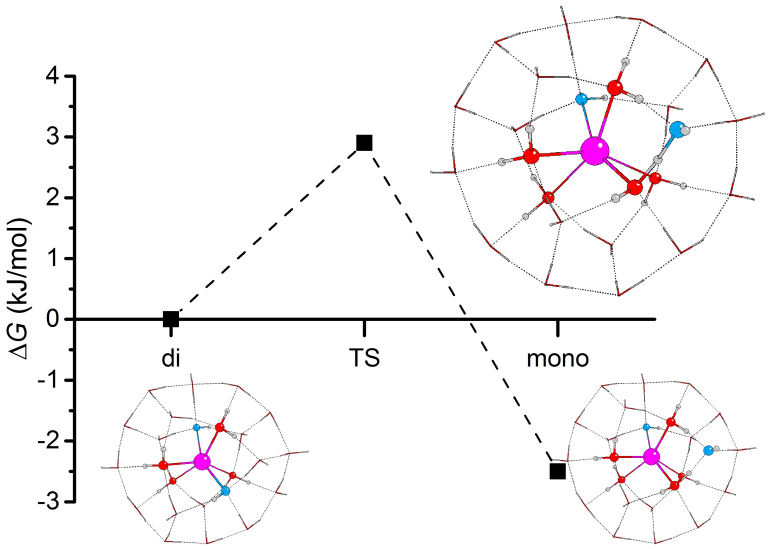

Figure 3.11: Free energy profile ($\triangle G$) of proton transfer between the most stable dihydroxide ([Sr:4/18:2/0]) and monohydroxide ([Sr:5/17:1/1]) complexes with 22 water molecules, from the second column of Table 3.8. TS = transition state.

Table 3.11: SCF ($\triangle E_{\mathrm{SCF}}$) and Gibbs free energy differences ($\triangle G$) of the dihydroxide $\longrightarrow$ monohydroxide proton transfer reaction. TS = transition state

	(E_{SCF}) (a.u.)	$\triangle E_{\mathrm{SCF}}$ (kJ/mol)	(SCF+G_{corr}) (a.u.)	$\triangle G$ (kJ/mol)
di [Sr:4/18:2/0]	-1865.326957	0.0	-1864.851310	0.0
TS	-1865.326349	1.6	-1864.850185	3.0
mono [Sr:5/17:1/1]	-1865.328093	-3.0	-1864.852268	-2.5

To rule out the possibility that the calculated small energy difference is a result of moving a negative charge closer to the cavity, we compared the charges of every oxygen atom in the complexes by QTAIM analysis. Although there is a slight difference between the charge of the moving OH^- ion between the two complex (OH2 changes from -1.274 to -1.210 in Table 3.12), it seems that the Sr-O distance is responsible for this change as the first shell oxygen atoms have a more negative charge in general than the second shell O atoms due to the polarising effect of the cation (average -1.26 compared to -1.18) and the -2 charge carried by two OH^- ions seems almost evenly distributed between the O atoms of the complex, i.e. the charges of oxygen atoms within the hydroxide ions are close to the average charge calculated for the solvation shell in which they are (e.g. OH1 is -1.269 and -1.271 while the average charge of oxygen atoms in the first solvation shell is 1.26). These results show no evidence of unrealistic charges and artificial charge distribution to the vicinity of the cavity, therefore we can conclude

Table 3.12: Oxygen charges of the dihydroxide ([Sr:4/18:2/0]) and monohydroxide ([Sr:5/17:1/1]) complexes with 22 water molecules calculated by QTAIM analysis. O(OH1) and O(OH2) are the charges of the oxygen atoms in the hydroxide ions while the following rows are the average charges and the related standard deviation calculated for the oxygen atoms in the first and second solvation shell.

	di [Sr:4/18:2/0]	mono [Sr:5/17:1/1]
O(OH1)	-1.269	-1.271
O(OH2)	-1.274	-1.210
average 1st	-1.260	-1.261
SD 1st	0.012	0.014
average 2nd	-1.180	-1.182
SD 2nd	0.015	0.015

that the free energy profile calculated plotted in Figure 3.11 is truly related to the investigated proton transfer mechanism.

3.4.3 The relative stability of Sr^{2+} hydroxide complexes in the presence of two explicit solvation shells

To study the effect of increasing the number of hydroxide ions present in the system, we have explored the energetics of two reactions. In the first of these, we have compared the free energies of the different Sr^{2+} hydroxide species with the most stable Sr^{2+} hydrate complex plus the solvated hydroxide ions (Eq. (3.2)). These reaction free energies are presented in Table 3.13 and in Figure 3.12a.

$$\mathrm{Sr}\left(\mathrm{H_2O}\right)_{24}^{2+} + n(\mathrm{OH})\left(\mathrm{H_2O}\right)_{23}^{-} = \mathrm{Sr(OH)}_n\left(\mathrm{H_2O}\right)_{24-n}^{(2-n)^+} + n\left(\mathrm{H_2O}\right)_{24} \tag{3.2}$$

We also wished to establish whether, for a structure with a given number of first or second shell hydroxides, it is energetically preferable for an additional hydroxyl group to enter the bulk solution or to become part of the strontium's primary or secondary coordination shell. We therefore calculated the energies of the reactions described by Eq. (3.3), and these are collected in Table 3.13 and Figure 3.12b.

$$\mathrm{Sr}\left(\mathrm{OH}\right)_{n-1}\left(\mathrm{H_2O}\right)_{24-(n-1)}^{(2-(n-1))^+} + (\mathrm{OH})\left(\mathrm{H_2O}\right)_{23}^{-} = \mathrm{Sr(OH)}_n\left(\mathrm{H_2O}\right)_{24-n}^{(2-n)^+} + \left(\mathrm{H_2O}\right)_{24} \tag{3.3}$$

All the elements in the reaction are calculated with the same computational parameters, both with an explicit and implicit solvent model, to cancel any systematic errors related to the solvent model or the functional/basis set combination. However, to probe the possible effect

Table 3.13: Relative SCF ($\triangle E_{\mathrm{SCF}}$) and Gibbs free energies ($\triangle G$) in kJ/mol for the reactions described by Eq. (3.2) **and Eq.** (3.3)**,calculated with the def2-TZVP basis set**

type of hydroxide	Reaction energies of Eq. (3.2)							
	total number of hydroxide ions							
	1		2		3		4	
	$\triangle E_{\mathrm{SCF}}$	$\triangle G$	$\triangle E_{\mathrm{SCF}}$	$\triangle G$	$\triangle E_{\mathrm{SCF}}$	$\triangle G$	$\triangle E_{\mathrm{SCF}}$	$\triangle G$
mono	-36.3	-32.5	-60.9	-62.3	-74.5	-75.6	-	-
di	-	-	-57.9	-59.4	-77.3	-78.5	-49.2	-54.4
tri	-	-	-	-	-72.2	-76.7	-60.1	-64.5
tetra	-	-	-	-	-	-	-57.6	-64.3
	Reaction energies of Eq. (3.3)							
mono	-36.3	-32.5	-24.6	-29.8	-13.6	-13.3	-	-
di	-	-	-21.6	-26.9	-16.4	-16.2	28.1	24.1
tri	-	-	-	-	-11.3	-14.4	17.2	14.0
tetra	-	-	-	-	-	-	19.7	14.2

of basis set size on reaction energies, we carried out single point test calculations for Eq. (3.2) with different basis sets (def2-SVP and def2-QZVP in addition to the originally chosen def2-TZVP) and compare the SCF energies in Table 3.14. It can be seen that, while the reaction energies obtained with polarised double-ζ (SVP) and polarised triple-ζ (TZVP) basis sets vary significantly, for a given total number of hydroxides there is an essentially constant energy shift between the polarised triple-ζ and the larger quadruple-ζ quality basis set (QZVP) data. This suggests that TZVP is sufficient to obtain reliable relative energies for the studied reactions.

Table 3.14: Dependence of SCF energies for Eq. (3.2) **on basis set quality. $\triangle E$ for the def2-SVP and def2-TZVP basis sets were calculated compared to the def2-QZVP results. All energies are in kJ/mol.**

Total number of OH	Type of hydroxide	SVP	$\triangle E$(QZVP-SVP)	TZVP	$\triangle E$(QZVP-TZVP)	QZVP
1	**mono [Sr:5/18:1/0]$^{+}$**	-49.3	16.0	-36.3	3.0	-33.3
2	**mono [Sr:5/17:1/1]**	-89.1	34.3	-60.9	6.1	-54.8
	di [Sr:4/18:2/0]	-80.3	28.2	-57.9	5.9	-52.0
3	**mono [Sr:5/16:1/2]$^{-}$**	-115.2	50.0	-74.5	9.3	-65.2
	di [Sr:4/17:2/1]$^{-}$	-114.6	46.6	-77.3	9.3	-67.9
	tri [Sr:3/18:3/0]$^{-}$	-104.8	41.9	-72.2	9.3	-62.9
4	**di [Sr:3/17:2/2]$^{2-}$**	-71.4	29.3	-49.2	7.1	-42.1
	tri [Sr:2/18:3/1]$^{2-}$	-79.2	26.2	-60.1	7.1	-53.0
	tetra [Sr:1/19:4/0]$^{2-}$	-72.6	22.2	-57.6	7.2	-50.4

Figure 3.12a shows that in all cases it is energetically favourable for hydroxides to coordinate the Sr^{2+} ion than to all exist as hydrated OH^{-}. If we introduce one hydroxide ion into the system, the formation of a monohydroxide lowers the energy by c. 32 kJ/mol. On increasing the number of hydroxide ions up to three, the reaction energy becomes increasingly negative,

before becoming less so for four hydroxides. Figure 3.12b reveals that the successive addition of one more hydroxide ion into the Sr coordination sphere has a less and less stabilising effect, to the point that the reaction energy associated with the introduction of a fourth OH^- ion into one of the strontium's solvation shells is positive, i.e. the OH^- prefers to exist as a hydrated ion. Thus, although a system with four hydroxides in the Sr coordination sphere is more stable than when all hydroxides exist as hydrated ions (Fig. 3.12a), such a complex is significantly less stable than one in which three hydroxides coordinate the Sr^{2+} ion, with the fourth existing as a hydrated ion (Fig. 3.12b). This allows us to predict that dianionic tetrahydroxide species will not exist. In agreement with this conclusion, $Sr(OH)_2$ is known to be a moderately strong base without amphoteric properties,[171] and as such it should not form negatively charged hydroxide complexes even in the presence of strong(er) bases.[iii]

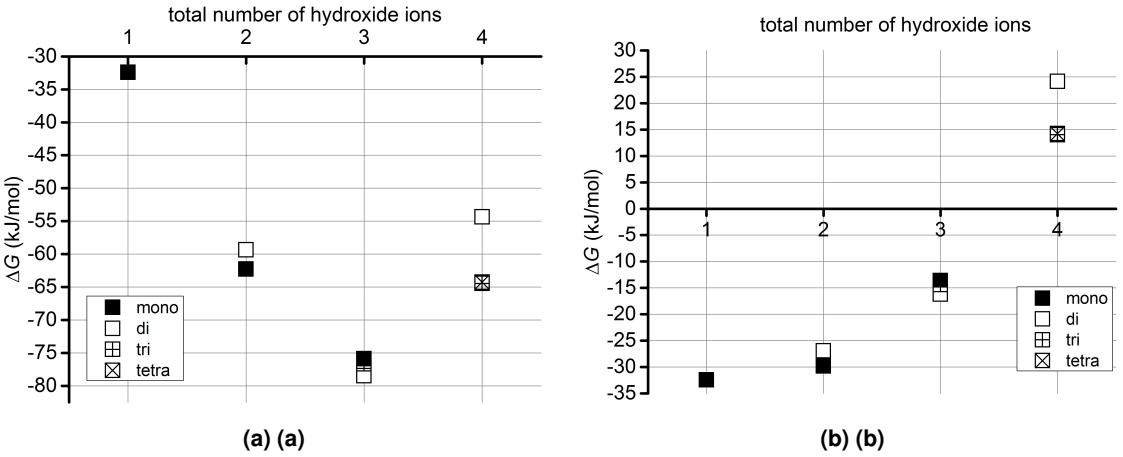

Figure 3.12: Gibbs free energies ($\triangle G$, kJ/mol) (a) for Eq. (3.2)**, and (b) for Eq.** (3.3) **for systems with 1 to 4 hydroxide ions.**

Figure 3.12b indicates that monoanionic species containing three hydroxides are stable within the confines of our model. For these systems, however, the most stable structure ($[Sr{:}4/17{:}2/1]^-$) has two hydroxides in the primary coordination shell with the third in the second shell. It is therefore entirely possible that monoanionic species are also unstable in solution, as the second shell hydroxide in $[Sr{:}4/17{:}2/1]^-$ may well prefer to migrate out of the Sr coordination environment altogether. Unfortunately, we cannot test this hypothesis within the limits of our present model, as to include an explicit third solvation would be computationally prohibitive.

[iii] The pH of our model systems, even with two shells of explicit waters, is > 14. Explicit inclusion of 1250 water molecules for every hydroxide ion would be required to lower the pH to 13.

3.5 Conclusions

Although Sr^{2+} hydrates were intensively studied in the past, there is only a limited information available about the structure of hydroxide complexes, especially in aqueous phase. Since the pH is high in the nuclear storage ponds and the formation of Sr hydroxide is likely, understanding the solvation of hydroxides in water is important to investigate their possible interactions with the hydrated brucite surface. Therefore, we have carried out DFT quantum chemical calculations to model the aqueous solvation of Sr^{2+} mono-, di-, tri- and tetrahydroxides, using a combination of the COSMO continuum solvent model and one or two explicit solvation shells. We have shown that including a second explicit solvation shell as well as carry out the full optimisation with the a polarisable solvent method is essential for the accurate modelling of these systems.

With only a single explicit solvation shell, the coordination number of the most stable mono-, di-, and trihydroxides is five, decreasing to four for the tetrahydroxides. In all cases we find open regions in the Sr coordination shell which would not exist in real aqueous complexes, and we often found our optimised structures to possess unavoidable energetic instabilities. Including a second shell of explicit waters with the application of the W24 water cluster, however, resulted in energetically minimal structures without open regions in the first Sr coordination shell. We also note, that test calculations on structures containing two explicit solvations shells in gas phase proved that the application of the COSMO solvation model significantly affects the obtained geometry and energy of the complexes, i.e. the long-range solvation effects have a key role in the formation of the solvated complexes and have to be included to obtain the right structures. The energetically-preferred coordination numbers obtained from the two-shell calculations increased with respect to those found in with the single shell model. For systems with one, two or three hydroxide ions, we found the most stable complexes to all be 6 coordinated with a distorted trigonal antiprismatic geometry, whereas systems with four OH^- ions have a most stable coordination number of five.

Comparison of the SCF and Gibbs free energies of the systems with two explicit solvation shells shows that there is only a small energy difference between the different types of hydroxide (c. 3 kJ/mol). Transformation from one coordination mode to another can easily occur via a proton transfer mechanism; e.g. the barrier in the Sr^{2+} dihydroxide ([Sr:4/18:2/0]) $\longrightarrow$ Sr^{2+} monohydroxide ([Sr:5/17:1/1]) reaction is only 3.0 kJ/mol.

We have evaluated the relative stabilities of the mono-, di-, tri- and tetrahydroxide species

by calculating the energies of two reactions (defined by equations (3.2) and (3.3)). We found that in all cases the Sr^{2+} hydroxide complexes are more stable than a Sr^{2+} hydrate plus hydrated OH^{-} ions. However, the addition of more hydroxide ions has a systematically weaker stabilising effect, terminating at the point when adding a fourth OH^{-} ion to the trihydroxide species is energetically unfavourable. Furthermore, the most stable trihydroxide structure has only two hydroxides in the first coordination shell of the Sr^{2+} ion, and we suggest that the third hydroxide ligand may migrate away from the Sr coordination environment altogether if our model contained a significantly larger number of explicit water molecules.

We conclude that the most likely Sr-hydroxide complexes to be found in high pH aqueous solutions are mono- and dihydroxides, and that they coexist. These species are therefore the most likely candidates for adsorption onto brucite surfaces under the pH conditions found in fuel storage ponds, and can be used as reference systems for the Sr^{2+} ion's behaviour in the bulk solution. In the next chapter, I focus on the simulation of brucite (0001); describe the development of the periodic electrostatic embedded cluster surface model and its validation by simple adsorption studies in gas phase. While in the final result chapter the main conclusions of this study (such as the necessary combination of an implicit solvent model with sufficient number of explicit water molecules and the obtained structures of the most stable Sr^{2+} hydrate and hydroxide complexes) are utilised for the investigation of Sr^{2+} adsorption on hydrated brucite surfaces, bringing together the results of the present chapter and the following one.

Chapter 4

Modelling the (0001) brucite surface with the periodic electrostatic embedded cluster method

4.1 Introduction

Developing a suitable surface representation for the (0001) brucite surface, which then can be used to study the adsorption of solvated ions, is a crucial part of the research project, as it has been shown that brucite is the most significant component of corroded Magnox sludge and is capable of adsorbing some of the existing radioactive ions in the nuclear storage ponds (see section 1.1). In this chapter, density functional theory at the meta-GGA level is employed within the periodic electrostatic embedded cluster method (PEECM, 2.6.2) to model the brucite (0001) surface. Representative studies are then used to demonstrate the reliability of the PEECM for the description of the interactions of various ionic species with the layered $Mg(OH)_2$ structure, and its performance is compared with periodic DFT.

4.2 Literature review

This literature review is a detailed introduction to brucite: summarising the structural properties of the mineral, continued by the results of previous electronic structure calculations and bond analysis and the introduction of brucite surfaces. It is followed by a comparison of theoretical approaches used to study ionic adsorption.

4.2.1 The structure of the mineral brucite

Brucite is a layered mineral, containing $Mg(OH)_2$ layers, in which the hydroxyl groups are orthogonal to the hexagonal basal plane, see Figure 4.1 (space group is D^3_{3d}, P3m1). The following parameters describe completely the structure: a and c lattice parameters and z_O, z_H atomic fractional coordinates (or alternatively the calculated internal coordinates, such as the Mg-O, O-H bond and H$\cdots$H inter- and O$\cdots$O intralayer distance).[200, 201]

Three neutron diffraction studies have been used to compare the calculated geometrical properties of different computational methods to experimental measurements in ambient conditions: the first was published by Zigan and Rothbauer in 1967[203] the second one was a high pressure study by Catti *et al.*[204] in which they measured the properties of brucite under

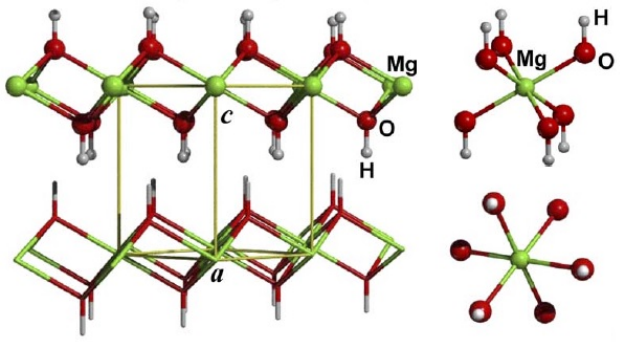

Figure 4.1: The layered structure of brucite showing the typical unit cell, beside the side and top view of the octahedral Mg coordination.[202]

a series of different conditions, similarly to Chakoumakos, Loong and Schultz, who studied the low-temperature structure of brucite.[205] Table 4.1 is a summary of some of the measured and calculated geometrical properties of brucite, which are found in the literature.

Table 4.1: Summary of the previously published geometrical properties of brucite. All values are in Å. (a, c are lattice parameters, z_O and z_H are fractional coordinates; Mg-O and O-H are bond lengths; H$\cdots$H and O$\cdots$O are atomic distances.)

ref	**[203]**	**[204]**	**[200]**	**[202]**				**[206]**	
exp/comp	neutron	neutron	CRYSTAL	CRYSTAL				CRYSTAL	
method	diffraction	diffraction	periodic HF	periodic DFT				periodic DFT	
basis set	-	-	Pople GTOs	Mg: 8-511G*, O: 8-411G*, H: 211G*				Mg: 8-511G* + TZP (O, H)	
functional	-	-	HF	HF	LDA	PW91	B3LYP	B3LYP	B3LYP-D
a	3.142	3.150	3.146	3.148	3.099	3.179	3.167	3.175	3.140
c	4.766	4.770	5.354	5.263	4.413	4.717	4.854	4.923	4.657
z_O	-	0.220	-	0.197	0.235	0.221	0.214	-	-
z_H	-	0.421	-	0.376	0.457	0.427	0.413	-	-
d (Mg-O)	2.102	2.100	2.103	2.093	2.067	2.111	2.104	-	-
d (O-H)	0.995	0.958	0.953	0.939	0.981	0.972	0.962	0.961	0.962
d (H$\cdots$H)	1.932	1.969	2.250	2.239	1.829	1.960	2.016	-	-
d (O$\cdots$O)	2.787	2.778	2.787	2.759	2.737	2.778	2.770	-	-

One of the first theoretical studies preformed on the bulk brucite crystal was done by LeSar and Gordon[207] and is based on an embedding fragment method. They used an electron-gas model in which the effect of the ionic crystal environment was included by an energy contribution evaluated by Ewald summation of the electrostatic potential, and they found a reasonable agreement with experimental results. Sherman[208] and D'Arco[200] carried out periodic HF calculations with the CRYSTAL code;[140] while Baranek *et al.*,[201] as well as Pascale and coworkers,[202] compared the HF method with DFT using different local density and generalised gradient approximation (LDA and GGA) based functionals and B3LYP as a hybrid functional, in conjunction with all electron Gaussian-type basis sets which were optimised to have the sufficient polarisation and diffuse functions. Winkler[209] and Azuma[210]

compared LDA and GGA functionals, using the CASTEP code[211] for periodic DFT calculations with plane wave basis sets. In general, the HF method is accurate for bond lengths, but severely overestimates the interlayer spacing; i.e. the lattice parameter c and the H$\cdots$H distance. LDA functionals give quite the opposite result: underestimated interlayer distances, Mg-O bonds and O$\cdots$O intralayer distances. The parameters calculated with GGA or hybrid functionals are located between the HF and LDA results and they are generally closer to the experimental values. According to Baranek and coworkers, besides the right level of DFT approximation, applying basis sets with polarization functions is also essential.[201] Ugliengo *el al*.[206] used the B3LYP and dispersion corrected B3LYP-D[212] functionals together the 8-511G* on Mg and triple-zeta (TZP) basis set on the O and H atoms to understand the origin of the interlayer forces in brucite. Based on their results, adding dispersion corrections increases the accuracy of the geometrical parameters. However, the study of Chaka and Felmy,[213] in which they calculated the structure of brucite and several types of magnesium-carbonates with periodic DFT in DMol^3 code,[214, 215], suggests that using semi-empirical dispersion interaction corrections leads to an underestimated interlayer distance.

4.2.2 Electronic structure and bond analysis

D'Arco *et al*.[200] studied the electronic structure by plotting the density of states (DOS) for bulk and a slab $Mg(OH)_2$ with the periodic HF method together with the 8-511G, 8-411G and 21G basis sets on the Mg, O and H atoms respectively. They found the results of the bulk and slab brucite to be very similar, which indicates weak interactions between the layers (Figure 4.2). Brucite is clearly an insulator with a significant HOMO-LUMO band gap, besides, there are wide gaps between the bands which is typical of ionic crystals. Although the HF method is known to grossly overestimate the electronic band gap, other electronic structure calculations predict qualitatively similar results. The embedded cluster model based HF study of Murakami, Honjo and Kuji resulted in a 7.00 eV band gap,[216] while Pishtshev *et al.* calculated band gaps of 3.83 and 7.70 eV, using periodic DFT with the PBE and HSE06 functionals respectively, for the bulk structure.[217] Experimental optical band gaps for brucite thin-films and nano-disks are estimated to be $\sim$5.17 and 5.70 eV.[218, 219] The DOS of D'Arco in Figure 4.2 show the strong covalent character of the OH bond, because of the mixed O-H contribution in the valence orbitals. The peaks between -0.7 and -0.4 a.u. have strong contributions from hydrogen and the O_{2p} orbital, while the other valence band corresponds to the O_{2s} orbital with hydrogen contribution and appears at lower energy, under -1.2 a.u..

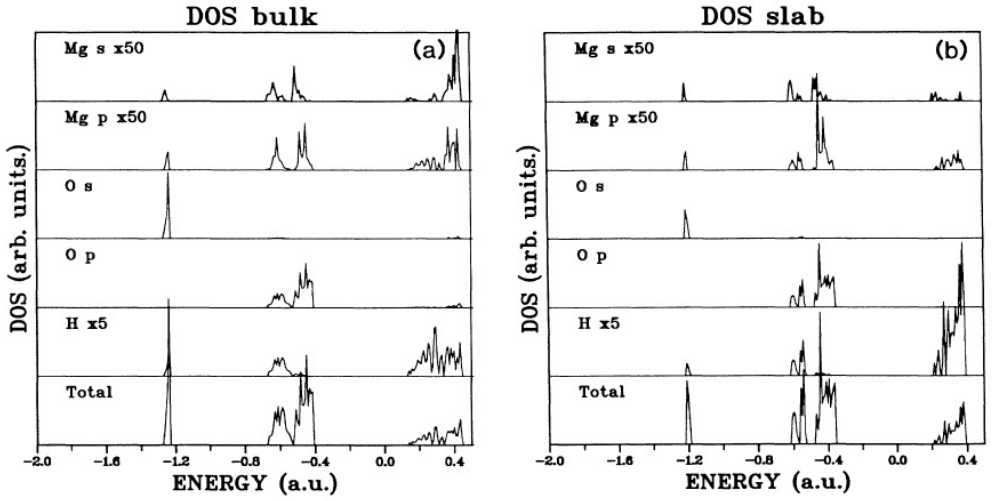

Figure 4.2: Total and projected DOS of the bulk and slab brucite obtained by D'Arco *et al.*[200]

The Mulliken population analysis[134] carried out by Baranek *et al.*,[201] supports the previous statement of D'Arco, since it predicts ionic character for the Mg-O interaction and covalent character for the O-H bond. According to their results, calculated with the B3LYP functional, the actual charge of the Mg atom is less than its formal +2 charge (+1.710), and the population of the Mg-O bond is small, only 0.054. By contrast, the O-H bond population (0.504) is close to the value of the population of the O-H bond in water (0.590), which they state is known to be strongly covalent. Pishtshev *et al.* used Bader analysis and the electron localisation function (ELF) approach to investigate the chemical bonding of brucite.[217, 220] They obtained Bader charges very similar to Baranek's Mulliken values, and showed the ionic character of the Mg-O bond based on the closed shell configuration of the Mg^{2+} cation and the OH^{-} anion by plotting the valence ELF, shown in Figure 4.3. Moreover, by looking at the ELF plot of the (110) plane, they predicted a total lack of hydrogen-bonding between the layers as no shared electron density is detected between the OH groups.

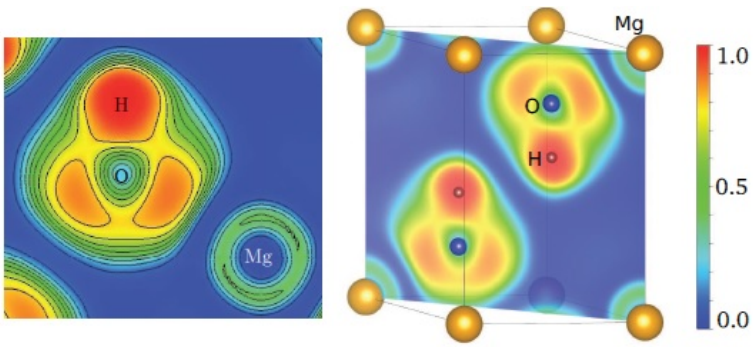

Figure 4.3: Representation of the valence ELF for the (110) plane of brucite, containing one (left) and two (right) units of Mg-OH. ELF values increase from blue to red.[217]

4.2.3 Interlayer forces in brucite

All the previous studies agree that the interlayer interactions are weak, but the nature of these interactions is not completely clear. A minority of the studies suggest some hydrogen-bonding between the layers, for example Kruger *et al.*, based on vibrational spectrum analysis done at various pressures, state that hydrogen-bonds are present in brucite even at high vacuum.[221] Haycock also assumed hydrogen-bonding during the analysis of his X-ray emission, X-ray photoelectron and Auger spectroscopy results.[222] But the majority of the studies predict only dispersion type forces between the brucite layers. For instance, Bernal and Megaw suggested a lack of hydrogen-bonding, based on the long O$\cdots$O intralayer distances in the structure.[223] While Chaka and Felmy explain the lack of hydrogen-bonding in terms of the coordination of the oxygen atoms: as all O atoms are coordinated to three Mg atoms and bonded to one hydrogen, there is no electron lone pair left for the hydrogen bonding.[213]

The O-H stretching frequency is a good indicator of hydrogen-bonding, since its value reflects the properties of the environment of the bond and therefore it is often evaluated in computational studies.[210] Based on the factor group analysis, there is a Raman-active OH stretch with A_{1g} symmetry and an IR-active A_{2u},[221] which both have high frequencies (Raman: $\sim$3655 cm^{-1} and IR $\sim$3700 cm^{-1})[221, 224–227] suggesting that the protons are not involved in hydrogen-bonding.[209] However, according to Pascale *et al.*, due to significant interlayer couplings, there are some differences in the translational modes between the calculated spectra of the bulk structure and the spectra of a single layer of brucite.[202]

Many of the previous studies contain calculations of the interlayer forces. The so called interlayer interaction energy (IE) is the energy difference between the optimised bulk structure and the energy of isolated two dimensional layers,[210] i.e. larger IE values correspond to stronger interlayer interaction. Some of the previously published results are summarised in Table 4.2. Neglecting the dispersion forces in the calculations can lead to artificially weak interaction and therefore an overestimated interlayer distance, as shown in the case of the HF calculations. LDA functionals predict an overly strong interaction which leads to a severely underestimated distance. GGA or hybrid functionals give interaction energies between the HF and LDA results, but still underestimate the strength of the attraction, according to Ugliengo *et al.*[206] They found that using a functional with dispersion corrections, such as B3LYP-D instead of B3LYP, may improve the accuracy of the calculations (structural optimisation and frequency) and give a much higher interaction energy (-22 kJ/mol instead of -3.8 kJ/mol,

Table 4.2). Besides the use of the right level of XC approximation, the correct treatment of the BSSE superposition error, either with sufficiently large basis set or CP correction, is particularly important in the calculation of the interlayer interaction energy. Therefore some of the authors, such as Baranek *et al.* and Pascale *et al.* reported Counterpoise corrected interaction energies, while others, e.g. Ungliengo *et al.* claimed to overcome of the BSSE error by using a sufficiently high level of basis sets.

Table 4.2: Comparison of the previously published interlayer interaction energies (IE) with different functionals. The LDA and GGA functionals used vary in the different studies, but the trend is similar. (^{a} BSSE correction was used in the given study.)

	IE (kJ/mol)				
	HF	**LDA**	**GGA**	**B3LYP**	**B3LYP-D**
Ref [201]^a	-2.6	-36.7	PP: -7.8	-5.2	-
Ref [202]	-2.8	-27.9	PW91: -10.4	-6.5	-
Ref [202]^a	-0.4	-22.6	PW91: -4.8	-1.9	-
Ref [210]	-	-36.5	PBE/PW91: -9.6/-10.1	-	-
Ref [206]	-	-	-	-3.8	-22.0

4.2.4 Surface structure and cleavage

As was shown in the previous sections; the interlayer distance is rather big due to weak, mainly dispersion type interlayer forces; therefore it is easy to cleave the structure. Applying the Wulff's construction method[228–231] predicts a hexagonal prismatic structure for the brucite crystal and transmission electron microscopy and X-ray diffraction studies[232] support to this statement. In every scenario, brucite has the (0001) surface as the most abundant while $(1\bar{1}00)$ as the less stable surfaces in T=0 equilibrium.[i] Figure 4.4d shows the equilibrium shape of the brucite crystal, obtained by Churakov *et al.*, using the Wulff method.[230] Besides (0001) and $(1\bar{1}00)$, they also considered a cleavage plane cutting the $(11\bar{2}0)$ surface and calculated the surface energies of the structures. They found the most abundant face (0001) to be the the most stable (3.3 meV/Å^2), in which the hydroxide ions surround the magnesium ion in an orthogonal coordination resulting in a hexagonal ordered Mg plane with OH groups facing outwards (see Figure 4.4a). The $(1\bar{1}00)$ formation is another possible but less frequent face, since it has a higher surface energy (14 meV/Å^2). In that case, the magnesium atoms at the surface are only five coordinated (Figure 4.4b). In the $(11\bar{2}0)$ cleavage plane the Mg atoms are four-fold coordinated, which makes this surface type even less favourable (28.5 meV/Å^2);

[i] Some publications may use the notation $\{hkl\}$ instead of $\{hkil\}$,[231] which includes an extra, redundant, Miller index and is usually used for hexagonal unit cells. However, due to the symmetry of the brucite structure, the two notation are interchangeable.

according to Masini and Bernasconi, it occurs only in metastable phases.[229] The latter two faces both have hydroxyl groups rotating outwards from the surface plane to minimise the electrostatic repulsion among them as shown in Figure 4.4b and 4.4c. Because of the less coordinated Mg atoms, there are dangling bonds at the surface which cause changes in the interlayer distances between the first few layers.[230]

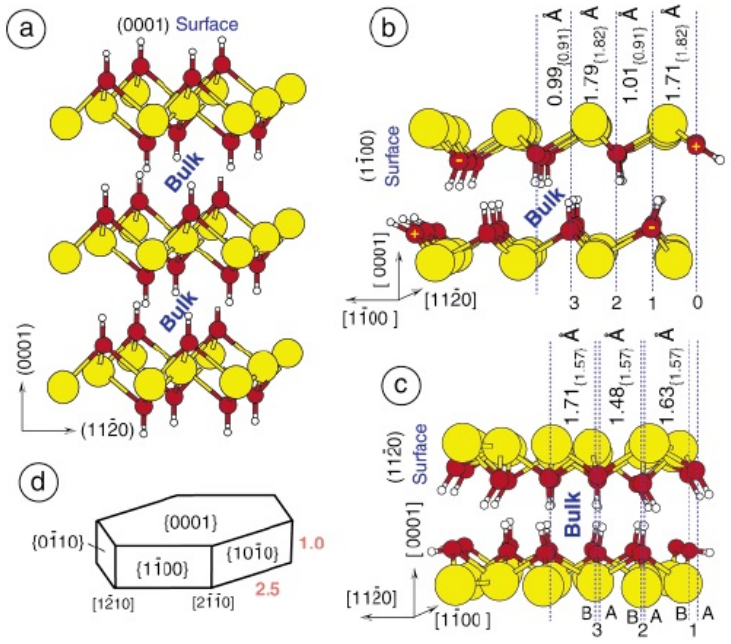

Figure 4.4: Optimised structures of the possible cleavages of the brucite surface: (a) side view of the (0001) structure, (b) of the (1$\bar{1}$00) surface and (c) of the (11$\bar{2}$0) cleavage. The dotted lines indicate the atomic planes in the surface, while the numbers are interatomic distances in the relaxed surface. Relative changes in the interatomic distances compared to the equilibrium bulk are shown in brackets. (d) is the equilibrium shape of the brucite crystal, obtained by the Wulf's construction method.[230]

Since the most common surface type is (0001) and water adsorption occurs on this hydroxyl terminated cleavage plane, its properties are better known than the other surfaces. Moreover, while the basal plane of brucite (0001) is generally well described by force field parameters, the description of the (1$\bar{1}$00) surface properties is less developed in molecular dynamics studies. As a consequence, the surface hydroxyl groups tend to distort in a non-realistic way which results in impossible mineral edges. To prevent this, Zeitler *et al.*[233] recently developed a modified force field to improve the accuracy of simulations involving these type of edges. The description of the (1$\bar{1}$00) surface can be important for example in dehydroxlation reactions, because, according to the CPMD study of Churakov *et al.*[230], it can be dehydroxlated easier than other surfaces. Churakov also states that layers under the top one in the slab does not take part in the studied reactions, therefore they can be fixed in

the calculations.

4.3 Modelling ionic adsorption on surfaces

Theoretical studies of physical and chemical interactions on surfaces play a key role in the understanding and predicting of many industrially relevant phenomena, including the ones related to nuclear waste, as demonstrated in section 1.4. However, choosing a suitable surface representation for the investigation of a particular adsorption mechanism is not always straightforward, and the choice can heavily influence the outcome of the results.

One of the most common approaches to model surfaces is periodic density functional theory (DFT), which operates with conventional unit cells and employs periodic boundary conditions (see 2.6.1). However, modelling charged systems using periodic boundary conditions is extremely difficult and is often treated by using background charges[38, 234, 235] or including counter ions in the simulation box.[38, 42] In principle, a non-neutral simulation box under PBCs (periodic boundary conditions) would result in an infinite, self-interacting charge and an infinitely large electrostatic energy.[108, 234, 235] Employing a compensating homogeneous background charge within the cell to have a finite energy will inevitably lead to artificial Coulomb interactions between the charged species and the background charge, and will not prevent the interaction of the charged species with their own periodic images, resulting in artificial components in the absolute energy of the system.[38] Weber *et al.* studied the adsorption of ionic liquid components on anatase with the periodic DFT method (PBE-D3 and PBE0 functional/GTH pseudopotential basis set), and showed that by using very large supercells (see Figure 4.5), the ionic species can be isolated from the neighbouring interaction sites and the background charge is ”diluted” enough to significantly decrease the magnitude of the artificial effect,[38] but with the price of significantly increased computational cost and limitations on the practicable size of the basis sets. Although the absolute energies of non-neutral systems obtained via PBC methods may not be always reliable, the calculation of relative energies and the comparison of different conformations is still possible upon the application of a background charge or counter ions with a sufficiently large cell size.

One alternative to modelling a surface with periodic DFT is to use isolated molecular clusters to represent the adsorption site of the surface. This approach has been used mainly for 2D materials, such as graphene,[41] where the far-field effects of the substrate on the adsorption reaction can be neglected, i.e. the interaction is very localised; or where the effect of extended surfaces were deliberately neglected for the sake of simplification[236, 237]. How-

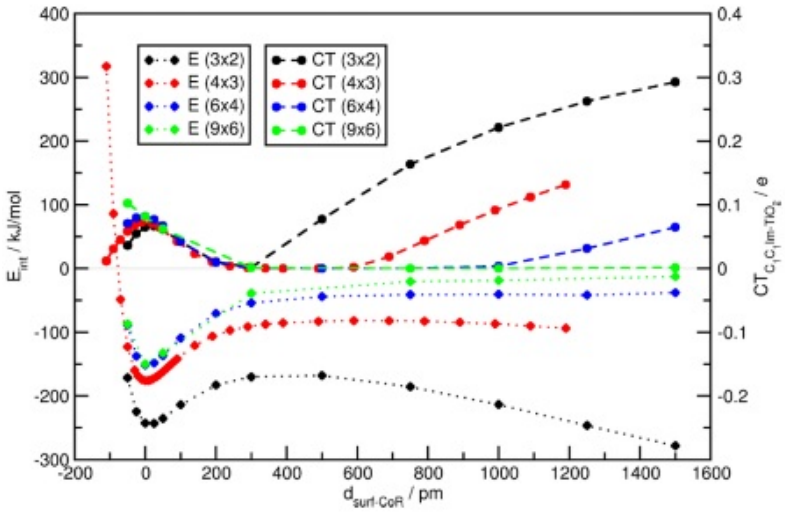

Figure 4.5: The interaction energy (E_{int}) of atanase and $[C_1C_1Im]^+$ ion (1,3-dimethylimidazolium ion) and the corresponding charge transfer (CT) based on Mulliken charges; and their dependence on the cell size. The interaction energy is converging to a negative value, which is presumably caused by attractive interactions between the positively charged ion and the negative background charge. Moreover, for smaller cell sizes E_{int} is decreasing again for larger ion-surface distances, probably due to an artificial charge transfer, induced by the repulsive interaction between the cation and its periodic images. [38]

ever, if one would like to consider the long-range electrostatic interactions and still be able to use high level of theory to study ionic adsorption, embedded cluster methods can be a viable alternative to replace periodic DFT.[55–57] One such technique is the periodic electrostatic embedded cluster method (PEECM)[56, 112] which features a quantum mechanically treated region (the QM cluster) embedded in an infinite periodic array of point charges (see 2.6.2). These approaches have the advantage of being able to study isolated adsorption sites and can deal with charged systems with levels of theory beyond the generalised gradient approximation (GGA) methods typical of periodic DFT calculations. This last feature is especially useful for systems such as metal-oxides and oxygen defects of metal oxides, where hybrid functionals are necessary for the accurate description of the electronic structure.[56, 238–240] As the embedded cluster itself is not repeated, it can carry basically any charge without further consequences, as long as the charge does not change throughout the study. For example, Burow and Sierka, the developers of the PEECM approach, used heavily charged QM clusters in their study of CeO_2.[56] However, systems with different charges may not be directly comparable and have to be treated carefully as the charge of the cluster still affects the overall Coulomb interaction and may lead to artificial differences in potential energies. Another aspect of the planned computational investigations which has not been mentioned so far, is the inclusion of possibly high number of explicit water molecules in the simulation, which will

significantly increase the computational cost and determines our choice in modelling methods; as the computational performance of PEECM is much more efficient for systems with low symmetry, than the periodic DFT methods.

After identifying the most stable hydroxide complexes of Sr^{2+} in aqueous solution in the previous chapter, here we move on to develop an efficient model for studying the adsorption of Sr^{2+} complexes on the hydrated (0001) brucite surface. Based on the considerations presented in the previous paragraphs, we decided to use the PEECM method, which has previously been successfully employed to study ionic materials.[55, 56] As it was shown in section 4.2.2; electronic structure calculations as well as Mulliken bond population analysis[201] predict largely ionic character for the Mg-O bond but more covalent character for the O-H bond. This feature of the material allows us to employ embedded methods, as we define the QM cluster without cutting covalent bonds at the boundaries.[216] Although there are a small number of examples for similar embedded calculations,[216, 241, 242] to the best of our knowledge, this is the first time a surface of a not purely ionic material has been modelled with the PEECM. The bulk of the results presented in this chapter was published in the following paper: E. Makkos, A. Kerridge, J. Austin, N. Kaltsoyannis, Journal of Chemical Physics, (2016) 145, 204708.[243]

4.4 Computational details

4.4.1 PEECM models

All calculations were performed with version 6.6 of the TURBOMOLE program[137] using resolution-of-the-identity density functional theory[180]. Results were visualised with the MOLDRAW chemical graphical software.[184] The TPSS exchange-correlation functional, which employs the meta-generalised gradient approximation (meta-GGA),[77] was used because it has been shown to describe Sr^{2+} complexes well in the past[149] and previous theoretical studies on brucite have shown that GGA functionals efficiently describe bulk properties.[201, 202, 209] Due to the large number of the quantum chemically treated atoms, the def2-SVP basis sets of polarised double-ζ quality[87, 96] were used for all QM atoms. Partial geometry optimisations, in which the boundary atoms of the cluster were held fixed and the inner atoms allowed to fully relax (see Figure 4.6[ii]), were carried out in the gas phase, with the m4 integration grid and the default convergence criteria: SCF energy: 10^{-6} a.u., structural

[ii] For the ***6x6_1+PC*** surface representation, the lower hydrogen atoms were also constrained during optimisation.

energy: 10^{-6} a.u. and energy gradient: 10^{-3} a.u.

For every s block ion investigated in section 4.5.1 (Na^+, Rb^+, Cs^+ and Mg^{2+}, Sr^{2+}, Ba^{2+}), the def2-SVP basis set[87, 94, 96] was used during the geometry optimisation along with the associated effective core potentials[97] for Rb, Cs, Sr and Ba. The electron density distribution calculations reported in section 4.5.1 were performed by generating wavefunction (.wfn) files from the output of the optimisation in TURBOMOLE using the molden2aim program[129] which served as an input for the Multiwfn code[139]. The electron density images were plotted with the VMD[244] visualisation code, using an isosurface value of 0.0025 a.u.

The Quantum Theory of Atoms in Molecules (QTAIM) calculations described in section 4.5.4 were performed with the professional version 13.11.04 of AIMAll[130] using the default parameters of the program. The required .wfn files were generated as described above.

Considerations of the QM cluster

Due to its layered structure, the brucite surface was considered as a slab containing one or more layers of $Mg(OH)_2$ and modelled using the periodic electrostatic embedded cluster method (PEECM, see section 2.6.2), implemented in the TURBOMOLE code. In this approach, a finite sized cluster of brucite was treated quantum chemically and embedded in a 2D infinite array of point charges (PCs) (aperiodic in the z direction). Experimental cell parameters, obtained via neutron diffraction measurements by Catti *et al.*,[204] were used to define both the initial geometry for the QM cluster and the positions of the PCs in the infinite two dimensional array: the a and b lattice parameters of the hexagonal unit cell were 3.15 Å, and the interlayer distance c was 4.77 Å. As it was described in section 4.2.3 and 4.2.4 the cleavage (0001) surface is the most stable brucite surface with a large interlayer distance and weak interlayer forces, i.e. the structural changes during surface relaxation are negligible[200, 202, 229] and therefore the use of experimental bulk parameters for the fixed position of boundary atoms and point charges should only introduce a negligible error in the obtained surface structures.

The basic structure used for the investigations was a single layer of brucite containing a stoichiometric 6x6 Mg atom QM cluster ($Mg_{36}(OH)_{72}$) embedded in the PCs, holding the boundary atoms of the cluster fixed during the optimisation (shown in Figure 4.6). Building on this geometry, several variations were proposed for the optimal surface representation, for which we use the following notation from now on: "***nxn_m***", where ***n*** is the number of Mg atoms in the x and y direction and ***m*** is the number of brucite layers explicitly included in the

cluster. Accordingly, we refer to the above introduced single layered structure as ***6x6_1***.

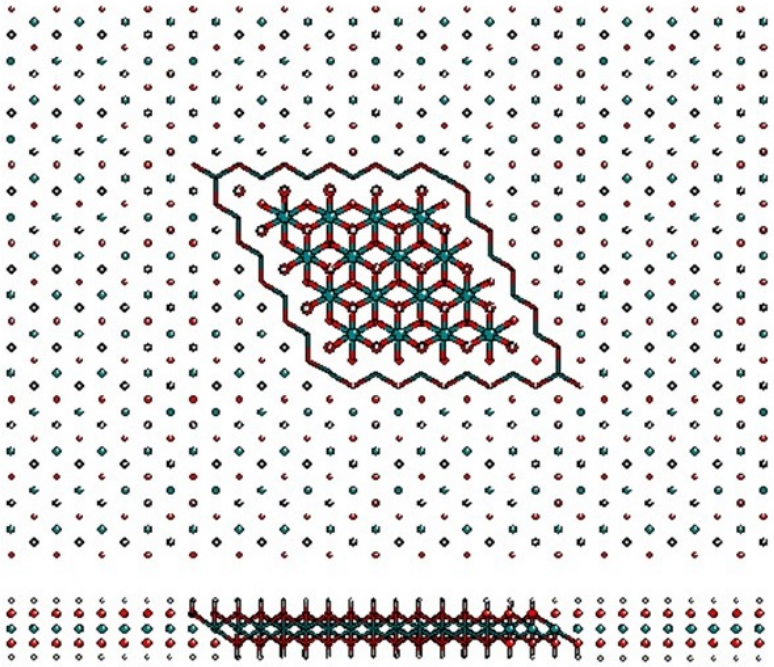

Figure 4.6: Illustration of the top and side view of the single layer PEECM model (*6x6_1*). The point charges are represented as balls around the QM cluster, the fixed boundary atoms as wires and the inner part of the cluster as balls and sticks. Bonds between the inside cluster and the boundary atoms are omitted for clarity. (Mg=green, O=red, H=grey)

To best of our knowledge, the PEECM approach has been previously used only for materials with conventional unit cell structures such as TiO_2[55] or CeO_2[56]. For these metal oxides effective core potentials (ECPs) were used on the neighbouring cations around the QM cluster to soften the effect of polarisation from the positive charges, as discussed in the section 2.6.2, while formal charges were used on the corresponding anions. By contrast to these examples, brucite has a layered structure, in which the covalently bonded OH group carries a -1 charge. In this case, the use of an ECP region is complicated and any attempts to create an isolating shell by surrounding the QM cluster with a region containing ECPs as Mg atoms and point charges as the O and H atoms are failed to converge. First, the 6x6 Mg QM cluster was extended to 7x7 and the Mg atoms at the boundary region were replaced by ECPs (mg ecp-10 hay&wadt) while the related O and H atoms were replaced by point charges, keeping the inner part of the QM region at the size of the original 6x6 stoichiometric cluster. Both formal charges and calculated natural charges (see the paragraph below) were considered on the O and H atoms (O/H -2/+1 and -1.33/+0.44 respectively). Second, clusters with two 6x6 Mg layer were modified by changing the second layer Mg atoms to ECPs then by adding an additional third

layer with ECPs on the positive ion and replace the related O and H with the same two type of point charges as for the single layer. All of these calculations are failed to converge even one SCF cycle, therefore, to avoid the artificial polarisation effect of neighbouring PCs on the QM cluster, we decided to employ natural charges in the PC region,[245] derived iteratively from natural population analysis(NPA).[131] Formal charges were used as an initial guess for the embedding array in a single point calculation, from which a new set of NPA charges inside the QM cluster was determined. The values obtained from the centre of the QM cluster were used as charges in the PC region for the following calculation and this step was repeated until no further variation occurred. The following natural charges were obtained through this process: Mg=+1.78, O=-1.33 and H=+0.44.[246] Applying these charges in the partial optimisation of ***6x6_1*** resulted in good geometrical agreement with experimental data (see Table 4.3): both the calculated bond lengths and atomic distances stayed reasonably close to the previously reported values. Moreover, the optimised QM cluster perfectly maintained the key features of the surface, such as the perpendicular position of the OH groups to the (0001) plane or the planarity of the Mg sites.

Table 4.3: Calculated average d(Mg-O) and d(O-H) bond lengths together with the d(O$\cdots$O) atomic distances of the QM cluster in *6x6_1*, compared with the structural parameters of a previous computational study and experiments. All values are in Å. (SD stands for the standard deviation of the calculated average parameter.)

	d(Mg-O)	**d(O-H)**	**d(O$\cdots$O)**
This work	2.104 (SD:0.0056)	0.969 (SD:0.0003)	2.777 (SD:0.0051)
Periodic HF[200]	2.103	0.953	2.787
Periodic DFT[202]	2.104	0.962	2.770
Exp 1[203]	2.102	0.995	2.787
Exp 2[204]	2.096	0.927	2.767

Several attempts were carried out to efficiently increase the system size in the z direction while keeping up the good agreement with the experimental parameters in the least computational time. In our first approach, we considered every layer underneath the first one as simple PC layers. Additional PC layers up to 8 with an interlayer distance of 4.77 Å were introduced in the system and the cluster was re-optimised to see if it significantly deviates from the experimental structure. Unfortunately, without fixing the H atoms of the down-facing OH groups, the cluster ”bends” after including one PC layer (Figure 4.7).

To quantify the bending, the RMS deviation for the z coordinates of the Mg atoms were calculated (summarised in Table 4.4), since those atoms are all in one plane originally with a z coordinate 0. While the RMS deviation is only 0.04 Å for a single layer, it rises to 0.55

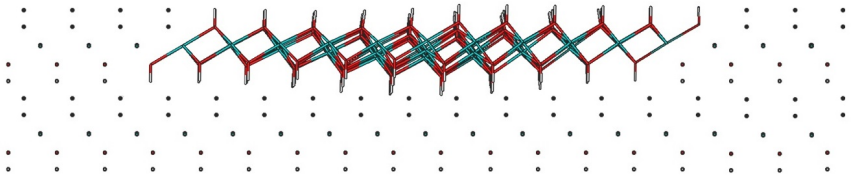

Figure 4.7: A side view of 6x6 Mg embedded brucite cluster ($Mg_{36}(OH)_{72}$) and one PC layer underneath. Atoms in the QM region are represented by wires, while the outer part by points. (Mg=green, O=red, H=grey)

Å on introducing a PC layer. Besides, there is a decrement in the SCF energy due to the electrostatic attraction of the first PC layer. Interestingly, after adding the first point charge layer underneath, including extra layers has no effect on the SCF energies or RMS deviation values, thus we did not pursue the addition of more than one PC layers further.

Table 4.4: SCF energies and the RMS deviation of the Mg z coordinates in the systems with a *6x6* $Mg(OH)_2$ cluster and 0 to 8 PC layers

total number of layers	PC layers	SCF energy (a.u.)	RMS z (Å)
1	**0**	-12666.68382	0.040
2	**1**	-12666.96102	0.550
3	**2**	-12666.96103	0.550
4	**3**	-12666.96103	0.550
5	**4**	-12666.96103	0.550
6	**5**	-12666.96104	0.550
7	**6**	-12666.96104	0.550
8	**7**	-12666.96104	0.550
9	**8**	-12666.96104	0.550

To eliminate the overly strong attraction of the underlying point charges, we either decrease the interlayer distance between the layers to create compensating repulsion forces between the layers, modify the relative charges of the O and H centres further; or fix the positions of the down-facing hydrogen atoms in the explicit cluster. We excluded the first solution because, although attempts to decrease the interlayer distance from 4.77 Å to 3.47 Å in a system with 1 extra PC layer resulted in an RMS and energy minima below 4 Åwith a RMS deviation 0.046 Å (Figure 4.8), which is close to the single layer value; SCF convergence problems appeared close to the energetic minimum. If we decreased the interlayer distance further, the explicit cluster, in addition to convex deformation, deprotonated and was impossible to stabilise. We also exluded the second approach, since it would require to change the relative charges for the O and H points, such that the -1 charge of the OH^- would be almost entirely on the O atoms (-1.03 and +0.14 respectively).[246] Therefore, we decided to simply constrain the lower hydrogen atoms, as we already do with the other boundary atoms in the sides. A double

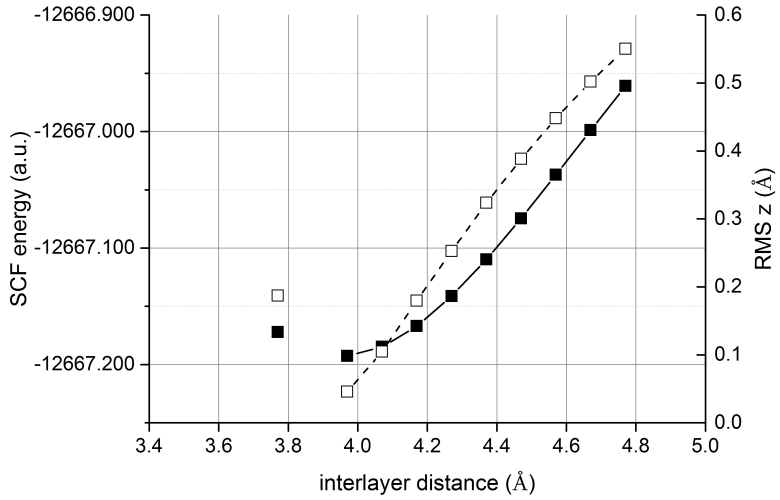

Figure 4.8: SCF energies (black squares) and RMS deviation of the Mg z coordinates (white squares) in the systems with 6x6 $Mg(OH)_2$ cluster and 1 extra PC layer but with different interlayer distances from 4.77 to 3.47 Å.

layer containing only point charges in the second is referred as ***6x6_1+PC***. We note that the attraction force of the underlying point charges is not eliminated in this case and may affect the adsorption energies of the investigated systems.

Embedding more explicit clusters under the top ***6x6*** one should improve the description of interlayer forces and prevent the top layer from deformation. But increasing the size of the QM region, which is already quite big (180 atoms) is computational demanding. Therefore, we attempted to insert smaller cluster sizes under the first layer by creating the following systems: ***6x6+4x4*** two- and ***6x6+4x4+2x2*** three-layered structures. Unfortunately, these cluster arrangements resulted in an asymmetric deformation in the top layer, presumably due to the asymmetric QM/PC region boundaries at side of the ***6x6*** cluster, shown in Figure 4.9.

Further attempts to equalise the PC environment on the two sides of the cluster region by modifying the structure of the ***4x4*** and ***2x2*** clusters, in which the terminating 4-fold coordinated Mg atoms at the corners of the 4x4 and 2x2 clusters were changed to 3- and 5-fold Mg (***6x6+(4x4)'*** and ***6x6+(4x4)'+(2x2)'***), could not successfully eliminate the visible deformation of the top cluster (Table 4.5). The related RMS z value is 0.221 Å for the modified ***6x6+4x4*** and 0.250 Å for the ***6x6+4x4+2x2*** system, which is still a significant deformation. However, applying a double layer system in which the second layer has the same sized explicit cluster of brucite as the first (***6x6_2***, $2xMg_{36}(OH)_{72}$), resulted in an RMS deviation almost identical to the value of a single layer (0.046 Å).

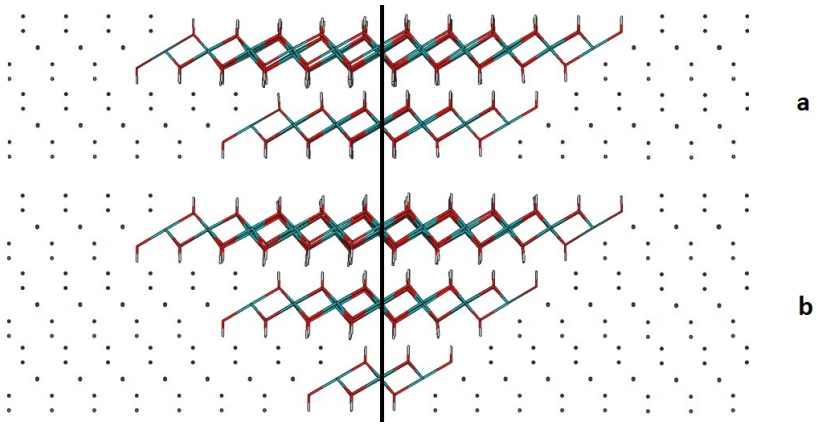

Figure 4.9: Side view of a system with two explicit $Mg(OH)_2$ cluster (*6x6+4x4*) (a); and a system with three explicit clusters (*6x6+4x4+2x2*) (b). Because of the asymmetrical geometry of the smaller clusters, the deformation in the left side of the upper cluster is greater. Atoms in the QM region are represented by wires, while the outer part by points. (Mg=green, O=red, H=grey)

Table 4.5: Comparison of SCF energies and RMS deviation of the Mg z coordinates in the first brucite layer, for systems with more explicit layers within the cluster and with or without extra PC layers. (*nxn* refers to the number of Mg atoms in the cluster, (*nxn*)' refers to clusters with modified geometries)

total number of layers	PC layers	SCF energy (a.u)	RMS z (Å)
	6x6+4x4		
2	0	-18297.0529	0.236
3	1	-18297.1564	0.265
4	2	-18297.1564	0.264
5	3	-18297.1564	0.265
	6x6+4x4+2x2		
3	0	-19705.0615	0.267
4	1	-19705.0861	0.270
5	2	-19705.0861	0.270
6	3	-19705.0861	0.270
	6x6+(4x4)'		
2	0	-18297.2397	0.221
3	1	-18297.3375	0.248
4	2	-18297.3375	0.246
5	3	-18297.3375	0.249
	6x6+(4x4)'+(2x2)'		
3	0	-19705.4253	0.250
	6x6+6x6		
2	0	-25333.7182	0.046
3	1	-25333.9664	0.127
4	2	-25333.9664	0.129
5	3	-25333.9664	0.126

To save computational cost, we tried four variations of fixed atomic positions in the ***6x6_2*** system, summarised in Table 4.6, which can be divided to two groups: the first two contain frozen coordinates only in the second layer, while in the second two there are fixed atomic positions in the first layer too. The SCF energies confirm our expectation that with increasing number of frozen coordinates the absolute energy of the system will become less negative. In case of fixing the down-facing hydrogen atoms in the bottom cluster or fixing the whole second layer in the cluster the RMS deviation is between 0.052 and 0.054 Å , while fixing the down-facing hydrogen atoms in both layers or freezing the coordinates of the whole second cluster and the bottom hydrogen atoms of the first layer, result in RMS values around 0.024-0.026 Å. We concluded that the best compromise between the criteria of computational time and geometrical parameters within the top cluster, is a system containing a frozen second explicit cluster: ***6x6_2_f***.

Table 4.6: Comparison of SCF energies and RMS deviation of the Mg z coordinates in the first cluster, for *6x6_2* systems with fixed atomic coordinates in different positions (with or without extra PC layers)

total number of layers	PC layers	SCF energy (a.u)	RMS z (Å)
Fully relaxed system			
2	0	-25333.71811	0.046
3	1	-25333.96642	0.127
4	2	-25333.96643	0.129
Fixed down-facing H atoms in the 2nd layer			
2	0	-25333.71721	0.054
3	1	-25333.93122	0.052
4	2	-25333.93121	0.050
Fixed 2nd layer			
2	0	-25333.7046	0.052
3	1	-25333.91806	0.054
4	2	-25333.91807	0.054
Fixed down-facing H atoms in the 1st and 2nd layers			
2	0	-25333.71435	0.026
3	1	-25333.92851	0.026
4	2	-25333.92851	0.026
Fixed 2nd layer and fixed down-facing H atoms in the 1st layer			
2	0	-25333.70193	0.025
3	1	-25333.91548	0.024
4	2	-25333.91549	0.024

4.4.2 Periodic DFT models

We chose the CRYSTAL14 code[138, 141] to model the brucite (0001) surface with periodic DFT, since this program allows us to use atom-centred basis sets, as used in TURBOMOLE. The TPSS meta-GGA exchange correlation functional, which was used for the development of the PEECM model, is not available in this code. Since TPSS was developed by Perdew and coworkers based on the same philosophy as PBE exchange-correlation functional[74], we decided to use the latter in CRYSTAL14. PBE is one of the most commonly used GGA functionals in solid state chemistry, besides, the general gradient approximation level of theory gave good agreement with the experimental parameters of brucite in previous studies.[201, 202, 209, 210] Following on from the work of Ungliengo *et al.*[206], we compared the geometrical parameters obtained with the use of PBE to the Grimme type dispersion corrected PBE-D functional[83, 84]. Since PBE-D resulted in an interlayer distance 0.15 Å less than the experimental values, we decided to continue with PBE, see Table 4.7.

Polarised triple-ζ basis sets, derived specifically for solid state calculations by Peintinger *et al.*[247] were used for the surface atoms (Mg_pob_TZVP_2012, O_pob_TZVP_2012, and H_pob_TZVP_2012) along with the Ca atom in the substitution study presented in section 4.5.3 (Ca_pob_TZVP_2102). In the case of Sr, the Sr_HAYWSC-311(d11f)G basis set[248] was used for geometry optimisations, whilst single point energies were calculated using doubly polarised triple-ζ basis sets for the valence electrons with the ECP28MWB multi-electron fit quasi-pseudopotential on the electrons of the core 1s-3d orbitals.[97] We used the 0D MOLECULE option of CRYSTAL14 for the single point energies of the isolated ions in section 4.5.1 and for the solvated $Sr(OH)_2$ complex in section 4.5.4, which allows to optimise systems as non-periodic, isolated structures in vacuum.[iii]

For the model studies presented in sections 4.5.3 and 4.5.4, to make comparison between the two different methods possible, we used the PBE functional with the same computational parameters for the PEECM calculations as was detailed for periodic DFT. Although for the embedded cluster structures def2-SVP basis sets were used for the geometry optimisation, single point energies were obtained after geometry optimisation with the above defined CRYSTAL14 basis functions.

[iii] Since we were using the same computational parameters, the calculated energies with both CRYSTAL14 and TURBOMOLE were essentially the same for isolated ions in vacuum (less than 10^{-6} a.u. difference).

Table 4.7: Geometrical properties of bulk brucite structure calculated with CRYSTAL, compared to previously published parameters. All values are in Å (a, c are lattice parameters, Mg-O and O-H are bond lengths; H$\cdots$H and O$\cdots$O are atomic distances) [a]Calculated based on published fractional coordinates (z_H, z_O)

		a	c	d (Mg-O)	d (O-H)	d(H$\cdots$H)	d(O$\cdots$O)
This work	**PBE**	3.177	4.751	2.112	0.972	1.966	2.785
	PBE-D	3.134	4.615	2.091	0.971	1.899	2.769
Periodic HF[200]	**HF**	3.146	5.354	2.103	0.953	2.250	2.787
Periodic DFT[202]	**HF**	3.148	5.263	2.093[a]	0.939	2.239[a]	2.759[a]
	LDA	3.099	4.413	2.067[a]	0.981	1.829[a]	2.737[a]
	PW91	3.179	4.717	2.111[a]	0.972	1.960[a]	2.778[a]
	B3LYP	3.167	4.854	2.104[a]	0.962	2.016[a]	2.770[a]
Periodic DFT[206]	**B3LYP**	3.175	4.923	-	0.961	-	-
	B3LYP-D	3.140	4.657	-	0.962	-	-
Exp1[203]		3.142	4.766	2.102	0.995	1.932	2.787
Exp2[204]		3.15	4.77	2.100	0.958	1.997	2.779

Considerations of the surface geometry

Creating starting geometries for the brucite surface in CRYSTAL14 involves several intermediate steps.[249] First, a full optimisation was performed on the primitive cell of bulk brucite, using a shrinking factor of 8 (convergence of the k mesh is shown in Appendix A) along with the energy criteria of 10^{-7} a.u. both for the SCF energy convergence and for the geometry optimisation. These parameters gave good agreement of geometrical properties with the experimental values as well as previous computational studies (shown in Table 4.7). We fixed the optimised lattice parameters of the bulk system to create a primitive cell for the (0001) surface and calculated the surface energy along with the Mulliken charges and populations (Table 4.8) for slabs incorporating different numbers of layers. The following equation was used to calculate the surface energy:

$$E_{surf} = \frac{E_{slab} - nE_{bulk}}{2A_{surf}} \tag{4.1}$$

Where E_{slab} is the SCF energy of the brucite slabs, n is the number of brucite layers in the slab, E_{bulk} is the SCF energy of the bulk structure and A_{surf} is the surface area of the unit cell, which is calculated with the equation: $A_{surf} = \frac{1}{2}\sqrt{3}a^2$, A_{surf}=8.738 Å^2. One layer of $Mg(OH)_2$ contains 5 atomic layers as shown in Figure 4.10.

Since, as was discussed in section 4.2.3, there are only weak dispersion forces between the layers in brucite, including a 2^{nd} layer in the unit cell has only a small effect on the surface energy (10^{-6} Hartree/Å^2), although three layers were required to recover the exact Mulliken

Table 4.8: Calculated surface energies, Mulliken atomic charges and bond populations for different number of brucite layers in the slab with CRYSTAL.

Atomic layers	Brucite layers	SCF energy (a.u.)	E_{surf} (Hartree/Å^2)	E_{diff} (Hartree/Å^2)	Mulliken charges Mg	O	H	Mulliken populations O-H	Mg-O
BULK		-351.7220	-	-	10.307	9.049	0.797	0.400	0.029
5	**1**	-351.7139	0.000458030	-	10.356	8.990	0.831	0.355	0.036
10	**2**	-703.4360	0.000453321	-4.7E-06	10.332	9.054	0.798	0.399	0.040
15	**3**	-1055.158	0.000455771	2.4E-06	10.308	9.049	0.797	0.400	0.029
20	**4**	-1406.880	0.000457659	1.9E-06	10.308	9.049	0.797	0.400	0.029
25	**5**	-1758.602	0.000458798	1.1E-06	10.308	9.049	0.797	0.400	0.029
30	**6**	-2110.324	0.000458988	1.9E-07	10.308	9.049	0.797	0.400	0.029
35	**7**	-2462.046	0.000458063	-9.2E-07	10.308	9.049	0.797	0.400	0.029

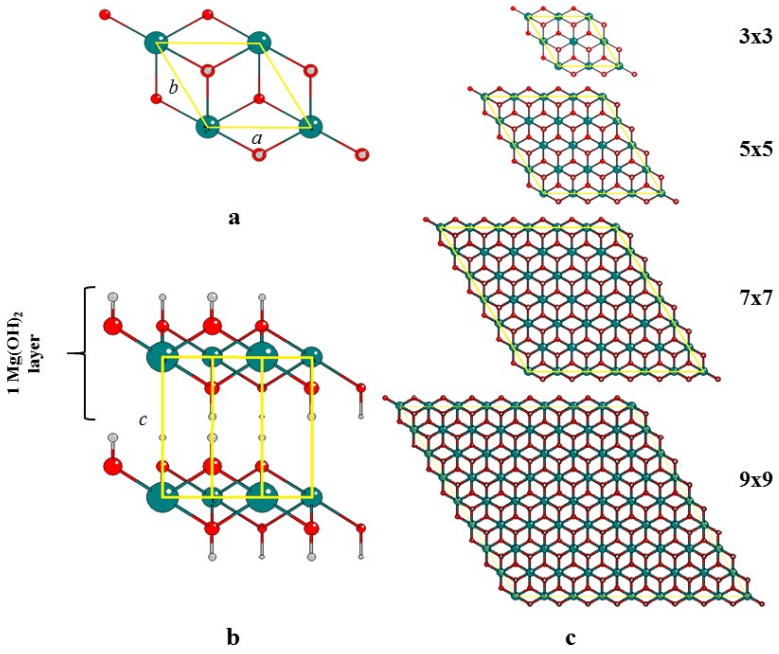

Figure 4.10: (a) Top view of the hexagonal unit cell in the brucite crystal structure (a, b are lattice parameters) (b) Side view of the hexagonal unit cell, c is the interlayer distance. 1 Mg(OH)$_2$ layer contains 5 atomic layers. (c) Illustration of the supercells employed (Mg=green, O=red, H=grey)

charges of the bulk in the middle of the slab. For the model studies in section 4.5.3 and 4.5.4, we created a series of Mg(OH)$_2$ slabs with different supercell sizes (***3x3***, ***5x5***, ***7x7*** and ***9x9***) and with 1, 2 and 3 layers of brucite (Figure 4.10) and optimised the internal coordinates for each using a shrinking factor of 4 along with the convergence criteria: SCF energy: 10^{-7} a.u. and structural energy: 10^{-7} a.u..

4.5 Results

The primary goal of the model studies presented in this section is to test the reliability of the embedded cluster model developed for the brucite (0001) surface. First, we examine the adsorption of charged systems, by investigating the interaction of a series of s block ions and a simple Sr^{2+} hydrate with brucite. Then, we move on to compare the embedded model calculations with a more widely established method (periodic DFT); we perform a substitution study for single ions into brucite and a second in which we look at the adsorption of differently coordinated [$Sr(OH)_2(H_2O)_4$] complexes on the surface, comparing their relative stability. We also used the periodic DFT model to carry out cell size studies on the systems of interest and to (indirectly) verify the size of the quantum chemically treated cluster in the PEECM approach.

Note that the adsorption and substitution energies presented in sections 4.5.1 and 4.5.3 are calculated without considering the effects of solvation on the adsorbed or substituted ions, and the model systems of 4.5.2 and 4.5.4 only contain a few explicit solvent molecules. This has been done partly to avoid the extra variability and complication that will inevitably arise from the treatment of solvation and because the purpose of these calculations is to provide as direct and straightforward a comparison of periodic DFT and PEECM as possible.

4.5.1 Single ion adsorption of Sr^{2+} and other s block elements on brucite

We calculated adsorption energies for a series of ions: Na^+, Rb^+, Cs^+ and Mg^{2+}, Sr^{2+}, Ba^{2+} from which Na^+, Cs^+, Sr^{2+} and Mg^{2+} are known to exist in the aqueous phase in Magnox storage ponds.[2] As described in the Introduction 1.2, we have a special interest in $^{90}Sr^{2+}$ and $^{137}Cs^+$, as their adsorption behaviour is especially important in the waste treatment process. We included Rb^+ and Ba^{2+} to make the series of the singly and double charged ions complete, and to allow us to test if the adsorption energies follow the trend expected based on the ionic radii and charges, i.e. the dications should have a stronger interaction with the surface, and the interaction energy should decrease with decreasing ionic charge density.

The following equation was used to calculate the adsorption energies presented in Table 4.11:

$$E_{ads} = E_{complex} - (E_{brucite} + E_{M^{2+}}) \tag{4.2}$$

$E_{complex}$ is the SCF energy of the adsorbed ion with the surface, while $E_{brucite}$ is the energy of the brucite surface model (***6x6_1***, ***6x6_1+PC***, or ***6x6_2***) and $E_{M^{2+}}$ is the energy of the adsorbed ion.

The counterpoise (CP) correction[98] was included to compensate for the artificial energy contribution to the adsorption energy due to the difference in the basis set sizes applied for the components of Eq. (4.2) (basis set superposition error, BSSE). CP corrected results are shown in brackets in Table 4.11. As expected, correcting for the effect of BSSE on the adsorption energies generally decreases the strength of the interaction, and the magnitude of the counterpoise correction is smaller when higher quality basis sets are used; the energetic order between the ions is not altered.

Before continue with the comparison of adsorption energies, we have to consider the possibility of some level of artificial energy difference, due to an electrostatic potential shift between systems with different charges. The PEECM is a reliable method for investigating charged systems. This is evidenced by the fact that the developers themselves used extensively charged clusters in PEECM calculations. Burow, Sierka, Döbler and Sauer used CaF_2 QM surface clusters with a total charge between -19 and +8 and used a CeO_2 cluster with a charge of -12.[56] However, comparing the energies of differently charged systems is not that straightforward, because their absolute energies contain a shift in the electrostatic potential, which would not exist in a neutral cluster.

As our adsorption energy equation Eq. (4.2) contains a neutral QM cluster ($E_{brucite}$) on one side, and a +1 or +2 charged cluster on the other ($E_{complex}$, with the adsorbed cations), there is a possibility that E_{ads} contains an artificial term arising from the charge differences. We consulted with Prof Marek Sierka on the matter and he confirmed that it can cause a potential problem.[250] However, this artificial energy shift is automatically cancelled if we calculate the relative energies applying the same charge within the QM cluster on both sides of the equation. Therefore, we carried out a series of test calculations where we replaced the bare surface and the isolated ion in equation (4.2) by the optimised brucite surface and a cation at 20 Å distance within one QM cluster (Eq. (4.3)).

$$E_{ads}(2) = E_{complex} - E_{brucite\_20\text{Å}\_ion} \tag{4.3}$$

As the brucite surface cluster is stoichiometric and neutral, while the adsorbing ion carries only a small charge, we would expect a small artificial effect on the adsorption energy. Indeed, for monocations (Na^+, Rb^+, Cs^+) the energy difference is negligible: 3 kJ/mol, and for the Ba^{2+} ion is 5.5 kJ/mol, which is still very small. However, in case of the Sr^{2+} and Mg^{2+} ion,

placing the cation 20 Å above the surface resulted in a total delocalisation of the charge over the cluster and therefore in non-realistic energies, see Table 4.9. Based on natural population analysis, in the (brucite_20Å_ion) systems with the adsorption energies shown in column (2) the natural charge on the Sr is +0.798 and +0.426 on the Mg ion, instead of +2.

The only way to prevent unphysical electronic charge residing on the Mg^{2+} or Sr^{2+} ion is to delete every basis function above those which describe the closed shell cation. This modification of the basis set may affect the description of the isolated ion and therefore the calculated adsorption energies too (column (3) in Table 4.9). To estimate the introduced error, we compared the energy of the lone cations with the original and truncated basis sets and corrected the adsorption energies with this ion specific terms (shown in Table 4.10). We found that the potential shift, i.e. the energy difference between adsorption energies calculated by Eq. (4.2) and Eq. (4.3) with using truncated basis sets and a ion related correction term, is 3.0/5.0 kJ/mol for monocations and 5.5/9.0 kJ/mol for dications (***6x6_1/6x6_2***), shown in the column (1)-(3)* in Table 4.9. These values are negligible compared to the magnitude of the absolute adsorption energies in Table 4.11 and since they are constant for ions with the same charge, they do not affect the energetic trend between mono- or dications.

Table 4.9: Adsorption energies of a series of s block ions: (1): calculated with Eq. (4.2) **and using a mixed basis set, ion_TZVP (def2-TZVP on the ion and def2-SVP on the surface) (2): with Eq.** (4.3) **and ion_TZVP, and (3): with Eq.** (4.3) **and using a modified closed shell basis set on the cation. $\triangle E_{ads}$ are the energy differences between the interaction energies evaluated with different methods. (3)* represents the adsorption energies calculated with the correction terms shown in Table 4.10.**

ion	layer	E_{ads} (kJ/mol)			$\triangle E_{ads}$ (kJ/mol)		
		(1)	(2)	(3)	(1)-(2)	(1)-(3)	(1)-(3)*
Na^+	***6x6_1***	-290.6	-293.7	-294.3	3.0	3.7	**3.0**
	6x6_2	-284.0	-	-289.6	-	5.6	**4.9**
Rb^+	***6x6_1***	-149.3	-152.3	-152.8	3.0	3.5	**3.0**
	6x6_2	-141.5	-	-147.0	-	5.4	**4.9**
Cs^+	***6x6_1***	-127.9	-130.9	-130.9	3.1	3.1	**3.1**
	6x6_2	-119.1	-	-124.1	-	5.0	**5.0**
Mg^{2+}	***6x6_1***	-1387.0	-515.0	-1395.0	-871.9	8.0	**5.5**
	6x6_2	-1404.6	-	-1416.1	-	11.5	**9.0**
Sr^{2+}	***6x6_1***	-901.7	-519.2	-907.5	-382.4	5.8	**5.5**
	6x6_2	-908.8	-	-918.2	-	9.3	**9.0**
Ba^{2+}	***6x6_1***	-793.4	-798.9	-799.0	5.5	5.6	**5.5**
	6x6_2	-798.8	-	-807.9	-	9.1	**9.0**

Nevertheless, the potential shift difference between the two surface representation (***6x6_1*** and ***6x6_2***), which is 2.0 kJ/mol for monocations and 3.5 kJ/mol for dications, is in comparable magnitude with the relative energy differences calculated in Table 4.11 with the ion-TZVP

Table 4.10: Estimated energy difference arising due to the truncation of the cation basis sets, calculated by comparing the energy of a lone ion with full and truncated basis set. ($\triangle E = E_{full}$-E_{trunc})

ion	SCF *E* (a.u)		$\triangle E$ (kJ/mol)
	truncated basis	def2-TZVP	correction term
Na^+	-162.09743740821	-162.09768921611	-0.7
Rb^+	-23.93140001154	-23.93158099072	-0.5
Cs^+	-20.00631910347	-20.00631965394	-0.0
Mg^{2+}	-199.24932352124	-199.25026866216	-2.5
Sr^{2+}	-30.07232983736	-30.07244486256	-0.3
Ba^{2+}	-24.91214729984	-24.91216867858	-0.1

mixed basis sets. However, we note that these potential shift energy differences are calculated using 20 Å ion-surface distance and by increasing the separation, as it is shown in Figure 4.11 for the example of Cs^+, they become gradually smaller while the adsorption energy converges to the energy of an isolated ion and a surface.

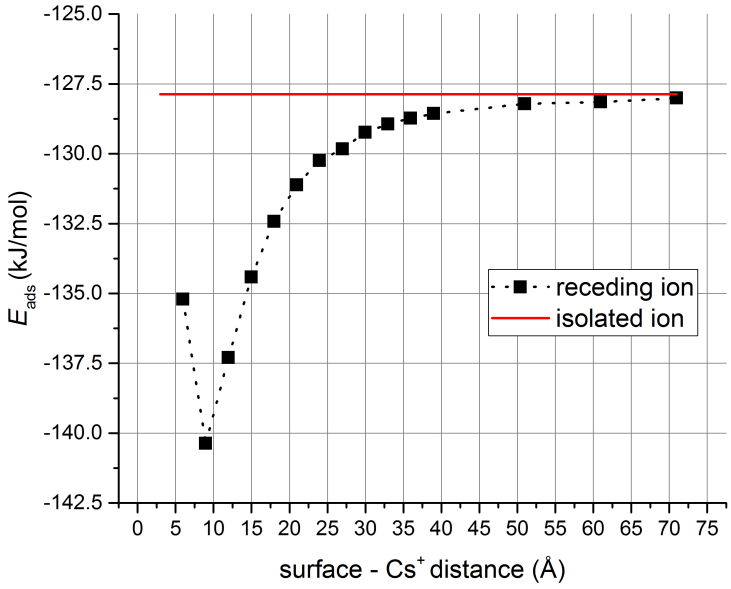

Figure 4.11: Energy convergence as a function of Cs^+-surface distance within the QM cluster. The red line shows the adsorption energy calculated with Eq. (4.2)**.**

After showing that the energy difference due to the artificial effect of differently charged QM clusters is negligible in the case of singly and doubly charged ions, by looking at the absolute adsorption energies in Table 4.11, the doubly charged ions indeed have a stronger interaction with the surface, the adsorption energy of Mg^{2+}, Sr^{2+} and Ba^{2+} being about an order of magnitude larger ($\sim$700-1200 kJ/mol) than the adsorption energy of Na^+, Rb^+ and Cs^+ ($\sim$100 kJ/mol).

Table 4.11: Adsorption energies (E_{ads}) of a series of s block ions and relative adsorption energies of different surface representations for a given ion, calculated by comparing the results to the adsorption energy of the *6x6_1* structures ($\triangle E_{ads}$). Counterpoise corrected energy values are presented in brackets (BSSE). (The adsorption energies with ion-SVP and ion-TZVP mixed basis sets are not calculated for *6x6_1+PC*.)

Studied system		E_{ads} (kJ/mol)								$\triangle E_{ads}$ (kJ/mol)			
ion	layer	def2-SVP	(BSSE)	def2-TZVP	(BSSE)	ion-TZVP	(BSSE)	ion-SVP	(BSSE)	def2-SVP	def2-TZVP	ion-TZVP	ion-SVP
Na^+	*6x6_1*	-131.0	(-118.2)	-249.7	(-244.7)	-290.6	(-277.2)	-96.2	(-93.7)	0.0	0.0	0.0	0.0
	+PC	-131.9	(-119.2)	-248.8	(-244.6)	-	-	-	-	-0.9 (-1.1)	0.9 (0.0)	-	-
	6x6_2	-123.6	(-108.4)	-212.1	(-206.7)	-284.0	(-267.4)	-58.8	(-55.9)	7.4 (9.7)	37.6(37.9)	6.7 (9.8)	37.3 (37.8)
Rb^+	*6x6_1*	-144.7	(-136.4)	-112.7	(-108.7)	-149.3	(-138.5)	-110.1	(-106.8)	0.0	0.0	0.0	0.0
	+PC	-144.7	(-136.6)	-110.5	(-106.7)	-	-	-	-	0.1 (0.2)	2.2 (2.0)	-	-
	6x6_2	-135.1	(-124.6)	-76.1	(-71.5)	141.5	(-127.2)	-73.0	(-69.7)	9.6 (11.8)	36.6(37.2)	7.8 (11.4)	37.1 (37.1)
Cs^+	*6x6_1*	-118.0	(-109.6)	-94.5	(-91.3)	-127.9	(-119.4)	-85.0	(-82.0)	0.0	0.0	0.0	0.0
	+PC	-117.5	(-109.3)	-92.1	(-89.2)	-	-	-	-	0.5 (0.3)	2.4 (2.2)	-	-
	6x6_2	-108.9	(-98.5)	-57.9	(-54.5)	-119.1	(-108.5)	-48.8	(-45.6)	9.1 (11.1)	36.6(36.8)	8.8 (10.9)	36.2 (36.4)
Mg^{2+}	*6x6_1*	-1182.7	(-1161.4)	-1319.6	(-1311.6)	-1387.0	(-1363.0)	-1123.7	(-1117.7)	0.0	0.0	0.0	0.0
	+PC	-1184.2	(-1168.0)	-1315.6	(-1308.3)	-	-	-	-	-1.5 (-6.6)	4.0 (3.3)	-	-
	6x6_2	-1199.2	(-1178.1)	-1272.5	(-1265.3)	-1404.6	(-1379.9)	-1077.6	(-1072.2)	-16.5(-16.7)	47.1(46.3)	-17.6 (-16.9)	46.1 (45.5)
Sr^{2+}	*6x6_1*	-890.9	(-874.6)	-835.4	(-828.5)	-901.7	(-882.1)	-825.6	(-819.5)	0.0	0.0	0.0	0.0
	+PC	-895.2	(-880.0)	-834.6	(-828.1)	-	-	-	-	-4.3 (-5.4)	0.8 (0.4)	-	-
	6x6_2	-898.5	(-881.2)	-780.5	(-774.1)	-908.8	(-888.4)	-771.3	(-765.7)	-7.6(-6.6)	54.9(54.4)	-7.2 (-6.3)	54.3 (53.8)
Ba^{2+}	*6x6_1*	-717.9	(-702.3)	-730.1	(-721.7)	-793.4	(-777.4)	-653.3	(-647.8)	0.0	0.0	0.0	0.0
	+PC	-722.6	(-707.6)	-729.4	(-723.7)	-	-	-	-	-4.7 (-5.3)	0.7 (-2.0)	-	-
	6x6_2	-723.5	(-706.7)	-674.1	(-665.9)	-798.8	(-781.5)	-598.6	(-591.5)	-5.5(-4.4)	55.9(55.8)	-5.4 (-4.1)	54.7 (56.3)

The difference in magnitude is most likely due to the greater polarisation effect of the dications, as shown by the electron density difference plots of Sr^{2+} and Cs^{+} in Figure 4.12. The blue regions represent electron accumulation while the red areas indicate electron depletion caused by ion adsorption. Sr^{2+} clearly polarises the oxygen atoms of the brucite cluster much more than Cs^{+} does; most likely that is why the Sr^{2+} binds much more strongly to the surface. Besides showing the different behaviour of the ions, the electron density difference plots also reassure us that there is no artificial polarisation at the edges of the cluster, caused by false interaction between the charged systems and the point charge region. Furthermore, the image in Figure 4.12b and 4.12d suggest only a small contribution from the 2^{nd} layer oxygen atoms to the interaction even in the case of Sr^{2+}.

Figure 4.12: Electron density difference plots of adsorbed Cs^{+} (a, b) and Sr^{2+} ion (c, d) on *6x6_1* (a,c) and on *6x6_2* (b,d). The isosurface value was chosen to be 0.0025 a.u. throughout. The red regions are indicative of electron depletion, while the blue regions to electron accumulation. Point charges are not shown. (Mg=pink, O=ochre, H=white, Sr=yellow, Cs=turquoise)[244])

Examination of the energy trends for the ions of the same charge reveals that, in the case of the monocations, there is a deviation in the adsorption energies from the expected trend based on ionic radii, i.e. ionic charge density; a weaker interaction is predicted for Na^{+} than Rb^{+}. This discrepancy does not vary with the number of layers included in the cluster, however, it is eliminated by the use of a higher quality basis set as is shown in Table 4.12; using triple-ζ basis sets (def2-TZVP) gives the expected energetic order. Exploring the effect of basis set quality further by using def2-QZVP for test calculations on the single layered systems seems to result in only a rather big but, constant shift in adsorption energies when compared to triple-ζ results.

Table 4.12: Adsorption energies of a series of s block ions on a single layer of brucite (*6x6_1*) calculated with def2-SVP, def2-TZVP and def2-QZVP and the adsorption energy differences between the TZVP/SVP and QZVP/TZVP results. All values are in kJ/mol.[a]The exceptional behaviour of the Mg^{2+} is explained in Figure 4.13.

ions	def2-SVP		def2-TZVP		def2-QZVP
	E_{ads}	$\triangle E$(TZVP-SVP)	E_{ads}	$\triangle E$(QZVP-TZVP)	E_{ads}
Na^+	-131.0	-118.7	-249.7	88.7	-161.0
Rb^+	-144.7	32.0	-112.7	82.7	-30.0
Cs^+	-118.0	23.5	-94.5	80.4	-14.1
Mg^{2+}	-1182.7	-136.9	-1319.6	207.3[a]	-1112.3
Sr^{2+}	-890.9	55.5	-835.4	164.4	-670.8
Ba^{2+}	-717.9	-12.2	-730.1	166.0	-564.1

To understand the effect of the surface representation on the adsorption energies, we looked at the adsorption of the same ions on three different surface models, a single layer, ***6x6_1***, a surface containing a point charge layer underneath the QM cluster, ***6x6_1+PC***, and a double layer with the same sized QM clusters in both, ***6x6_2***. The relative adsorption energies were calculated by comparing the energies of the different systems to the original single layer results (see Table 4.11). Including an extra PC layer (***6x6_1+PC***) results in negligible difference in the adsorption energies. With def2-SVP basis sets, the $\triangle E_{ads}$ are c. 0.9 kJ/mol for Na^+, Rb^+ and Cs^+, while they are slightly larger (1.5-4.7 kJ/mol) for Mg^{2+}, Sr^{2+} and Ba^{2+}. To place these differences in context, they are no more than 0.7% of the original interaction energies in each case. These results suggest only a small electrostatic contribution from the second layer to the ion/surface interaction.

Including the atoms of the second layer in the quantum chemically treated cluster (***6x6_2***) increases the dication adsorption energies slightly, except for Mg^{2+}, which has a systematically different behaviour compared to Sr^{2+} and Ba^{2+} throughout this study. Presumably this is because the individual Mg^{2+} ion incorporates more into the brucite layer, while an ion with a bigger ionic radius (e.g. Sr^{2+}) coordinates to the surface with a larger distance, which also effects the level of electron donation from the surface oxygen atoms (see Figure 4.13). Opposite to the dications, the energies of monocations decrease by 7.4-9.1 kJ/mol, 6-8% of the actual adsorption energies. These values are in line with our previous suggestion based on Figure 4.12, i.e. that there is only a small electron donation from the second layer oxygens in the case of Sr^{2+} and a negligible effect for Cs^+. We conclude that the adsorption of singly charged ions slightly distorts the positions of the second layer atoms, but with minimal polarisation, therefore a quantum chemically treated second layer weakens the interactions

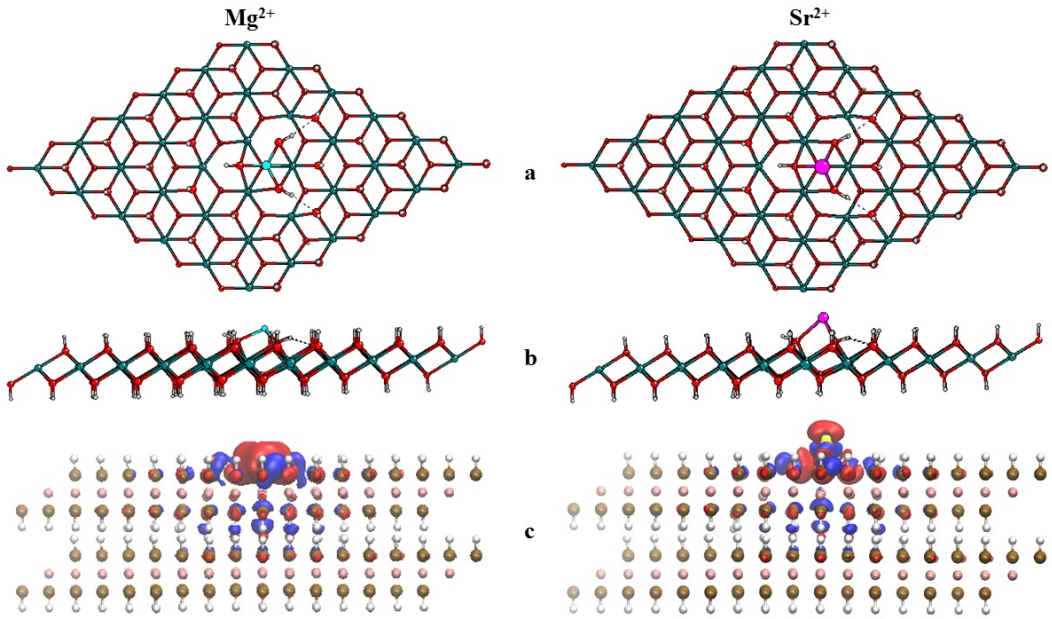

Figure 4.13: (a) top view, (b) side view of the QM cluster containing adsorbed Mg^{2+}/Sr^{2+} on the surface. (c) the electron density difference plot for Mg^{2+} and Sr^{2+} on the *6x6_2* brucite model.

overall.

A problem emerges when we use higher quality basis sets for the ***6x6_2*** systems. The relative adsorption energies with the def2-TZVP basis sets are ∼36 kJ/mol for the monocations and ∼55 kJ/mol for the diactions. The significant shifts in energies, which are more than the 30% of the actual adsorption energies for the singly charged ions, are very likely the consequence of an artificial interaction. Larger basis sets might cause charge density increase closer to or overlapping the PC region leading to a falsely enhanced interaction. (The point charges were originally calculated with NPA in an iterative process using def2-SVP basis sets for the QM cluster). To probe this further, we explored a range of mixed basis set calculations. *Ion-TZVP* in Table 4.11 and Figure 4.14 indicates systems with the def2-SVP basis set on the surface atoms but def2-TZVP on the adsorbed ion - and vice versa for *Ion-SVP*. Based on these results, we find that the deviation from the expected order in adsorption energies is clearly a function of basis set quality on the adsorbed ion, while the shift in the relative adsorption energies is related only to the basis sets of the surface atoms.

In summary, we conclude that our PEECM brucite model is capable of describing the energetics of ion/surface interactions, providing sufficiently high quality basis sets are applied on the ions. Considering the surface as a two layered slab only slightly affects the adsorption energies, which suggests only a small contribution from the second layer atoms in the inter-

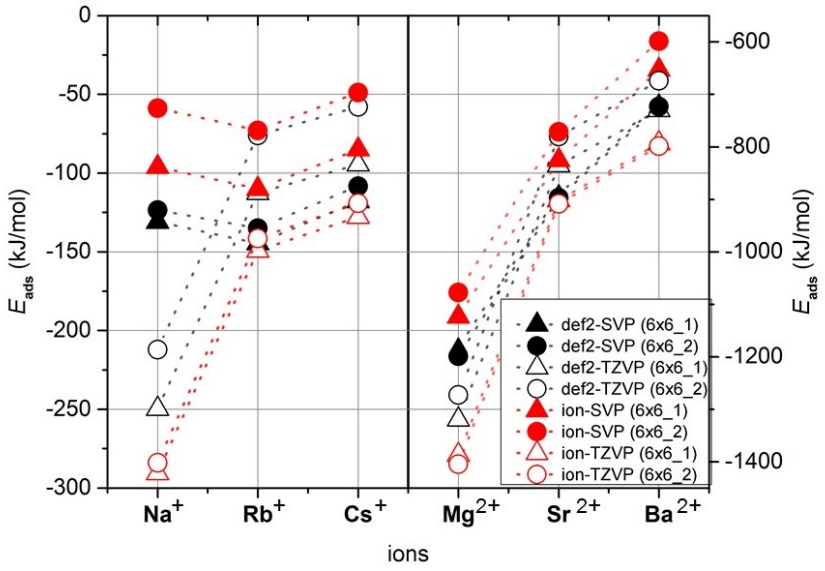

Figure 4.14: Adsorption energies for a series of ions adsorbed on the *6x6_1* and *6x6_2* model surfaces, using different quality basis sets (def2-SVP, def2-TZVP or mixed basis sets)

action, but further investigations are necessary to sufficiently explore the effect of different surface representations. Therefore, in the next section we continued to compare the adsorption energies of different PEECM models, considering slightly more variation in the surface structure.

4.5.2 Adsorption of Sr^{2+} hydrates

Moving on to a slightly more complex system, we considered the adsorption of a single Sr^{2+} cation bound to three water molecules. The main purpose of this short investigation was to understand the effect of different starting positions on the surface and explore the effect of more than three surface representations. The definition of the adsorption energy was different from Eq. (4.2) by the energy of three additional water molecules on the right site of the equation, next to the energy of the adsorbed ion ($Sr(H_2O)_3^{2+}$):

$$E_{ads} = E_{complex} - (E_{brucite} + E_{Sr^{2+}} + 3E_{H_2O} \tag{4.4}$$

The two adsorption sites considered for this complex on the ***6x6_1*** brucite surface are shown in Figure 4.15a and 4.15b. Although both cases result in the same optimised Sr^{2+} complex geometry, there is a 16 kJ/mol energy difference[iv] between the structures in favour of structure **a**, presumably due to the different position relative to the cluster boundaries (and therefore to the point charges). But, considering that the magnitude of the calculated E_{ads} for these

[iv] It is a 15.4 kJ/mol energy difference with the *ion-TZVP* mixed basis set.

systems is around 1200 kJ/mol, the 16 kJ/mol energy difference between the two positions is no more than 1-2% of the absolute adsorption energies. In both cases, the formed complex is a 6 coordinated tetrahydroxide because the Sr^{2+} is directly connected to three hydroxyl groups from the surface and one water is deprotonated by an other surface OH^{-}, as shown in Figure 4.15c.

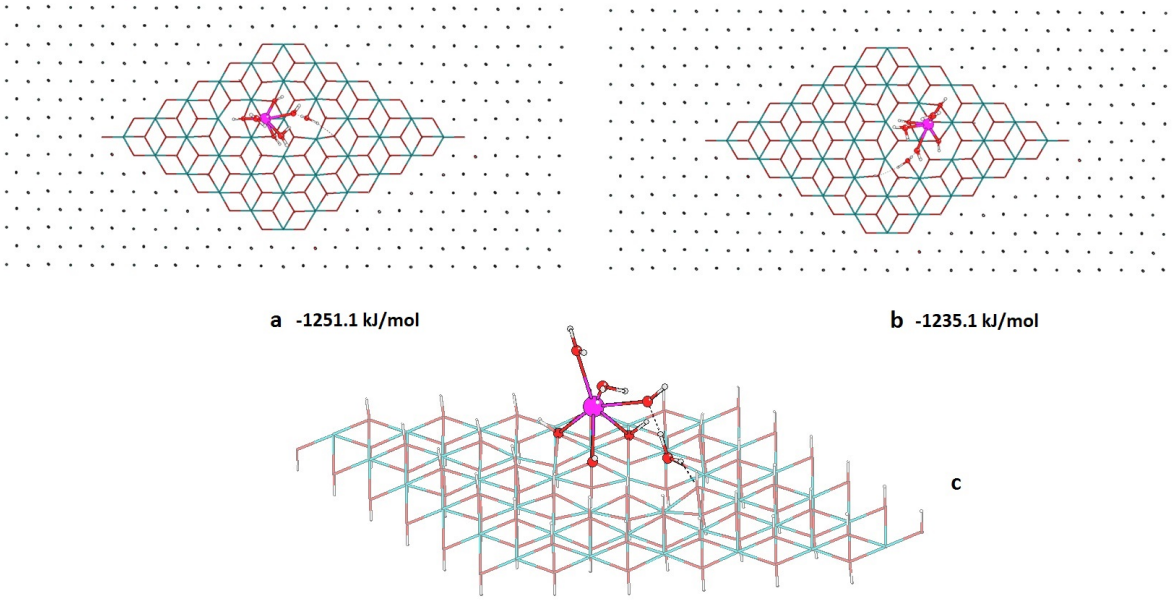

Figure 4.15: Top view of an adsorbed Sr^{2+} hydrate complex with three water molecules in two different positions on a single layer brucite ((a) and (b)). The perspective view of the formed complex in position (a) is shown in (c). Surface atoms in the QM region are represented by wires and the atoms of the complex with balls, while the outer part by points. (Mg=green, O=red, H=grey, Sr=magenta)

For the calculations with the different surface representations we used this optimised complex geometry in position 4.15a as a starting point and calculated the adsorption energy similarly to the previous section 4.5.1, for the following surface representations: ***6x6_1***, ***6x6_1+PC*** and ***6x6_2*** (see Table 4.13). The trend between the different surface models is very similar to the previously detected order in Table 4.11: 0.0 kJ/mol $>$ -4.3 kJ/mol $>$ -7.6 kJ/mol for the single Sr^{2+} cation, while 0.0 kJ/mol $>$ -6.2 kJ/mol $>$ -12.2 kJ/mol for the Sr^{2+} hydrate (***6x6_1*** $>$ ***6x6_1+PC*** $>$ ***6x6_2***). Applying def-TZVP basis set on the Sr^{2+} cation, as in the previous section for the *ion-TZVP* mixed basis set calculations, resulted in an almost constant energy shift in the absolute adsorption energies ($\sim$7.5 kJ/mol) and no significant change in the relative energies comparing the different surface representations, see the *ion-TZVP* results in Table 4.13.

For a more detailed investigation, we expanded the studied surface representations with two new models: a system with fixed bottom hydrogen atoms but without a PC layer (***6x6_1_f***)

Table 4.13: Adsorption energies (E_{ads}) and relative adsorption energies (ΔE_{ads}) of the Sr^{2+} hydrate complex with different surface representations. The relative energies are calculated by comparing the results to the energy of the complex on a single layer.

	E_{ads} (kJ/mol)		ΔE_{ads} (kJ/mol)	
	def2-SVP	**ion-TZVP**	**def2-SVP**	**ion-TZVP**
6x6_1	-1251.1	-1258.8	0.0	0.0
6x6_1+PC	-1257.3	-1265.0	-6.2	-6.2
6x6_2	-1263.3	-1270.7	-12.2	-11.9
6x6_1_f	-1228.4	-1236.1	22.7	22.7
6x6_2_f	-1243.3	-1250.7	7.8	8.1

and a system with fixed second brucite layer (***6x6_2_f***). Using the first model resulted in an adsorption energy 22.7 kJ/mol smaller, than the energy of the single layered system. This is probably a result of the fixed coordinates; the oxygen atoms cannot rearrange themselves in a way to maximise their interaction with the Sr^{2+}. Consequently, the extra PC layer is responsible for the stronger attraction forces and the bigger adsorption energy (ΔE_{ad}=-6.2 kJ/mol) in ***6x6_1+PC***; and the relatively small energy difference between the results with ***6x6_1_f*** and ***6x6_1+PC*** is rather the consequence of the compensating effect of the fixed atomic positions vs. extra point charge layer, than the lack of strong electrostatic interactions, as was suggested in the previous section (4.5.1). If we compare the adsorption energies to the energy of the fully relaxed double layered system (***6x6_2***) with the one containing a frozen second layer (***6x6_2_f***), we get an energy difference around 20 kJ/mol, showing that fixing more atomic positions of the whole second layer weakens the adsorption, similar to the single layer results (Table 4.14). Considering more variations of fixed atomic positions by using the same systems mentioned in Table 4.6, supports the above stated observation that increasing the total number of fixed positions weakens the adsorption, while introducing an extra PC layer under the second explicit layer has a constant strengthening effect.

Visualising the electron density difference for the adsorbed complexes of the Sr^{2+} hydrate shows a significant electron donation from the oxygen atoms of the coordinated water molecules, which is expected to weaken the Sr^{2+}-surface polarisation compared to the single ion adsorption, since the positive charge of the Sr has been, to some extent, passivated. But if we look at the top views of the electron density distribution pictures in Figure 4.16, we can see that similar number of surface oxygen atoms are involved in the interaction compared to surface with a single Sr^{2+} ion. If we think about the value of the adsorption energy, which is between -1251 and 1263 kJ/mol in the case of the Sr^{2+} hydrate and approximately -890

kJ/mol for the single Sr^{2+}, the enhanced stability (more than 300 kJ/mol energy difference) is likely to come from some kind of water-surface or water-water interactions, which are not taken into account in the E_{ads} equation.

Table 4.14: Adsorption energies (E_{ads}) and relative adsorption energies (ΔE_{ads}) of the Sr^{2+} hydrate complex with different surface representations containing two explicit 6x6 layers in the QM cluster, fixed atomic positions and 0 or 1 PC layer. The relative energies are calculated by comparing the results to the energy of the complex on the fully relaxed *6x6_2* system without a PC layer. (All energies are calculated with the def2-SVP basis set.)

PC layers	E_{ads} (kJ/mol)	ΔE_{ads} (kJ/mol)
Fully relaxed system (*6x6_2*)		
0	-1263.3	0.0
1	-	-
Fixed down-facing H atoms in the 2^{nd} layer		
0	-1260.3	3.0
1	-1279.6	-16.4
Fixed 2^{nd} layer		
0	-1243.3	20.0
1	-1263.0	0.3
Fixed down-facing H atoms in the 1^{st} and 2^{nd} layers		
0	-1245.2	18.1
1	-1264.5	-1.2
Fixed 2^{nd} cluster and fixed down-facing H atoms in the 1^{st} layer		
0	-1231.8	31.4
1	-1251.3	11.9

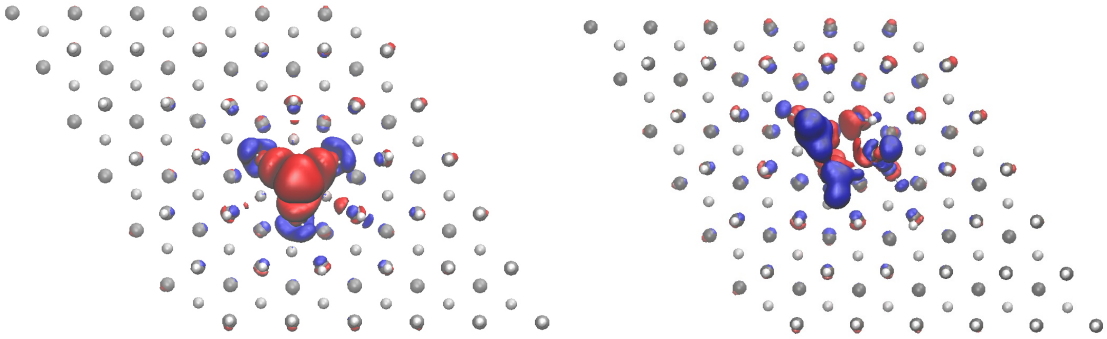

(a) top view of adsorbed Sr^{2+} **(b) top view of adsorbed $Sr(H_2O)_3^{2+}$**

Figure 4.16: Top view pictures of the electron density distribution of the adsorbed Sr^{2+} ion (a) as a single ion and (b) with three water molecules, on *6x6_1* surface. The isosurface value was chosen to be 0.0025 a.u. in all cases. The red regions are related to the electron depletion, while the blue regions to the electron accumulation. All atoms are presented in grey for simplicity.

Figure 4.17c with the surface model ***6x6_2*** reveals the top oxygen atoms in the second layer are also involved in the electron donation, in agreement with the previous results in Figure 4.12c, The fact that including an extra explicit layer strengthens the adsorption energy by -12.2 kJ/mol, leads us to conclude that, while simply fixing the down-facing hydrogen atoms and consider the second layer as PCs proved is not sufficient, modelling two explicit layer is necessary for the description of the adsorption mechanism, even if the second layer is fixed.

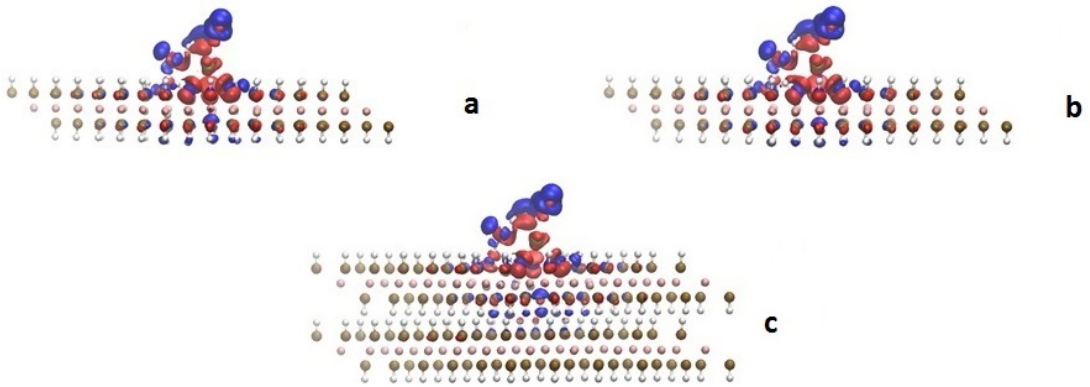

Figure 4.17: Electron density distribution of the adsorbed Sr^{2+} ion with three water molecules, on a single layer brucite (a), on a cluster with fixed bottom hydrogen atoms and one PC layer (b) and on a surface containing two explicit 6x6 clusters (c). The isosurface value was chosen to be 0.0025 in all cases. The red regions are related to the electron depletion, while the blue regions to the electron accumulation. The point charges are not represented on the pictures. (Mg=pink, O=ochre, H=white, Sr=yellow)

Based on the results presented in this section, we conclude that although the position of the adsorbed complex compared to the cluster boundaries matters, the arising energy difference is only a small portion of the absolute adsorption energy. Extending the studied surface representations with ***6x6_1_f*** and ***6x6_2_f***, showed that fixing atomic positions results in smaller interaction energies. Further investigation of second layer effect confirmed that minimum of one explicit layer is acceptable for the accurate description of the adsorption.

4.5.3 Substitution of Ca^{2+} and Sr^{2+} into brucite

Our next study was aimed to benchmark the PEECM results with periodic DFT methods (CRYSTAL code). We used a substitution reaction of heavier group II ions for Mg^{2+} in brucite (Ca^{2+}, Sr^{2+}). Besides comparing the reaction energies calculated with our PEECM model, we study the effect of smaller/larger unit cells and the number of brucite layers on the adsorption energy too. The substitution energies were calculated with both the PEECM model and periodic DFT, using the same functional (PBE) and basis sets (section 4.4.2) with the two different codes. We optimised structures with one (***6x6_1***) and two (***6x6_2***) layers included in

the QM cluster for the PEECM model, excluding the ***6x6_1+PC*** surface representation which is not easily comparable with periodic DFT. We substituted each ion into the same position in the upper layer to avoid the possible effect of different relative positions related to the cluster boundaries. We considered four different supercell sizes with 1, 2 and 3 layers of brucite within the periodic DFT model. The following equation was used to calculate the substitution energy:

$$E_{sub} = \left(E_{brucite-M} + E_{Mg^{2+}}\right) - \left(E_{brucite-Mg} + E_{M^{2+}}\right) \tag{4.5}$$

$E_{brucite-M}$ is the computed SCF energy of the optimised substituted structure, $E_{brucite-Mg}$ is the energy of the perfect brucite slab with the same surface representation as $E_{brucite-M}$, while $E_{Mg^{2+}}$ and $E_{M^{2+}}$ are the single point energies of the isolated ions. The substitution energies are summarised in Table 4.15.

Both models yield the expected order based on the size of the ionic radii (72 pm (Mg^{2+}) $<$ 95 pm (Ca^{2+}) $<$ 118 pm (Sr^{2+})), i.e. the substitution of Ca^{2+} is less unfavoured than that for Sr^{2+}. If we compare the energies obtained with the largest (***9x9***) cell size in the periodic DFT calculations to the results of the isolated PEECM model, the two methods give reasonably similar results. Although the difference between them is not constant for the two ions, it is always less than c. 6% of the substitution energies. Including a 2^{nd} layer of brucite in the surface model has only a slight effect on the substitution energy, which is interesting given that the substitution distorts the surface geometry much more than an adsorption reaction. The 2^{nd} layer results in only a 2-6 kJ/mol difference in energy for each ion, irrespective of the method used.

Table 4.15: Substitution energies (E_{sub}) calculated with periodic DFT (PBC) and with the PEECM, including 1 or 2 explicit layers of brucite in the model. The energy differences between the two models are represented in percentages (E_{diff}) relative to the periodic DFT values

Surface models		Substitution energies			
Method	layer	Ca^{2+}		Sr^{2+}	
		E_{sub}(kJ/mol)	E_{diff}(%)	E_{sub}(kJ/mol)	E_{diff}(%)
PBC	***9x9_1***	446.8		571.5	
PEECM	***6x6_1***	456.1	2.1	598.2	4.7
PBC	***9x9_2***	441.0		567.2	
PEECM	***6x6_2***	453.4	2.8	601.9	6.1

The substitution energies as a function of cell size for different number of layers are plotted in Figure 4.18 and summarised in Table 4.16. With the use of bigger cell sizes in the periodic

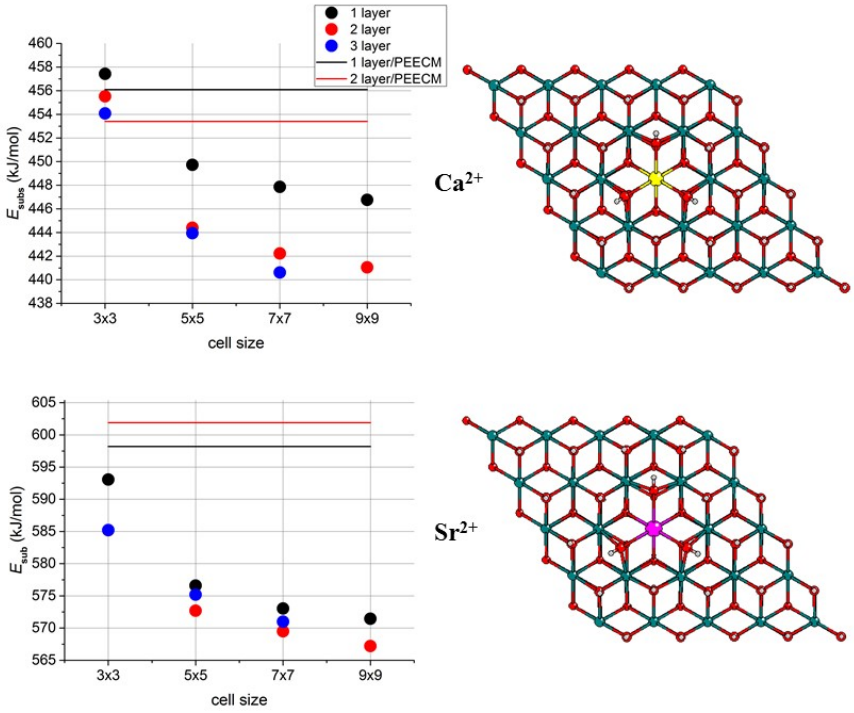

Figure 4.18: Periodic DFT-calculated substitution energies as a function of cell size for systems containing 1, 2 or 3 brucite layers for Ca^{2+} and Sr^{2+}. Energies calculated for isolated systems in the PEECM method are represented with horizontal lines. Images are the optimised structures of substituted Ca^{2+} (yellow) and Sr^{2+} (magenta) into a *5x5_2* brucite cell. (Mg=green, O=red, H=grey). Note that the gradient of the *7x7_3* system did not fully converge (the max gradient was 0.000501 while the convergence criterion is 0.000450), although the energy did.

DFT model the substitution energy converges, presumably towards the energy of a completely isolated interaction site. However, with cell sizes bigger than ***3x3*** the differences are small, 3-5 kJ/mol for each case, i.e. the effect of the substituted ion on the crystal structure is so localised that the ions are close to being isolated even with a ***5x5*** supercell. Adding a 2^{nd} layer lowers the energy by 4-6 kJ/mol and including a 3^{rd} layer has an even smaller effect on the energies.

Table 4.16: Periodic DFT-calculated substitution energies (E_{sub}) as a function of cell size for Ca^{2+} and Sr^{2+}, considering 1,2 and 3 number of brucite layers in the slab. (^{a}Note that the gradient of the *7x7_3* system did not fully converge (the max gradient was 0.000501 while the convergence criterion is 0.000450), although the energy did.)

E_{sub} (kJ/mol)									
layer	Ca^{2+}				layer	Sr^{2+}			
	3x3	***5x5***	***7x7***	***9x9***		***3x3***	***5x5***	***7x7***	***9x9***
_1	457.4	449.7	447.9	446.8	***_1***	593.1	576.6	573.0	571.5
_2	455.5	444.4	442.2	441.0	***_2***	585.2	572.7	569.5	567.2
_3	454.1	443.9	440.6	-	***_3***	585.2	575.2	571.0^a	-

This study of Ca^{2+} and Sr^{2+} substitution within a periodic DFT model suggests that moving from two- to three-layer slabs has little effect on substitution energies. This provides indirect evidence that the ***6x6_2*** QM cluster in the PEECM model includes all the necessary interactions and there is no need to increase the cluster size or the number of brucite layers in the QM region.

4.5.4 Adsorption of Sr[$(OH)_2(H_2O)_4$] on brucite

The ultimate aim of this project is to understand the interactions between hydrated brucite surfaces and solvated, fission generated strontium. This study will involve many differently coordinated complexes and will use their relative energies to identify the most stable among them. Here we describe a first step towards this aim, i.e. an investigation of adsorbed $Sr(OH)_2$ complexes, surrounded by their first coordination shell. [$Sr(OH)_2(H_2O)_4$] was chosen based on the most stable Sr^{2+} dihydroxide coordination with two solvation shells from the previous chapter (Table 3.8). We searched for the most stable structure of [$Sr(OH)_2(H_2O)_4$] adsorbed on brucite by placing it above the surface, and by generating three more initial structures via random rotation of the original molecule. We optimised the geometries in CRYSTAL, representing the brucite surface by a single layer ***5x5*** supercell slab (Figure 4.19). These optimised geometries were then used as starting structures in our TURBOMOLE simulations, where they were reoptimised with the PEECM model, placing each complex at the same initial position relative to the QM cluster.

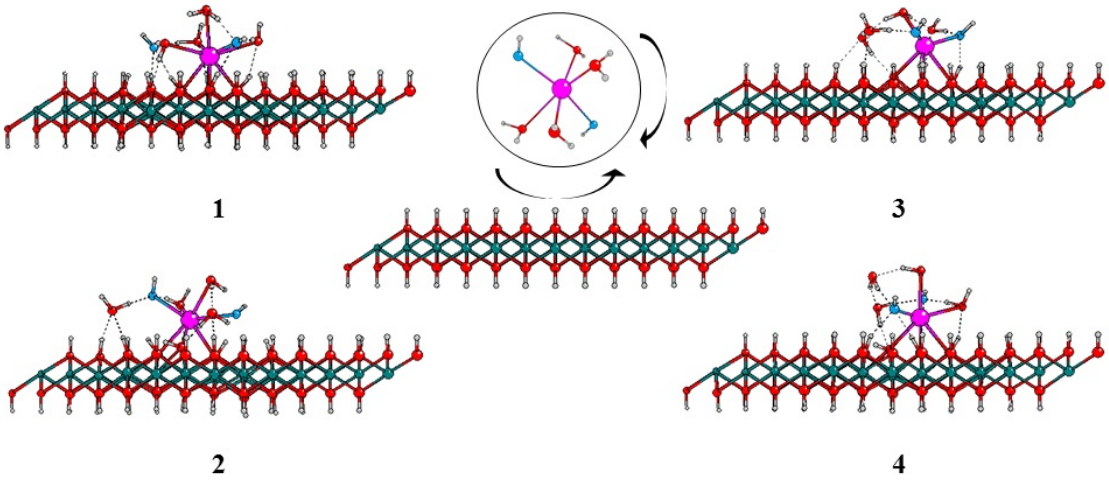

Figure 4.19: ***Middle*****:The ball and stick representation of the** ***5x5_1*** **supercell and the original $Sr(OH)_2$ complex with its complete first coordination shell.** ***Side*****:1,2,3,4 are the optimised structures of the adsorbed complexes with periodic DFT. (Mg=green, O=red, H=grey, Sr=magenta, O in the coordinated OH groups=blue)**

We used an equation analogous to Eq. (4.2) in section 4.5.1 to calculate the adsorption energies, replacing the single point energy of a single ion with that of the solvated complex (first coordination shell, gas phase). The first part of Table 4.17 contains the obtained absolute energies for both methods, considering single-, double- and fixed double-layered surface models with either ***5x5*** or ***6x6*** unit cell sizes. There is excellent agreement between the absolute adsorption energies obtained from the two methods: the energy difference is between 1.6 and 3.6% in each case with a single layer surface representation and 0.2-4.0% for two-layered surface models. Structure **3** is predicted to be the most stable and in the second part of Table 4.17 the relative adsorption energies (ΔE_{ads}) are obtained by comparing the energies of the other structures to that of structure **3**. The differences between the calculated relative energies are less than 2 kJ/mol using periodic DFT (***5x5*** cell size) and the PEECM model for the single layer surface representation, with the exception of structure **4**, where the geometry of the optimised complexes differs between the two methods, therefore there is a more significant energy difference (8 kJ/mol).

Table 4.17: Absolute (E_{ads}) and relative adsorption energies (ΔE_{ads}) of four Sr[$(OH)_2(H_2O)_4$] complexes, calculated by comparing each system to the most stable structure. Counterpoise corrected energy values are presented in brackets (BSSE).

E_{ads} (kJ/mol)													
structure		**1**			**2**			**3**			**4**		
coordination		**CN=8**			**CN=7-8**			**CN=6**			**CN=7-8**		
Method	**layer**	**E**	**(BSSE)**	E_{diff}	**E**	**(BSSE)**	E_{diff}	**E**	**(BSSE)**	E_{diff}	**E**	**(BSSE)**	E_{diff}
PBC	**5x5_1**	-431.7			-402.3			-444.4			-416.1		
PEECM	**6x6_1**	-422.7	(-366.7)	2.1%	-393.8	(-332.7)	2.1%	-437.2	(-380.2)	1.6%	-401.1	(-349.2)	3.6%
PBC	**5x5_2**	-428.4			-403.2			-438.6			-419.9		
PEECM	**6x6_2**	-424.6	(-371.2)	0.9	-391.8	(-332.4)	2.8	-439.6	(-384.3)	0.2	-403.3	(-353.0)	4.0
PBC	**5x5_2_f**	-430.1			-401.1			-435.9			-422.5		
PEECM	**6x6_2_f**	-411.3	(-358.2)	4.4	-379.9	(-320.8)	5.3	-428.0	(-372.9)	1.8	-391.4	(-341.1)	7.4
ΔE_{ads} (kJ/mol)													
Method	**layer**	**E**	**(BSSE)**		**E**	**(BSSE)**		**E**	**(BSSE)**		**E**	**(BSSE)**	
PBC	**5x5_1**	12.7			42.1			0.0			28.2		
PEECM	**6x6_1**	14.5	(13.5)		43.4	(47.5)		0.0	(0.0)		36.1	(30.9)	
PBC	**5x5_2**	10.2			35.4			0.0			18.7		
PEECM	**6x6_2**	14.9	(13.2)		(47.8	(51.9)		0.0	(0.0)		36.2	(31.3)	
PEECM	**6x6_2_f**	16.7	(14.7)		48.1	(52.1)		0.0	(0.0)		36.6	(31.8)	

BSSE was considered and the counterpoise corrected values are presented in brackets in Table 4.17 BSSE significantly decreases the absolute adsorption energies (by c. 55-60 kJ/mol), but the relative energies are only slightly different from the uncorrected ones; this type of error largely cancels in the definition of the relative adsorption energy.[v]

[v]We did not calculate the BSSE in CRYSTAL since it largely depends on the geometry and the basis functions employed, both of which are almost the same in the two methods. Hence we expect the BSSE to be very similar

When we consider a two-layer model in the PEECM via a second ***6x6*** cluster under the first (***6x6_2***), the relative adsorption energies are found to be very similar to the single layer results (***6x6_1***). Comparing ΔE_{ads} for ***5x5_1*** and ***5x5_2*** surface models, there are differences in relative adsorption energies due to minor structural differences affecting only water molecules which are not directly coordinated to the Sr^{2+} ion, but there is no change in terms of either energetic trends or coordination numbers.

Freezing layers beneath the surface in a slab structure, besides improving the cost efficiency of the calculations, is a common approach to mimic the behaviour of the bulk underneath the top layer(s).[57] Although the biggest systems considered in this study contain only two-layered slabs, we calculated adsorption energies for surface representations in which the atomic positions in the second brucite layer are fixed to study their possible effects on the adsorption: ***6x6_2_f*** was already introduced in section 4.4.1, while ***5x5_2_f*** was calculated by freezing the coordinates of the second layer in the original ***5x5_2*** cell before its optimisation. Turning to the periodic DFT results first, the adsorption energies for ***5x5_2_f*** are within $\pm$2 kJ/mol of to the ***5x5_2*** results, i.e. fixing the atomic positions has no significant effect on the structures. In the case of the ***6x6_2_f*** PEECM model, E_{ads} is $\sim$12 kJ/mol higher than the adsorption energies of ***6x6_2***. Since comparing the optimised geometries did not reveal changes in the adsorbed structures, we surmise that this constant energy shift is probably due to the fact that, in addition to using constraints within the QM cluster, we used the experimental crystal parameters for the PEECM surface, while the crystal parameters, therefore the original atomic positions too, were previously optimised for the bulk mineral structure in periodic DFT. But despite the less accurate crystal structure description in the embedded methods, ΔE_{ads} values are not affected by changes in the second layer, as shown in Table 4.17: energies for ***6x6_2_f*** are very close to the ***6x6_1*** and ***6x6_2*** results.

Changing the cell size for the most stable structure (**3**) has very small effect on the adsorption energies: comparing the ***5x5_1*** result to the biggest cell size, ***9x9_2***, gives an energy difference of 3.4 kJ/mol. Although we did not consider every cell size for the less stable structures, the results in Table 4.18 show that increasing the cell size up to ***7x7*** and ***9x9*** in periodic DFT causes a less than 7 kJ/mol energy difference in the absolute adsorption energies for structure **1**,**2** and **4**. Although the values of the relative adsorption energy change more with bigger cell sizes compared with the excellent agreement showed for the ***5x5*** and ***6x6*** compar-

in the two models. Besides, the relative adsorption energies, in which we are primarily interested, are largely unaffected by this type of error.

ison in Table 4.17, the energetic trend is not affected (see Table 4.19), which suggests that the ***5x5*** cell size is reasonable for periodic DFT and indirectly shows that the ***6x6*** cluster size used in the PEECM contains all the atoms in the QM region which play a part in the adsorption.

Table 4.18: Periodic DFT-calculated adsorption energies (E_{ads}) as a function of cell size for structure 1-4. A full cell size study was performed for the most stable structure (3) and cell sizes of *7x7_1*, *7x7_2* and *9x9_1* were calculated for the less stable structures. (^{a}Note that the total energy of structure 2 with *7x7_2* cell size converged to 10^{-5} a.u.)

	E_{ads} (kJ/mol)											
	1			**2**			**3**			**4**		
	5x5	***7x7***	***9x9***	***5x5***	***7x7***	***9x9***	***5x5***	***7x7***	***9x9***	***5x5***	***7x7***	***9x9***
_1	-431.7	-434.1	-435.1	-402.3	-406.8	-408.9	-444.4	-443.5	-444.2	-416.1	-422.0	-418.7
_2	-428.4	-431.4	-	-403.2	-406.0^a	-	-438.6	-441.0	-441.0	-419.9	-414.4	-
_3	-	-	-	-	-	-	-439.1	-441.0	-	-	-	-
_2_f	-430.1	-	-	-401.1	-	-	-435.9	-	-	-422.5	-	-

Table 4.19: Periodic DFT-calculated relative adsorption energies ($\triangle E_{ads}$) of four [Sr(OH)$_2$(H$_2$O)$_4$] complexes, calculated by comparing each system to the most stable structure (3) with different cell sizes (^{a}Note that the total energy of structure 2 with *7x7_2* cell size converged to 10^{-5} a.u.)

$\triangle E_{ads}$ (kJ/mol)				
Cell	**1**	**2**	**3**	**4**
5x5_1	12.7	42.1	0.0	28.2
5x5_2	10.2	35.4	0.0	18.7
7x7_1	9.4	36.7	0.0	21.5
7x7_2	9.6	35.0^a	0.0	26.6
9x9_1	9.2	35.3	0.0	25.5

Overall, this study suggests that including a relaxed or fixed 2nd layer in the surface model has only minor effects on the relatively weak adsorptions of the hydrated complexes. While there are some small differences in relative adsorption energies, the energetic trends within structures **1**-**4** and the geometries of the coordinated Sr^{2+} complexes do not change. Results obtained from periodic DFT and PEECM predict similar structures and have the same energetic trends.

Assesment of local coordination *via* the QTAIM

In order to probe further the comparison between the periodic DFT and the PEECM generated structures, we explored the coordination environment around the Sr^{2+} ion by examining the Sr-O distances and by calculating QTAIM bond critical point (BCP) electron densities for the Sr-O interactions (Table 4.20). The QTAIM is a well-known theory which uses the topology of the electron density to analyse atomic properties in molecules or complexes (see section 2.7.3.1).[118, 119] Bond critical points are stationary points in the electron density distribution

where the minimum along the path of maximum electron density between two nuclei is found at the interatomic surface. The electron density at the BCPs is often related to the strength of the interaction,[121, 126] with higher values indicating stronger bonds.

The final structures obtained with the two different methods are found to be generally very similar by topological analysis. The coordination environment of the Sr is almost the same in complexes **1** and **3**, although there is a slight difference in structure **2**, in which the $H_2O(3)$ water molecule (see structure **2** in Figure 4.20) is predicted to be very weakly coordinated to the Sr in the PEECM (ρ = 0.0153 a.u.), while there is not even a weak interaction between the Sr and that water molecule in the periodic DFT model. Defining coordination to be the presence of a Sr-O BCP, we conclude that the overall coordination number (CN) in complex **2** is 8 with PEECM and 7 with periodic DFT. The difference in the geometry of structure **4** is more significant (Figure 4.20); due to the different orientation of the $H_2O(3)$ water molecule in the embedded model, it is weakly coordinated to the Sr (d = 2.941 Å, ρ = 0.0137 a.u.) and it also modifies the strength of the other coordinated ligands, e.g. OH(5) has a shorter Sr-O distance (2.865 Å) and higher electron density at the BCP (0.0133 a.u.) in the PEECM geometry than in the final structure of periodic DFT (3.072 Å, 0.0083 a.u.).

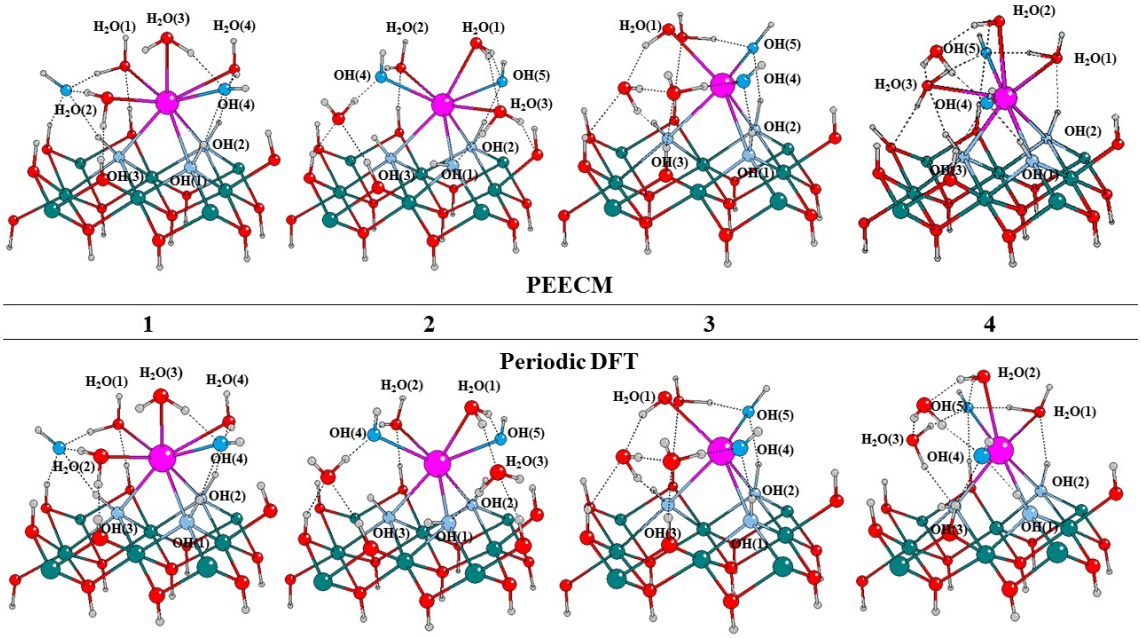

Figure 4.20: The optimised geometries of structures 1-4 in PEECM or periodic DFT. The coordinated H_2O molecules and OH groups are labelled according to Table 4.20. (Mg=green, O=red, H=grey, Sr^{2+}=magenta, O in the coordinated OH^- ion=dark blue, O in the coordinated OH groups of the surface=light blue)

Previous studies predict a generally good correlation between BCP electron densities and related bond lengths[121, 123, 251] and indeed, plotting the electron densities at the BCPs against the Sr-O distances (Table 4.21) reveals a strong correlation between the two properties (calculated R^2 values for the linear regression are summarised in Table 4.20) and also illustrate the similarity in coordination between analogous structures calculated with PEECM and periodic DFT.

Table 4.20: Sr-O distances (d) and electron densities at the bond critical points (ρ) for each coordinated OH group or H_2O molecule calculated with QTAIM for the optimised structures in PEECM or periodic DFT (PBC). R^2 is the coefficient of determination for the linear regression between d and ρ and CN is the total coordination number. For structures and Sr-O labels see Figure 4.20. (^{a}In structure 1, there is a fourth water coordinated to the Sr instead of a fifth OH group.)

	1				**2**			
	PEECM		**PBC**		**PEECM**		**PBC**	
Sr-O	**d (Å)**	**ρ (a.u.)**	**d (Å)**	**ρ (a.u.)**	**d (Å)**	**ρ (a.u.)**	**d (Å)**	**ρ (a.u.)**
Sr-OH(1)	2.710	0.0230	2.698	0.0234	2.630	0.0276	2.612	0.0285
Sr-OH(2)	2.572	0.0314	2.566	0.0318	2.562	0.0315	2.582	0.0306
Sr-OH(3)	2.564	0.0322	2.555	0.0327	2.760	0.0213	2.672	0.0252
Sr-OH(4)	2.553	0.0278	2.597	0.0253	2.481	0.0378	2.512	0.0365
Sr-OH(5)^a	2.724	0.0217	2.783	0.0192	2.574	0.0294	2.579	0.0304
Sr-H_2O(1)	2.562	0.0311	2.583	0.0297	2.648	0.0274	2.642	0.0278
Sr-H_2O(2)	2.624	0.0284	2.644	0.0270	2.746	0.0202	2.793	0.0181
Sr-H_2O(3)	2.672	0.0255	2.695	0.0244	2.871	0.0153	3.331	-
R^2	**0.818**		**0.853**		**0.973**		**0.982**	
complex	**$[Sr(OH)_4(H_2O)_4]^{2+}$**				**$[Sr(OH)_5(H_2O)_3]^{3+}$**		**$[Sr(OH)_5(H_2O)_2]^{3+}$**	
CN	**8**				**8**		**7**	
	3				**4**			
	PEECM		**PBC**		**PEECM**		**PBC**	
	d (Å)	**ρ (a.u.)**	**d (Å)**	**ρ (a.u.)**	**d (Å)**	**ρ (a.u.)**	**d (Å)**	**ρ (a.u.)**
Sr-OH(1)	2.680	0.0247	2.700	0.0236	2.685	0.0243	2.751	0.0210
Sr-OH(2)	2.629	0.0275	2.623	0.0277	2.602	0.0296	2.579	0.0310
Sr-OH(3)	2.595	0.0299	2.577	0.0309	2.567	0.0315	2.519	0.0355
Sr-OH(4)	2.422	0.0407	2.438	0.0399	2.427	0.0406	2.422	0.0419
Sr-OH(5)^a	2.470	0.0375	2.495	0.0361	2.865	0.0133	3.072	0.0083
Sr-H_2O(1)	2.548	0.0336	2.574	0.0317	2.761	0.0205	2.853	0.0170
Sr-H_2O(2)	-	-	-	-	2.644	0.0278	2.595	0.0309
Sr-H_2O(3)	-	-	-	-	2.941	0.0137	3.166	-
R^2	**0.995**		**0.996**		**0.974**		**0.981**	
complex	**$[Sr(OH)_5(H_2O)]^{3+}$**				**$[Sr(OH)_5(H_2O)_3]^{3+}$**		**$[Sr(OH)_5(H_2O)_2]^{3+}$**	
CN	**6**				**8**		**7**	

Table 4.21: Electron densities at the Sr-O BCPs plotted against Sr-O distances for the four Sr[$(OH)_2(H_2O)_4$] complexes optimised with PEECM or periodic DFT (PBC). Red squares are related to the Sr-O(OH) interactions in the solvation shell, crossed squares to the Sr-O(H_2O) interactions in the solvation shell and black squares to the Sr-O(surface) interactions with the surface OH groups.

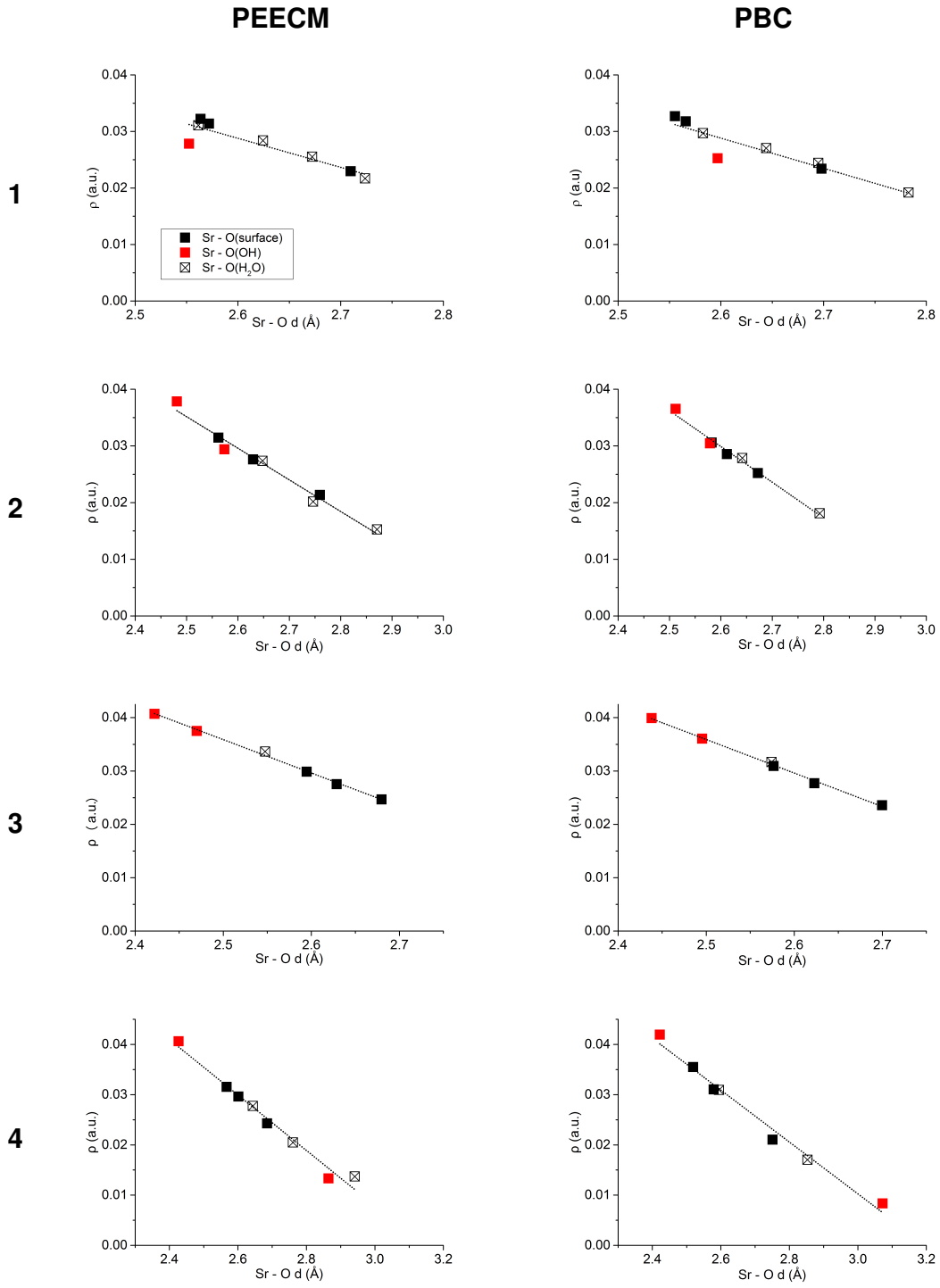

There are three types of Sr-O interactions, based on the type of the coordinating oxygen atom: O of the OH^- ions in the solvation shell, surface OH groups (referred as O(OH) and

O(surface) in the following text) and H_2O molecules in the solvation shell (O(H_2O)). The ones expected to have the strongest interaction with the Sr^{2+} ion are the OH^- ions in the solvation shell. However, this is not always the case, in fact, in structure **1** the only OH^- ion directly coordinating to the Sr is slightly outstanding from the trend, resulting in an R^2 value of 0.818 (0.853) with PEECM (periodic DFT). The O(OH) in this case has a weaker interaction according to the QTAIM analysis than the Sr-O distance would suggest, but the reason for this behaviour is unknown. Furthermore, in structure **4**, there is a very weakly coordinated O(OH) in the complex (OH(5)), as opposed to the other OH ion, OH(4), which has the strongest coordination to the Sr ion. In structure **3**, which is predicted to be the most stable, the OH^- ions in the solvation shell have the strongest interaction, followed by the only coordinated water molecule and then the surface OH groups which exhibit the weakest interaction.

4.6 Conclusions

The (0001) brucite surface is one of the most common solid surfaces existing in the nuclear sludge. To efficiently study its possible interaction with the Sr^{2+} ion we were aiming for a surface model which has a moderate computational cost and is compatible with the solvated complexes described in the previous chapter. We therefore used the PEECM implemented in the TURBOMOLE code, which makes this study the first time to model a layered, not purely ionic surface (brucite (0001) with this method. After the careful development of the PEECM model, it has been tested in studies related to our final goal, studying the adsorption of radioactive ions on hydrated brucite surfaces.

The PEECM is capable of describing the adsorption of single s block ions onto brucite, although the basis set quality has to be carefully considered. At least triple-zeta quality is necessary to obtain the correct energetic ordering between the ions, but these larger basis functions must be avoided in the QM representation of the surface cluster, since they can cause artificial interactions between the boundary atoms and the point charge region.

Combining the results of the s block ion adsorption with the short study of a Sr^{2+} hydrate showed that the calculated adsorption energies slightly depend on the position of the adsorption site relative to the cluster boundaries and the type of the surface model used. Fixing more atomic positions always lowers the interaction energy, while introducing a PC layer underneath the cluster increases the attraction. The two effects combined, results in slightly more favourable adsorption (***6x6_1+PC***). Embedding a second layer in the QM cluster also predicts the adsorption of ions and complexes more favourable (***6x6_2***) than results in

a single layer. Electron density difference plots suggest that atoms in the second layer are also involved in the interaction and therefore including the second layer explicitly is preferred instead the addition of a PC layer.

Through a comparison with periodic DFT, we have demonstrated that the PEECM sufficiently reflects the qualities of the brucite surface to be able to describe both the substitution of Ca^{2+} or Sr^{2+} into brucite and the surface complexation of [$Sr(OH)_2(H_2O)_4$]. Based on the cell size studies and the interaction energies obtained with multiple layers of brucite, the size of the quantum chemically treated cluster is found to be reasonable in all cases. The agreement between adsorption energies and the optimised geometries obtained with PEECM or periodic DFT is excellent in the case of the adsorption of [$Sr(OH)_2(H_2O)_4$] complexes.

These results give us confidence to step forward and use the embedded brucite (0001) model in future investigations of Sr^{2+} complex ion adsorptions on hydrated surfaces. They demonstrate that the PEECM is capable of describing sorption mechanisms on brucite-like surfaces, and that the approach is a viable alternative to periodic DFT when ionic species are involved in surface interactions. Furthermore, we note that there is a significant difference in computational speed between the two methods: if we consider structure **1** in section 4.5.4 as a test system, one optimisation step with a ***5x5_1*** cell in periodic DFT took an average 15 minutes using 192 cores; while the same structure on a ***6x6_1*** cluster did an average 1 optimisation step in 15 minutes using 10 cores with the PEECM. The embedded cluster calculations presented here were run largely on our local departmental compute server, with a modest number of cores per calculation, by contrast to the periodic DFT calculations, which required the massively parallel version of the CRYSTAL code and were run on the UK's national supercomputing facility. This difference in computational requirements makes the application of PEECM especially relevant in case of industry related problems.

Moving on to more realistic models of the hydrated surface, we extended our PEECM study to include many more water molecules in the QM region, allowing to probe effects of second shell water molecules on the adsorption. The results of this study are presented in the following chapter.

Chapter 5

Studying the interaction between solvated Sr^{2+} and the hydrated (0001) brucite surface

5.1 Introduction

This chapter presents the results of our investigation on possible strontium uptake by the corroded Magnox cladding. In this study, we investigate the water/solid interface on an atomic scale, by including the first two water layers explicitly along with the brucite surface in a periodic embedded cluster model. This method allows us to consider the effect of crystal structure, electronic properties and water coordination, along with the ionic charge, on the interactions between Sr^{2+} and the surface. We use a theoretical equation based on the results of previous solvation studies to calculate adsorption energies as realistically as possible. We also include the effect of bulk solvent by using the COSMO implicit solvent model on the bulk solvated structures, as well as evaluate a COSMO correction term on the adsorbed complexes.

5.2 Literature review

The first part of this literature review revisits the basic concepts of sorption mechanisms on liquid/solid interfaces (5.2.1), while the second part concentrates on the behaviour of brucite in aqueous environments: section 5.2.2 summarises the published results on the formation of hydrated $Mg(OH)_2$ surfaces, either through the hydroxylisation of MgO or directly from brucite, and section 5.2.3 contains examples of molecular or ionic adsorption studies on the brucite (0001) surface, with special emphasis on the adsorption of strontium.

5.2.1 Sorption processes at water/solid interfaces

It is well-known that in the near-surface region, both phases (liquid and solid) behave differently compared to their structural and dynamic behaviour in the bulk. Properties such as water coordination or surface reactivity and functionality, can potentially be affected in the interfacial region. Therefore, it is important to study water sorption to be able to describe other surface related reactions, such as adsorption of other molecules or ions, substitution, nucleation or crystal growth on the surface and catalytic reactivity.[252]

Depending on the type of interaction, water can physisorb or chemisorb on a surface. In the first case, there are non-specific, weak interactions between the two phases, which allow the spontaneous formation of multilayers of water on the surface without disturbing its structure. In the second case, the interactions involve electron sharing or electronic charge transfer between the phases, eventually leading to water dissociation, but after passing over an activation barrier. Chemisorption is energetically more stable and generally results in a monolayer interface with chemically modified surface properties.[253] One example of the two different processes is shown in the computational study of Corno *et al.*, carried out on the hydration of hydroxyapatite ($Ca_5(PO_4)_3OH$ phosphate mineral). The (001) surface of this material physisorbs water molecules with a binding energy of $\sim$80 kJ/mol, while its (010) surface chemisorbs water molecules, resulting in the dissociation of the water molecules and the formation of a new surface termination, with an energy around 250-320 kJ/mol. The resulting modified monolayer continues to adsorb water molecules similarly to the (001) surface.[254]

After the formation of the liquid/solid interface, the following solvated ion-related sorption processes can happen: ion adsorption and ion exchange. The first phenomenon is an increase in the ion concentration at the interface due to the operation of surface forces,[255] while the latter is the adsorption of one or several ionic species, accompanied with a simultaneous desorption or displacement of an equivalent amount of one or more other ionic species (see Figure 5.1).[256] A general requirement of substitution is that the atomic radius of the substituting ion has to be smaller (or equivalent) to that of the original ion in the crystal structure. For instance, Andersson, Sakuma and Stipp studied the possibility to substitute strontium, nickel, cadmium or lead into calcite with periodic DFT calculations, and found that the substitution of Sr^{2+}, which has a bigger ionic radius than Ca^{2+}, is unfavoured, while the other, smaller ions substitute exothermically into the surface.[257]

Naturally, any interface-related process is the function of many factors: e.g. temperature and pressure, and solvent properties such as pH or concentration of competitor ions in the solution. Furthermore, surface properties, for example crystal structure, morphology, surface area and porosity; or adsorbent properties, such as ionic strength, ionic/particle size, solubility, concentration etc.; are all crucial influencing factors in ionic sorption processes. Since differentiating between ion uptake due to adsorption or substitution, not to mention possible precipitation of crystallisation on the surface, is difficult with macroscopic techniques, experimental studies in general report adsorption isotherms and the sorption capacity of surfaces for certain ions, collectively considering every sorption processes.

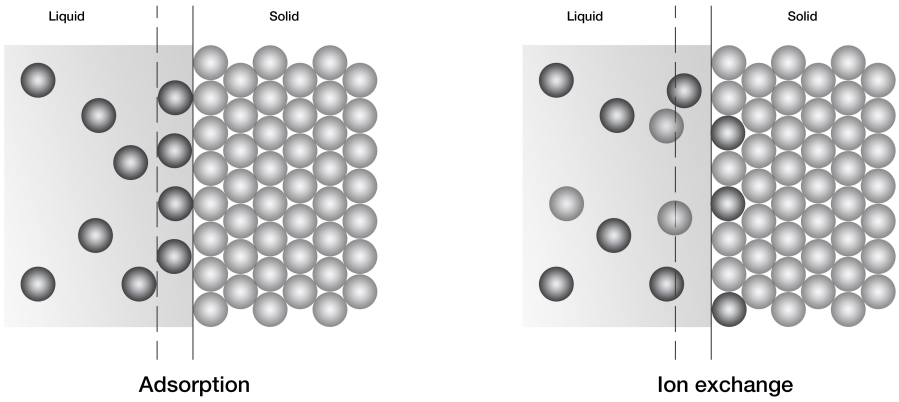

Figure 5.1: Schematic representation of adsorption and ion substitution at liquid/solid interfaces

5.2.2 Hydration of MgO and $Mg(OH)_2$ surfaces

The behaviour of interfacial water on MgO (periclase) and $Mg(OH)_2$ (brucite) surfaces has been extensively studied with both experimental[258–268] and theoretical methods[261, 269–280]. Magnesium-oxide is important for this study, because brucite is the most common alteration product[i] of periclase in nature.[281] Although the (001) surface of MgO is known to be the most stable and the hydroxylation of a perfect (001) surface is predicted to be unfavoured,[272–274] experimental results show that, MgO is generally highly defective[262–264, 269] and there are hydroxyl groups on its surface in aqueous media.[258–260] The water chemisorbs on the low-coordinated defect sites,[269, 274, 276] such as the 4-fold-coordinated edges[275] or 3-fold-coordinated corners, and forms OH surface groups, eventually turning the surface to (0001) brucite.[261, 265]

In fact, Refson *et al.*[275] computationally showed that, instead of the (001) MgO surface, the otherwise metastable (111) phase is the most stable in aqueous solution, which can easily be hydroxylated and transformed to (0001) brucite (see Figure 5.2). When the possible adsorption sites at the MgO surfaces are fully protonated, additional water starts to physisorb on the (0001) surface of the $Mg(OH)_2$.

Depending on the surrounding conditions, the formation of $Mg(OH)_2$ from periclase can be reversible; with water removal, brucite decomposes via a dehydroxylation process: $Mg(OH)_2 \longrightarrow MgO + H_2O$.[282] Early experimental studies of water vapour adsorption on brucite under vacuum, show that during the hydration-dehydration cycles the surface ages quickly, i.e. it decomposes to MgO with the removal of the water molecules.[266, 267, 282] However,

[i] Mineral alteration refers to natural chemical or mineralogical processes which change the chemical composition of the mineral.

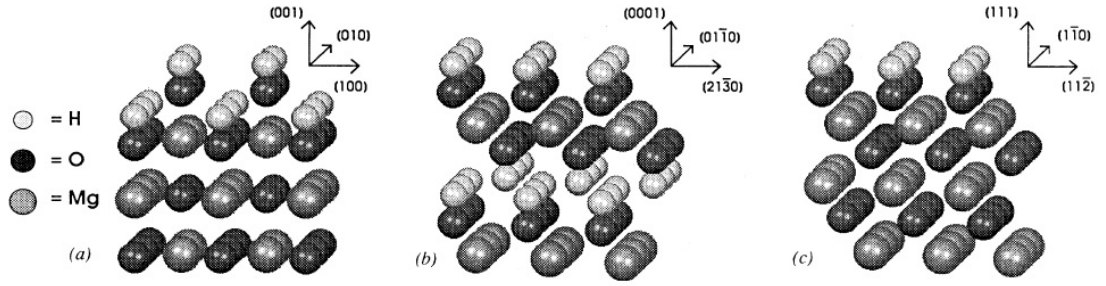

Figure 5.2: Side view of the (a) hypothetical hydroxylated (001) surface of MgO, (b) (0001) surface of $Mg(OH)_2$ and (c) hydroxylated (111) surface of MgO [275]

the equilibrium of this reaction is strongly related to the vapor pressure and under ambient conditions the dehydroxylation is unlikely to happen (the reaction starts at 275℃ under 1 bar).[283, 284] *Ab initio* studies on the decomposition of $Mg(OH)_2$ were carried out to identify the most reactive surface sites for the reaction[229, 230] and by comparing the dehydroxylation energies at the different brucite surfaces, they suggest that the reaction starts at $(1\bar{1}00)$ surface.[230]

The behaviour of brucite under ambient conditions in aqueous phase, depending on the pH conditions, the surface can be protonated or deprotontated which also affects the dissolution rate of the mineral. According to electrophoretic measurements[285] and the experimental work of Pokrovsky *et al.*[268], the isoelectric point (pH_{IEP}) of brucite is close to pH 11; and the net surface charge is positive under this point and negative above it (see Figure 5.3).

By investigating the surface speciation of brucite at different pH, Pokrovsky and Schott found that the dominant species below pH 8 are $>MgOH_2^+$,[ii] formed by the protonation of the OH surface groups, while the concentration of the deprotonated $>MgO^-$ species becomes significant only above pH 12, although the neutral $>MgOH^0$ species are still favoured, see Figure 5.3. The increased concentration of protonated species with decreasing pH, results in an increase in the dissolution rate of the mineral, suggesting that the protonation of the surface OH group helps to initiate the dissociation reaction.[268, 286]

Although protonation/deprotonation reactions can occur on the surface, force field based molecular dynamic studies[277–280] have to assume conditions near to the zero point of net proton charge, because simulating bond breaking or bond formation is not possible with this method.[279] Despite the lack of possible protonation, classical MD calculations still provide crucial information about the effect of the vicinity of the surface on the behaviour of interfacial

[ii]The notation ">" refers to the fact that the following chemical formula ($MgOH_2^+$) describes a surface specimen, i.e. it is related to one Mg-OH group.

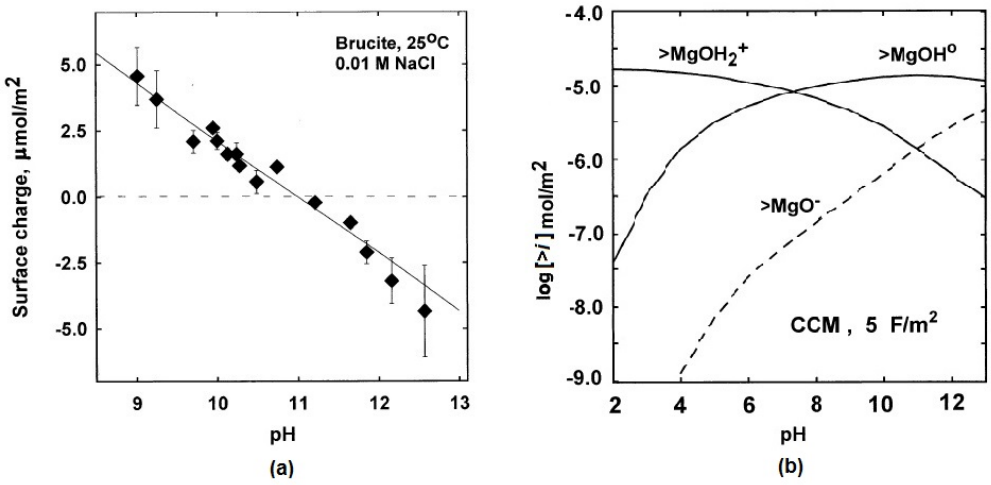

Figure 5.3: (a)The pH dependence of the net surface charge of brucite determined by acid/base titration and (b) the estimated concentration of the dominant surface species at different pH calculated with the Surface Complexation Model by Pokrovsky and Schott[268]

water molecules. Simulations predict that the surface of $Mg(OH)_2$ attracts water molecules and affects their coordination and hydrogen-bond organisation near the surface.[279]

Sakuma and his coworkers published two interesting papers on the molecular dynamics simulation of water adsorption on brucite, in which they constructed *ab initio* model potentials for the water-surface interaction by calculating potential curves for a single water molecule and five-member water cluster and studied the local behaviour of water molecules close to the surface.[277, 278] They embedded a thin water film between two brucite surfaces and divided the film into 0.25 nm thick layers along the z-axis, as shown in Figure 5.4a, to be able to investigate the distance dependent properties of the system. Based on orientation statistics of water molecules, there are three types of water orientation close to the brucite surface (Figure 5.4b).

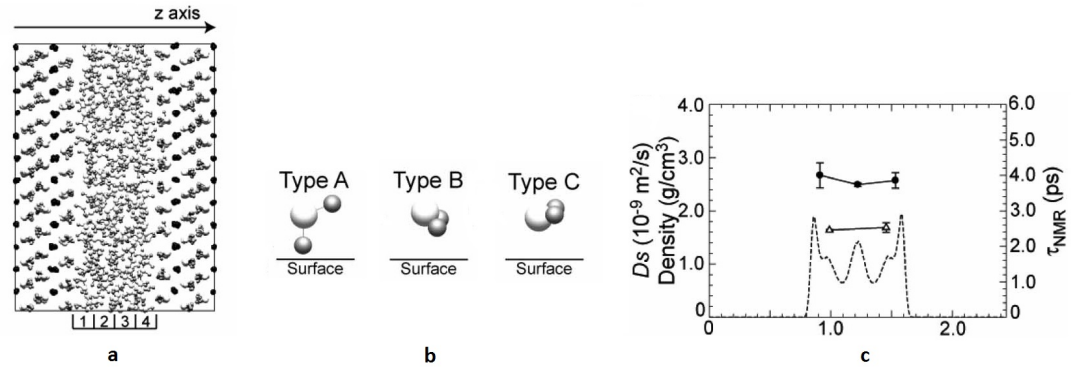

Figure 5.4: (a): unit cell arrangement in the water adsorption study of Sakuma *et al.*; (b): the specific water orientations close to the surface; (c): water density, self-diffusion coefficient (D_S) and reorientation time (τ_{NMR}) plotted as a function of distance in the z direction. [278]

Type A is the most common, and is connected to the surface hydroxyl groups via a hydrogen-bond, formed between one of its protons and the oxygen of the down-facing OH groups of the top layer. But Sakuma *et al.* note that based on the potential energy curves that they calculated and compared to the potential of a water-water interaction, the hydrogen-bonding between the water molecules and the surface is weaker than the hydrogen-bonds between water molecules. Type C is a less frequent coordination mode which makes connections with the surface via its oxygen. Type B makes hydrogen-bonds only with type A and C molecules.

Sakuma and coworkers also calculated solution properties, such as the density, self-diffusion coefficient and reorientation time, shown as a function of the distance along the z axis in Figure 5.4c.[277, 278] The density of the water molecules is significantly higher in water layers close to the surface. The two highest peaks on the symmetrical density diagram are related mainly to water molecules with type A orientation, and the shoulders correspond to type C. The second biggest peak in the middle has no specific orientation and it represents the density in the middle of the water film. Besides the density distribution, they evaluated the self-diffusion coefficient (D_S) and the reorientation time (τ_{NMR}). Surprisingly, they found a larger D_S and a smaller τ_{NMR} close to the surfaces, which is anomalous,[279] if we consider that bound water molecules are less likely to change coordination in a short time, and their results indicate that the water molecules next to the surface can move and rotate faster than in the bulk.

Wang *et al.* carried out a similar MD study on the water/brucite interface, but looking at different pore sizes, by representing them with a series of water films with different thicknesses between the brucite layers.[279] Their results show that under a pore size of 12 Å, all water molecules are affected by the presence of the brucite, but above 12 Å, the middle of the water film has similar properties to the bulk aqueous phase. They also studied the structure of the first two water layers and they found that they are on average 2.40 Å and 4.95 Å away from the surface,[280] and the water molecules within them have limited positions and orientations, very similar to the A, B and C positions which were identified by Sakuma *et al.* They also predicted that the A structure is more likely to appear, with a 5/4 ratio between A and C. Interestingly, they also found a small fraction of water molecules to be coordinated to the surface via two hydrogen bonds with their two H atoms. They suggest that this indicates a possible proton transfer between the water molecules and surface OH groups which cannot be addressed by classical MD.[279]

5.2.3 Adsorption studies on brucite

Layered hydroxides, such as brucite, are reported to be potential adsorbents of several ions and molecules.[287, 288] Although synthesised double layered hydroxides are more popular for engineered sorption processes, there are several studies regarding the adsorption behaviour of different compounds or ions on synthesised or natural brucite. For example Estrada *et al.* measured the adsorption of the amino-acid L-aspartate on $Mg(OH)_2$ powder at ambient conditions[289] and Vaiss and coworkers calculated sarin degradation starting with molecular adsorption on the surface of brucite.[290]

Both anions and cations were considered for possible interactions with the brucite surface before. An example for anionic processes is the work of Cao *et al.*, who measured the adsorption of $UO_2(CO_3)_3^{4-}$ complex on $Mg(OH)_2$ nanosheets. Based on adsorption isotherms and zeta-potential measurements they reported a strong electrostatic interaction between the negatively charged complexes and the surface, resulting in the formation of a monolayer of adsorbants on the surface.[12] Vaiss *et al.* used periodic DFT methods to calculate possible reaction mechanisms for the interaction between a HF molecule with the brucite surface, and concluded that the F^- would incorporate into a hydroxyl vacancy in the first surface layer, after the protonation of a surface OH group and water liberation.[291] These results were backed by experimental studies showing the formation of $Mg(OH)_{2-x}$-F_x with chemical bonding between the F and Mg atoms.[291] Wang and coworkers simulated the adsorption of Cl^- and Ca^{2+} ions with the force field method and, unlike for the fluorine ion, the chlorine ion is reported to weakly adsorb on the brucite surface (without incorporation). In fact, according to Wang *et al.* the adsorption energies for both the negatively charged chlorine ion and for the positively charged calcium ion on different surfaces of brucite are all in the range of -0.8 to -2.1 kJ/mol.[231] [iii]

Several studies on cations interacting with the brucite surface can be found in the literature.[14, 292–296] The high adsorption affinity of nano-$Mg(OH)_2$ for the uranyl ion was measured by Chen and coworkers, reporting an adsorption-induced crystallisation of uranyl nanoparticles on the surface.[292] The mechanism of this adsorption was later studied by Ou *et al.* using molecular dynamics, and they concluded that due to the repulsive interactions between the oxygen atoms of the uranyl ion and the surface OH groups, the hydroxyls rearrange on the surface, resulting in a more negatively charged surface site which can accommodate

[iii] We note that the reported results of this study[231] are perhaps questionable, as the crystal structure parameters employed are different from the commonly used ones.

the uranyl. [293] A high adsorption capacity of mesoporous brucite was also detected for the complexes of U^{4+} ion by Yan *et al.*, who also studied the effect of pH on the adsorption efficiency and found that the adsorption affinity of the ion is related to its hydrolysis; at low pH where only UO^{2+} exist the adsorption is weak, because it competes with the H_3O^+ ions which are present in high concentration in the solution.[294] At around neutral pH, several hydroxylated complexes of uranyl coexist in the solution, which rather bond with the OH groups of the $Mg(OH)_2$ surface to form an inner shell complex than coordinate to the first water layer. At higher pH, the adsorption efficiency decreases, because $UO_2(OH)_2$, which is the dominant complex under these conditions, precipitates from the solution.[294]

Besides the above mentioned several experimental and theoretical works on the adsorption of uranium ions, there is one publication regarding the adsorption behaviour of strontium on brucite. Bochkarev and Pushkareva published their results on the strontium uptake of natural and modified $Mg(OH)_2$ mineral in 2009.[14] They considered the pH range 3.5-9.5, and detected an increasing sorption capacity with increasing pH, with a generally good adsorption affinity of brucite for strontium. However, by analysing their samples with IR spectroscopy, they suggest that the strontium is adsorbed on the surface in the form of a carbonate compound instead of a hydroxide complex.[14]

Kerridge and Kaltsoyannis used the periodic electrostatic embedded cluster method to investigate possible interactions between Sr^{2+} hydrates and the (0001) brucite surface.[246, 297] Their embedded cluster model was very similar to the one which is used in this thesis: a 6x6 QM cluster of $Mg_{36}(OH)_{72}$ was embedded in an infinite array of point charges, keeping the atomic positions of the boundary atoms fixed. The values of the point charges were evaluated by natural population analysis (NPA).[131] In contrast to our models, it contained one underlying point charge layer with the experimental interlayer distance (c=4.770 Å), which originally caused a serious deformation in the explicit cluster which was eliminated by varying the relative charges of the O and H atoms.

A monolayer of water molecules was introduced on the surface by placing a water molecule either in type A or C orientations (which were described by Sakuma *et al.*[277, 278]) above every down-facing or up-facing OH groups in the QM cluster respectively. The positions of the waters above the boundary atoms of the cluster were fixed. This resulted in 36 water molecules within the QM region, as there are 36 stoichiometric units of $Mg(OH)_2$ in the 6x6 cluster, out of which 16 molecules were allowed to move. Based on previous studies of the solvation of Sr^{2+} in aqueous media,[149] they placed a six, seven or eight coordinated Sr^{2+}

hydrate at different distances from the brucite surface and optimised the structure. Based on these results, they identified three coordination regimes, as shown in Figure 5.5: an inner shell ($r < 4$ Å) where the Sr^{2+} is directly coordinated to the OH groups on the surface; an outer shell ($4 < r < 6$ Å) where the complex is coordinated to the monolayer of water on the surface; and an uncoordinated regime ($r > 6$ Å). Based on the relative energies of the studied systems, they found the coordinated complexes (inner or outer shell ones) to be ∼40 kJ/mol more stable than the uncoordinated ones.[246]

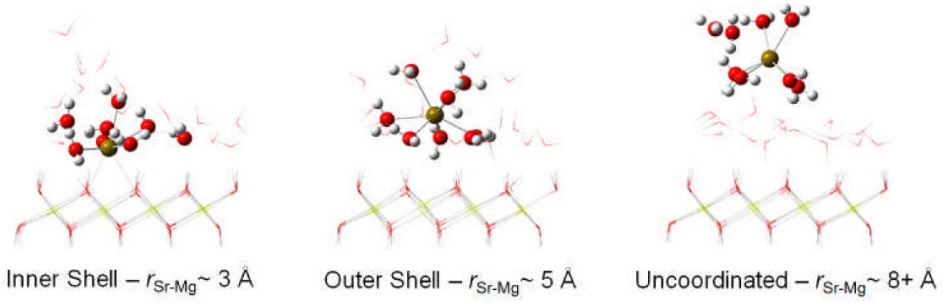

Figure 5.5: The three coordination regimes of the Sr^{2+} hydrates on brucite. The surface and the monolayer of water are represented by wires and the complex by balls and sticks.(Sr=gold, O=red, H=white)[246]

The study reported in this chapter is strongly related to the studies of Kerridge and Kaltsoyannis; by continuing to use the same approaches, this work extends the existing with model with more explicit water molecules above the surface and a COSMO-based correction term to account for the effect of bulk solvent above the hydrated surface. The possible adsorption of both Sr^{2+} hydrate and hydroxide complexes are investigated, concentrating on possible links between coordination structure, the number of solvated OH^- ions or Sr-surface distance and the adsorption energies.

5.3 Computational details

The general computational details are identical to the ones used in chapter 3 and 4 section 4.4.1: all calculations were performed with version 6.6 of the TURBOMOLE program[137] using resolution-of-the-identity density functional theory[180] and the results were visualised with the MOLDRAW chemical graphical software.[184] The TPSS exchange-correlation functional[77] was used together with the def2-SVP basis sets of polarised double-ζ quality[87, 96] and the associated Sr effective core potential (def2-ecp), which replaces the electrons occupying the 1s-3d orbitals. The periodic electrostatic embedded cluster method (2.6.2) was employed throughout this study, using the ***6x6_1*** (a stoichiometric 6 by 6 Mg atom unit cell) and ***6x6_2_f*** slabs, introduced in section 4.4.1, to represent the brucite surface. The point

charge region was described with the same set of point charges as in chapter 4: Mg=+1.78, O=-1.33 and H=+0.44. Partial geometry optimisations, in which the boundary atoms of the cluster were held fixed and the inner atoms allowed to fully relax, were carried out in the gas phase, with the m4 integration grid and the default convergence criteria: SCF energy: 10^{-6} a.u., structural energy: 10^{-6} a.u. and energy gradient: 10^{-3} a.u.

5.3.1 Introducing water layers above the brucite surface

To introduce water layers in the PEECM model, we followed the previous work of Kerridge *et al.*,[246] and used two starting geometries for water shown in Figure 5.6 and 5.4b. The molecular dynamics studies of Sakuma and coworkers[278] suggested that the water coordinations, called A and C, are the most stable in the first water layer. In position A, the water coordinates with one of its hydrogen atoms to the oxygen of the down-facing OH of the brucite surface (Fig. 5.6a); while in position C, the oxygen atom of the water is hydrogen bonded to the hydrogen atom of the up-facing OH group (Fig. 5.6b).

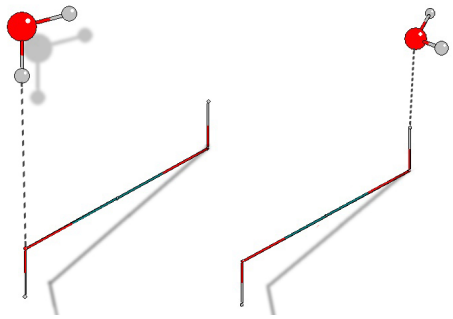

(a) A **(b) C**

Figure 5.6: A and C positions of water molecules above brucite

Based on these results, we created two hydrated brucite surface models by placing 36 explicit water molecules per layer above the surface in the QM region, either in the A or C position, and extending the point charge region with water equivalents using the following values: O=-0.85, H=+0.425.[246] The water molecules at the QM cluster boundaries were fixed and the remaining molecules were free to relax. In this way, we created a ”quasi-random” water cluster above the brucite surface, which is surrounded by a continuous electrostatic potential representing the aqueous environment. As the number of explicit water molecules is computationally limited, we did not go further than two layers above the surface (72 water molecules in total, 32 free to relax), for which the structures obtained are shown in Figure 5.7. This choice of system size allowed us to operate within the coordination regimes explained in Figure 5.5[246].

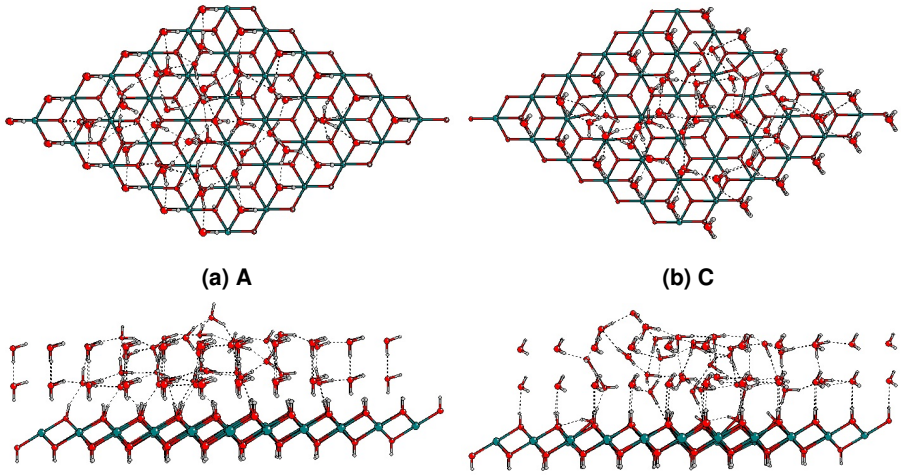

Figure 5.7: Ball and stick representations of the optimised geometries of two layers of explicit water molecules above the brucite surface in (a) A or (b) C coordination. (Mg=green, O=red, H=grey)

Although position A is closest to the most stable optimised structure of a single water molecule on the (0001) brucite surface[278] and it is expected to be more frequent in the first water layer,[278, 279] our attempts to optimise a stable structure for a system based on this coordination is failed, as they always resulted in an unrealistic electronic structure, meaning that upon inspection of the molecular orbitals, there is an unoccupied orbital with lower energy than the highest occupied. Thus, in the following study, we only used the hydrated surface model containing two water layers starting from position C (fig. 5.7b).

The charges obtained by natural population analysis for structure C are represented in Figure 5.8 as a function of their x and y coordinates, and show that the charges of the boundary atoms in the surface may stand out from the average charges of a particular atom type, but the charges in the middle of the surface cluster are relatively constant. There is more variation in the water charges (fig. 5.8d and 5.8e), which is expected due to the formation of a complex hydrogen-bond network. The optimised C surface model contains two surface sites in the QM cluster, at which the up-facing OH group of the surface is protonated by a water molecule, leaving a solvated OH^- ion in the hydration layers. These positively charged surface sites are clearly distinguishable on plotting the natural charge of the oxygen atoms of the surface and of the water molecules in the xy plane of the QM cluster, shown in figure 5.8b and 5.8d. While the majority of the O_{surf} atoms have charges between -1.35 and -1.40 a.u., the protonated sites stand out with their smaller negative charges (-1.10 and -1.15 au.), values closer to the calculated oxygen charges in water. The solvated OH^- ions have more negative charges compared to the O_{water} atoms in the hydration layers. Although such reactions on

the water/brucite interface has not been reported in simulations, those studies were molecular dynamic simulations[277–279] in which the brucite-water pair potentials usually inhibit any bond breaking mechanism. However, the formation of positively charged surface species by protonation ($>MgOH^0 + H^+ \longrightarrow >MgOH_2^+$) is predicted to be a common surface reaction below pH 8 in the experimental study of Pokrovosky and Schott[268], and is supported by the fact that the surface charge of brucite in water is positive until pH 11, where it becomes 0.

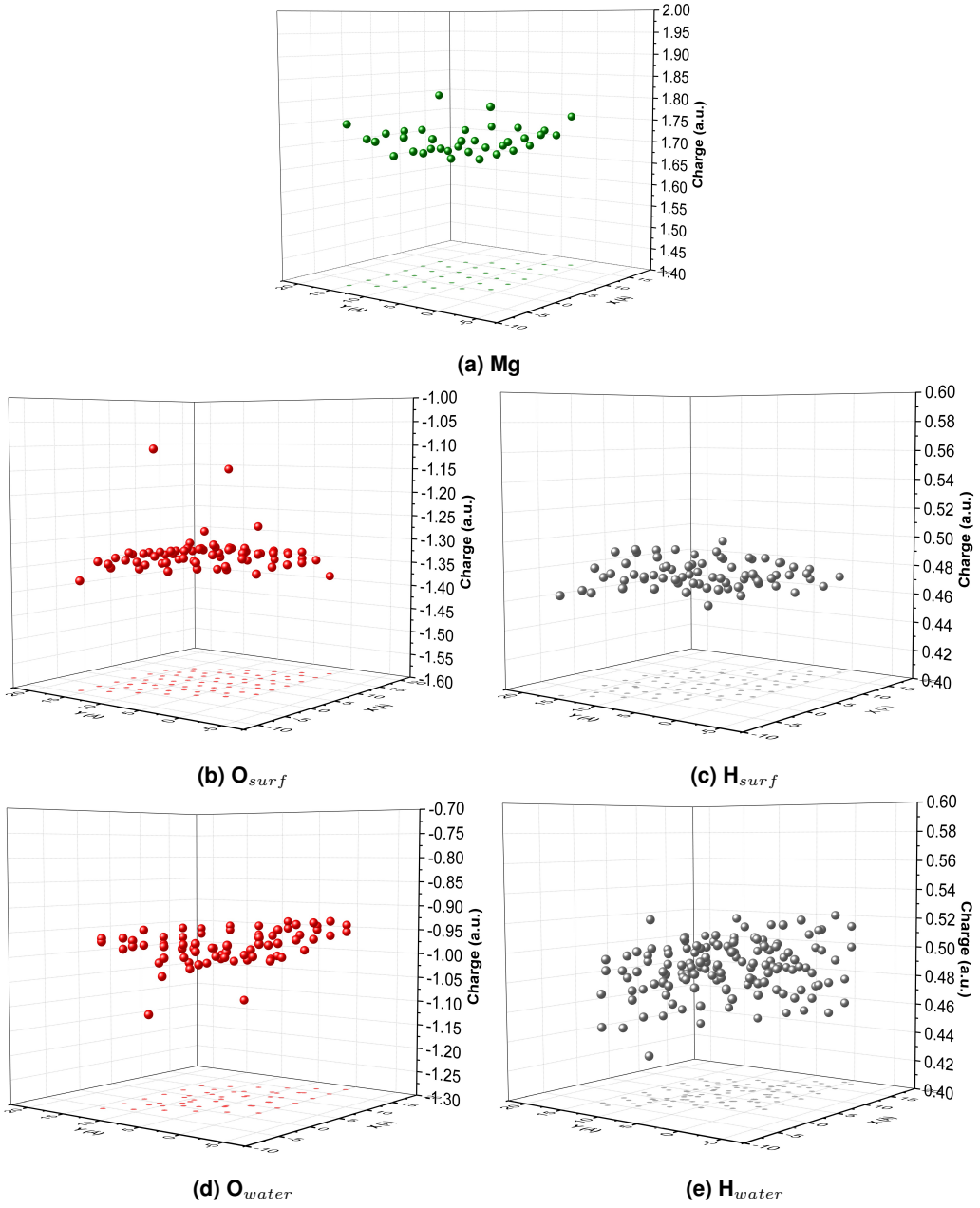

Figure 5.8: Natural charges in the C hydrated brucite surface, differentiated by atomic types and plotted against the x and y coordinates of the atoms. (a) Mg atoms, (b) and (c) are surface O and H atoms, while (d) and (e) O and H atoms of the water molecules (Mg=green, O=red, H=grey)

The good agreement with the experimental findings in neutral conditions gave us the confidence to continue with the developed hydrated surface model and introduce Sr complexes above it. In the results section we investigate the adsorption behaviour of Sr^{2+} hydrates and hydroxide complexes on the hydrated brucite (0001) surface.

5.4 Results

The first two sections (5.4.1 and 5.4.2) contain the description of the optimised complexes obtained for systems with 0, 1 and 2 OH^- ions (called group **C**, **C_OH1** and **C_OH2** respectively), while the following sections describe the analysis of the effects of different properties on the adsorption, such as the Sr-surface distance (5.4.3.1), the number of solvated OH^- ions (5.4.3.2) or the total coordination number.

By applying the previously introduced hydrated brucite surface including 2 water layers (5.7b), we generated a series of structures in the following way: first, we modelled the adsorption of two Sr^{2+} hydrate and two hydroxide complexes in group **C** and **C_OH2** by placing a cation at the same position on the xy plane (middle of the cluster) but at varying distances in the z direction, and optimised the geometry of the whole systems. Then, we modified these optimised structures by protonating the solvated hydroxide ions or deprotonating water molecules to create more initial geometries for the other group. Moreover, structures in **C_OH1** were all calculated based on previously optimised hydrate and hydroxide complexes, and thus they are discussed after the results of the **C_OH2** groups in section 5.4.2. The following labelling scheme is employed for the obtained structures:

$$[Sr : a : b : c]^{(2-b)+} \tag{5.1}$$

where a, b and c represent the number of water molecules, solvated OH^- ions and surface OH groups coordinated to the cation respectively. For instance, the $[Sr:3:0:3]^{2+}$ hydrate complex has a total coordination number of six and is directly coordinated to the surface through 3 OH groups with 3 water molecules in its first solvation shell. To decide if a particular molecule is coordinated to the ion or not, we arbitrarily used the ranges of Sr-ligand distances obtained in section 4.5.4. If an oxygen atom is further from the Sr than the largest ion-ligand distance calculated via AIM in that section (d(Sr-O(surf)) $>$ 2.760 Å, d(Sr-O(OH)) $>$ 2.865 Å, d(Sr-O(H_2O)) $>$ 2.940 Å, see Table 4.20), it is considered not coordinated to the cation.

To describe the Sr-surface interactions as realistically as possible, we created a theoretical

reaction in which we compare the energy of the adsorbed ion with the energy of a solvated one in the W24 water cluster, i.e. we look at the propensity of the Sr^{2+} ion to coordinate with the surface (inner complex) or with its first hydration layer (outer complex) rather than remaining in the aqueous phase. We used our previous results obtained in chapter 3 to represent the most stable structures in solution and calculated the interaction energy with the following equation:

$$E_{ads} = (E_{complex} + E_{W24}) - (E_{hydrated\_brucite} + E_{W24\_complex}) \tag{5.2}$$

$E_{complex}$ is the SCF energy of the adsorbed complex on the hydrated surface, while E_{W24} is the energy of a 24 water molecule cluster representing the bulk water phase (fig. 3.5). $E_{hydrated\_brucite}$ is the energy of the hydrated brucite surface without the Sr^{2+} ion (fig. 5.7b).[iv] Since we are looking at the adsorption of different types of Sr^{2+} complexes, the reference system used for $E_{W24\_complex}$ changes accordingly: for systems in section 5.4.1 $[Sr:6/18:0/0]^{2+}$ from fig. 3.6a is used, while for systems containing one or two solvated OH^- ions in section 5.4.2, the $[Sr:5/18:1/0]^+$ and [Sr:5/17:1/1] hydroxide complexes are employed from table 3.8.

It is important to note, that the chosen reference structures are optimised and predicted to be the most stable with the use of an implicit solvent model. As it was shown in chapter 3, applying the COSMO model can have significant effect on the energetic stability and the structure, but its use is not straightforward when an other embedding approach (PEECM) is employed. Therefore, for initial comparison the SCF energies of E_{W24} and $E_{W24\_complex}$ were obtained by single point calculations of the most stable structures obtained with the COSMO method in gas phase using the TPSS/def2-SVP functional-basis set pair. These gas phase energies were used to calculate the relative adsorption energies of adsorbed structures as they are summarised in sections 5.4.1 and 5.4.2. The evaluation of absolute adsorption energies with and without COSMO correction terms is described in more details in section 5.4.3.2.

5.4.1 Adsorption of Sr^{2+} on a hydrated brucite surface

In this section we present the structure of Sr^{2+} complexes obtained for a hydrated brucite surface without solvated hydroxide ions, shown in Figure 5.10 and summarised in Table 5.1. **C1** and **C3** complexes were optimised by placing the Sr^{2+} ion above the hydrated ***6x6_1***

[iv] The $E_{hydrated\_brucite}$ term is always the optimised C hydration model of a protonated surface, i.e. represents the surface in a pH below 11 conditions. Attempts to optimise unprotonated surfaces with the introduction of solvated OH^- ions within the hydrated surface model, failed due to the difficulties arising from the total negative charge of the QM cluster.

surface model at two different initial distances in the z direction. While **C2**, **C4** and **C5** were obtained from two of the optimised **C_OH2** structures by changing their two hydroxide ions to waters. All ***6x6_2_f*** results shown in Table 5.1 and in Figure 5.10 are calculated by placing the previously optimised complexes with the hydration layers above the ***6x6_2_f*** surface model before reoptimising them.

The adsorption energies relative to **C1** are all within 100 kJ/mol (Table 5.1). Test calculations show that the energy obtained from the formation of a single hydrogen bond between two water molecules or between one proton donating water molecule and a hydroxide ion acceptor is $\sim$14 and $\sim$50 kJ/mol respectively (Figure 5.9a and Figure 5.9b). Moreover, by calculating the potential curve for a single Sr^{2+}-H_2O and Sr^{2+}-OH^- interaction we found that energy gain of the first interaction is around $\sim$47 and $\sim$160 kJ/mol (Figure 5.9c and Figure 5.9d). Considering that the **C1**-**5** complexes vary in their hydrogen bond network as well as in the Sr coordination, the energy difference between the complexes is reasonably small. However, we note that in systems where there is a hydrogen-bond network or more ligands are coordinated to the ion, the interaction energies will not be the simple sum of these pair potentials.

Table 5.1: The inner and outer shell complexes obtained for systems without additional OH^- ion. The relative absorption energies ($\triangle E_{ads}$) were calculated by using Eq. (5.2) **along with the reference system [Sr:6/18:0/0]$^{2+}$ and by comparing every structure to the most stable one (C1), OH_{surf} is the number of Sr-coordinated OH surface groups in the system, CN is the total coordination number of the Sr^{2+} complex and $d_{Sr-surf}$ is the cation-surface distance**[v]

Name	Surface	Structure	$\triangle E_{ads}$ (kJ/mol)	OH_{surf}	CN	$d_{Sr-surf}$ (Å)
C1	***6x6_1***	$[Sr:4:0:3]^{2+}$	0.0	3	7	2.856
	6x6_2_f	$[Sr:4:0:3]^{2+}$	0.0	3	7	2.861
C2	***6x6_1***	$[Sr:3:0:3]^{2+}$	34.1	3	6	2.735
	6x6_2_f	$[Sr:3:0:3]^{2+}$	30.0	3	6	2.762
C3	***6x6_1***	$[Sr:6:1:0]^{+}$	48.2	0	7	4.265
	6x6_2_f	$[Sr:5:1:0]^{+}$	71.1	0	6	4.272
C4	***6x6_1***	$[Sr:4:3:0]^{-}$	54.7	0	7	5.178
	6x6_2_f	[Sr:5:2:0]	47.7	0	7	5.211
C5	***6x6_1***	$[Sr:6:1:0]^{+}$	90.2	0	7	4.475
	6x6_2_f	$[Sr:6:1:0]^{+}$	-90.1	0	7	4.504

The two complexes with the lowest energy are both Sr^{2+} hydrates directly coordinated to the surface via 3 OH surface groups (See Figure 5.10). **C1**, which is the most stable one, has a total coordination number of 7, while **C2** is 6 coordinated and, probably due to the extra water

[v] In practice, $d_{Sr-surf}$ is the z coordinate of the cation, since the Mg atoms are positioned at z=0 Å and we consider the Sr-surface distance from the middle of the first layer.

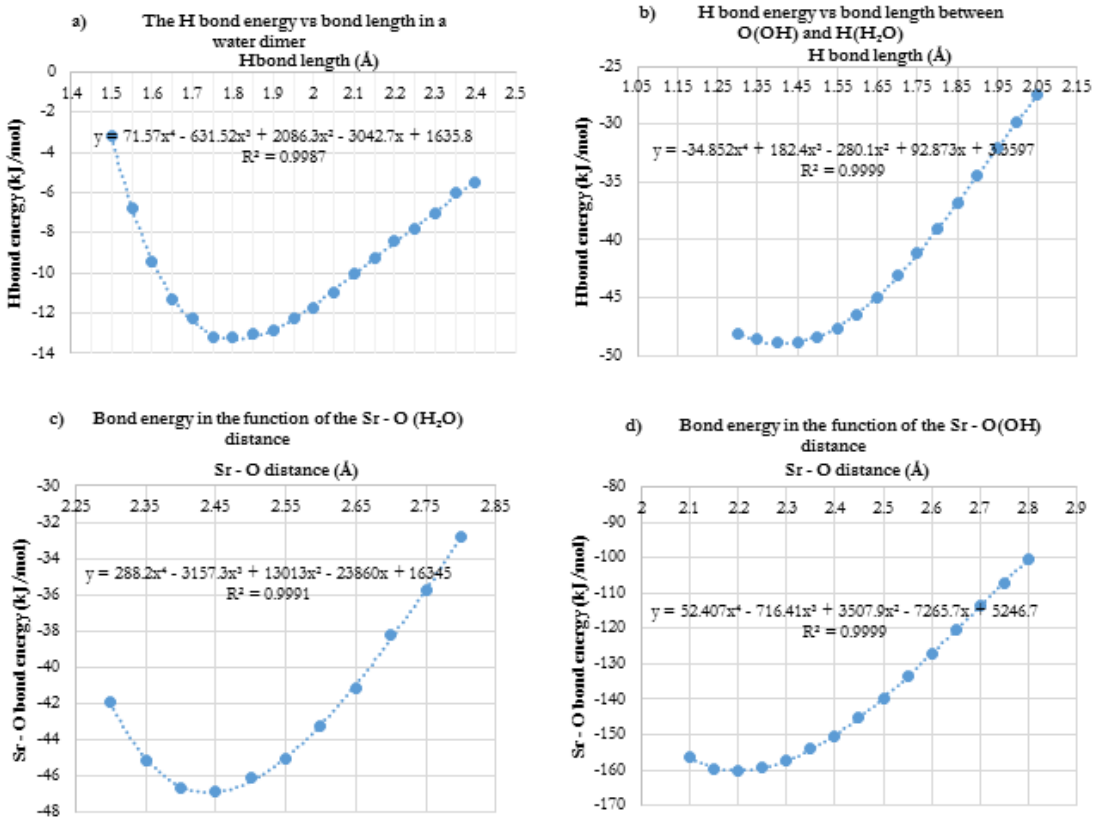

Figure 5.9: To evaluate the strength of different type of interactions, we studied the relation between interaction energies and hydrogen bond lengths or Sr-O distances. The minima of these curves are the energy of a single interaction at an ideal distance. The following calibration curves are plotted with the fitted polynomial (y) and the related coefficient of determination (R^2) : (a) the hydrogen bond energies between two water molecules; (b) between a water and the oxygen of a hydroxide molecule; (c) interaction energies between the Sr-O(H_2O); (d) and between Sr-O(OH).

coordinated to the Sr^{2+}, **C1** has a slightly longer Sr-surface distance (by 0.12 Å). Although there were no OH^- ions introduced by us in the system, the complexes which are not directly coordinated to the surface (**C3**-**5**) have OH^- ions in their first solvation shell formed by the protonation of one or more surface OH groups, as was discussed at the end of section 5.3.1. Structure **C4** has the longest Sr-surface distance (5.178 Å), which is probably related to its high OH^- coordination number: a complex which is negatively charged in total is less likely to favour the proximity of the surface OH groups. Interestingly, **C3** and **C5** differ only in the geometry of the coordinated ligands and slightly in $d_{Sr-surf}$, but there is still a relatively large $\sim$40 kJ/mol energy difference between them in favour of **C3**.

Upon the inclusion of a fixed second brucite layer (see the ***6x6_2_f*** results in Table 5.1), the structures **C1**, **C4** and **C5** stay very similar to the ones obtained with a ***6x6_1*** model. **C3**

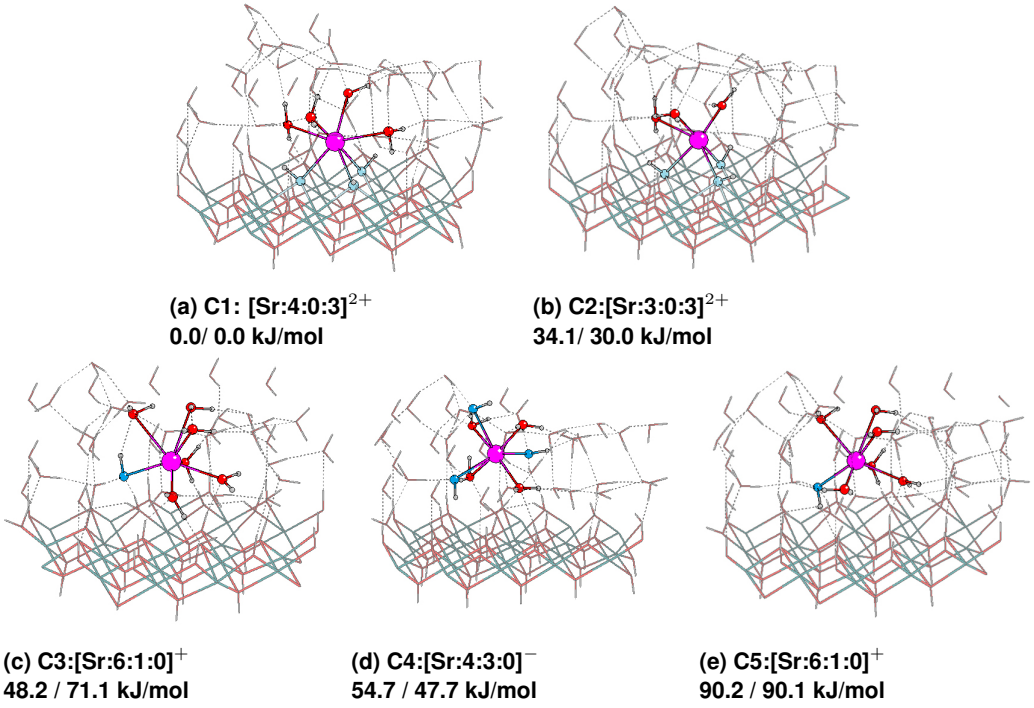

Figure 5.10: Optimised Sr^{2+} complexes of the C systems from Table 5.1 represented as balls and sticks, surrounded by a section of the hydrated brucite surface represented as tubes. The relative absorption energies are obtained by comparing the absorption energies of each structure to the most stable one (C1), using two different surface models (*6x6_1* /*6x6_2_f*). (Sr^{2+}=magenta, O=red, H=grey, Mg=green, O in the and coordinated OH^{-}=dark blue, O in the coordinated OH surface groups=light blue).

changes in its total coordination number from 7 to 6 by losing a weakly coordinated water molecule (based on Sr-O distance), and becomes less stable than before. The **C4** 6 coordinated Sr^{2+} trihydroxide becomes a slightly more stable dihydroxide with a total coordination number 7, as expected based on the predicted unlikely formation of a trihydroxide (see Chapter 3).

Natural population analysis of the absorbed Sr^{2+} complexes

Plotting the natural charges obtained for the oxygen atoms of the water molecules (O(H_2O)) and of the surface (O(surf)) in the xy plane (Figure 5.11) can help to understand how the vicinity of the Sr^{2+} affects the oxygen atoms, and to differentiate between coordinated OH^{-} ions and H_2O molecules. Therefore, we plotted the oxygen charges for the most stable inner (**C1**) and outer (**C3**) complex in Figure 5.11. The black dot in the xy projection with the corresponding black line represents the position of the Sr^{2+} in the systems. The dark red spheres are the charges of the non-coordinated oxygen atoms. In figures 5.11a and 5.11b the light green balls are charges of the Sr-coordinated oxygen atoms in water molecules (O(H_2O)) and the dark blue ones are the oxygen charges of solvated (coordinated or not coordinated) OH^{-} ions

($O(OH^-)$). In figures 5.11c and 5.11d the light green balls represent the oxygen charges of the protonated surface OH groups and the light blue balls the Sr-coordinated ones.

Figure 5.11a shows that although the **C1** system contains one solvated OH^- ion (due to surface protonation), it does not coordinate directly to the Sr^{2+}, while the oxygen atoms of the first shell water molecules slightly stand out from the oxygen charges of the hydration layers. Additionally, figure 5.11c suggests that while the protonated OH group becomes significantly less negative, the charges of the Sr-coordinated oxygen atoms of the surface do not change in the same way due to the vicinity of the cation, becoming slightly more negative instead. In the case of **C3**, 3 solvated OH^- ions are present in the hydration layers due to surface protonation, but only one of them is directly coordinated to the Sr^{2+}. The water oxygen atoms around the cation are clearly more disturbed in figure 5.11b than they are in 5.11a, showing more variation in charge.

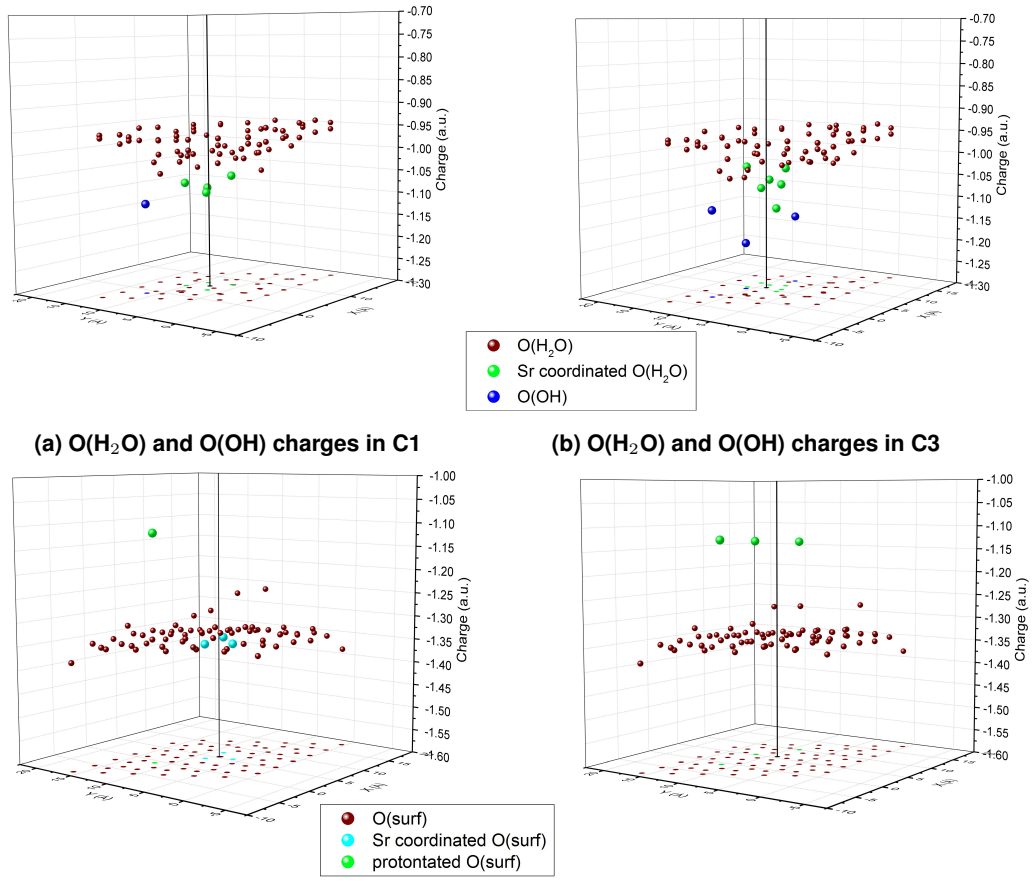

(a) $O(H_2O)$ and O(OH) charges in C1

(b) $O(H_2O)$ and O(OH) charges in C3

(c) O(surf) charges in C1

(d) O(surf) charges in C3

Figure 5.11: Natural charges of the oxygen atoms in the most stable inner (C1, (a) and (c)) and outer complexes (C3, (b) and (d)) plotted against the xy coordinates of the atoms. Black line and dot represents the xy position of the cation in the system.

Collecting data from the natural population analysis of every structure in Table 5.2, shows that the direct coordination of the Sr^{2+} lowers the average charge of the surface oxygen atoms (from around -1.318 to -1.325). Moreover, every atom coordinated to the cation has a more negative charge than the calculated average for that group of atoms.[vi] The standard deviation of the oxygen atoms in the hydration layers (SD(hydr)) is smaller for the surface coordinated complexes ($\sim$0.036), as fewer O atoms are affected by the Sr^{2+}, while it is higher ($\sim$0.05) for systems in which the ion is situated between the water layers. Differences in the cation charges indicate that there is a relation between the Sr charge and the total number of coordinated OH^- ions (solvated): the Sr ion becomes less and less positive (**C2**, **C1**: 1.780, 1.777 $>$ **C5**, **C3**: 1.764, 1.760 $>$ **C4**: 1.734) as more OH^- ions are in its first solvation shell (hydrates $>$ monohydroxides $>$ trihydroxide). This observation indirectly suggests that the interactions between the coordinated surface OH groups and the Sr, or the solvated OH^- ions and the cation, are qualitatively different, as they do not have the same effect on the Sr charge.

Table 5.2: Natural charges of the oxygen atoms for each Sr-coordinated OH surface group (O(surf)), H_2O molecule (O(H_2O)) and solvated OH^- ion (O(OH)), and the natural charge of the Sr atom, for the optimised structures in Figure 5.10 and Table 5.1. The average charge together with the corresponding standard deviation was calculated for the surface oxygen atoms (AVE(surf) and SD(surf)) and the oxygen atoms in the hydration layers (AVE(hydr) and SD(hydr)).

C1		**C2**		**C3**		**C4**		**C5**	
atom	**charge**	**atom**	**charge**	**atom**	**charge**	**atom**	**charge**	**atom**	**charge**
O(surf)	-1.352	O(surf)	-1.351	O(OH)	-1.197	O(OH)	-1.184	O(OH)	-1.245
O(surf)	-1.351	O(surf)	-1.369	O(H_2O)	-1.114	O(OH)	-1.198	O(H_2O)	-1.053
O(surf)	-1.345	O(surf)	-1.355	O(H_2O)	-1.033	O(OH)	-1.153	O(H_2O)	-1.062
O(H_2O)	-1.086	O(H_2O)	-1.083	O(H_2O)	-1.081	O(H_2O)	-1.072	O(H_2O)	-1.032
O(H_2O)	-1.070	O(H_2O)	-1.058	O(H_2O)	-1.063	O(H_2O)	-1.057	O(H_2O)	-1.090
O(H_2O)	-1.085	O(H_2O)	-1.108	O(H_2O)	-1.027	O(H_2O)	-1.064	O(H_2O)	-1.063
O(H_2O)	-1.056	-	-	O(H_2O)	-1.059	O(H_2O)	-1.075	O(H_2O)	-1.032
AV(surf)	-1.325	AV(surf)	-1.325	AV(surf)	-1.319	AV(surf)	-1.316	AV(surf)	-1.318
SD(surf)	(0.037)	SD(surf)	(0.038)	SD(surf)	(0.051)	SD(surf)	(0.056)	SD(surf)	(0.046)
AV(hydr)	-1.013	AV(hydr)	-1.013	AV(hydr)	-1.028	AV(hydr)	-1.030	AV(hydr)	-1.024
SD(hydr)	(0.036)	SD(hydr)	(0.037)	SD(hydr)	(0.053)	SD(hydr)	(0.057)	SD(hydr)	(0.052)
Sr	1.777	Sr	1.780	Sr	1.760	Sr	1.734	Sr	1.764

The electron density difference plots of the **C1** and **C3** structures in Figure 5.12 show that every ligand which is directly coordinated to the Sr^{2+} (even the surface OH groups) are affected, most likely polarised, by the positive cation, which is presumably the reason for the generally more negative oxygen charges calculated for the coordinated ligands in Table 5.2.

[vi] The average charges (AVE(surf) and AVE(hydr)) are calculated by considering only the charges of the unfixed oxygen atoms, as the boundary atoms may be affected by the surrounding point charges and by the fact that their coordinates are frozen. AVE(hydr) contains the charge of every oxygen atom in the relaxed part of the hydration layer, even the O atoms of the solvated OH^- ions.

The size of the red and blue regions in Figure 5.12 suggests that the effect of the Sr^{2+} is relatively local, and does not go further than two coordination shells. Moreover, by comparing the electron density difference plots of **C1** and **C3** with figure 4.17 in section 4.5.2, we can conclude that in the presence of two hydration layers, the surface atoms are much less affected by the cation than in the case of a Sr^{2+} hydrate with only three water molecules in its first solvation shell.

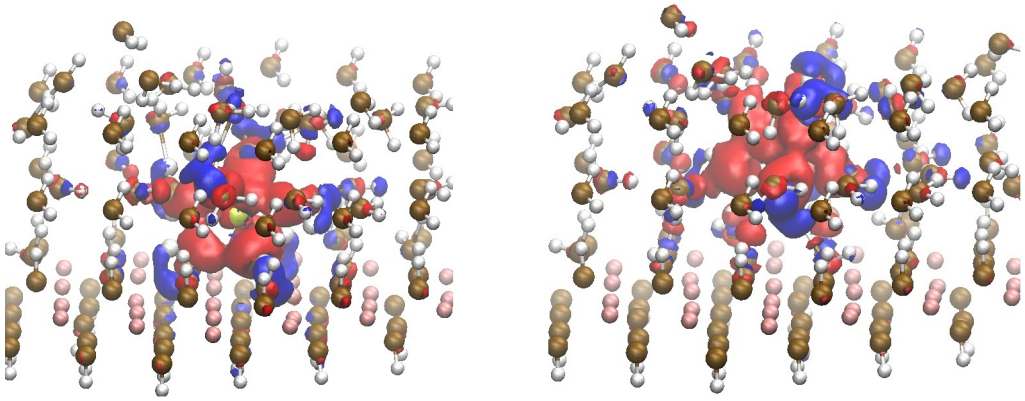

(a) C1 **(b) C3**

Figure 5.12: Electron density distribution of the C1 (a) and C3 complexes (b). The isosurface value is 0.0025 a.u.. The red regions indicate electron depletion, while the blue regions electron accumulation. The point charges are not shown. (Mg=pink, O=ochre, H=white, Sr=yellow)

5.4.2 Adsorption of Sr^{2+} hydroxides on a hydrated brucite surface

To observe the effect of differently charged environments on the adsorption, we replaced one or two water molecules with OH^- ions (in addition to the Sr^{2+} ion and the already existing hydroxide ions due to the surface protonation). The results summarised in Table 5.3 (**C_OH2**) are obtained similarly to the those presented in the previous section, i.e. two structures were optimised based on the ***6x6_1*** hydration model at different Sr-surface distances (**C_OH2_3** and **C_OH2_4**) and the others were initiated from the deprotonation of **C1** and **C3**. Systems containing only one OH^- ion in Table 5.4 are made by the protonation/deprotontation of the previously optimised **C_OH2** and **C** structures and therefore discussed at last.

Considering the relative energies of the **C_OH2** structures in Table 5.3, we find that the energy range of these values is close to those of the **C** systems in Table 5.1. Another similarity is, that the two most stable structures (**C_OH2_1** and **C_OH2_2**, see Figure 5.13) are effectively Sr^{2+} hydrates directly coordinated to the surface; the introduced OH^- ions are located in the second coordination shell of the ion. The small energy difference between these two complexes (21.2 kJ/mol) is most likely the consequence of changing one Sr-O(surf) to a Sr-

O(H_2O) coordination ($[Sr:4:0:3]^{2+} \longrightarrow [Sr:5:0:2]^{2+}$). The third directly surface coordinated structure (**C_OH2_3**), which has the two OH^- ions in its first coordination shell, is significantly less stable (with the ***6x6_1*** surface representation) compared to the absorbed Sr^{2+} hydrates. This result suggests that an inner shell complex prefers to have only water molecules in its first hydration shell.

In both **C_OH2_4** and **C_OH2_5**, the Sr^{2+} ion is located between the two water layers and attracts two or three of the available OH^- ions into its direct solvation shell. These structures are energetically less stable than the hydrates, although this difference might be the consequence of the fact that **C_OH2_4** has a total coordination number 8 while the favoured coordination is 6 or 7 for dihydroxides (chapter 3) and **C_OH2_5** is a 5 coordinated trihydroxide, also predicted to be energetically less stable than other coordinations. This is confirmed by the fact that using the ***6x6_2_f*** surface model instead of ***6x6_1*** changes the total coordination number to 6 for the previously 5 coordinated systems,(**C_OH2_3** and **C_OH2_5**) which makes these structures more stable than before. For the other complexes, a fixed second layer causes only small changes in the Sr-surface distance and in the relative adsorption energies.

Table 5.3: The inner and outer shell complexes obtained for systems with 2 additional OH^- ions. The relative absorption energies (ΔE_{ads}) are calculated by using Eq. (5.2) along with the reference system [Sr:5/17:1/1] and by comparing every structure to the most stable one (C1_OH2_1), OH_{surf} is the number of Sr-coordinated OH surface groups in the system, CN is the total coordination number of the Sr^{2+} complex and $d_{Sr-surf}$ is the cation-surface distance.

Name	Surface	Structure	ΔE_{ads} (kJ/mol)	OH_{surf}	CN	$d_{Sr-surf}$ (Å)
C_OH2_1	***6x6_1***	$[Sr:4:0:3]^{2+}$	0.0	3	7	3.071
	6x6_2_f	$[Sr:4:0:3]^{2+}$	0.0	3	7	2.970
C_OH2_2	***6x6_1***	$[Sr:5:0:2]^{2+}$	21.2	2	7	3.246
	6x6_2_f	$[Sr:5:0:2]^{2+}$	3.3	2	7	3.165
C_OH2_3	***6x6_1***	[Sr:0:2:3]	113.5	3	5	2.841
	6x6_2_f	[Sr:1:2:3]	40.5	3	6	2.848
C_OH2_4	***6x6_1***	[Sr:6:2:0]	93.5	0	8	4.800
	6x6_2_f	[Sr:6:2:0]	86.8	0	8	4.785
C_OH2_5	***6x6_1***	$[Sr:2:3:0]^-$	107.3	0	5	4.416
	6x6_2_f	$[Sr:3:3:0]^-$	59.2	0	6	4.622

Structures with a total charge of +1 were all calculated based on previously optimised **C** or **C_OH2** complexes, and the stable structures are summarised in Table 5.4 and Figure 5.14. The four inner shell complexes (**C_OH1_1** to **C_OH1_4**) were obtained by changing, one by one, the four first solvation shell water molecules of **C1** to a hydroxide ion or changing one of the coordinated OH^- ions of **C_OH2_3** to H_2O. Using these two different starting geometries

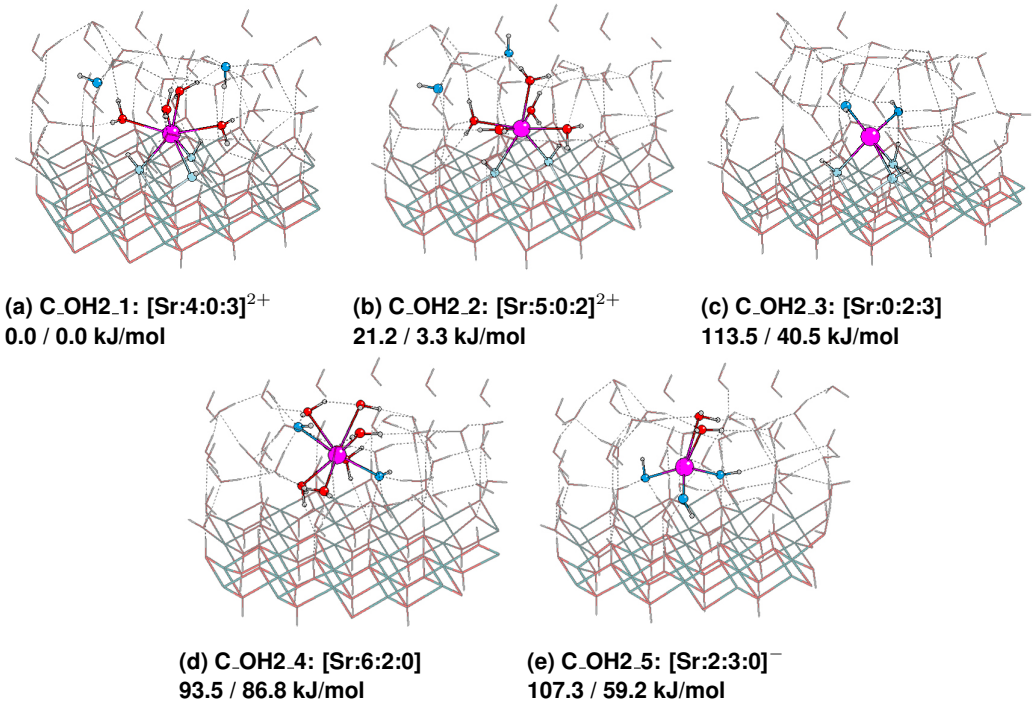

(a) C_OH2_1: $[Sr:4:0:3]^{2+}$
0.0 / 0.0 kJ/mol

(b) C_OH2_2: $[Sr:5:0:2]^{2+}$
21.2 / 3.3 kJ/mol

(c) C_OH2_3: [Sr:0:2:3]
113.5 / 40.5 kJ/mol

(d) C_OH2_4: [Sr:6:2:0]
93.5 / 86.8 kJ/mol

(e) C_OH2_5: $[Sr:2:3:0]^{-}$
107.3 / 59.2 kJ/mol

Figure 5.13: Optimised Sr^{2+} complexes of the C_OH2 systems (Table 5.3) represented as balls and sticks, surrounded by section of the hydrated brucite surface represented as tubes. The relative absorption energies are obtained by comparing the absorption energies of each structure to the most stable one (C_OH2_1), using two different surface models (*6x6_1* / *6x6_2_f*). (Sr^{2+}=magenta, O=red, H=grey, Mg=green, O in the and coordinated OH^{-}=dark blue, O in the coordinated OH surface groups=light blue).

resulted in the exactly same structure and energy in one case (**C_OH1_2**). Accordingly, **C3** and **C_OH2_4** were used as initial structures and modified by deprotonation or protonation to optimise the outer shell complexes (**C_OH1_5**to **C_OH1_7**).

Similarly to the **C** and **C_OH2** groups, the complexes directly coordinated to the surface are more stable (by at least 50 kJ/mol) than the outer shell ones. Since they are based on the same original complex (**C1**), the inner shell complexes are very close in absorption energy to each other. The **C_OH1** group presents several differences from the previously made observations: So far every stable inner shell complex is a Sr^{2+} hydrate, but in this group **C_OH1_4** is a monohydroxide with a relative adsorption energy very close to the most stable structure (4.6 kJ/mol). Moreover, the **C_OH1_5** outer shell complex is a 5 coordinated dihydroxide, but it appears to be more stable by $\sim$ 33 kJ/mol than the 7 coordinated monohydroxide, **C_OH1_6**. The total coordination number 5 is clearly unfavoured compared to 7 in the previous groups.

Structures obtained with the ***6x6_2_f*** surface model generally stay very close to the ***6x6_1*** optimised structures, with few exceptions: the relative absorption energy of **C_OH1_5** notably increases (up to 80.1 kJ/molcompared to C1_OH_1 with the same surface representation), which can be rationalised by the above mentioned general observation, that the total coor-

dination number 5 is usually less favourable than 7; and **C_OH1_7** becomes an outer Sr^{2+} hydrate complex, the first one optimised so far.

Table 5.4: The inner and outer shell complexes obtained for systems with 1 additional OH^- ion. The relative absorption energies ($\triangle E_{ads}$) are calculated by using Eq. (5.2) along with the reference system [Sr:5/18:1/0]$^+$ and by comparing every structure to the most stable one (C1_OH1_1, OH_{surf} is the number of Sr-coordinated OH surface groups in the system, CN is the total coordination number of the Sr^{2+} complex and $d_{Sr-surf}$ is the cation-surface distance.

Name	Surface	Structure	$\triangle E_{ads}$ (kJ/mol)	OH_{surf}	CN	$d_{Sr-surf}$ (Å)
C_OH1_1	*6x6_1*	$[Sr:4:0:3]^{2+}$	0.0	3	7	2.925
	6x6_2_f	$[Sr:4:0:3]^{2+}$	0.0	3	7	2.910
C_OH1_2	*6x6_1*	$[Sr:4:0:3]^{2+}$	1.8	3	7	2.925
	6x6_2_f	$[Sr:4:0:3]^{2+}$	-5.8	3	7	2.917
C_OH1_3	*6x6_1*	$[Sr:4:0:3]^{2+}$	16.7	3	7	2.982
	6x6_2_f	$[Sr:4:0:3]^{2+}$	6.8	3	7	2.908
C_OH1_4	*6x6_1*	$[Sr:3:1:3]^{+}$	4.6	3	7	2.995
	6x6_2_f	$[Sr:3:1:3]^{+}$	-0.3	3	7	2.962
C_OH1_5	*6x6_1*	[Sr:3:2:0]	55.5	0	5	4.522
	6x6_2_f	[Sr:3:2:0]	80.1	0	5	4.459
C_OH1_6	*6x6_1*	$[Sr:6:1:0]^{+}$	88.4	0	7	4.778
	6x6_2_f	$[Sr:6:1:0]^{+}$	87.3	0	7	4.785
C_OH1_7	*6x6_1*	$[Sr:6:1:0]^{+}$	119.6	0	7	4.659
	6x6_2_f	$[Sr:7:0:0]^{2+}$	96.8	0	7	4.586

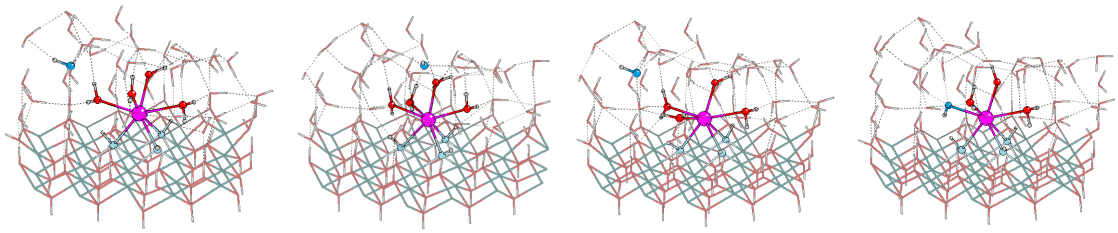

(a) C_OH1_1: $[Sr:4:0:3]^{2+}$ 0.0 / 0.0 kJ/mol **(b) C_OH1_2: $[Sr:4:0:3]^{2+}$ 1.8 / -5.8 kJ/mol** **(c) C_OH1_3: $[Sr:4:0:3]^{2+}$ 16.7 / 6.8 kJ/mol** **(d) C_OH1_4: $[Sr:3:1:3]^{+}$ 4.6 / -0.3 kJ/mol**

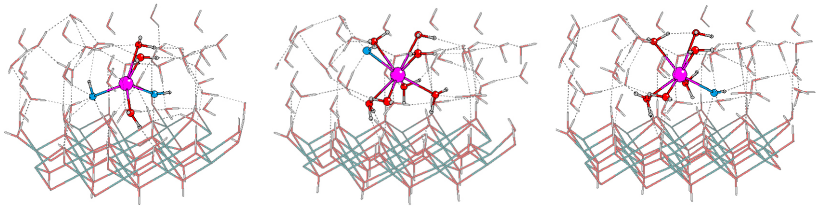

(e) C_OH1_5: [Sr:3:2:0] 55.5 / 80.1 kJ/mol **(f) C_OH1_6: $[Sr:6:1:0]^{+}$ 88.4 / 87.3 kJ/mol** **(g) C_OH1_7: $[Sr:6:1:0]^{+}$ 119.6 / 96.8 kJ/mol**

Figure 5.14: Optimised Sr^{2+} complexes of the C_OH1 systems (Table 5.4) represented as balls and sticks, surrounded by section of the hydrated brucite surface represented as tubes. The relative absorption energies are obtained by comparing the absorption energies of each structure to the most stable one (C_OH1_1), using two different surface models (*6x6_1* / *6x6_2_f*). (Sr^{2+}=magenta, O=red, H=grey, Mg=green, O in the and coordinated OH^-=dark blue, O in the coordinated OH surface groups=light blue).

5.4.3 The relative stability of Sr^{2+} complexes on a hydrated brucite surface

In this section, we investigate the effect of the following factors on the adsorption energies: the Sr-surface distance, the total coordination number, the number of Sr-coordinated solvated OH^- ions and the total number of OH^- ions introduced in the system. In section 5.4.3.1 we concentrate on the first three properties, while in section 5.4.3.2 we attempt to draw conclusions regarding the number of OH^- ions in the system. But first, we exclude the possibility that the slight changes in the xy position of the Sr^{2+} during the optimisation process could be related to the energy differences; a concern raised in section 4.5.2 for the absorption of a single Sr^{2+} hydrate. By plotting the Sr x and y coordinates of each structure in a 3D plot (Figure 5.15), we show that the differences in the final cation positions are very small and that there is no direct relation between the obtained absorption energies and the Sr's x and y coordinates.

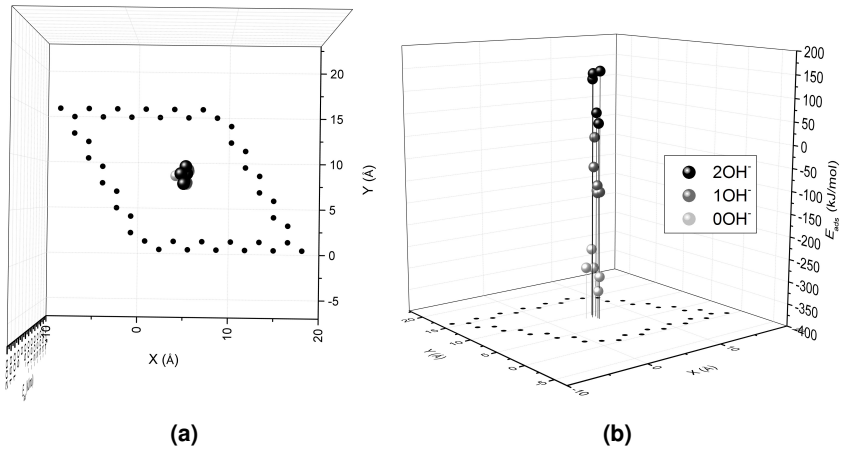

Figure 5.15: (a) The xy projection of the Sr positions within the QM cluster, (b) the absorption energies of every system from Table 5.1, 5.4 and 5.3 vs. the x and y Sr coordinates within the QM cluster. (The boundary atoms of the QM cluster are projected on the xy plane as black dots, while the position of the Sr atoms every adsorbed complexes are shown with white-grey-black balls.)

5.4.3.1 Interaction energies in different coordination regimes

Kerridge and Kaltsoyannis predicted three distinctive coordination regimes for Sr^{2+} hydrate adsorption based on 38 possible complexes,[246] and a very similar conclusion is suggested by plotting the relative adsorption energies of the optimised systems of section 5.4.1 and 5.4.2 as a function of $d_{Sr-surf}$, shown in Figure 5.16.

To study the possible relations between relative adsorption energies and the Sr-surface distance in more detail, we chose one or two of the optimised surface coordinated complexes of each group (for systems with 0,1 or 2 solvated OH^- ions, the **C1**, **C_OH1_4**, and

C_OH2_1, **C_OH2_3** were used respectively) and performed a step by step optimisation with fixed $d_{Sr-surf}$ values from the starting geometry until $\sim$ 5 Å, with a step size of 0.5 Å. We note that we do not study explicitly the third, uncoordinated, regime ($>$ 8 Å), instead, we consider every non-coordinated structure in the theoretical equation (Eq. (5.2)) as a solvated complex in the bulk solution. Note that, although the ***6x6_2_f*** surface representation seems to have an effect on the geometry of some structures, due to considerable longer optimisation runs of structures with a fixed second layer, we limited ourselves to the use of the ***6x6_1*** surface model for these scanning studies.

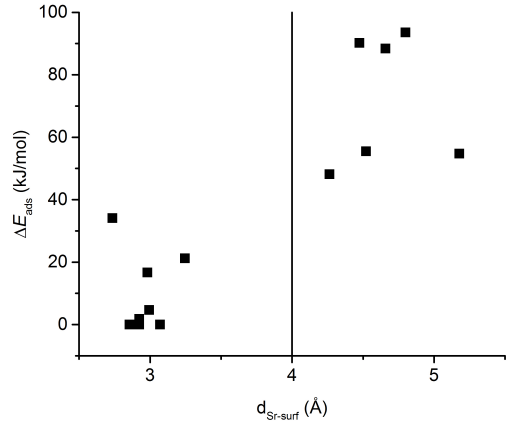

Figure 5.16: Relative absorption energies of the obtained complexes plotted against the Sr-surface distances. We note that the relative energy values of different groups (C, C_OH1 and C_OH2) were calculated compared to different reference structures. The suggested barrier between the coordination regimes by Kerridge *et al.*[246] is shown with a vertical line at 4 Å.

Figures 5.17, 5.19 and 5.18 summarise the obtained complexes for 0, 1 and 2 solvated OH^- ions respectively. In each case, the adsorption energies are relative to the chosen starting geometry for the Sr-surface distance scan. Structures represented by circles are calculated with fixed $d_{Sr-surf}$ values, while the ones shown by squares are obtained with the free movement of the Sr^{2+} (and summarised previously in Table 5.1, 5.3 and 5.4). To examine the complex relations between the different properties of the structures, we use different marking for Sr^{2+} hydrate (black), monohydroxide (white), dihydroxide (plus) and trihydroxide complexes (cross), while showing the total coordination number of each system as the label of the data point. The vertical line crossing the x axis shows the barrier between the two coordination regimes, defined by the Sr-surface distance of the last directly coordinated Sr^{2+} complex.

C1 is chosen as the starting point of the scan shown in Figure 5.17, as it is predicted to be the most stable Sr^{2+} hydrate directly coordinated to the surface among the systems without

OH^- ions. The path of the calculated scan is shown by the black dotted line and suggests a relatively big jump between the energies of the inner shell complexes and the first outer shell complex (∼55 kJ/mol), combined with a decrease in the total coordination number from 7 to 5 and with a change in the complex type (monohydroxide). Interestingly, with further increase of $d_{Sr-surf}$, the adsorption energy gradually decreases to similar levels as the energy of the last inner shell complex, with the total coordination becoming 7 again. Combining these results with the data points of Table 5.1 suggests the possibility of a lower energy path, where the coordination number does not change at the regime boundary. To explore this possibility, we calculated additional points starting from the last data point of the original scan and decreasing the Sr-surface distance with the same step size. The red dotted line shows this other possible pathway by connecting 7 coordinated complexes with lower energies.

Figure 5.17 suggests that every inner shell complex is a Sr^{2+} hydrate, and upon moving away from the surface, the complex type changes first to monohydroxide then the di- and trihydroxide, with 7 coordination being favoured generally. Although increasing $d_{Sr-surf}$ seems to decrease the stability compared to **C1**, the majority of the 7 coordinated complexes stay within a 40 kJ/mol energy range.

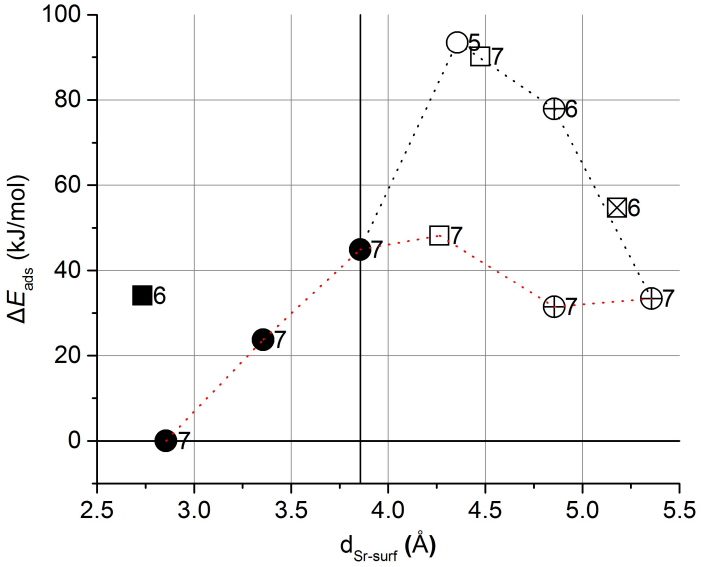

Figure 5.17: Relative adsorption energies of every structure obtained with 0 solvated OH^- ions compared to C1. The numbers next to each data point ranging between 5-7 are the total coordination numbers of the complexes. Data points represented by circles are obtained with fixed Sr-surface distances, starting from the $d_{Sr-surf}$ of C1 with an increment of 0.5 Å. Squares are structures from Figure 5.10. (black=hydrates, white=monohydroxides, plus=dihydroxides, cross=trihydroxides, black dotted line: constrained optimisation initiated from C1, red dotted line=possible pathway connecting complexes with a total coordination number of 7.)

Originally, we chose **C_OH2_3** for the starting point of the scan (black dotted line) for sys-

tems containing 2 OH^- ions, as this structure was the only $Sr(OH)_2$ complex directly coordinated to the surface, but we found that the structure obtained at the next step is 50 kJ/mol more stable and 6 coordinated (see Figure 5.18). This observation, and the fact that including a fixed second layer also resulted in a total coordination number 6 for **C_OH2_3** (Table 5.3), implies that a more stable complex can exist at the same Sr-surface distance, and indeed, we were able to optimise a 80 kJ/mol more stable 6 coordinated Sr^{2+} dihydroxide complex for the same $d_{Sr-surf}$ as **C_OH2_3**. This energy difference also shows the limitation of our method, as the statistical sampling of local minima at certain Sr-surface distances does not guarantee that there are no further coordinations more stable than the ones found by the optimisation method. Moving further from the surface resulted in no change in the complex type and a gradual increase in the relative adsorption energy, suggesting that even the dihydroxide complexes are more favoured as inner shell for systems containing 2 OH^- ions.

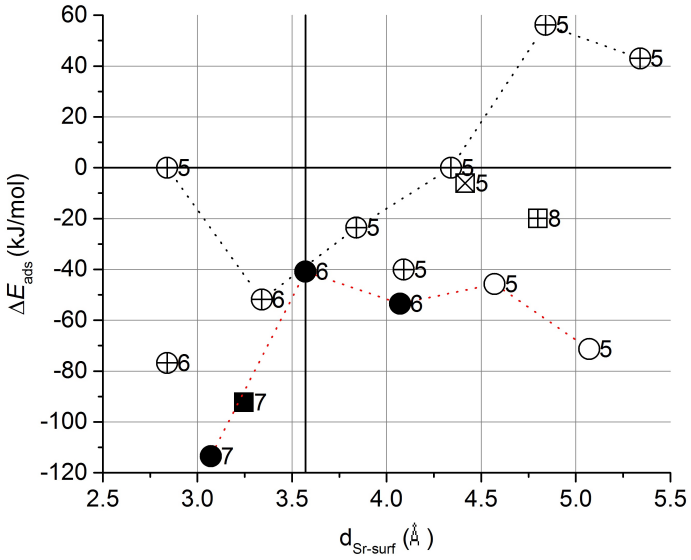

Figure 5.18: Relative adsorption energies of every structures in the C_OH2 group compared to C_OH2_3. The numbers next to each data point ranging between 5-7 are the total coordination numbers of the complexes. Data points represented by circles are obtained with fixed Sr-surface distances, starting from the $d_{Sr-surf}$ of C_OH2_3 (black dotted line) and of C_OH2_1 (red dotted line) with an increment of 0.5 Å. Squares are structures from Figure 5.13. (black=hydrates, white=monohydroxides, plus=dihydroxides, cross=trihydroxides)

However, the effect of increasing the Sr-surface distance becomes slightly more complicated if we carry out a similar scan for the most stable structure of the **C_OH2** group (**C_OH2_1**), which is a 7 coordinated Sr^{2+} hydrate (red dotted line in Figure 5.18). Each point of this scan is below the path of the original scan, suggesting that although inner shell Sr^{2+} dyhixdoxide complexes can exist, the surface coordinated hydrates will always be more stable, even for systems containing 2 solvated OH^- ions. The course of the second Sr-surface

distance scan (red dotted line) is similar to the results without OH^- ions (shown with a black dotted line in fig. 5.17) in the sense that a relatively large energy difference ($\sim$50 kJ/mol) is found between structures with a total coordination number of 7 or less.

The transition between the regimes of inner and outer shell complexes is not exact for the systems in Figure 5.18, because the complexes lying in a coordination distance of 3.5-4.3 Å are still weakly coordinated to the surface with 1 OH surface group, and while the most stable inner shell complexes are still Sr^{2+} hydrates, the most stable outer shell ones are monohydroxides and dihydroxides, and they are always higher in adsorption energy.

Continuing the exploration with systems containing 1 OH^- ions, we carried out a step by step constrained optimisation starting with the only monohydroxide directly coordinated to the surface (**C_OH1_4**). The results presented in Figure 5.19 somewhat contradict the previous conclusions based on Figure 5.17 and 5.18 in the following way: on one hand **C_OH1_4** Sr^{2+} monohydroxide is 7 coordinated and as stable as the optimised hydrate complexes, while on the other hand, there are two, also 7 coordinated, monohydroxides which are outer shell complexes and are less stable than the 5 coordinate ones at similar Sr-surface distances (between 4.5-5 Å). We note, that while in the previous cases more alternatives were explored for the same Sr-surface distance, for the **C_OH1** group we calculated fewer data points. But, despite the differences, the general conclusion that the directly coordinated Sr^{2+} complexes are all 7 coordinated hydrates or monohydroxides has not changed.

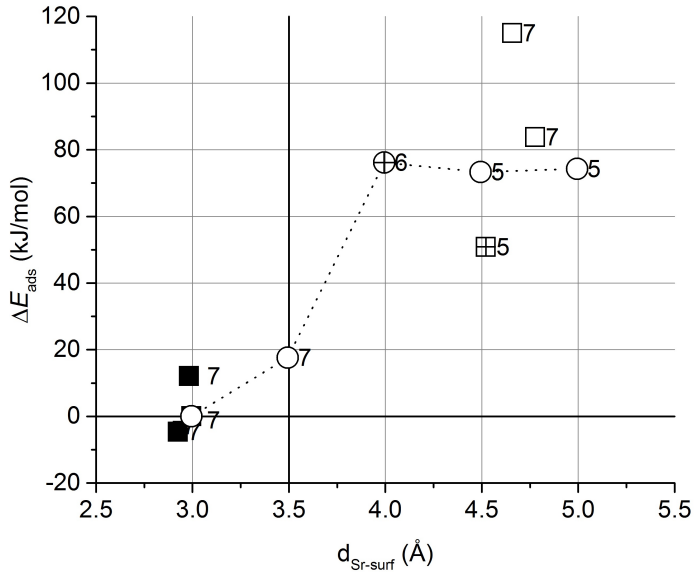

Figure 5.19: Relative adsorption energies of every structures in the C_OH1 group compared to C_OH1_4. The numbers next to each data point ranging between 5-7 are the total coordination numbers of the complexes. Data points represented by circles are obtained with fixed Sr-surface distances, starting from the $d_{Sr-surf}$ of C_OH1_4 with an increment of 0.5 Å. Squares are structures from Figure 5.14. (black=hydrates, white=monohydroxides, plus=dihydroxides, cross=trihydroxides)

5.4.3.2 The effect of solvated OH^- ions

In this section, we attempt to understand the effect of the number of solvated hydroxide ions on the absorption energies. Although we are aware that the systems with 0, 1 and 2 OH^- ions carry a total charge of +2, +1 and 0 respectively, and applying the PEECM model for differently charged systems can cause an artificial potential shift in the absolute absorption energies, based on test calculations made for the adsorption of s block ions carrying +1 or +2 charge, we expect this error to be relatively small compared to the adsorption energies (see section 4.5.1).

Figure 5.20 shows the absolute absorption energies of every system (both with relaxed and fixed Sr^{2+} positions) as a function of the number of OH^- ions in the system without taking into account the effect of bulk solvent.[vii] The structures (both inner and outer shell complexes), obtained for systems without additional OH^- ions are all more stable by 250-340 kJ/mol compared with an empty hydrated brucite surface and a Sr^{2+} hydrate complex in the bulk aqueous phase ([Sr:6/18:0/0]$^{2+}$ from fig 3.6a). In contrast, the adsorbed complexes with 2 OH^- ions introduced in the system all appear unfavourable by 40-210 kJ/mol compared with the most stable hydroxide complex ([Sr:5/17:1/1] from table 3.8) in a solution containing the same number of OH^- ions. The absolute adsorption energies of the **C_OH1** structures lie between the ones obtained for the **C** and **C_OH2** groups (from -115 to 5 kJ/mol) compared with the most stable monohydroxide complex ([Sr:5/18:1/0]$^+$). Overall, Figure 5.20 suggests a high dependence on the total charge of the system and shows that in an environment where solvated OH^- ions are available next to the strontium, the formation of hydroxide species in solution is more favourable than the adsorption of the Sr^{2+} on the hydrated (and protonated) brucite surface.

However, the solvated reference structures used above are originally optimised with the COSMO implicit solvent model, i.e. with a homogeneous background potential representing the bulk aqueous phase. In this environment, the energy differences between the reference structures using Eq. (3.2) in chapter 3 are the following: [Sr:6/18:0/0]$^{2+}$+2OH^-: 0.0 kJ/mol $>$ [Sr:5/18:1/0]$^+$+OH^-: -36.3 kJ/mol $>$ [Sr:5/17:1/1]: -60.9 kJ/mol (see Figure 3.12a and Table

[vii] The direct comparison of the energies is not straightforward, because, to keep the total charge equal in both side of the theoretical equation (Eq. (5.2)), the reference systems are different for the three groups (**C**, **C_OH1**, **C_OH2**), i.e. for systems containing 0 OH^- we chose a reference complex without solvated OH^- etc. Therefore, using the same scale for the obtained energies of the three groups might be misleading. However, the reference complexes were energetically compared to each other with an other theoretical equation (Eq. (3.2)) in section 3, and after all, all energies are adsorption energies calculated to three different charge environment, which makes us to believe that they are reasonably comparable within the same scale.

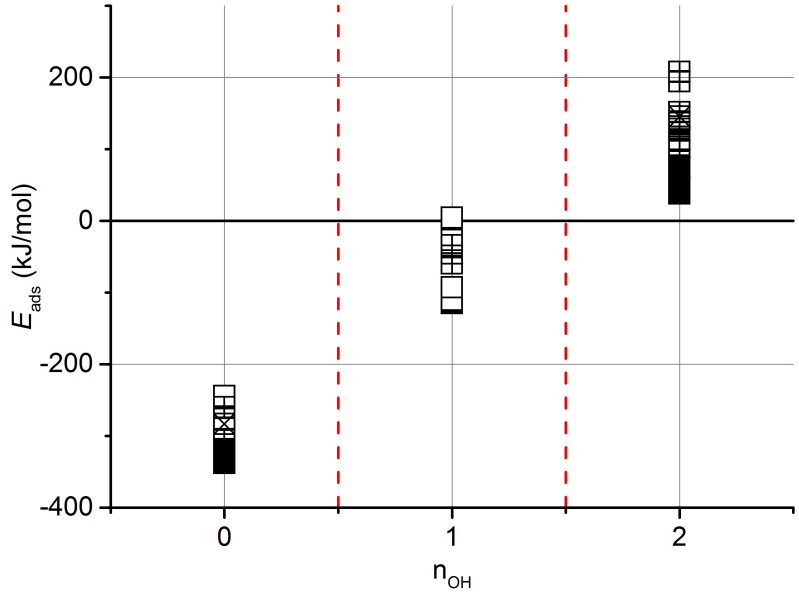

Figure 5.20: Absolute absorption energies obtained by using Eq. 5.2 with the appropriate reference system for the C, C_OH1 and C_OH2 groups vs. the total number of solvated OH^- ions in the system. (black=hydrates, white=monohydroxides, plus=dihydroxides, cross=trihydroxides)

3.13 in section 3.4.3). Using the same equation but without the COSMO method (gas phase) and with def2-SVP basis sets dramatically changes the energies and enormously favours the solvated $2OH^-$ systems: 0.0 kJ/mol $>$ -575.8 kJ/mol $>$ -917.5 kJ/mol. As we cannot use the COSMO and PEECM approaches at the same time, the adsorption energies shown in Figure 5.20 must be affected by this extreme difference in the relative energies of the reference structures.

The importance of the basis set on the Sr^{2+} ion was explained previously in section 3.4.3. However, due to the size of the whole PEECM system ($\sim$ 396 atoms for ***6x6_1*** and 576 atoms for ***6x6_2_f***), applying higher quality basis sets for every atom type would be computationally very expensive. Moreover, results in section 4.5.1 for the absorption of s block ions suggest that larger basis set sizes on the surface atoms may have artificial side effects. Therefore, to probe the possible effect of basis set size on the absorption energies, we carried out single point calculations for every system in Table 5.1, 5.3 and 5.4 with def2-TZVP and def2-QZVP basis set only on the Sr^{2+}. The obtained adsorption energies are summarised in Table 5.5. Applying the def2-TZVP on the cation decreases the absorption energies by c. 10 kJ/mol on average for each group (**C**: 9.6 kJ/mol, **C_OH1**: 8.2 kJ/mol and **C_OH2**: 7.3 kJ/mol). Increasing the basis set quality to quadruple-ζ decreases the absorption energies further by c. 0.1-5.0 kJ/mol compared with the triple- and $\sim$ 7-14 kJ/mol compared with the double-ζ results.

Although the energy differences vary slightly between the different groups (and reference systems), this deviation is relatively small and there is essentially a constant energy shift between the double-ζ and higher basis sets.

Table 5.5: Dependence of the absolute adsorption energies (kJ/mol) on the basis set quality of the Sr^{2+} for systems from Table 5.1, 5.3 and 5.3 calculated with Eq. (5.2). (Standard deviations calculated for each averages are shown in brackets.)

systems	def2-SVP	$\triangle E$(TZVP-SVP)	def2-TZVP	$\triangle E$(QZVP-TZVP)	def2-QZVP
C1	-338.1	-10.8	-348.9	-6.9	-355.8
C2	-304.0	-12.7	-316.7	-4.6	-321.4
C3	-289.9	-7.8	-297.7	-5.3	-303.0
C4	-283.4	-7.2	-290.6	-2.6	-293.2
C5	-247.9	-9.7	-257.6	-5.6	-263.2
average		-9.6 (2.0)		-5.0 (1.4)	
C_OH2_1	38.1	-5.9	32.2	-0.7	31.5
C_OH2_2	59.3	-8.9	50.3	-0.4	49.9
C_OH2_3	151.6	-8.2	143.4	1.8	145.2
C_OH2_4	131.6	-6.9	124.7	-0.1	124.6
C_OH2_5	145.4	-6.5	139.0	0.1	139.1
average		-7.3 (1.1)		0.1 (0.9)	
C_OH1_1	-115.1	-7.3	-122.4	-3.9	-126.3
C_OH1_2	-113.3	-8.9	-122.2	-2.8	-125.0
C_OH1_3	-98.4	-9.9	-108.3	-2.5	-110.8
C_OH1_4	-110.5	-8.4	-118.9	-4.7	-123.7
C_OH1_5	-59.6	-7.0	-66.6	-1.8	-68.4
C_OH1_6	-26.7	-6.8	-33.5	-2.0	-35.5
C_OH1_7	4.5	-8.4	-3.9	-2.4	-6.2
average		-8.1 (1.0)		-2.9 (1.0)	

We attempted to evaluate a COSMO correction term for the adsorbed complexes by using a similar solvation scheme as Faheem *et al.*[298]. They proposed an approach called implicit solvation model for solid surfaces (iSMS), in which they use a combination of periodic slab calculations with plane wave DFT code in the absence of solvent and cluster models embedded in the implicit continuum solvent to evaluate correct energies for the studied reactions; in their case for the C-C bond cleavage of dehydrogenated ethylene glycol on Pt (111) in water. To obtain constant correction terms for the three groups, first we evaluated the adsorption energies with the same theoretical equation (5.2) for every structure in each group, but with the COSMO implicit solvent model on the W24 complexes (gas phase PEECM surface structures vs COSMO solvated complexes). Then, we calculated COSMO single point energies for the

optimised QM clusters without the PC region for one structure in each group and used these to recalculate the adsorption energies (COSMO QM clusters vs COSMO solvated complexes). We considered the differences between the two type of interaction energies as COSMO correction terms for the PEECM system and used them to modify the absorption energy of every structure in each group. The obtained energies are summarised in Figure 5.21.

Using the modified values results in positive absolute adsorption energies in almost every case, suggesting that the existence of adsorbed complexes on the protonated surfaces is always unfavoured compared with the solvated Sr^{2+} structures. The **C** systems are predicted to be 50-140 kJ/mol less stable in energy than the solvated complex used for reference, while the **C_OH1** structures are unfavourable by 30-150 kJ/mol and the adsorption energies of the **C_OH2** systems are between -20 and +150 kJ/mol, leaving one structure (**C_OH2_1**) with a slightly negative adsorption energy.

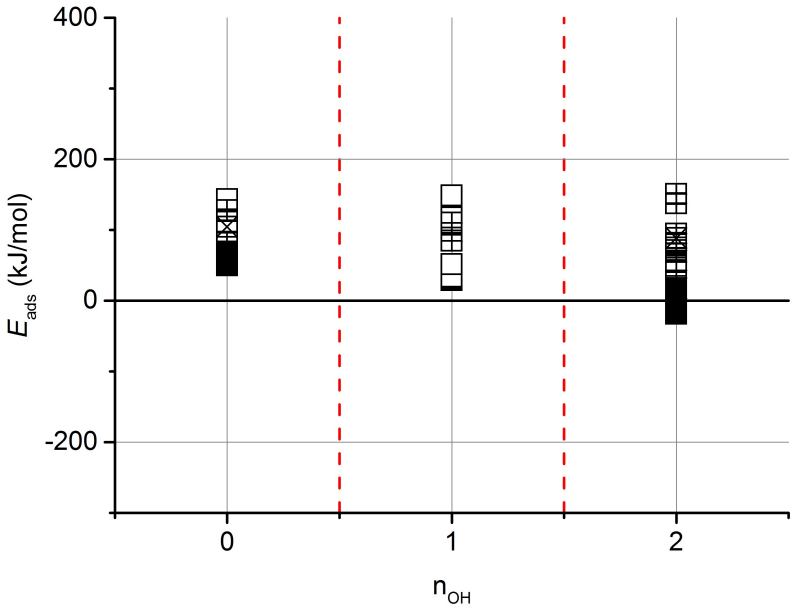

Figure 5.21: Absolute absorption energies obtained by using the COSMO corrected version of Eq. 5.2 with the appropriate reference systems in aqueous phase for the C, C_OH1 and C_OH2 groups vs. the total number of solvated OH^- ions introduced in the system. (black=hydrates, white=monohydroxides, plus=dihydroxides, cross=trihydroxides)

The recent experimental study of the National Nuclear Laboratory on Sr^{2+} ion adsorption on brucite shows only a weak or no interaction between the hydrated mineral and the cation in a $<$ pH 11 environment, (i.e. when the terminating OH groups are protonated) and a favoured adsorption above that.[299] Since we use a protonated neutral surface model for representing the empty hydrated brucite surface, we always remain in the former pH regime. Both Figure 5.20 and 5.21 predicts weak or unfavourable interactions in the presence of solvated OH^-

ions, but the COSMO corrected results show a generally unfavoured interaction regardless of the charge environment. Since the model used in Figure 5.21 considers the reference systems in aqueous phase and contains a limited solvent correction for surface model too, we assume that it represents a more realistic picture and therefore its results are closer to the true values. However, by artificially combining two originally incompatible methods (PEECM and COSMO), we may introduce unexpected errors during the ”tailoring” which cannot occur when every component of the equations is in gas phase.

5.5 Conclusions

To study the interaction which is the main focus of this project, namely the adsorption behaviour of Sr^{2+} ions on brucite in the aqueous phase, the previously optimised PEECM model was improved by introducing hydration layers above the surface and a theoretical equation was used to evaluate adsorption energies. Overall, we found that the adosrption of Sr^{2+} hydrates and hydroxides is not favoured close to neutral pH conditions.

To model water layers above the surface cluster, the initial geometries of the explicit water molecules and the positions of the point charge water equivalents are based on the molecular dynamic studies of Sakuma *et al.*[278] The final model contains 2 hydration layers in the so-called C water coordination, with 72 explicit water molecules in the QM cluster above the surface. During the optimisation, spontaneous surface protonation occurred between the first layer water molecules and the up-facing OH groups of brucite, which resulted in two solvated OH^- ions in the hydration layers. The formation of positive surface species in neutral solutions is expected on the basis of the experimental study of Pokrovosky and Schott[268] and therefore we proceeded with that optimised model without further corrections.

The Sr^{2+} was introduced to the system by placing it at different distances from the surface but always in the middle of the QM cluster. Systems containing 0, 1 and 2 additional solvated OH^- ions, were examined to study the effect of differently charged environments. The structures of the Sr complexes obtained were analysed based on their total coordination number, the Sr-surface distance and the number of directly coordinated OH^- ions or OH surface groups. The adsorption energies were calculated from an equation which compares the energy of the adsorbed Sr^{2+} ions with the energy of the chosen W24 water cluster based reference systems in gas phase and with an additional COSMO correction term.

Structures obtained in each of the three different groups (**C**, **C_OH1**, **C_OH2**) are all in a $\sim$100-120 kJ/mol energy range, which is reasonable considering the fact that they may vary

in their hydrogen bond network as well as in the Sr coordination, and test calculations show that, for example, the energy gain by the formation of a single hydrogen bond is $\sim$14 kJ/mol between two water molecules and $\sim$50 kJ/mol between an OH^- ion and a water molecule.

After analysis of the optimised complexes in Figure 5.10, 5.13 and 5.14 and further studies of the Sr-surface distance relations by constrained optimisations in Figure 5.17, 5.18 and 5.19, we can conclude that generally the inner shell complexes tend to be more stable than the outer shell ones. In addition, the most stable directly surface coordinated structures are usually Sr^{2+} hydrates with a total coordination number of 7. This result is consistent with previous solvation studies, which predict the most stable coordination of a hydrated complex to be between 6 or 8 (see chapter 3). Gradually moving away from the surface, the outer shell complexes, with only a few exceptions, have a lower total coordination number as well as more OH^- ions coordinated to the cation than the inner shell ones.

Using a surface model ***6x6_2_f*** to account for the effect of a second brucite layer on the adsorption, in some cases affects the geometries and the absorption energies, but usually only for the less stable complexes. The most stable ones and the general energetic order are unaffected. This observation is supported by the electron density difference plots of structures **C1** and **C3**, where we see smaller contributions from the surface groups (Figure 5.12) than in the case of adsorbed complexes on a bare brucite surface (Figure 4.12 and 4.17).

The natural charges in the **C** structures show a clear difference between the oxygen atoms of the solvated OH^- ions and the OH surface groups, as well as suggest a qualitative difference between Sr-O(surf) and Sr-O(OH) coordinations. The obtained oxygen charges (Table 5.2) together with the electron density difference plots (Figure 5.12) show the relatively local effect of the cation and the polarisation of the directly coordinated O atoms.

Finally, we attempted to study the effect of differently charged aqueous environments on the adsorption behaviour, by comparing the obtained adsorption energies of the **C**, **C_OH1** and **C_OH2** groups. In the gas phase, the Sr-brucite interaction is unfavoured in the presence of additional OH^- ions; while based on COSMO corrected energies, the adsorption of Sr species on brucite is generally unfavoured in the aqueous phase, which is consistent with recent experimental results in below pH 11 conditions. Based on these results, we conclude that our PEECM-COSMO model of the (0001) surface successfully describes the interaction of Sr complexes and hydrated (0001) surface in neutral conditions.

Chapter 6

Conclusions

In this chapter, we reflect back on our original computational goals and results, how well they have been accomplished and what are the possible ways forward. We also draw a final conclusion based on our findings for the proposed industry related question: what are the possible interactions between Sr^{2+} and brucite surfaces?

6.1 Computational achievements

6.1.1 Studying the hydrolysis of Sr^{2+} in aqueous environment

The accurate modelling of solvated Sr^{2+} hydroxide complexes was an important first step for creating a reference system for the ion's behaviour in the liquid phase of the nuclear storage ponds (see section 1.4.1). While Sr^{2+} hydrates were extensively studied before, the formation hydroxide complexes in water has not been modelled so far. In our DFT based computational study presented in chapter 3, we showed the importance of carrying out geometry optimisations with the use of an implicit solvent model and with a sufficiently large explicit solvation shell in investigating the structure and energetics of Sr^{2+} hydroxide complexes.

We used the W24 water cluster (which has been employed for modelling the solvation shell of organic molecules and ions before but not of single ions) as the first two solvation shell of Sr, because on one hand, it contained enough number of water molecules to account for maximum 8 Sr coordinated waters and 2 additional water molecules for each first shell ligand; and on the other hand, it allowed us to establish proton transfer with a small energy barrier and predict the generally less favoured hydroxide complexes (tri- and tetrahydroxide). However, we note that treating systems containing negatively charged species is generally difficult in implicit solvent models due to the more diffuse nature of negative charge, and therefore systems with and overall negative charge are usually avoided.

Overall, with the use of a combined implicit and explicit solvent model containing both the first and second hydration shells, we found that the mono- and dihydroxides are the thermodynamically most stable Sr complexes in a high pH aqueous solution and that they coexist. The obtained stable species play an important role in chapter 5, where they are used to calculate the stability Sr^{2+} complexes adsorbed on the (0001) surface of brucite.

Based on the successful prediction of the energetics of Sr^{2+} hydrolysis, we suggest that a similar model could be applied to study the solvation of other relevant ions and complexes in the nuclear waste industry, such as the much less investigated Cs^{+}, or the carbonate complex of strontium.

6.1.2 Creating a suitable surface representation of (0001) brucite surface

A significant part of this thesis is concerned with optimising a surface model for studying the adsorption of Sr^{2+} on the hydrated (0001) brucite surface (chapter 4). To meet with the specified requirements in section 1.4.2, we decided to employ a PEECM model, because it is implemented in the same code we used for the solvation study, it describes isolated adsorption sites and charged systems, does not require supercomputers to run and our main interest is the local environment of the possible reactions and we were less concerned with the large-scale surface properties.

Surface models, containing one or two layers in the QM cluster and iteratively defined natural charges in the PC region, were optimised and validated through several model adsorption studies involving single ions and Sr complexes. To verify that the PEECM model is as capable of describing adsorption on the brucite surface as well as other periodic DFT based methods, we carried out further test investigations comparing the energies obtained with the two different methods, with great success. As opposed to other previously modelled surfaces with PEECM, brucite (0001) is not purely ionic and has a layered structure with a large interfacial distance. Our research showed that this method can be successfully extended to be applied to the most stable surface of brucite, and hopefully it will be used for similar materials in the future.

As the purpose of the completed test calculations were to prove that the PEECM model gives realistic energetic orders for the adsorption of Sr and other alkaline metal ions, we did not investigated the structural differences of individual structures in detail and did not explore the possibility to improve every test system further with introducing hydration or solvent molecules. This could be the subject of an individual study in which the presented single ion adsorption and substitution could be extended with similar solvation models as it was established in chapter 5 and more in-depth structural analysis could be do to justify the experienced differences between ions.

6.1.3 Studying the interactions between the solvated Sr^{2+} and hydrated (0001) brucite surface

Perhaps the greatest challenge of this project was to combine the approaches applied in chapter 3 and 4 to investigate the adsorption of Sr^{2+} hydrate and hydroxide complexes on a hydrated (0001) surface. To allow this, we extended the established surface model with layers of water above it. To the best of our knowledge, although other QM/MM methods have been employed to model hydrated surfaces before, the PEECM has not yet been used for such problems. We used the results of previous MD studies to introduce water molecules both within the QM and PC region. Although we simplified our model by only using one of the predicted stable water coordinations, the created model gave reasonable results compared with experimental findings, e.g. it predicted the protonation of surface species. However, it is possible that with the construction of an optimised water cluster based on more than one type of the MD simulated water positions in the PC and QM region, the created hydrated surface model would be even more realistic, at least more in agreement with the MD results.

We used a theoretical reaction to compare the energies of Sr complexes adsorbed to the hydrated brucite surface and solvated in water, and calculated adsorption energies ion with or without additional hydroxides available in the water layers. With the application of a COSMO correction to account for long-range solvation effects, we came to the main conclusion that the interaction between the Sr^{2+} cation and brucite (0001) is unfavoured in below pH 11 aqueous environment. This results agreed with the recent experimental findings and made us believe that the application of the PEECM model and the three step approach for investigating the interactions between the Sr ion and the (0001) brucite surface presented in this thesis, can be generalised and employed to other problems of nuclear relevance, such as uranyl ion transport in common soil components or sorption mechanisms in zeolite type ion exchangers.

The whole project was carried out using different implementations of the TURBOMOLE program, which makes the investigation relatively simple. Since this code does not require a massively parallelised version and it can be run efficiently on a local computer server (see section 2.7.4.1), the presented calculations are very cost efficient making the developed process a viable alternative for studying surface mechanisms on similar surface.

6.1.4 Future Works

We propose several possible ways where this project could directly progress, such as the solvation study of Cs^{+} or carbonated strontium with the combined explicit-implicit solvent

model and the extended study of ionic adsorption and substitution on brucite (0001) involving other industrially relevant alkaline earth ions and their detailed structural analysis. Subsequently, the description of the hydrated brucite surface could be improved by considering a combination of the MD predicted water coordinations in the PC and QM region or, as an alternative hydrated surface model, the application of a droplet-like water cluster above the surface without water equivalents in the PC region could be explored.

As the solvation/hydrolysis of Sr^{2+} and its behaviour at the water/brucite interface is a dynamic phenomenon with average coordination properties, *ab initio* MD simulations would be perfect to complement our study. A similar project is already on-going in the research group of Dr Andy Kerridge at Lancaster University by Olivia Lynes who also uses the herein optimised structures as templates for further investigation. However, based on this work and the recent experimental results of NNL, the Sr/brucite interaction is insignificant in the sludge when the brurcite surface is protonated,[299] and investigating the other surfaces of brucite or even other minerals might be more useful.

6.2 Industrial relevance

As far as our model can predict, there are no favoured interactions, between the solvated Sr^{2+} complexes and the hydrated (0001) brucite surface in $<$ pH 11 conditions where the solvated complexes are always be more favourable than the adsorbed ones. These findings are backed with recent experimental results, which show no significant interaction between the brucite and Sr^{2+} ion below pH 11 solutions.[299] Nonetheless, a significant strontium uptake is detected in the settling tanks of the ion exchange process, i.e. some material which has a bigger particle size interacts with the ion. Therefore the question remains, what happens to the strontium in the ponds?

One possibility is that the majority of the Sr^{2+} ions are carbonated by dissolved carbon dioxide and the formed Sr-carbonate complexes interact with the brucite surface similarly to reported uranyl-carbonate complexes [12]. However, $SrCO_3$ most likely precipitates from the solution as a white powder, since it is practically insoluble in water (unless the solution is not saturated with carbon dioxide). In case of precipitation, the usual particle size of the $SrCO_3$ is small (submicron), thus it is more likely to be filtered out in the sand bed filters than remain in the settling tanks, where the uptake was measured.

The fact that some sorption capacity was measured for Sr^{2+} on brucite [14], could be due to other, non-basal surfaces. In the case of similar minerals to brucite, it is sometimes reported

that surface protonation/deprotonation, which create possible adsorption sites for future ionic interactions, can occur only on lateral surfaces.[300, 301] However, since the (0001) basal surface is by far the most stable and therefore the most common surface of brucite, even if the Sr^{2+} ion favourably interacts with the edges, they are so much less common, that they cannot possibly be solely responsible for the significant strontium uptake.

Overall, it is more likely that another material, which co-exists with the formed magnesium-hydroxide in the solid phase, adsorbs the Sr^{2+} complexes. According to Gregson *et al.*[11], there are other Mg based phases, such as hydrotalcite and Mg-hydroxycarbonate, together with *in-situ* formed uranium oxide particles within the corroded Magnox sludge. Preliminary experimental results predict possible interactions between uranium oxide and Sr^{2+}, therefore the industrially most useful continuation of this project would be to investigate those interactions with computational methods.

Bibliography

[1]J. J. Hastings, D. Rhodes, A. S. Fellerman, D. Mckendrick, and C. Dixon, “New approaches for sludge management in the nuclear industry”, Powder Technology **174**, 18–24 (2007).

[2]S. Owens, M. Higgins-Bos, M. Bankhead, and J. Austin, “Using Chemical And Process Modelling to Design, Understand and Improve an Effluent Treatment Plant”, NNL Science, 4–13 (2015).

[3]S. E. Jensen and E. Nonbøl, *Description of the Magnox Type of Gas Cooled Reactor (MAGNOX)*, November (Risø National Laboratory, Roskilde, Denmark, 1999), pp. 1–83.

[4]P. Greenfield, “A Comparison of Magnox A 12 and ZA Alloys as Canning Materials for Nuclear Reactors”, Journal of Nuclear Materials **11**, 121–134 (1964).

[5]G. T. Higgins, “Secondary Recrystallisation in Magnox AL 80”, Journal of Nuclear Materials **8**, 153–159 (1963).

[6]G. T. Higgins and B. W. Pickles, “Some observations of the pick-up of hydrogen in MAGNOX ZR 55 and its relation to mechanical properties”, Journal of Nuclear Materials **8**, 160–168 (1963).

[7]Photo Credit: Prof. B. Marsden, University of Manchester, NGRG, *Oldbury visit part one, Oldbury MAGNOX fuel element in graphite brick - http://www.nuclearbritain.com*.

[8]Sellafield Ltd., *Risk&Hazard Solution, http://www.sellafieldsites.com*.

[9]M. E. Pick, “Magnox Graphite Core Decommissioning and Disposal Issues”, in *Progress in radioactive graphite waste management* (Waste Technology Section , International Atomic Energy Agency, Vienna International Centre, 2010), pp. 1–14.

[10]Nuclear Decommissioning Authority, Deparment of Energy & Climate Change, *Radioactive Wastes in the UK : A Summary of the 2013 Inventory*, tech. rep. (2013), pp. 1–15.

[11]C. R. Gregson, D. T. Goddard, M. J. Sarsfield, and R. J. Taylor, “Combined electron microscopy and vibrational spectroscopy study of corroded Magnox sludge from a legacy spent nuclear fuel storage pond”, Journal of Nuclear Materials **412**, 145–156 (2011).

[12]Q. Cao, F. Huang, Z. Zhuang, and Z. Lin, “A study of the potential application of nano-$Mg(OH)_2$ in absorbing low concentrations of uranyl tricarbonate from water”, Nanoscale **4**, 2423–2430 (2012).

[13]J. D. Farr, M. P. Neu, R. K. Schulze, and B. D. Honeyman, “Plutonium uptake by brucite and hydroxylated periclase”, Journal of Alloys and Compounds **444-445**, 533–539 (2007).

[14]G. R. Bochkarev and G. I. Pushkareva, “Mineral Dressing - Strontium Removal from Aqeous Media by Natural and Modified Sorbents”, Journal of Mining Science **45**, 290–294 (2009).

[15]S. H. Wallace, S. Shaw, K. Morris, J. S. Small, A. J. Fuller, and I. T. Burke, “Effect of groundwater pH and ionic strength on strontium sorption in aquifer sediments: Implications for ^{90}Sr mobility at contaminated nuclear sites”, Applied Geochemistry **27**, 1482–1491 (2012).

[16]A. J. Francis, C. J. Dodge, and T. Ohnuki, “Microbial Transformations of Plutonium”, Journal of Nuclear and Radiochemical Sciences **8**, 121–126 (2007).

[17]H. Boukhalfa, G. A. Icopini, S. D. Reilly, and M. P. Neu, “Plutonium(IV) Reduction by the Metal-Reducing Bacteria *Geobacter metallireducens* GS15 and *Shewanella oneidensis* MR1.”, Applied and Environmental Microbiology **73**, 5897–5903 (2007).

[18]K. Hirose and M. Aoyama, “Chemical speciation of plutonium in seawater”, Analytical and Bioanalytical Chemistry **372**, 418–420 (2002).

[19]W. Runde, S. D. Conradson, D. W. Efurd, N. Lu, C. E. VanPelt, and C. D. Tait, “Solubility and sorption of redox-sensitive radionuclides (Np, Pu) in J-13 water from the Yucca Mountain site: comparison between experiment and theory”, Applied Geochemistry **17**, 837–853 (2002).

[20]G. Meinrath, “Uranium (VI) speciation by spectroscopy”, Journal of Radioanalytical and Nuclear Chemistry **224**, 119–126 (1997).

[21]D. Langmuir, “Uranium Solution - Mineral Equilibria at Low Temperatures with Applications to Sedimentary Ore Deposits”, Geochimica et Cosmochimica Acta **42**, 547–569 (1978).

[22]A. L. Nichols, D. L. Aldama, and M. Verpelli, “C-3.3. U-235 cumulative fission yields for selected fission products”, in *Handbook of nuclear data for safeguards: database extensions*, August (Nuclear Data Section , International Atomic Energy Agency, Wagramer Strasse 5, A-1400 Vienna, Austria, 2008), pp. 105–106.

[23]M.-M. Bé, V. Chisté, C. Dulieu, E. Browne, C. Baglin, V. Chechev, N. Kuzmenco, R. Helmer, F. Kondev, D. MacMahon, and K. B. Lee, in *Table of radionuclides - a=3 to 244*, Vol. 3, Monographie BIPM-5 (Bureau International des Poids et Mesures, Pavillon de Breteuil, F-92310 Sèvres, France, 2006).

[24]D. Di Tommaso and N. H. de Leeuw, “First principles simulations of the structural and dynamical properties of hydrated metal ions Me^{2+} and solvated metal carbonates (Me = Ca, Mg, and Sr)”, Crystal Growth and Design **10**, 4292–4302 (2010).

[25]*Some aspects of strontium radiobiology*, Vol. Report No. 110 (NCRP, National Council on Radiation Protection and Measurements, Bethesda, MD, 1991), p. 94.

[26]United States Environmental Protection Agency, *Radiation Protection - Radionuclide Basics, http://www.epa.gov*.

[27]F. Cadini, E. Tosoni, and E. Zio, "Modeling the release and transport of ^{90}Sr radionuclides from a superficial nuclear storage facility", Stochastic Environmental Research and Risk Assessment **30**, 693–712 (2016).

[28]Z. Maher, J. Storey, J. Rawcliffe, D. Goddard, L. O'Brien, and N. Bryan, *Actinide Abatement in SIXEP*, tech. rep. (University of Manchester, 2012).

[29]J. E. Earp and D. R. Thompson, "Radio Active Waste Plants - Back to the Future - 8324", in Proceedings of the WM2008 Conference (2008).

[30]Ion Exchange Application in Wastewater Treatment, *http://www.wastewatersystem.net*.

[31]International Atomic Energy Agency, "Application of Ion Exchange Processes for the Treatment of Radioactive Waste and Management of Spent Ion Exchangers", Technical reports series No.408 (2002).

[32]S. A. Fuente, C. A. Ferretti, N. F. Domancich, V. K. Díez, C. R. Apesteguía, J. I. Di Cosimo, R. M. Ferullo, and N. J. Castellani, "Adsorption of 2-propanol on MgO surface: A combined experimental and theoretical study", Applied Surface Science **327**, 268–276 (2015).

[33]J. R. B. Gomes and J. A.N. F. Gomes, "Adsorption of the formyl species on transition metal surfaces", Journal of Electroanalytical Chemistry **483**, 180–187 (2000).

[34]X.-Y. Pang, C. Wang, Y.-H. Zhou, J.-M. Zhao, and G.-C. Wang, "DFT study of the structure sensitivity for the adsorption of methyl, methoxy, and formate on Ni(111), Ni(100), and Ni(110) surfaces", Journal of Molecular Structure: THEOCHEM **948**, 1–10 (2010).

[35]E. Veilly, J. Roques, M.-C. Jodin-Caumon, B. Humbert, R. Drot, and E. Simoni, "Uranyl interaction with the hydrated (001) basal face of gibbsite: A combined theoretical and spectroscopic study", Journal of Chemical Physics **129**, 244704 (2008).

[36]K. W. Corum and S. E. Mason, "Establishing trends in ion adsorption on the aqueous aluminium hydroxide nanoparticle Al_{30}", Molecular Simulation **41**, 146–155 (2015).

[37]S. Chrétien and H. Metiu, "Density functional study of the charge on Au_n clusters (n=1-7) supported on a partially reduced rutile TiO_2(110): Are all clusters negatively charged?", Journal of Chemical Physics **126**, 104701 (2007).

[38]H. Weber, T. Bredow, and B. Kirchner, "Adsorption Behavior of the 1,3-Dimethylimidazolium Thiocyanate and Tetracyanoborate Ionic Liquids at Anatase (101) Surface", Journal of Physical Chemistry C **119**, 15137 (2015).

[39]S. K. Ramadugu and S. E. Mason, "DFT Study of Antimony (V) Oxyanion Adsorption on α-Al_2O_3 ($1\bar{1}02$)", Journal of Physical Chemistry C **119**, 18149–18159 (2015).

[40]S. E. Mason, C. R. Iceman, K. S. Tanwar, T. P. Trainor, and A. M. Chaka, "Pb(II) Adsorption on Isostructural Hydrated Alumina and Hematite (0001) Surfaces: A DFT Study", Journal of Physical Chemistry C **113**, 2159–2170 (2009).

[41]S. Yang, C. Chen, Y. Chen, J. Li, D. Wang, X. Wang, and W. Hu, "Competitive Adsorption of Pb^{II}, Ni^{II}, and Sr^{II} Ions on Graphene Oxides: A Combined Experimental and Theoretical Study", ChemPlusChem **80**, 480–484 (2015).

[42]G. García, M. Atilhan, and S. Aparicio, "Adsorption of choline benzoate ionic liquid on graphene, silicene, germanene and boron-nitride nanosheets: a DFT perspective", Physcal Chemistry Chemical Physics **17**, 16315–16326 (2015).

[43]X. Tan, M. Fang, and X. Wang, "Sorption Speciation of Lanthanides/Actinides on Minerals by TRLFS, EXAFS and DFT Studies: A Review", Molecules **15**, 8431–8468 (2010).

[44]J. A. Greathouse, R. J. O'Brien, G. Bemis, and R. T. Pabalan, "Molecular Dynamics Study of Aqueous Uranyl Interactions with Quartz (010)", The Journal of Physical Chemistry B **106**, 1646–1655 (2002).

[45]S. Lectez, J. Roques, M. Salanne, and E. Simoni, "Car-Parrinello molecular dynamics study of the uranyl behaviour at the gibbsite/water interface.", The Journal of Chemical Physics **137**, 154705 (2012).

[46]T. Hattori, T. Saito, K. Ishida, A. C. Scheinost, T. Tsuneda, S. Nagasaki, and S. Tanaka, "The structure of monomeric and dimeric uranyl adsorption complexes on gibbsite: A combined DFT and EXAFS study", Geochimica et Cosmochimica Acta **73**, 5975–5988 (2009).

[47]A. Kremleva, S. Krüger, and N. Rösch, "Toward a Reliable Energetics of Adsorption at Solvated Mineral Surfaces: A Computational Study of Uranyl(VI) on 2:1 Clay Minerals", Journal of Physical Chemistry C **120**, 324–335 (2016).

[48]F. M. Higgins, N. H. de Leeuw, and S. C. Parker, "Modelling the effect of water on cation exchange in zeolite A", Journal of Materials Chemistry **12**, 124–131 (2002).

[49]M. Johnson, D. O'Connor, P. Barnes, C. R. A. Catlow, S. L. Owens, G. Sankar, R. Bell, S. J. Teat, and R. Stephenson, "Cation exchange, Dehydration, and Calcination in Clinoptilolite: In situ X-ray Diffraction and Computer Modeling", Journal of Physical Chemistry B **107**, 942–951 (2003).

[50]E. Shock, D. C. Sassani, M. Willis, and D. Sverjensky, “Inorganic species in geologic fluids: Correlations among standard molal thermodynamic properties of aqueous ions and hydroxide complexes”, Geochimica et Cosmochimica Acta **61**, 907–950 (1997).

[51]H Arcis, G. H. Zimmerman, and P. R. Tremaine, “Ion-pair formation in aqueous strontium chloride and strontium hydroxide solutions under hydrothermal conditions by AC conductivity measurements.”, Physical Chemistry Chemical Physics **16**, 17688–17704 (2014).

[52]V. Vallet, P. Macak, U. Wahlgren, and I. Grenthe, “Actinide chemistry in solution, quantum chemical methods and models”, Theoretical Chemistry Accounts **115**, 145–160 (2006).

[53]D. Rios, M. C. Michelini, A. F. Lucena, J. Marçalo, T. H. Bray, and J. K. Gibson, “Gas-Phase Uranyl, Neptunyl, and Plutonyl: Hydration and Oxidation Studied by Experiment and Theory.”, Inorganic chemistry **51**, 6603–6614 (2012).

[54]R. Dovesi, B. Civalleri, R. Orlando, C. Roetti, and V. R. Saunders, “Ab Initio Quantum Simulation in Solid State Chemistry”, Reviews in Computational Chemistry **21**, 1–126 (2005).

[55]S. C. Ammal and A. Heyden, “Modeling the noble metal/TiO_2 (110) interface with hybrid DFT functionals: A periodic electrostatic embedded cluster model study”, Journal of Chemical Physics **133**, 164703 (2010).

[56]A. M. Burow, M. Sierka, J. Döbler, and J. Sauer, “Point defects in CaF_2 and CeO_2 investigated by the periodic electrostatic embedded cluster method.”, The Journal of Chemical Physics **130**, 174710 (2009).

[57]A. V. Bandura, D. G. Sykes, V. Shapovalov, T. N. Troung, J. D. Kubicki, and R. A. Evarestov, “Adsorption of Water on the TiO_2 (Rutile) (110) Surface: A Comparison of Periodic and Embedded Cluster Calculations”, Journal of Physical Chemistry B **108**, 7844–7853 (2004).

[58]A. Szabo and N. S. Ostlund, *Modern Quantum Chemistry, Introduction to Advanced Electronic Structure Theory*, Frist Edition Revised (Dover Publication Inc., Mineola, New York, 1996).

[59]T. Veszprémi and M. Fehér, *A kvantumkémia alapjai és alkalmazása* (Műszaki Könykiadó, Budapest, 2002).

[60]F. Jensen, *Introduction to Computational Chemistry*, Second Edition (John Wiley & Sons Ltd., Chichester, West Sussex, England, 2007).

[61]D. Hartree, “The Wave Mechanics of an Atom with a Non-Coulomb Central Field. Part I. Theory and Methods”, Mathematical Proceedings of the Cambridge Philosophical Society **24**, 89–110 (1928).

[62]V. A. Fock, “Näherungsmethode zur Lösung des quantenmechanischen Mehrkörperproblems”, Zeitschrift für Physik **61**, 126–148 (1930).

[63]C. C. J. Roothaan, “New Developments in Molecular Orbital Theory”, Reviews of Modern Physics **23**, 69–89 (1951).

[64]K. Burke, “http://chem.ps.uci.edu/kieron/dft/book/ The ABC of DFT”, (2007).

[65]K. Burke and L. O. Wagner, “DFT in a nutshell”, International Journal of Quantum Chemistry **113**, 96–101 (2013).

[66]P. Hohenberg and W. Kohn, “Inhomogeneous Electron Gas”, Physical Review **136**, B864–B871 (1964).

[67]L. H. Thomas, “The calculation of atomic fields”, Mathematical Proceedings of the Cambridge Philosophical Society **23**, 542–548 (1927).

[68]E. Fermi, “Eine statistische Methode zur Bestimmung einiger Eigenschaften des Atoms und ihre Anwendung auf die Theorie des periodischen Systems der Elemente .”, Zeitschrift für Physik **48**, 73–79 (1928).

[69]P. A. M. Dirac, “Note on Exchange Phenomena in the Thomas Atom”, Mathematical Proceedings of the Cambridge Philosophical Society **26**, 376–385 (1930).

[70]L. J. Kohn, W; Sham, “Self-Consistent Equations Including Exchange and Correlation Effects”, Physical Review **140**, A1133–A1138 (1965).

[71]J. P. Perdew, A. Ruzsinszky, J. Tao, V. N. Staroverov, G. E. Scuseria, and G. I. Csonka, “Prescription for the design and selection of density functional approximations: more constraint satisfaction with fewer fits.”, The Journal of Chemical Physics **123**, 62201–62210 (2005).

[72]S. H. Vosko, L. Wilk, and M. Nusair, “Accurate spin-dependent electron liquid correlation energies for local spin density calculations: a critical analysis”, Canadian Journal of Physics **58**, 1200–1211 (1980).

[73]D. M. Ceperley and B. J. Alder, “Ground State of the Electron Gas by a Stochastic Method”, Physical Review Letters **45**, 566–569 (1980).

[74]J. Perdew, K. Burke, and M. Ernzerhof, “Generalized Gradient Approximation Made Simple.”, Physical Review Letters **77**, 3865–3868 (1996).

[75]A. D. Becke, “Density-functional exchange-energy approximation with correct asymptotic behavior”, Physical Review A **38**, 3098–3100 (1988).

[76]C. Lee, W. Yang, and R. G. Parr, “Development of the Colle-Salvetti correlation-energy formula into a functional of the electron density”, Physical Review B **37**, 785–789 (1988).

[77]J. Tao, J. P. Perdew, V. N. Staroverov, and G. E. Scuseria, “Climbing the Density Functional Ladder: Nonempirical Meta-Generalized Gradient Approximation Designed for Molecules and Solids”, Physical Review Letters **91**, 146401–146405 (2003).

[78]A. D. Becke, “Density-functional thermochemistry. III. The role of exact exchange”, The Journal of Chemical Physics **98**, 5648–5652 (1993).

[79]P. J. Stephens, F. J. Delvin, C. F. Chabalowski, and M. J. Frisch, “*AB INITIO* CALCULATION OF VIBRATIONAL ABSORPTION AND CIRCULAR DICHROISM SPECTRA USING DENSITY FUNCTIONAL FORCE FIELDS”, The Journal of Physical Chemistry **98**, 11623–11627 (1994).

[80]M. Ernzerhof and G. E. Scuseria, “Assessment of the Perdew-Burke-Ernzerhof exchange-correlation functional”, The Journal of Chemical Physics **110**, 5029–5036 (1999).

[81]V. N. Staroverov, G. E. Scuseria, J. Tao, and J. P. Perdew, “Comparative assessment of a new nonempirical density functional: Molecules and hydrogen-bonded complexes”, The Journal of Chemical Physics **119**, 12129–12137 (2003).

[82]Y. Zhao, N. González-Graíca, and D. G. Truhlar, “Benchmark Database of Barrier Heights for Heavy Atom Transfer, Nucleophilic Substitution, Association, and Unimolecular Reactions and Its Use to Test Theoretical Methods”, The Journal of Physical Chemistry A **109**, 2012–2018 (2005).

[83]S. Grimme, “Semiempirical GGA-Type Density Functional Constructed with a Long-Range Dispersion Correction”, Journal of Computational Chemistry **27**, 1787–1799 (2006).

[84]S. Grimme, J. Antony, S. Ehrlich, and H. Krieg, “A consistent and accurate *ab initio* parameterization of density functional dispersion correction (DFT-D) for the 94 elements H-Pu”, The Journal of Chemical Physics **132**, 154104 (2010).

[85]S. Grimme, “Accurate Description of van der Waals Complexes by Density Functional Theory Incuding Empirical Corrections”, Journal of Computational Chemistry **25**, 1463–1473 (2004).

[86]M. Sierka, A. Hogekamp, and R. Ahlrichs, “Fast evaluation of the Coulomb potential for electron densities using multipole accelerated resolution of identity approximation”, The Journal of Chemical Physics **118**, 9136–9148 (2003).

[87]K. Eichkorn, F. Weigend, O. Treutler, and R. Ahlrichs, “Auxiliary basis sets for main row atoms and transition metals and their use to approximate Coulomb potentials”, Theoretical Chemistry Accounts **97**, 119–124 (1997).

[88]F. Furche, R. Ahlrichs, C. Hättig, W. Klopper, M. Sierka, and F. Weigend, “Turbomole”, Wiley Interdisciplinary Reviews: Computational Molecular Science **4**, 91–100 (2014).

[89]J. C. Slater, “The Theory of Complex Spectra”, Physical Review **34**, 1293–1322 (1929).

[90]J. C. Slater, “Atomic Shielding Constants”, Physical Review **36**, 57–64 (1930).

[91]S. F. Boys, “Electronic wave functions: I. A general method of calculation for the stationary states of any molecular system”, Proceedings of the Royal Society of London A **200**, 542–554 (1950).

[92]R. C. Raffenetti, “General contraction of Gaussian atomic orbitals : Core , valence , polarization , and diffuse basis sets ; Molecular integral evaluation”, The Journal of Chemical Physics **58**, 4452–4458 (1973).

[93]J. S. Binkley, J. A. Pople, and W. J. Hehre, “Self-Consistent Molecular Orbital Methods. 21. Small Split-Valence Basis Sets for First -Row Elements”, Journal of the American Chemical Society **102:3**, 939–947 (1980).

[94]F. Weigend and R. Ahlrichs, “Balanced basis sets of split valence, triple zeta valence and quadruple zeta valence quality for H to Rn: Design and assessment of accuracy.”, Physical Chemistry Chemical Physics **7**, 3297–3305 (2005).

[95]T. R. Cundari, M. T. Benson, M. L. Lutz, and S. O. Sommerer, “Effective Core Potential Approaches to the Chemistry of the Heavier Elements”, Reviews in Computational Chemistry **8**, 145–202 (1996).

[96]A. Schaäfer, H. Horn, and R. Ahlrichs, “Fully optimized contracted Gaussian basis sets for atoms Li to Kr”, The Journal of Chemical Physics **97**, 2571 (1992).

[97]M. Kaupp, P. V. R. Schleyer, H. Stoll, and H. Preuss, “Pseudopotential approaches to Ca, Sr, and Ba hydrides. Why are some alkaline earth MX2 compounds bent?”, The Journal of Chemical Physics **94**, 1360–1366 (1991).

[98]S. F. Boys and F. Bernardi, “The calculation of small molecular interactions by the differences of separate total energies. Some procedures with reduced errors”, Molecular Physics **19**, 553–566 (1970).

[99]H. Ågren and K. V. Mikkelsen, “Theory of solvent effects on electronic spectra”, Journal of Molecular Structure: THEOCHEM **234**, 425–467 (1991).

[100]C. J. Cramer and D. G. Truhlar, “Implicit Solvation Models: Equilibria, Structure, Spectra, and Dynamics.”, Chemical Reviews **99**, 2161–2200 (1999).

[101]J. Tomasi, B. Mennucci, and R. Cammi, “Quantum mechanical continuum solvation models”, Chemical Reviews **105**, 2999–3093 (2005).

[102]P. Koehl, M. Levitt, and H. Edelsbrunner, “ProShape: Understanding the Shapes of Protein Structures (Volume, Surface and Pockets of Proteins), http://csb.stanford.edu/∼koehl/ProShape/protsurf.php”,

[103]J. Tomasi and M. Persico, “Molecular Interactions in Solution: An Overview of Methods Based on Continuous Distributions of the Solvent”, Chemical Reviews **94**, 2027–2094 (1994).

[104]A. Klamt and G. Schüürmann, “COSMO : A New Approach to Dielectric Screening in Solvents with Explicit Expressions for the Screening Energy and its Gradient”, Journal of Chemical Society, Perkin Transactions **2**, 799–805 (1993).

[105]A. Klamt, “The COSMO and COSMO-RS solvation models”, Wiley Interdisciplinary Reviews: Computational Molecular Science **1**, 699–709 (2011).

[106](2012).

[107]A. Klamt and V. Jonas, “Treatment of the outlying charge in continuum solvation models”, The Journal of Chemical Physics **105**, 9972 (1996).

[108]G. Makov and M. C. Payne, “Periodic boundary conditions in ab initio calculations”, Physical Review B **51**, 4014–4022 (1995).

[109]R. Beaume, J. Manuceau, A. Pellet, and M. Sirugue, “Translation Invariant States in Quantum Mechanics”, Communications in Mathematical Physics **38**, 29–45 (1974).

[110]F. Bloch, “Uber die Quantenmechanik der Elektronen in Kristallgittern”, Zeitschrift für Physik **52**, 555–600 (1928).

[111]R. Dovesi, V. R. Saunders, C. Roetti, R. Orlando, C. M. Zicovich-Wilson, F. Pascale, B. Civalleri, K. Doll, N. M. Harrison, I. J. Bush, P. D’Arco, M. Llunell, M. Causà, and Y. Noël, “Crystal14’s manual”, in (, 2014) Chap. Chapter 13: Theoretical framework.

[112]“TURBOMOLE USER’S MANUAL”, in *Turbomole version 6.5 : user’s manual program package for ab initio electronic structure calculations* (2012) Chap. 6.6 Period, pp. 132–139.

[113]W. W. Lee and S.-i. Choi, “Determination of the Madelung potential of ionic crystals with a polar surface by the Ewald method”, The Journal of Chemical Physics **72**, 6164–6168 (1980).

[114]P. P. Ewald, “Die Berechung optischer und elektrostatischer Gitterpotentiale”, Ann. Phys. (Leipzig) **64**, 253–287 (1921).

[115]K. N. Kudin and G. E. Scuseria, “A fast multipole method for periodic systems with arbitrary unit cell geometries”, Chemical Physics Letters **283**, 61–68 (1998).

[116]C. G. Broyden, “Quasi-Newton Methods and Their Application to Function Minimisation”, Mathematics of Computation **21**, 368–368 (1967).

[117]J. Nocedal and S. J. Wright, *Numerical Optimization*, 2nd ed. (Spring-Verlag New York, 2006).

[118]R. J. Boyd and C. F. Matta, *An Introduction to the Quantum Theory of Atoms in Molecules* (2007).

[119]R. F. W. Bader, *Atoms in Molecules: A Quantum Theory* (Oxford University Press, New York, 1990).

[120]C Gatti and S Casassa, *TOPOND14: User's Manual* (2014), pp. 1–48.

[121]S. J. Grabowski, “Hydrogen bonding strengthmeasures based on geometric and topological parameters”, Journal of Physical Organic Chemistry **17**, 18–31 (2004).

[122]A. Kerridge and N. Kaltsoyannis, “The coordination of Sr^{2+} by hydroxide : a density functional theoretical study”, Dalton Transactions **40**, 11258 (2011).

[123]B. Bankiewicz, P. Matczak, and M. Palusiak, “Electron Density Characteristics in Bond Critical Point (QTAIM) versus Interaction Energy Components (SAPT): The Case of Charge-Assisted Hydrogen Bonding”, Journal of Physical Chemistry A **116**, 452–459 (2012).

[124]N. Castillo, K. N. Robertson, S. C. Choi, R. J. Boyd, and O. Knop, “Bond Length and the Electron Density at the Bond Critical Point : X - X , Z - Z , and C - Z Bonds (X = Li-F, Z = Na-Cl)”, Journal of Computational Chemistry **29**, 367–379 (2007).

[125]I. Love, “Polar Covalent Bonds : An AIM Analysis of S,O Bonds”, Journal of Physical Chemistry A **113**, 2640–2646 (2009).

[126]A. R. E. Mountain and N. Kaltsoyannis, “Do QTAIM metrics correlate with the strength of heavy element-ligand bonds?”, Dalton Transactions **42**, 13477–13486 (2013).

[127]Q.-r. Huang, J. R. Kingham, and N. Kaltsoyannis, “The strength of actinide-element bonds from the quantum theory of atoms-in-molecules”, Dalton Transactions **44**, 2554–2566 (2015).

[128]P. D. Pietro and A. Kerridge, “Stretching Vibrations as a Quantitative Measure of the Equatorial Bond Covalency in Uranyl Complexes: A Quantum- Chemical Investigation”, Inorganic Chemistry **55**, 573–583 (2016).

[129]W. Zou, D. Nori-Shargh, and J. E. Boggs, “On the covalent character of rare gas bonding interactions: A new kind of weak interaction”, Journal of Physical Chemistry A **117**, 207–212 (2013).

[130]T. A. Keith, “AIMALL (Version 13.11.04)”, AIMALL (Version 13.11.04), Overland Park KS, USA, TK Gristmill Software (2013).

[131]A. E. Reed, R. B. Weinstock, and F. Weinhold, “Natural population analysis”, The Journal of Chemical Physics **83**, 735–746 (1985).

[132]P.-O. Löwdin, “Quantum Theory of Many-Particle Systems. I. Physical Interpretations by Means of Density Matrices, Natural Spin-Orbitals, and Convergence Problems in the Method of Configurational Interaction”, Physical Review **97**, 1474–1489 (1955).

[133]P.-O. Löwdin and H. Shull, “Natural Oribtals in the Quantum Theory of Two-Electron Systems”, Physical Review **101**, 1730–1739 (1956).

[134]R. S. Mulliken, “Criteria for the Construction of Good Self-Consistent-Field Molecular Orbital Wave Functions, and the Significance of LCAO-MO Population Analysis”, The Journal of Chemical Physics **36**, 3428–3439 (1962).

[135]T. Lu, *Multiwfn, A Multifunctional Wavefunction Analyzer: Software Manual for Version 3.3.9* (Beijing Quanton Technology Co. Ltd., Beijing Kein Research Center for Natural Sciences, 2016).

[136]TURBOMOLE V6.5 2013, a development of University of Karlsruhe and Forschungszentrum Karlsruhe GmbH, 1989-2007, TURBOMOLE GmBH, since 2007: available from http://www.turbomole.com.

[137]TURBOMOLE V6.6 2014, a development of University of Karlsruhe and Forschungszentrum Karlsruhe GmbH, 1989-2007, TURBOMOLE GmBH since 2007: available from http://www.turbomole.com.

[138]R. Dovesi, R. Orlando, A. Erba, C. M. Zicovich-Wilson, B. Civalleri, S. Casassa, L. Maschio, M. Ferrabone, M. De La Pierre, P. D’Arco, Y. Noël, M. Causà, M. Rérat, and B. Kirtman, “CRYSTAL14: A program for the *ab initio* investigation of crystalline solids”, International Journal of Quantum Chemistry **114**, 1287–1317 (2014).

[139]T. Lu and F. Chen, “Multiwfn: A multifunctional wavefunction analyzer”, Journal of Computational Chemistry **33**, 580–592 (2012).

[140]R. Dovesi, C. Pisani, C. Roetti, M. Causà, and V. R. Saunders, *CRYSTAL 88, An Ab Initio All-Electron LCAO-HARTREE-FOCK Program for Periodic Systems*, Indiana University, Bloomington, 1989.

[141]R. Dovesi, V. R. Saunders, C. Roetti, R. Orlando, C. M. Zicovich-Wilson, F. Pascale, B. Civalleri, K. Doll, N. M. Harrison, I. J. Bush, P. D’Arco, M. Llunell, M. Causà, and Noël (University of Torino, Torino).

[142]A. R. Felmy, D. A. Dixon, J. R. Rustad, M. J. Mason, and L. M. Onishi, “The hydrolysis and carbonate complexation of strontium and calcium in aqueous solution. Use of molecular

modeling calculations in the development of aqueous thermodynamic models", The Journal of Chemical Thermodynamics **30**, 1103–1120 (1998).

[143]S. E. Rodriguez-Cruz, R. A. Jockusch, and E. R. Williams, "Hydration Energies and Structures of Alkaline Earth Metal Ions, $M^{2+}(H_2O)_n$, n = 5-7, M = Mg, Ca, Sr, and Ba", Journal of the American Chemical Society **121**, 8898–8906 (1999).

[144]D. R. Carl, B. K. Chatterjee, and P. B. Armentrout, "Threshold collision-induced dissociation of $Sr^{2+}(H_2O)_x$ complexes (x=1-6): An experimental and theoretical investigation of the complete inner shell hydration energies of Sr^{2+}.", The Journal of Chemical Physics **132**, 044303 (2010).

[145]M. Peschke, A. T. Blades, and P. Kebarle, "Hydration Energies and Entropies for Mg^{2+}, Ca^{2+}, Sr^{2+}, and Ba^{2+} from Gas-Phase Ion-Water Molecule Equilibria Determinations", Journal of Physical Chemistry A **102**, 9978–9985 (1998).

[146]I. Persson, M. Sandström, and H. Yokoyama, "Structure of the Solvated Strontium and Barium Ions in Aqueous, Dimethyl Sulfoxide and Pyridine Solution, and Crystal Structure of Strontium and Barium Hydroxide Octahydrate", Z. Naturforsch **50 a**, 21 (1995).

[147]V. H. W. Grueninger and H. Bärnighausen, "Die Kristallstruktur von Strontiumhydroxid $Sr(OH)_2$", Zeitschrift für anorganische und allgemeine Chemie **368**, 53–61 (1969).

[148]E. D. Glendening and D. Feller, "Dication-Water Interactions : $M^{2+}(H_2O)_n$ Clusters for Alkaline Earth Metals M=Mg, Ca, Sr, Ba and Ra", Journal of Physical Chemistry **100**, 4790–4797 (1996).

[149]A. Kerridge and N. Kaltsoyannis, "Quantum Chemical Studies of the Hydration of Sr^{2+} in Vacuum and Aqueous Solution.", Chem. Eur. J. **17**, 5060–5067 (2011).

[150]A. Boda, S. De, S. M. Ali, S. Tulishetti, S. Khan, and J. K. Singh, "From microhydration to bulk hydration of Sr^{2+} metal ion: DFT, MP2 and molecular dynamics study", Journal of Molecular Liquids **172**, 110–118 (2012).

[151]A. Y. Mehandzhiyski, E. Riccardi, T. S. van Erp, T. T. Trinh, and B. A. Grimes, "Ab Initio Molecular Dynamics Study on the Interactions between Carboxylate Ions and Metal Ions in Water", The Journal of Physical Chemistry B **119**, 150803215345002 (2015).

[152]J. N. Albright, "X-Ray Diffraction Studies of Aqueous Alkaline-Earth Chloride Solutions", The Journal of Chemical Physics **56**, 3783–3786 (1972).

[153]R. Caminiti, A. Musinu, G. Paschina, and G. Pinna, "X-Ray-Diffraction Study of Aqueous $SrCl_2$ Solutions", Journal of Applied Crystallography **15**, 482–487 (1982).

[154]S. Ramos, G. W. Neilson, a. C. Barnes, and M. J. Capitán, "Anomalous x-ray diffraction studies of Sr^{2+} hydration in aqueous solution", The Journal of Chemical Physics **118**, 5542–5546 (2003).

[155]D. M. Pfund, J. G. Darab, J. L. Fulton, and Y. Ma, "An XAFS Study of Strontium Ions and Krypton in Supercritical Water", The Journal of Physical Chemistry **98**, 13102–13107 (1994).

[156]G. Moreau, L. Helm, J. Purans, and A. E. Merbach, "Structural Investigation of the Aqueous Eu^{2+} Ion : Comparison with Sr^{2+} Using the XAFS Technique", Journal of Physical Chemistry A **106**, 3034–3043 (2002).

[157]P. D'Angelo, H.-F. Nolting, and N. V. Pavel, "Evidence for multielectron resonances at the Sr *K* edge", Physical Review A **53**, 798–805 (1996).

[158]T. M. Seward, C. M. B. Henderson, J. M. Charnock, and T. Driesner, "An EXAFS study of solvation and ion pairing in aqueous strontium solutions to 300℃", Geochimica et Cosmochimica Acta **63**, 2409–2418 (1999).

[159]T. Driesner and P. T. Cummings, "Molecular simulation of the temperature- and density-dependence of ionic hydration in aqueous $SrCl_2$ solutions using rigid and flexible water models", The Journal of Chemical Physics **111**, 5141 (1999).

[160]E. Spohr, G. Pálinkas, K. Heinzinger, P. Bopp, and M. M. Probst, "Molecular Dynamics Study of an Aqeous $SrCl_2$ Solution", Journal of Physical Chemistry **92**, 6754–6761 (1988).

[161]P. D'Angelo, V. Migliorati, F. Sessa, G. Mancini, and I. Persson, "XANES Reveals the Flexible Nature of Hydrated Strontium in Aqueous Solution", Journal of Physical Chemistry B **120**, 4114–4124 (2016).

[162]M. I. Cabaço, M. I. de Barros Marques, M. A. Marques, A. M. Gaspar, and M. L. de Almeida, "X-ray diffraction and Raman spectroscopy investigations in concentrated aqueous solutions of yttrium and strontium nitrates", Journal of Molecular Liquids **117**, 69–76 (2005).

[163]R. H. Parkman, J. M. Charnock, F. R. Livens, and D. J. Vaughan, "A study of the interaction of strontium ions in aqueous solution with the surfaces of calcite and kaolinite", Geochimica et Cosmochimica Acta **62**, 1481–1492 (1998).

[164]B. J. Palmer, D. M. Pfund, and J. L. Fulton, "Direct Modeling of EXAFS Spectra from Molecular Dynamics Simulations", The Journal of Physical Chemistry **100**, 13393–13398 (1996).

[165]L. X. Dang, G. K. Schenter, and J. L. Fulton, "EXAFS Spectra of the Dilute Solutions of Ca^{2+} and Sr^{2+} in Water and Methanol", Journal of Physical Chemistry B **107**, 14119–14123 (2003).

[166]D. J. Harris, J. P. Brodholt, and D. M. Sherman, "Hydration of Sr^{2+} in Hydrothermal Solutions from ab initio Molecular Dynamics", Journal of Physical Chemistry B **107**, 9056–9058 (2003).

[167]L. Axe, G. B. Bunker, P. R. Anderson, and T. A. Tyson, "An XAFS Analysis of Strontium at the Hydrous Ferric Oxide Surface", Journal of Colloid and Interface Science **199**, 44–52 (1998).

[168]G. W. Neilson and R. D. Broadbent, "The Structure of Sr^{2+} in Aqueous Solution", Chemical Physics Letters **167**, 429–431 (1990).

[169]J. Åqvist, "Ion-Water Interaction Potentials Derived from Free Energy Perturbation Slmulations", Journal of Physical Chemistry **94**, 8021–8024 (1990).

[170]T. S. Hofer, B. R. Randolf, and B. M. Rode, "Sr(II) in Water: A Labile Hydrate with a Highly Mobile Structure", Journal of Physical Chemistry B **110**, 20409–20417 (2006).

[171]N. N. Greenwood and A. Earnshaw, "Beryllium, Magnesium, Calcium, Strontium, Barium and Radium", in *Chemistry of the Elements*, 2nd (Elsevier Ltd, Linacre House, Jordan Hill, Oxford, 1997) Chap. 5, pp. 107–138.

[172]P. Patnaik, *Handbook of Inorganic Chemicals* (The McGraw-Hill Companies Inc., 2003), p. 886.

[173]M. D. Judd and M. I. Pope, "Monohydrates of Strontium and Barium Hydroxide, Their Preparation and X-ray Powder Patterns", Journal of Thermal Analysis **3**, 397–402 (1971).

[174]H. D. Lutz, W. Eckers, G. Schneider, and H. Haeuseler, "Raman and infrared spectra of barium and strontium hydroxides and hydroxide hydrates", Spectrochimica Acta **37A**, 561–567 (1981).

[175]H. D. Lutz, P. Kuske, and J. Henning, "LATTICE VIBRTION SPECTRA Part XLVI. Raman single crystal measurments on isostructural $Sr(OH)_2{\cdot}H_2O$ and $Ba(OH)_2{\cdot}H_2O$ o. - rh.: structure and bonding of hydroxide ions and water molecules", Journal of Molecular Structure **176**, 149–157 (1988).

[176]H. G. Smith, "The Crystal Structure of Strontium Hydroxide Octahydrate, $Sr(OH)_2{\cdot}8H_2O$", Acta Crystallographica **6**, 604–609 (1953).

[177]J. S. Ricci, R. C. Stevens, R. K. McMullan, and W. T. Klooster, "Structure of strontium hydroxide octahydrate, $Sr(OH)_28H_2O$, at 20, 100 and 200 K from neutron diffraction", Acta Crystallographica Section B: Structural Science **61**, 381–386 (2005).

[178]K. E. Gutowski and D. A. Dixon, “Predicting the Energy of the Water Exchange Reaction and Free Energy of Solvation for the Uranyl Ion in Aqueous Solution.”, The Journal of Physical Chemistry A **110**, 8840–56 (2006).

[179]E. Makkos, A. Kerridge, and N. Kaltsoyannis, “The importance of second shell effects in the simulation of hydrated Sr^{2+} hydroxide complexes”, Dalton Transactions **44**, 11572–11581 (2015).

[180]K. Eichkorn, O. Treutler, H. Öhm, M. Häser, and R. Ahlrichs, “Auxiliary basis sets to approximate Coulomb potentials”, Chemical Physics Letters **240**, 283–290 (1995).

[181]F. Weigend, “Accurate Coulomb-fitting basis sets for H to Rn”, Physical Chemistry Chemical Physics **8**, 1057–1065 (2006).

[182]J. P. Merrick, D. Moran, and L. Radom, “An Evaluation of Harmonic Vibrational Frequency Scale Factors”, The Journal of Physical Chemistry A **111**, 11683–11700 (2007).

[183]P. Ugliengo, *MOLDRAW: A Program to Display and Manipulate Molecular and Crystal Structures, Torino (2006) available on the web at: http:\\www.moldraw.unito.it*, Torino University.

[184]P. Ugliengo, G. Borzani, and D. Viterbo, “MOLDRAW - program for the graphical manipulation of molecules on personal computers”, Journal of Applied Crystallography **21**, 75 (1988).

[185]P. Ugliengo, D. Viterbo, and G. Chiari, Z. Kristallogr. **207**, 9 (1993).

[186]P. Terleczky and L. Nyulászi, “The Effect of the Primary Solvate Shell on the Mechanism of the Stöber Silica Synthesis. A Density Functional Investigation”, Journal of Physical Chemistry A **113**, 1096–1104 (2009).

[187]O. Hollóczki, P. Terleczky, D. Szieberth, G. Mourgas, D. Gudat, and L. Nyulászi, “Hydrolysis of Imidazole-2-ylidenes”, Journal of the American Chemical Society **133**, 780–789 (2011).

[188]R. Ludwig and F. Weinhold, “Quantum cluster equilibrium theory of liquids: Freezing of QCE/3-21G water to tetrakaidecahedral Bucky-ice”, The Journal of Chemical Physics **110**, 508–515 (1999).

[189]M. V. Kirov, “Atlas of Optimial Proton Configuration of Water Clusters in the Form of Gas Hydrate Cavities”, Journal of Structural Chemistry **43**, 790–797 (2002).

[190]R. Ludwig, “Water: From Clusters to the Bulk.”, Angewandte Chemie (International ed. in English) **40**, 1808–1827 (2001).

[191] P. Wernet, D. Nordlund, U. Bergmann, M. Cavalleri, M. Odelius, H. Ogasawara, L. A. Näslund, T. K. Hirsch, L. Ojamäe, P. Glatzel, L. G. M. Pettersson, and A. Nilsson, "The Structure of the First Coordination Shell in Liquid Water", Science **304**, 995–999 (2004).

[192] S. Myneni, Y. Luo, L. A. Näslund, M. Cavalleri, L. Ojamäe, H. Ogasawara, A. Pelmenschikov, P. Wernet, P. Väterlein, C. Heske, Z. Hussain, L. G. M. Pettersson, and A. Nilsson, "Spectroscopic probing of local hydrogen-bonding", Journal of Physics: Condensed Matter **14**, 213–219 (2002).

[193] E. Schwegler, G. Galli, and F. Gygi, "Water under Pressure", Physical Review Letters **84**, 2429–2432 (2000).

[194] J. D. Smith, C. D. Cappa, K. R. Wilson, B. M. Messer, R. C. Cohen, and R. J. Saykally, "Energetics of Hydrogen Bond Network Rearrangements in Liquid Water.", Science **306**, 851–853 (2004).

[195] H.-S. Lee and M. E. Tuckerman, "Structure of liquid water at ambient temperature from *ab initio* molecular dynamics performed in the complete basis set limit.", The Journal of Chemical Physics **125**, 154507 (2006).

[196] A. K. Soper, F. Bruni, and M. A. Ricci, "Site-site pair correlation functions of water from 25 to 400℃: Revised analysis of new and old diffraction data", The Journal of Chemical Physics **106**, 247–254 (1997).

[197] C. Nieto-Draghi, J. B. Avalos, and B. Rousseau, "Dynamic and structural behavior of different rigid nonpolarizable models of water", The Journal of Chemical Physics **118**, 7954–7964 (2003).

[198] H. Ohtaki and T. Radnai, "Structure and Dynamics of Hydrated Ions", Chemical Reviews **93**, 1157–1204 (1993).

[199] J. Burgess, "Basic Principles of Chemical Interactions", in *Ions in solution* (Horwood Publishing Limited, Chichester, West Sussex, England, 1999) Chap. 9, pp. 111–123.

[200] P. D'Arco, M. Causà, C. Roetti, and B. Silvi, "Periodic Hartree-Fock study of a weakly bonded layer structure: Brucite $Mg(OH)_2$", Physical Review B **47**, 3522–3529 (1993).

[201] P. Baranek, A. Lichanot, R. Orlando, and R. Dovesi, "Structural and vibrational properties of solid $Mg(OH)_2$ and $Ca(OH)_2$ - performances of various hamiltonians", Chemical Physics Letters **340**, 362–369 (2001).

[202] F. Pascale, S. Tosoni, C. Zicovich-Wilson, P. Ugliengo, R. Orlando, and R. Dovesi, "Vibrational spectrum of brucite, $Mg(OH)_2$: a periodic ab initio quantum mechanical calculation including OH anharmonicity", Chemical Physics Letters **396**, 308–315 (2004).

[203]F. Zigan and R. Rothbauer, “Neutronenbeugungsmessungen am Brucit”, Neues Jahrbuch fuer Mineralogie **4**, 137–143 (1967).

[204]M. Catti, G. Ferraris, S. Hull, and A. Pavese, “Static Compression and H Disorder in Brucite , $Mg(OH)_2$, to 11 GPa: a Powder Neutron Diffraction Study”, Physics and Chemsitry on Minerals **22**, 200–206 (1995).

[205]B. C. Chakoumakos, C.-K. Loong, and A. J. Schultz, “Low-Temperature Structure and Dynamics of Brucite”, Journal of Physical Chemistry B **101**, 9458–9462 (1997).

[206]P. Ugliengo, C. M. Zicovich-Wilson, S. Tosoni, and B. Civalleri, “Role of dispersive interactions in layered materials: a periodic B3LYP and B3LYP-D* study of $Mg(OH)_2$, $Ca(OH)_2$ and kaolinite”, Journal of Materials Chemistry **19**, 2564–2572 (2009).

[207]R. LeSar and R. G. Gordon, “Electron-gas model for molecular crystals. Application to the alkali and alkaline-earth hydroxides”, Physical Review B **25**, 7221–7237 (1982).

[208]D. M. Sherman, “Hartree-Fock band structure, equation of state, and pressure-induced hydrogen bonding in brucite, $Mg(OH)_2$”, American Mineralogist **76**, 1769–1772 (1991).

[209]B. Winkler, V. Milman, B. Hennion, M. C. Payne, M.-H. Lee, and J. S. Lin, “Ab Initio Total Energy Study of Brucite, Diaspore and Hypothetical Hydrous Wadsleyite”, Physics and Chemsitry on Minerals **22**, 461–467 (1995).

[210]K. Azuma, T. Oda, and S. Tanaka, “Vibration analysis of O-H stretching mode in $Mg(OH)_2$, $Ca(OH)_2$, LiOH, and NaOH by plane-wave pseudopotential DFT calculation”, Computational and Theoretical Chemistry **963**, 215–220 (2011).

[211]S. J. Clark, M. D. Segall, C. J. Pickard, P. J. Hasnip, M. J. Probert, K Refson, and M. C. Payne, “First principles methods using CASTEP”, Zeitschrift fuer Kristallographie **220**, 567–570 (2005).

[212]B. Civalleri, C. M. Zicovich-Wilson, L. Valenzano, and P. Ugliengo, “B3LYP augmented with an empirical dispersion term (B3LYP-D*) as applied to molecular crystals”, CrystEngComm **10**, 405–410 (2008).

[213]A. M. Chaka and A. R. Felmy, “Ab Initio Thermodynamic Model for Magnesium Carbonates and Hydrates”, The Journal of Physical Chemistry A **118**, 7469–7488 (2014).

[214]B. Delley, “An all-electron numerical method for solving the local density functional for polyatomic molecules”, The Journal of Chemical Physics **92**, 508–517 (1990).

[215]B. Delley, “From molecules to solids with the DMol3 approach”, The Journal of Chemical Physics **113**, 7756–7764 (2000).

[216]T. Murakami, T. Honjo, and T. Kuji, “DOS Calculation Analysis of New Transparent Conductor $Mg(OH)_2$-C”, Materials Transactions **52**, 1689–1692 (2011).

[217]A. Pishtshev, S. Z. Karazhanov, and M. Klopov, “Materials properties of magnesium and calcium hydroxides from first-principles calculations”, Computational Materials Science **95**, 693–705 (2014).

[218]C.-H. Huang, Y.-L. Jan, and W.-C. Lee, “Investigation of Mg(O,OH) Films Prepared by Chemical Bath Deposition as Buffer Layers for Cu(In,Ga)Se_2 Solar Cells”, Journal of The Electrochemical Society **158**, H879–H888 (2011).

[219]L. Kumari, W. Z. Li, C. H. Vannoy, R. M. Leblanc, and D. Z. Wang, “Synthesis, characterization and optical properties of $Mg(OH)_2$ micro-/nanostructure and its conversion to MgO”, Ceramics International **35**, 3355–3364 (2009).

[220]S. Z. Karazhanov, A. Pishtshev, and M. Klopov, “Electronic and optical properties of magnesium and calcium hydroxides: The role of covalency and many-body effects”, Physica Scripta **90**, 094015 (2015).

[221]M. B. Kruger, Q. Williams, and R. Jeanloz, “Vibrational spectra of $Mg(OH)_2$ and $Ca(OH)_2$ under pressure”, The Journal of Chemical Physics **91**, 5910–5915 (1989).

[222]D. E. Haycock, M. Kasrai, C. J. Nicholls, and D. S. Urch, “The Electronic Structure of Magnesium Hydroxide (Brucite) using *X*-Ray Emission, *X*-Ray Photoelectron and Auger Secptroscopy”, Journal of Chemical Society, Dalton Transactions **12**, 1791–1796 (1978).

[223]J. D. Bernal and H. D. Megaw, “The Function of Hydrogen in Intermolecular Forces”, Proceedings of the Royal Society of London A **151**, 384–420 (1935).

[224]P. Dawson, C. D. Hadfield, and G. R. Wilkinson, “The Polarized Infra-Red and Raman Spectra of $Mg(OH)_2$ and $Ca(OH)_2$”, Journal of Physics and Chemistry of Solids **34**, 1217–1225 (1973).

[225]B. Weckler and H. D. Lutz, “Near-infrared spectra of M(OH)Cl (M = Ca, Cd, Sr), Zn(OH)F, (γ-$Cd(OH)_2$), $Sr(OH)_2$, and brucite-type hydroxides $M(OH)_2$ (M=Mg, Ca, Mn, Fe, Co, Ni, Cd)”, Spectrochimica Acta A **52**, 1507–1513 (1996).

[226]E. F. de Oliveira and Y. Hase, “Infrared study and isotopic effect of magnesium hydroxide”, Vinrational Spectroscopy **25**, 53–56 (2001).

[227]P. S. Braterman and R. T. Cygan, “Vibrational spectroscopy of brucite: A molecular simulation investigation”, American Mineralogist **91**, 1188–1196 (2006).

[228]G. Wulff, “Zur Frage der Geschwindigkeit des Wachsthums und der Auflösung der Krystallflächen”, Zeitschrift für Krystallographie und Mineralogie **34**, 449 (1901).

[229]P. Masini and M. Bernasconi, "*AB INITIO* SIMULATIONS OF HYDROXYLATION AND DEHYDROXYLATION REACTIONS AT SURFACES: AMORPHOUS SILICA AND BRUCITE", Journal of Physics: Condensed Matter **14**, 4133–4144 (2002).

[230]S. V. Churakov, M. Iannuzzi, and M. Parrinello, "Ab Initio Study of Dehydroxylation - Carbonation Reaction on Brucite Surface", Journal of Chemical Physics B **108**, 11567–11574 (2004).

[231]Q. Wang, L. Xiang, Y. C. Zhang, and Y. Jin, "Simulation of the adsorption of $CaCl_2$ on $Mg(OH)_2$ planes", Journal of Materials Science **43**, 2387–2392 (2008).

[232]M. R. Carrott, P. Carrott, M. B. de Carvalho, and K. S. W. Sing, "Ex-hydroxide Magnesium Oxide as a Model Adsorbent for Investigation of Micropore Filling Mechanisms", Journal of Chemical Society, Faraday Transactions **87**, 185–191 (1991).

[233]T. R. Zeitler, J. A. Greathouse, J. D. Gale, and R. T. Cygan, "Vibrational Analysis of Brucite Surfaces and the Development of an Improved Force Field for Molecular Simulation of Interfaces", The Journal of Physical Chemistry C **118**, 7946–7953 (2014).

[234]V. Ballenegger, A. Arnold, and J. J. Cerdà, "Simulations of non-neutral slab systems with long-range electrostatic interactions in two-dimensional periodic boundary conditions", The Journal of Chemical Physics **131**, 094107 (2009).

[235]J. S. Hub, B. L. de Groot, H. Grubmüller, and G. Groenhof, "Quantifying Artifacts in Ewald Simulations of Inhomogeneous Systems with a Net Charge", Journal of Chemical Theory and Computation **10**, 381–390 (2014).

[236]A. A. Shubin, G. M. Zhidomirov, V. B. Kazansky, and R. A. van Santen, "DFT cluster modeling of molecular and dissociative hydrogen adsorption on Zn^{2+} ions with distant placing of aluminum in the framework of high-silica zeolites", Catalysis Letters **90**, 137–142 (2003).

[237]D. M. Sherman, C. L. Peacock, and C. G. Hubbard, "Surface complexation of U(VI) on goethite (α-FeOOH)", Geochimica et Cosmochimica Acta **72**, 298–310 (2008).

[238]G. Pacchioni, "Modeling doped and defective oxides in catalysis with density functional theory methods: Room for improvements", Journal of Chemical Physics **128**, 182505 (2008).

[239]B. Herschend, M. Baudin, and K. Hermansson, "CO adsorption on CeO2(110) using hybrid-DFT embedded-cluster calculations", Chemical Physics **328**, 345–353 (2006).

[240]J. L. F. Da Silva, M. V. Ganduglia-Pirovano, J. Sauer, V. Bayer, and G. Kresse, "Hybrid functionals applied to rare-earth oxides: The example of ceria", Physical Review B **75**, 045121 (2007).

[241] E. H. Teunissen, A. P. J. Jansen, R. A. van Santen, R. Orlando, and R. Dovesi, "Adsorption energies of NH_3 and NH_4^+ in zeolites corrected for the long-range electrostatic potential of the crystal", The Journal of Chemical Physics **101**, 5865–5874 (1994).

[242] J. M. Vollmer, E. V. Stefanovich, and T. N. Truong, "Molecular Modeling of Interactions in Zeolites : An Ab Initio Embedded Cluster Study of NH_3 Adsorption in Chabazite", The Journal of Physical Chemistry B **103**, 9415–9422 (1999).

[243] E. Makkos, A. Kerridge, J. Austin, and N. Kaltsoyannis, "Ionic adsorption on the brucite (0001) surface : A periodic electrostatic embedded cluster method study", Journal of Chemical Physics **145**, 204708 (2016).

[244] "This image was made with VMD software support. VMD is developed with NIH support byt the Theoretical and Computational Biophysics group at the Beckman Institute, University of Illinois at Urbana-Champaign. http://www.ks.uiuc.edu/",

[245] J. P. W. Wellington, A. Kerridge, and N. Kaltsoyannis, "Should environmental effects be included when performing QTAIM calculations on actinide systems? A comparison of QTAIM metrics for $Cs_2UO_2Cl_4$, $U(Se_2PPh_2)_4$ and $Np(Se_2PPh_2)_4$ in gas phase, COSMO and PEECM", Polyhedron **116**, 57–63 (2016).

[246] A. Kerridge and N. Kaltsoyannis, "Theoretical studies of the surface complexation of strontium hydrates with brucite", Proceedings of the DIAMOND 2011 Conference, Coventry, UK (2011).

[247] M. F. Peintinger, D. V. Oliveira, and T. Bredow, "Consistent Gaussian Basis Sets of Triple-Zeta Valence with Polarization Quality for Solid-State Calculations", Journal of Computational Chemistry **34**, 451–459 (2013).

[248] A. Erba, K. E. El-Kelany, M. Ferrero, I. Baraille, and M. Rérat, "Piezoelectricity of SrTiO: An *ab initio* description", Physical Review B **88**, 035102 (2013).

[249] J. L. F. Da Silva, C. Stampfl, and M. Scheffler, "Converged properties of clean metal surfaces by all-electron first-principles calculations", Surface Science **600**, 703–715 (2006).

[250] M. Sierka, personal communication, 15th of November, 2016.

[251] I. Alkorta, I. Rozas, and J. Elguero, "Bond Length-Electron Density Relationships: From Covalent Bonds to Hydrogen Bond Interactions", Structural Chemistry **9**, 243 (1998).

[252] M. A. Henderson, "The interaction of water with solid surfaces : fundamental aspects revisited", Surface Science Reports **46**, 1–308 (2002).

[253]K. Oura, V. G. Lifshits, A. A. Saranin, A. V. Zotov, and M. Katayama, "Surface Phases in Submonolayer Adsorbate/Substrate Systems", in *Surface science, an introduction* (Springer-Verlag Berlin Heidelberg, 2003) Chap. 9. Pp. 195–196.

[254]M. Corno, C. Busco, V. Bolis, S. Tosoni, and P. Ugliengo, "Water Adsorption on the Stoichiometric (001) and (010) Surfaces of Hydroxyapatite: A Periodic B3LYP Study", Langmuir **25**, 2188–2198 (2009).

[255]"Adsorption", in *IUPAC Compendium of Chemical Terminology, The "Orange Book"*, Vol. 62, edited by A. D. McNaught, A Wilkinson, M Nic, J Jirat, B Kosata, and A Jenkins (Blackwell Scientific Publications, Oxford, 1990) Chap. Glossary of atmospheric chemistry terms (Recommendations 1990, p. 2171.

[256]"Ion Exchange", in *IUPAC Compendium of Chemical Terminology, The "Orange Book"*, Vol. 31, edited by A. D. McNaught, A Wilkinson, M Nic, J Jirat, B Kosata, and A Jenkins (Blackwell Scientific Publications, Oxford, 1972) Chap. Manual of Symbols and Terminology for Physicochemical Quantities and Units, Appendix II: Definitions, Terminology and Symbols in Colloid and Surface Chemistry, p. 585.

[257]M. P. Andersson, H. Sakuma, and S. L. S. Stipp, "Strontium, Nickel, Cadmium, and Lead Substitution into Calcite, Studied by Density Functional Theory", Langmuir **30**, 6129–6133), year = 2014.

[258]S. Coluccia, L. Marchese, S. Lavagnino, and M. Anpo, "Hydroxyls on the surface of MgO powders", Spectrochimica Acta Part A: Molecular Spectroscopy **43**, 1573–1576 (1987).

[259]Y. Kuroda, E. Yasugi, H. Aoi, K. Miura, and T. Morimoto, "Interaction of Water with the Magnesium Oxide Surface", Journal of Chemical Society, Faraday Transactions **84**, 2421–2430 (1988).

[260]E. Knözinger, K.-H. Jacob, S. Singh, and P. Hofmann, "Hydroxyl groups as IR active surface probes on MgO crystallites", Surface Science **290**, 388–402 (1993).

[261]J. A. Mejias, A. J. Berry, K. Refson, and D. G. Fraser, "The kinetics and mechanism of MgO dissolution", Chemical Physics Letters **314**, 558–563 (1999).

[262]P. Liu, T. Kendelewicz, G. E. Brown Jr., and G. A. Parks, "Reaction of water with MgO(100) surfaces. Part I: Synchrotron X-ray photoemission studies of low-defect surfaces", Surface Science **412-13**, 287–314 (1998).

[263]P. Liu, T. Kendelewicz, and G. E. Brown Jr., "Reaction of water with MgO(100) surfaces. Part II: Synchrotron photoemission studies of defective surfaces", Surface Science **412-13**, 315–332 (1998).

[264]P. Liu, T. Kendelewicz, E. J. Nelson, and G. E. Brown Jr., "Reaction of water with MgO(100) surfaces: Part III. X-ray standing wave studies", Surface Science **415**, 156–169 (1998).

[265]A. J. Berry, D. G. Fraser, G. W. Grime, J. Craven, and J. T. Sleeman, "The hydration and dissolution of periclase", Mineralogical Magazine **62A**, 158–159 (1998).

[266]R. F. Horlock, P. L. Morgan, and P. J. Anderson, "Effects of Water Vapour on the Decomposition of Magnesium Hydroxide", Transactions of the Faraday Society **59**, 721–728 (1963).

[267]S. M. Nelson, A. C. D. Newman, T. E. Tomlinson, and L. E. Sutton, "A Dielectric Study of the Adsorption of Water by Magnesium Hydroxide", Transactions of the Faraday Society **55**, 2186–2202 (1959).

[268]O. S. Pokrovsky and J. Schott, "Experimental study of brucite dissolution and precipitation in aqueous solutions: surface speciation and chemical affinity control", Geochimica et Cosmochimica Acta **68**, 31–45 (2004).

[269]W. Langel and M. Parrinello, "Hydrolysis at stepped MgO surfaces", Physical Review Letters **73**, 504–507 (1994).

[270]W. Langel and M. Parrinello, "*AB INITIO* MOLECULAR DYNAMICS OF H_2O ADSORBED ON SOLID MGO", The Journal of Chemical Physics **103**, 3240–3252 (1995).

[271]N. H. de Leeuw and S. C. Parker, "Molecular-dynamics simulation of MgO surfaces in liquid water using a shell-model potential for water", Physical Review B **58**, 13901–13908 (1998).

[272]C. A. Scamehorn, A. C. Hess, and M. I. McCarthy, "Correlation corrected periodic Hartree-Fock study of the interactions between water and the (001) magnesium oxide surface", The Journal of Chemical Physics **99**, 2786–2795 (1993).

[273]C. Minot, "Water molecule dissociation at ice/MgO(100) interface", Surface Science **562**, 237–246 (2004).

[274]M. I. McCarthy, G. K. Schenter, C. A. Scamehorn, and J. B. Nicholas, "Structure and Dynamics of the Water/MgO Interface", Journal of Physical Chemistry **100**, 16989–16995 (1996).

[275]K. Refson, R. A. Wogelius, D. G. Fraser, M. C. Payne, M. H. Lee, and V. Milman, "Water chemisorption and reconstruction of the MgO surface", Physical Review B **52**, 823–827 (1995).

[276]I. D. Gay and N. M. Harrison, "A density functional study of water and methanol chemisorption on MgO(110)", Surface Science **591**, 13–22 (2005).

[277]H. Sakuma, T. Tsuchiya, K. Kawamura, and K. Otsuki, “Large self-diffusion of water on brucite surface by ab initio potential energy surface and molecular dynamics simulations”, Surface Science **536**, L396–L402 (2003).

[278]H. Sakuma, T. Tsuchiya, K. Kawamura, and K. Otsuki, “Local Behavior of Water Molecules on Brucite, Talc, and Halite Surfaces: A Molecular Dynamics Study”, Molecular Simulation **30**, 861–871 (2004).

[279]J. Wang, A. G. Kalinichev, and R. J. Kirkpatrick, “Molecular modeling of water structure in nano-pores between brucite (001) surfaces”, Geochimica et Cosmochimica Acta **68**, 3351–3365 (2004).

[280]J. Wang, A. G. Kalinichev, and R. J. Kirkpatrick, “Effects of substrate structure and composition on the structure, dynamics, and energetics of water at mineral surfaces: A molecular dynamics modeling study”, Geochimica et Cosmochimica Acta **70**, 562–582 (2006).

[281]W. A. Deer, R. A. Howie, and J. Zussman, “Oxides”, in *An introduction to the rock-forming minerals*, second edi (Longman Group Ltd. and John Wiley & Sons Inc., 1992), pp. 532–533.

[282]P. J. Anderson and R. F. Horlock, “Thermal Decomposition of Magnesium Hydroxide”, Transactions of the Faraday Society **58**, 1993–2004 (1962).

[283]D. P. Butt, K. S. Lackner, C. H. Wendt, S. D. Conzone, H. Kung, Y.-C. Lu, and J. K. Bremser, “Kinetics of Thermal Dehydroxylation and Carbonation of Magnesium Hydroxide”, Journal Of The American Ceramic Society **79**, 1892–1898 (1996).

[284]H. Béarat, M. J. McKelvy, A. V. G. Chizmeshya, R. Sharma, and R. W. Carpenter, “Magnesium Hydroxide Dehydroxylation/Carbonation Reaction Processes: Implications for Carbon Dioxide Mineral Sequestration”, Journal of the American Ceramic Society **85**, 742–748 (2002).

[285]H. Schott, “Electrokinetic Studies of Magnesium Hydroxide”, Journal of Pharmaceutical Sciences **70**, 486–489 (1981).

[286]W. Strumm and J. J. Morgan, “Simple Rate Laws in Dissolution”, in *Aquatic chemistry: chemical equilibria and rates in natural waters*, third (J. Wiley & Sons, 1996) Chap. 13.4, p. 779.

[287]Q. Wang and D. O’Hare, “Recent Advances in the Synthesis and Application of Layered Double Hydroxide (LDH) Nanosheets”, Chemical Reviews **112**, 4124–4155 (2012).

[288]C. Li, M. Wei, D. G. Evans, and X. Duan, “Layered Double Hydroxide-Based Nanomaterials as Highly Efficient Catalysts and Adsorbents”, Small **10**, 4469–4486 (2014).

[289]C. F. Estrada, D. A. Sverjensky, M. Pelletier, A. Razafitianamaharavo, and R. M. Hazen, "Interaction between L-aspartate and the brucite [$Mg(OH)_2$]-water interface", Geochimica et Cosmochimica Acta **155**, 172–186 (2015).

[290]V. S. Vaiss, I. Borges Jr., and A. A. Leit, "Sarin Degradation Using Brucite", The Journal of Pysical Chemistry C **115**, 24937–24944 (2011).

[291]V. S. Vaiss, R. A. Berg, A. R. Ferreira, I. Borges Jr., and A. A. Leitão, "Theoretical Study of the Reaction bBetween HF Molecules and Hydroxyl Layers of $Mg(OH)_2$", The Journal of Physical Chemistry A **113**, 6494–6499 (2009).

[292]Z. Chen, Z. Zhuang, Q. Cao, X. Pan, X. Guan, and Z. Lin, "Adsorption-Induced Crystallization of U-Rich Nanocrystals on Nano-$Mg(OH)_2$ and the Aqueous Uranyl Enrichment", ACS Applied Materials and Interfaces **6**, 1301–1305 (2014).

[293]X. Ou, Z. Zhuang, J. Li, F. Huang, and Z. Lin, "Mechanism of adsorption affinity and capacity of $Mg(OH)_2$ to uranyl revealed by molecular dynamics simulation", RSC Advances **6**, 31507–31513 (2016).

[294]H. Yan, J. Bai, X. Chen, J. Wang, H. Zhang, Q. Liu, M. Zhang, and L. Liu, "High U(VI) adsorption capacity by mesoporous $Mg(OH)_2$ deriving from MgO hydrolysis", RSC Advances **3**, 23278–23289 (2013).

[295]W. Liu, F. Huang, Y. Liao, J. Zhang, G. Ren, Z. Zhuang, J. Zhen, Z. Lin, and C. Wang, "Treatment of Cr^{VI} -Containing $Mg(OH)_2$ Nanowaste **", Angewandte Chemie - International Edition **120**, 5701–5704 (2008).

[296]C. Li, Z. Zhuang, F. Huang, Z. Wu, Y. Hong, and Z. Lin, "Recycling Rare Earth Elements from Industrial Wastewater with Flowerlike Nano-$Mg(OH)_2$", ACS Applied Materials and Interfaces **5**, 9719–9725 (2013).

[297]A. Kerridge and N. Kaltsoyannis, "Microsolvation of the Sr^{2+} ion and its interactions with the brucite [001] surface", Proceedings of the DIAMOND 2010 Conference, Manchester, UK (2010).

[298]M. Faheem, S. Suthirakun, and A. Heyden, "New Implicit Solvation Scheme for Solid Surfaces", The Journal of Physical Chemistry C **116**, 22458–22462 (2012).

[299]J. Austin and S. Kellett, confidential National Nuclear Laboratory reports, personal communication.

[300]B. Prélot, F. Villiéras, M. Pelletier, G. Gérard, F. Gaboriaud, J. J. Ehrhardt, J. Perrone, M. Fedoroff, J. Jeanjean, G. Lefèvre, L. Mazerolles, J. L. Pastol, J. C. Rouchaud, and

C. Lindecker, “Morphology and surface heterogeneities in synthetic goethites”, Journal of Colloid and Interface Science **261**, 244–254 (2003).

[301] X. Liu, J. Cheng, M. Sprik, X. Lu, and R. Wang, “Understanding surface acidity of gibbsite with first principles molecular dynamics simulations”, Geochimica et Cosmochimica Acta **120**, 487–495 (2013).

Appendices

Appendix A

Periodic DFT models

The k mesh convergence for the bulk structure was calculated with using a primitive unit cell and 3D periodic conditions, while both the cell parameters and atomic positions were free to move. Above the shrinking factor of 8 the a and c cell parameters did not change and the energy difference was always below 10^{-6} a.u..

Table A.1: k mesh convergence for the bulk structure calculations with CRYSTAL. (IS=shrinking factor in reciprocal space)

IS	SCF energy (a.u.)	E_{diff} (a.u.)	a (Å)	c (Å)
2	-351.7079874	-	3.23355	4.69382
4	-351.7218124	-1.38E-02	3.17736	4.75045
6	-351.7219477	-1.35E-04	3.17653	4.75109
8	-351.7219507	-3.06E-06	3.17651	4.75114
10	-351.7219509	-1.21E-07	3.17651	4.75114
12	-351.7219509	-6.40E-09	3.17651	4.75114

The k mesh convergence of the ***5x5_1*** unit cell was calculated for the unrelaxed cell, directly constructed from the optimised bulk geometry.

Table A.2: k mesh convergence for the *5x5_1* structure calculations with CRYSTAL. (IS=shrinking factor in reciprocal space)

IS	SCF energy (a.u.)	E_{diff} (a.u.)
2	-8792.8529891	
4	-8792.8529891	-4.20E-08
6	-8792.8529893	-1.68E-07
8	-8792.8529892	6.00E-08
10	-8792.8529892	0.00E+00

Table A.3: Calculated SCF energies of the considered supercells in CRYSYAL, including 1,2 and 3 brucite layers in the slab.

SCF energy (a.u.)			
Unit cell size	**Number of brucite layers**		
	_1	***_2***	***_3***
3x3	-3165.4270	-6330.9254	-9496.4228
5x5	-8792.8530	-17585.9044	-26378.9525
7x7	-17233.9919	-34468.3726	-51702.7472
9x9	-28488.8437	-56978.3301	-85467.8063